

TECHNISCHE UNIVERSITÄT MÜNCHEN

Lehrstuhl für Technische Elektronik

**Perpendicular Nanomagnetic Logic:
Digital Logic Circuits from Field-coupled Magnets**

Stephan Werner Georg Breitzkreutz-von Gamm

Vollständiger Abdruck der von der Fakultät für Elektrotechnik und Informationstechnik der Technischen Universität München zur Erlangung des akademischen Grades eines

Doktor-Ingenieurs

genehmigten Dissertation.

Vorsitzender: Univ.-Prof. Dr. rer. nat. Marc Tornow

Prüfer der Dissertation:

1. Univ.-Prof. Dr. rer. nat. Doris Schmitt-Landsiedel
2. Prof. György Csaba
University of Notre Dame, USA

Die Dissertation wurde am 13.01.2015 bei der Technischen Universität München eingereicht und durch die Fakultät für Elektrotechnik und Informationstechnik am 10.04.2015 angenommen.

Preface

"Engineering (from Latin ingenium, meaning 'cleverness' and ingeniare, meaning 'to contrive, devise') is the application of scientific, economic, social, and practical knowledge in order to invent, design, build, maintain, and improve structures, machines, devices, systems, materials and processes." [1]

This work is about engineering the characteristics and interaction of nanoscale magnets with perpendicular magnetization in order to provide digital computation in nonvolatile logic circuits from field-coupled magnets. The corresponding technology is stated as *perpendicular Nanomagnetic Logic* and one of the promising emerging technologies for future logic devices [2].

Abstract

The progressive improvement of common complementary metal-oxide semiconductor (CMOS) technology implicates increasing technological challenges and dramatically raising manufacturing costs with every new technology node. Due to physical, technological and economical constraints of future nodes, several emerging beyond-CMOS technologies are explored, which compete for the succession of CMOS or the implementation in hybrid integrated circuits (ICs). One promising candidate is Nanomagnetic Logic (NML), which employs the interaction of field-coupled, nonvolatile magnets to perform logic operations.

This work investigates perpendicular Nanomagnetic Logic (pNML), using magnets with a bistable, perpendicular magnetization state (up/down), which is binary coded to represent the digital states 1 and 0. In addition to general features of NML like non-volatility and majority logic, pNML provides fundamental advantages of tunable, but shape-independent switching characteristics and inherent directed signal flow.

This work demonstrates operating, digital logic circuits from such field-coupled magnets at the nanoscale by experiment. Special focus is put on the demonstration of the fundamental principles of pNML and their application in basic computing devices and logic circuits.

Magnetic force and magneto-optical measurements are performed to investigate the characteristics of field-coupled magnets and to image the computational states within pNML logic circuits. Majority gates, inverter structures and magnetic interconnects as elemental devices required to form logic circuits are developed, demonstrated and characterized by experiment.

Digital logic circuits are exemplary demonstrated by proving correct logic operating of a 1-bit full adder circuit. Benefits of the implementation of threshold logic into pNML are experimentally demonstrated. Simulations using calibrated, physical-based compact models substantiate the experimental results and provide an outlook on pNML in terms of scaling and material improvements. Suitable architectures, methods for signal routing and processing of bit streams within complex pNML systems are discussed.

The present work demonstrates that pNML in some extent even exceeds the requirements on emerging beyond-CMOS devices and is a promising emerging device candidate for hybrid CMOS/pNML integrated circuits.

Contents

1	Introduction	1
1.1	Emerging beyond-CMOS devices	1
1.1.1	Requirements on beyond-CMOS devices	3
1.1.2	Overview on beyond-CMOS device candidates	5
1.2	Nanomagnetic Logic (NML)	6
1.2.1	Historical evolution	7
1.2.2	Perpendicular Nanomagnetic Logic (pNML)	10
1.3	Contribution of this work	13
1.4	Outline of the thesis	14
2	Basic Principles of pNML Magnetism	15
2.1	Micromagnetics	15
2.1.1	Micromagnetic energies	16
2.1.2	Magnetization dynamics	19
2.2	Magnetic multilayers	21
2.2.1	Anisotropy in magnetic multilayers	21
2.2.2	Co/Pt multilayers for pNML	22
2.2.3	Anisotropy tuning by focused ion beam irradiation	25
2.3	Domain theory	27
2.3.1	Domain walls (DWs)	28
2.3.2	Nucleation of DWs	29
2.3.3	DW propagation	31
2.3.4	Pinning of DWs	33
2.3.5	DW nucleation from artificial nucleation centers	36
2.4	Hysteresis curve	37
2.5	Time-dependent magnetization dynamics	39
2.6	Magnetic fringing fields	40
2.6.1	Point-dipole approximation	41
2.6.2	Coupling field of a Co/Pt nanomagnet	41
3	Metrology of Magnetic Nanostructures	43
3.1	Magneto-optical microscopy	43
3.1.1	Magneto-optical Kerr effect (MOKE)	44
3.1.2	Laser-scanning Kerr microscopy (LSMOKE)	50

3.1.3	Wide-field Kerr microscopy (WMOKE)	55
3.2	Magnetic force microscopy (MFM)	59
3.2.1	Basic working principle of MFM	59
3.2.2	Extension by a 3D magnetic field module	61
3.3	Further magnetic metrology	61
4	Fabrication Technology	63
4.1	Sample preparation	63
4.2	Co/Pt multilayer deposition	65
4.3	Patterning of Co/Pt nanomagnets	66
4.3.1	FIB lithography	66
4.3.2	Hard mask evaporation & lift-off	67
4.3.3	Ion beam etching	67
4.4	Partial FIB irradiation	67
4.5	On-chip coil fabrication	69
5	Fundamentals of pNML	71
5.1	Partial irradiation	73
5.1.1	Fabrication of ANCs in magnetic multilayers	73
5.1.2	Application of ANCs to Co/Pt nanomagnets	74
5.1.3	Characteristics of FIB-induced ANCs	74
5.2	Directed signal flow	78
5.3	Clocking and speed	80
5.3.1	DW velocity	82
5.3.2	DW nucleation probability	84
5.3.3	Influence of field-coupling	87
5.4	Logic operation	90
6	Basic pNML Devices	93
6.1	Inverter	93
6.1.1	Basic principle	93
6.1.2	Improvement of field-interaction	95
6.2	Majority gate	96
6.2.1	Concept	96
6.2.2	Experimental demonstration	97
6.2.3	Advanced calculations	101
6.3	Magnetic interconnects	104
6.3.1	Magnetic nanowires	104
6.3.2	Fanout structures	107

7	pNML Circuitry	111
7.1	1-bit full adder	111
7.1.1	Signal analysis and model synthesis	111
7.1.2	Signal propagation and clocking	114
7.1.3	Experiment	115
7.2	Threshold logic gate-based pNML	117
7.2.1	Threshold Logic	118
7.2.2	Threshold logic gates in pNML	119
7.2.3	TLG-based 1-bit full adder	120
7.3	Simulation of pNML circuitry	125
7.3.1	Compact modeling	125
7.3.2	Potential of pNML	129
8	Towards pNML Systems	133
8.1	Architecture	133
8.2	Signal routing	135
8.2.1	Processing of magnetic bit streams	135
8.2.2	Controlled DW motion	136
8.3	Domain wall gate (DWG)	137
8.3.1	Working principle	138
8.3.2	Micromagnetic simulation	140
8.3.3	Notches in magnetic nanowires	142
8.3.4	Experimental demonstration of the DWG	143
8.3.5	3D integration and applications	147
8.4	Alternative concepts for signal routing	149
8.5	Arithmetic logic unit (ALU)	150
8.5.1	Working principle	151
8.5.2	Simulation	152
8.5.3	Application in pNML systems	154
9	Conclusion	155
	Acronyms	159
	List of Symbols	163
	Publications of the Author	169
	Contributions of the Author	173
	References	177
	Related Theses	195

List of Figures

1.1	Technology node of the semiconductor manufacturing process. . .	2
1.2	Relationship of "More Moore", "More-than-Moore" and "Beyond-CMOS"	3
1.3	Research on Magnetic Logic and milestones in the evolution of perpendicular Nanomagnetic Logic (pNML).	7
1.4	Vision of an integrated pNML system.	11
2.1	Magnetization dynamics and its application in micromagnetic simulations.	19
2.2	Sketch (a) and TEM image (b) of an as-grown Co/Pt multilayer stack.	24
2.3	a) Irradiation-induced atom displacement leads to interface roughening (short-range motion) and alloying (long-ranged intermixing). b) TEM images of a Co/Pt multilayer stack as deposited and after Ga^+ irradiation.	26
2.4	The magnetization tends to form domains separated by domain walls in order to minimize the total energy (a). The magnetization in DWs can rotate parallel (Bloch wall) or perpendicular (Néel wall) to the wall plane (b).	27
2.5	Stoner-Wohlfarth model (a) and domain wall nucleation in magnetic multilayers with PMA (b).	30
2.6	Domain wall velocity in magnetic multilayers with PMA depending on the applied perpendicular field.	32
2.7	Domain wall pinning at geometric deformations and anisotropy gradients.	34
2.8	DW nucleation field H_{nuc} to nucleate a DW from the ANC into the non-irradiated area of a magnet.	36
2.9	Hysteresis and corresponding virgin curves from the demagnetized state of a common magnetic multilayer film (a) and an ideal multilayer film for pNML (b).	37
2.10	Strayfield $\mathbf{H}(\mathbf{m}, \mathbf{r})$ of a small magnetic volume using the point-dipole approximation (a). The coupling field $\mathbf{C}(\mathbf{r})$ of a nanomagnet is determined by numerical finite-element calculations (b).	42
3.1	Sketch of a linear and a circular polarized propagating wave. . . .	45

3.2	Various geometries of the magneto-optical Kerr effect.	46
3.3	Polar magneto-optical Kerr effect.	47
3.4	Origin of the magneto-optical Kerr effect.	48
3.5	Sketch of the laser-scanning MOKE microscope.	51
3.6	Feedback controlled X-Y-scanner at LMOKE with a mounted chip carrier with an embedded micro coil.	55
3.7	Sketch of the wide-field MOKE microscope based on a common optical microscope which is enhanced by two polarizers.	56
3.8	Image processing for the reference image (a) and the magnetic image (b) of magnetic nanowires after measuring by WMOKE. . . .	58
3.9	Height (a) and magnetization (b) of a magnetic full adder structure imaged by MFM.	60
4.1	Manufacturing process of pNML devices consisting of Co/Pt nanomagnets with ANCs and on-chip coils.	64
4.2	Hysteresis curve (a) and magnetic domains (b) of an as-grown Co/Pt multilayer stack measured by LMOKE.	66
4.3	Lithography mask (a), corresponding microscope (b) and SEM images (c,d) of patterned pNML full adder circuits.	68
4.4	Sample with on-chip coil bonded on a chip carrier.	69
5.1	Fundamentals of logic operation in pNML.	72
5.2	Magnetization reversal in a magnetic multilayer film with ANCs generated by high ion dose irradiation.	73
5.3	Partial irradiation of a Co/Pt magnet.	75
5.4	Experimental results for the DW nucleation field H_{nuc} depending on dose and size of partial FIB irradiation.	76
5.5	SFD of the nucleation field H_{nuc} depending on the irradiation dose of the ANC.	77
5.6	Device under test to prove the fundamental principle of directed signal flow.	79
5.7	Demonstration of directed signal flow in a chain of three magnets.	80
5.8	Switching process of field-coupled magnets.	81
5.9	Snake-like Co/Pt nanowire to measure the DW velocity.	82
5.10	Domain wall velocity v_{DW} depending on the field pulse amplitude H_{pulse} measured in the snake-like Co/Pt nanowire.	84
5.11	DW nucleation probability depending on the applied field pulse time and amplitude.	85
5.12	Evaluation of the DW nucleation model by calibration and comparison to experimental results.	87
5.13	Influence of the coupling field on the DW nucleation time in a pNML inverter structure.	88

5.14	Clocking of a pNML inverter structure.	90
5.15	Logic operation in pNML by utilizing the interaction of field-coupled magnets.	91
6.1	Inverter structure and comparison between square magnets and fork-like design.	94
6.2	Concept of the majority logic gate for pNML.	96
6.3	Majority gate for perpendicular Nanomagnetic Logic.	98
6.4	Switching characteristics of the pNML majority gate.	99
6.5	Experimental demonstration of the majority gate.	101
6.6	Margins for correct logic operation of the majority gate.	104
6.7	Magnetic interconnects in pNML circuitry.	105
6.8	Theory and experiment on the DW motion in magnetic nanowires.	106
6.9	Theory and experimental demonstration of a fanout structure.	108
7.1	Schematics of majority logic gate-based 1-bit full adder circuits.	112
7.2	Model of the pNML 1-bit full adder circuit.	113
7.3	1-bit full adder circuit fabricated in the experiments.	115
7.4	Clocking and logic operation of the investigated 1-bit full adder circuit.	116
7.5	Basic principle of threshold logic and TLG-based full adder circuit.	118
7.6	Equivalent of a threshold logic gate in pNML.	119
7.7	TLG-based 1-bit full adder circuit in pNML.	121
7.8	Experiment on the fabricated TLG-based 1-bit full adder circuit.	122
7.9	Logic operation of the TLG-based 1-bit full adder.	123
7.10	Measurement and simulation of the coupling fields of the TLG-based full adder.	124
7.11	Coupling field calculation for compact modeling of pNML circuitry.	126
7.12	Compact modeling of pNML circuitry.	128
7.13	Simulated error rate of the TLG-based 1-bit full adder.	130
8.1	PNML system based on a systolic array.	134
8.2	Working principle of a domain wall gate.	138
8.3	Micromagnetic simulation of a DWG.	141
8.4	Experiment on notches in magnetic nanowires.	142
8.5	Experimental demonstration of the domain wall gate.	144
8.6	Influence of the clocking speed on a DWG.	146
8.7	3D integration of a DWG and possible applications.	147
8.8	Alternative concept for signal routing in pNML.	150
8.9	Arithmetic Logic Unit in pNML.	151
8.10	Simulation results for processing two 4-bit streams depending on the operating mode of the ALU.	153

List of Tables

3.1	Magnetic fields provided by the measurement setup.	54
4.1	Sputtering parameters for a conventional Co/Pt multilayer film. .	65
6.1	Measured DW nucleation field H_{nuc} of the majority gate depending on the input configuration.	102
8.1	Summary of theoretical, simulation and experimental results of the domain wall gate.	145

1 Introduction

The evolution of CMOS and ICs according to Moore's law has been the market-dominating technology driver for the recent half century [3, 4]. During this time, the CMOS technology node has been improved roughly every two years shrinking the transistor feature size by approx. 30 % with each generation. Progressive scaling enables to increase the transistor density by a factor of 2 per node, which on the one hand increases the speed of the ICs (35 % per node) and on the other hand reduces the manufacturing costs per transistor [5, 6]. This improvement of performance, power and costs by the scaling of solid-state devices prompted the semiconductor industry to advance the technology node from 10 μm in 1971 to 14 nm today [8, 9] (cp. Fig. 1.1). And the trend is still continuing: The 10 nm (in 2016) and the 7 nm (2018) technology nodes are for the most part already developed and are firmly established in the International Technology Roadmap for Semiconductors (ITRS) [7, 10].

Indeed with every new technology node also the technological challenges (e.g. lithography, transistor scaling, interconnects, and circuit design) as well as the total manufacturing costs are significantly increasing [7, 11]. Naturally, this trend of conventional dimensional and functional scaling cannot be maintained in perpetuity. Sooner or later, insuperable technological or economical limits to continue conventional scaling will be reached [12, 13]. For instance, manufacturable solutions in the semiconductor fabrication process for CMOS devices in 2020 (5 nm node) and beyond are presently not known [7]. It is true that through innovations (e.g. Strain, High-k + metal gate, TriGate (FinFET), see. Fig. 1.1) this border has been repeatedly postponed backwards [14–17] - and according to some experts, this limit is indeed always at least ten years away. However, the physical limit of scaling is inevitable, making it necessary to think about the future "beyond CMOS".

1.1 Emerging beyond-CMOS devices

Conventional dimensional and functional scaling according to Moore's law to expand the CMOS platform ("More Moore") is - from the industrial point of view - the preferred path for the further evolution of CMOS technology [8]. Nevertheless, due to the increasing technological and economical challenges for the development of future technology nodes, the research on "More-than-Moore" and "Beyond-

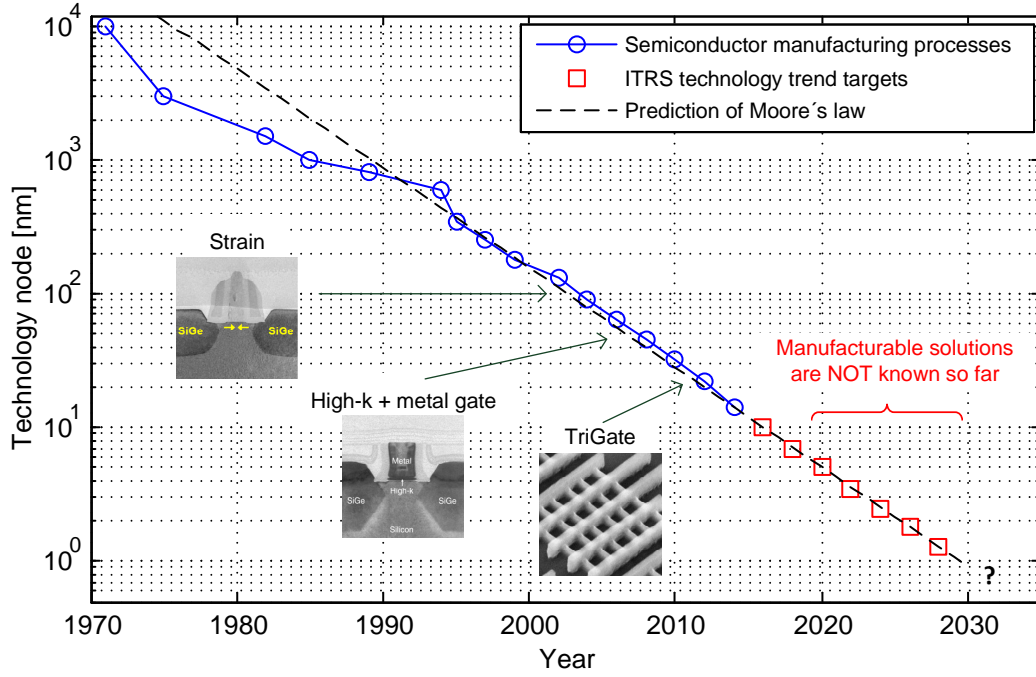


Figure 1.1: Technology node of the semiconductor manufacturing process from 1971 until today and for the next 15 years as scheduled in the International Technology Roadmap for Semiconductors (ITRS)[7].

CMOS" devices has been enforced in recent years [12, 18]. These two approaches differ fundamentally in their basic approach and their area of application [2].

More-than-Moore

More-than-Moore devices are handled as *non-digital information processing devices to extend the CMOS functionality* e.g. by wireless functionality or image processing. In principle, the idea is to partition generic high-level functions (e.g. wireless communication) into lower-level functions (e.g. antenna, filter, local oscillator), which then could use in some extend More-than-Moore devices like graphene radio frequency (RF) transistors or Spin Torque Oscillators (STOs) [2]. The advantage of this approach would be that these technologies can be implemented to replace the corresponding CMOS components. Thus, the conversion costs and effort for their implementation would be manageable and the CMOS technology could be retained on a long-term basis.

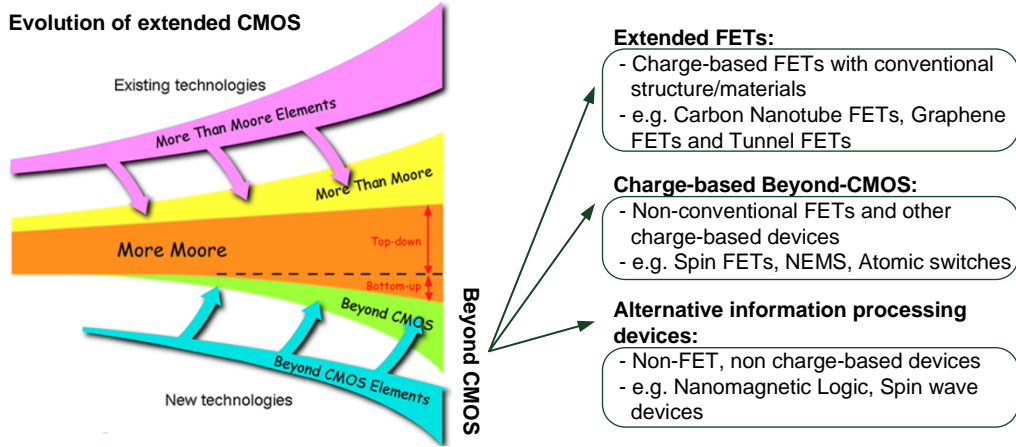


Figure 1.2: Relationship among "More Moore", "More-than-Moore" and "Beyond-CMOS" taken from [2]. Beyond-CMOS devices are classified depending on their state variable (charge-based / non charge-based) and their structure and material (conventional / novel).

Beyond-CMOS

By contrast, beyond-CMOS devices are classified as *logic and alternative information processing devices* not only to extend but also to *partially replace the CMOS platform functionality* [2]. While changing the design or materials of conventional metal-oxide semiconductor field effect transistors (MOSFETs) might improve their operation for a few generations, a new device is needed to allow long-term continued scaling [18]. Currently, such devices, also handled as post-CMOS logic, are intensively developed, investigated and benchmarked by both industry and academic research [2, 18, 19]. However, in order to augment or even substitute present and future CMOS technology, emerging devices have to meet several indispensable characteristic and technological requirements to be handled as serious beyond-CMOS device candidates [20, 21].

1.1.1 Requirements on beyond-CMOS devices

Theoretical and experimental approaches for novel beyond-CMOS devices are many, but not all of them are suitable for the post-CMOS era. Therefore, several requirements, a novel device candidate has to meet to be considered as CMOS successor, were established in recent years [21]. Those requirements can be divided into three basic domains:

Tenets of logic

The tenets of logic are five aspects, a solid-state device has to fulfill in order to be suited as information processing device [20]. These necessary conditions affect the characteristic properties a device has to provide for usability in logic circuits:

1. Nonlinear characteristics;
2. Power amplification (gain);
3. Concatenation (output of one device can drive another one);
4. Feedback prevention (output does not affect input);
5. Complete set of Boolean operators (NOT, AND, OR, or equivalent).

As the majority of today's information-processing circuits is based on these characteristics and simultaneously a broad paradigm shift is not desired, also novel devices have to meet these demands.

Physical measures

Furthermore, there are several quantitative physical measures in which the device needs to be competitive to current and further scaled CMOS technology:

6. Area (scalability);
7. Switching time (delay);
8. Switching energy (power dissipation).

Those quantitative metrics are the main drivers for the technology evolution, as their improvement enables to increase the device performance and at the same time to reduce the manufacturing costs according to Moore's law. Hence, also the beyond-CMOS device needs to compete in those aspects to be economically interesting for the semiconductor industry.

Technological requirements

After all, several technological requirements have to be achieved by the device to be claimed as convenient candidate:

9. Room temperature or higher operation;
10. Low parameter sensitivity (e.g. fabrication variations);
11. Operational reliability;
12. CMOS architectural compatibility;

13. Compatibility to CMOS processes;
14. Comprehending parasitics and their interface to interconnect.

Interestingly, it is these points that are often neglected in the exploration of novel devices. But obviously, especially those aspects decide about a device to be an attractive CMOS successor or not.

1.1.2 Overview on beyond-CMOS device candidates

In recent years several candidates for beyond-CMOS information processing devices have been proposed and investigated [2]. Currently about 15 to 20 different candidates fulfill the strict prerequisites. Besides their basic working principle (barrier, tunneling, magnetic, etc.), those devices mainly differ in terms of their state variable (e.g. charge, electron spin, magnetization) and their input, output and control signal character (i.e. voltage, current, magnetization) [18, 21]. In [2], those devices are categorized in three different groups:

- **Extended field effect transistors (FETs)** utilize the proven working principle of the conventional MOSFET, but try to improve its functionality by modifying the channel material, e.g. by carbon nanotubes, graphene or semiconducting nanowires. The Tunnel FETs utilizing gate-controlled band-to-band-tunneling in a p-i-n junction, is one of the most prominent members of this class.
- **Non-conventional FETs and other charge-based devices** are charge-based devices utilizing novel materials. Thereby, the signal character is still classical voltage or current. For example, in Spin FETs, source and drain are replaced by several ferromagnetic materials to utilize the electron spin for operation. Nano-Electro-Mechanical switches (NEMS) employ the electrostatic force to actuate a movable, conducting structure between two electrodes (contacted or not).
- **Non-FET, non charge-based devices** make use of novel materials to employ non-conventional state variables and/or signal characters (e.g. spin or magnetization) for operation. Spin Wave devices exploiting collective spin oscillations for signal operation and NML, which is described in more detail in the following section, are mentioned here as representatives of this class.

In order to select the most suitable successor from the multitude of candidates, benchmarking is of great importance [19, 22]. Here, quantitative physical measures (area, switching time and switching energy) and costs play an essential role, as they are the main technology drivers for industry. Or more precisely, also the

CMOS successor should be able to somehow continue Moore’s law. As beyond-CMOS candidates in some extent strongly differ in structure and their mode of operation (i.e. working principle, state variable and signal character), essential logic elements and ICs are used for benchmarking purposes (e.g. inverters, NAND gates or adder circuits) [21]. Thereby, such standard circuits based on novel devices are benchmarked and compared in terms of area, switching time (delay) and switching energy (power). In order to succeed in the highly competitive market of beyond-CMOS devices, the suitable candidates therefore have to perform in those benchmarks at the best.

1.2 Nanomagnetic Logic (NML)

Among non charge-based beyond-CMOS devices, magnetic devices gain much attention due to their inherent nonvolatile characteristics [23–25]. One of the promising, magnetic beyond-CMOS devices is NML. The principle idea is to utilize the magnetic field interaction of nonvolatile, field-coupled nanomagnets to perform logic operations [SB14e]. Thereby the bistable magnetization state of the nanomagnets serves as state variable and is coded with logic ‘0’ or logic ‘1’. Depending on the utilized magnetic material, the magnetization orientation of the nanomagnets can be in-plane (in-plane Nanomagnetic Logic (iNML)) or perpendicular to the plane (pNML)¹. Clocking and switching of the nanomagnets is realized by an externally applied magnetic field, the so-called clocking field.

The application of field-coupled magnets to provide logic functionality brings, amongst others, two major advantages compared to conventional CMOS logic:

- The inherent **non-volatility** of the magnets allows to implement memory functionality in the underlying logic operation. This step is already perceived as a revolutionary approach in the ITRS [2]. The combination of memory and logic in a single device could overcome the classical von-Neumann architecture and advance the design of future ICs.
- The superposition of magnetic stray fields in NML logic gates upgrades the set of boolean operators by the universal **majority decision**. Majority gates and threshold logic gates (TLGs) enable to reduce the number of logic gates per function and therefore dramatically decrease the circuit complexity [27],[SB14a].

The combination of these two outstanding characteristics is to our knowledge provided by no other hitherto known logic device and therefore also justifies the attraction of this technology. Further prominent features of NML are high density

¹A detailed description of the difference between iNML and pNML can be found in [26].

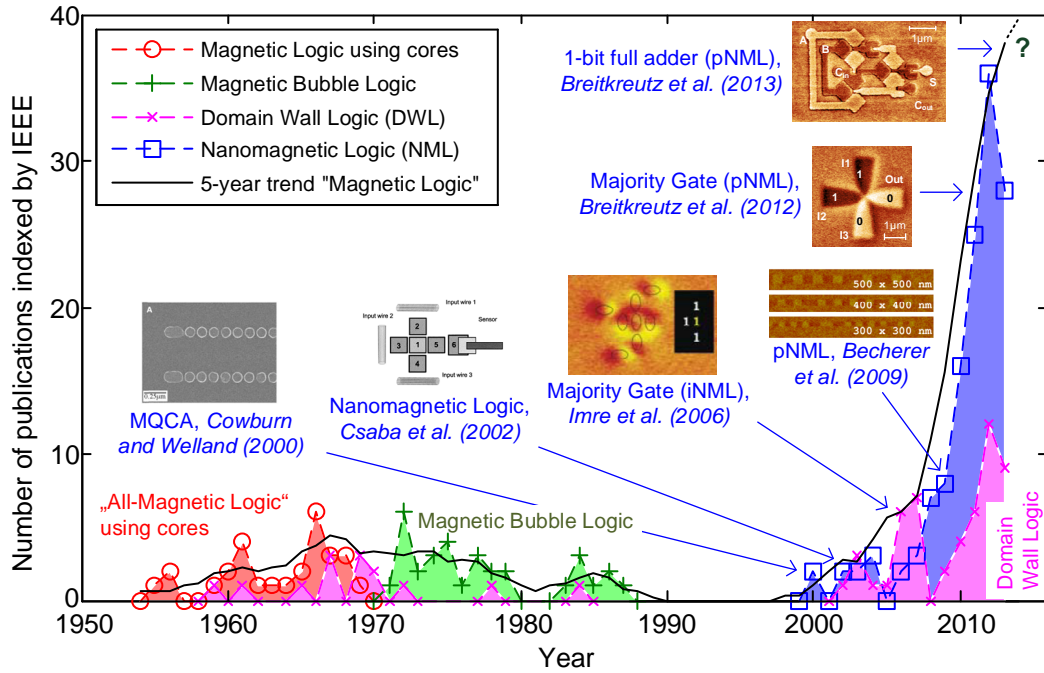


Figure 1.3: Research on Magnetic Logic² and milestones in the evolution of perpendicular Nanomagnetic Logic (pNML).

integration, low power computing, zero leakage, interconnect-free signal transmission and radiation hardness [2].

1.2.1 Historical evolution

This section gives a short overview on the historical evolution of Magnetic Logic from the beginning in the 1950s using ring cores to the modern implementation of NML using field-coupled nanomagnets with perpendicular magnetic anisotropy (PMA). For a more detailed description of the development of NML the reader is referred to [26] and [28]. Fig. 1.3 shows the amount of research on Magnetic Logic and the associated evolution of pNML.

Beginning of Magnetic Logic

Magnetic Logic was basically developed and investigated for the first time in the 1950s and 60s. *All-Magnetic Logic* utilized ring cores wrapped by several input

²The amount of research on Magnetic Logic is based on the number of publications indexed in Institute of Electrical and Electronics Engineers (IEEE) Xplore Digital Library with specific keywords, i.e. "Magnetic Logic", "Magnetic Bubble Logic", "Domain Wall Logic (DWL)", "Magnetic Quantum Cellular Automata (MQCA)" and "Nanomagnet(ic) Logic (NML)".

and output coils to store digital information and provide logic computation (e.g. [29–33]). Other approaches explored propagating domain walls (DWs) (*Domain-tip Propagation Logic (DTPL)*, e.g. [34–36]) and magnetic bubbles (*Magnetic Bubble Logic*, e.g. [37–40]) in magnetic thin films for the application in logic and memory devices.

However, due to the size, speed and costs of such magnetic components they were outperformed by the emerging transistor, MOSFET and ICs technology first in logic circuits (e.g. [41–43]), and shortly thereafter also in memories by on-chip memory technologies (e.g. [43–45]). Therefore, research on Magnetic Logic devices disappeared until the year 2000. Due to the previously discussed impending end of CMOS scaling and the unique benefits non-volatility and majority logic in magnetic devices, Magnetic Logic has regained its attractiveness. Thereby, the discovery of the spin transfer torque (STT) for the electrical on-chip integration of magnetic structures as well as the development of modern manufacturing equipment have been of great importance.

The Origin of NML: Quantum Cellular Automata

The present "boom" of Magnetic Logic devices is based on the exploration of Quantum Cellular Automata (QCA) [46]. Here, the Coulomb interaction between electrons from different, bistable quantum cells is used to perform logic operations. Furthermore, the design of basic QCA computing elements like wires, inverter structures as well as AND / OR gates and later on majority gates for the realization of more complex devices has been postulated [46, 47]. No interconnects, ultra-high-density computing, low-power dissipation and ultra-fast computing are the promising features of QCA. However, challenges in the uniformity of cell occupancy, fabrication variations and especially the required cryogenic temperature of operation shifted the application of electronic room temperature QCA to molecular electronics (*Molecular QCA*) [46, 48].

Magnetic Quantum Cellular Automata

The breakthrough of QCA and thus the beginning of NML was the transfer of QCA towards magnetic materials into Magnetic Quantum Cellular Automata (MQCA) in 2000 by Cowburn and Welland [49]. MQCA uses small magnetic dots (later called nanomagnets) as *quantum cells* which interact by their magnetic stray field. The magnetization state of the magnetic dots serves as state variable and is, depending on size and shape of the dots, stable at room temperature (RT). In 2002, Csaba et al. [50] proposed the magnetic majority gate as basic building block for *Nanomagnet Logic*, including electrical integration and clocking of such magnetic circuits. In the following years, MQCA gained more and more interest due to the combination of the advantages of QCA together with RT stability [51].

Several studies explored the physical properties of magnetic dots and investigated inverter chains as first MQCA devices [52–55]. Afterwards, research focused on the fabrication of the majority gate, which was finally demonstrated in 2006 using nanomagnets with in-plane magnetization made of Permalloy (Py) [56]. The fabrication of a functional MQCA logic gate working at RT is one of the milestones in the development of NML. Since then, interest and thus research on NML has risen sharply (see Fig. 1.3). The advantages of QCA (majority decision, no interconnects, ultra-high-density computing and low-power dissipation) combined with the benefits of magnetic devices (non-volatility, stable operation at room temperature) are unique in the highly competitive research field of beyond-CMOS devices.

Domain Wall Logic

Magnetic Logic using propagating domain walls has been rediscovered as Domain Wall Logic (DWL) in the beginning of the 20th century [57, 58]. Here, logic operations are performed by shifting different configurations of DWs (i.e. head-to-head or tail-to-tail) in a structured in-plane material through geometric gates by a rotating magnetic field. However, the sensitivity to geometric imperfections as well as the handicap of the required rotating magnetic field make these devices seem to be rather unsuitable as beyond-CMOS technology. But in recent years, DWL received again growing interest due to the application of magnetic materials with PMA in both DW-based logic and memory devices (e.g. [SB13c],[59]).

The beginning of pNML

In principle, Csaba et al. [50] proposed Magnetic Logic using nanomagnets with out-of-plane magnetization in 2002. However, the challenging fabrication of the suggested structures (vertical magnetic pillars) compared to in-plane Py magnets, led to an inobservance of this technology until the year 2007. In 2007, Becherer et al. [60] from the Technische Universität München (TUM) started, in cooperation with the University of Notre Dame (ND), to investigate the feasibility of Magnetic Logic using Cobalt (Co)/Platinum (Pt) nanomagnets with out-of-plane magnetization. At the beginning of their fundamental studies, they explored ordering phenomena in focused ion beam (FIB) patterned Co/Pt multilayer films with PMA [60–62]. One of the milestones of their research is the demonstration of magnetic ordering in FIB patterned wires of field-coupled Co/Pt magnets as well as electrical I/O structures for such magnetic devices in 2009 [63]. This thesis started at that time and is therefore mainly based on their fundamental results.

Modern pNML

In recent years, research on Magnetic Logic devices has impressively increased in both iNML and pNML due to the impending end of the progressive scaling of conventional CMOS technology [2, 12, 13, 21]. In addition to the general features of NML (or MQCA), pNML provides the major advantages of shape-independent, but tunable switching behavior of the magnets [SB12b] and programmable, directed signal flow [SB11a]. Analog to the rise of iNML, one of the milestones for the evolution of pNML was the demonstration of the majority gate using Co/Pt magnets with PMA [SB12a]. In 2013, we experimentally demonstrated a 1-bit full adder in pNML [SB13b], which is the most complex fully functional NML circuit published so far. As a preliminary highlight, pNML (mentioned as Perpendicular Magnetic Logic (PML)) is listed as an individual device technology in the current edition of the pathbreaking ITRS, chapter for Emerging Research Devices (ERD) [2].

1.2.2 Perpendicular Nanomagnetic Logic (pNML)

This work deals with pNML, which is for various reasons nowadays considered as the most suitable technological implementation of NML [64],[65, 66]. Fig. 1.4 shows the vision of an integrated pNML system consisting of a logic part for digital computation as well as electrical input/output devices and on-chip clocking structures for integration. The logic computation is the centerpiece of this technology and is mainly treated in this work by both experiment and simulation.

Basic working principle

Perpendicular NML utilizes nanomagnets with PMA, which interact by antiferromagnetic field-coupling [2, 63]. The magnetization state of the magnets serves as state variable and is encoded with logic '1' (magnetization up) or logic '0' (magnetization down). The switching of the magnets is based on DW nucleation in the weakest spot followed by DW propagation through the entire magnet to completely reverse it [SB12b]. In order to control the switching of the nanomagnets, the PMA is locally tuned by FIB irradiation to create artificial nucleation centers (ANCs) for DWs. Therefore, the magnet (output) is sensitized to only specific neighbors (inputs) close-by to the ANC providing directed signal flow integrated in the magnets themselves [SB12b, SB11a]. The energy needed to switch the magnets is provided by the clocking field - alternating, perpendicular magnetic field pulses with adequate amplitude [BKB⁺13].

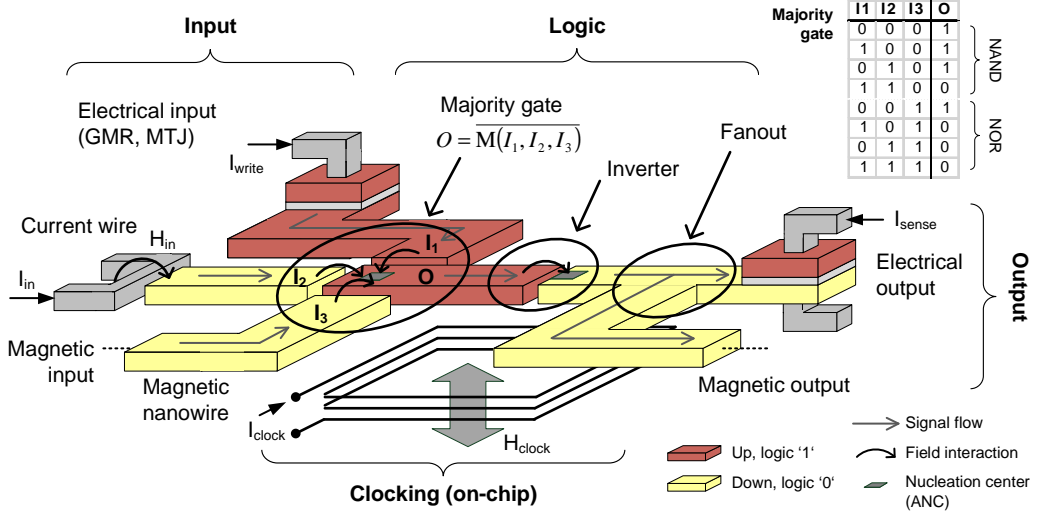


Figure 1.4: Vision of an integrated pNML system. Majority gates, inverters and fanout structures provide logic computation. Electrical I/O devices and on-chip clocking structures enable electrical integration.

Digital logic computation

In order to enable logic operation, the clocking field induced DW nucleation at the ANC is enforced or prevented by the superposing fringing fields of the input magnets, depending on their magnetization state [SB12a]. The inverter structure is the most common logic element. In pNML, the antiferromagnetic field coupling between adjacent magnets enables to invert the magnetization state from input to output by just 2 interacting magnets [SB13b].

The majority gate is the basic computing element for logic operation (cp. Fig. 1.4). Here, the ANC of the output magnet O is surrounded by three (or more) input magnets I_1 , I_2 and I_3 . Their superposed fringing fields enforce or prevent the DW nucleation, depending on the majority of the input states [SB12a]. The majority decision provides the basic logic operations NAND and NOR by just setting on of the input states (e.g. I_3) to a fixed '0' ($O = \text{NAND}(I_1, I_2)$) or '1' ($O = \text{NOR}(I_1, I_2)$).

The switching process of propagating DWs offers the use of magnetic nanowires as interconnects between subsequent logic gates [SB12b, SB13b]. Once a magnet is switched, it can serve as input for subsequent gates. Therefore, information is processed stepwise according to the alternating clocking field pulses [KBE⁺13a]. Fanout structures required to drive multiple gates by a single output are simply realized by splitting up the magnetic nanowire into several branches [SB12b]. In summary, it can be stated that pNML provides the complete set of logic tenets [BBE⁺15], as premised by [21].

Electrical integration

In order to be considered as serious beyond-CMOS device candidate, electrical integration and thereby compatibility to CMOS is of great importance [21]. Electrical I/O structures can be realized either by modern STT devices or, more classical, by current wires (as input) and hall sensing devices (as output).

Modern STT devices utilize the giant magnetoresistance (GMR) or tunnel magnetoresistive (TMR) effect, which are both suitable to read (output) and write (input) the magnetization state of structured magnetic layers (e.g. [67–69]). Such devices utilize the magnetoresistive effect between ferromagnetic layers separated by a nonmagnetic conductive layer (GMR, e.g. [69–71]) or a tunnel barrier (magnetic tunnel junction (MTJ), e.g. [72–74]). Depending on the alignment of the magnetization in both ferromagnetic layers (parallel or antiparallel), the electric resistance of the structure is either low (parallel) or high (antiparallel). The application of such devices for NML has been and is currently investigated in several studies (e.g. [28, 75–78]).

By contrast, more classical approaches using current wires as input structures and hall sensing devices for read-out are well understood and already applied in NML. Current wires enable to switch adjacent magnets by Oersted switching. Depending on the strength and the direction of the current, a magnetic field is generated which is sufficient to set the close-by input magnets [63],[KBC⁺12]. A hall sensing device in split current design (e.g. [BKB⁺10],[28]) allows to read out the magnetic state of a magnet without interrupting the signal flow in a circuit, although the sensitivity (measurement ratio between 'up' and 'down' state) is rather small ($< 0.5\%$) compared to that of STT devices ($> 100\%$) [28, 72].

Clocking

Nowadays, clocking of pNML circuitry is realized by on-chip coils, which employ alternating sub- μs field pulses to switch the magnets. Therefore, the clocking field acts as both power supply and internal clock. The on-chip clocking concept is the most significant aspect whether pNML can be considered as low-power technology or not. The major part of the total power dissipation is caused by the on-chip inductor, but high-permeability claddings significantly reduce the required clocking current [BKB⁺13]. Furthermore, the clocking concept affects the speed and the operational reliability of NML circuitry [SB14b],[BKB⁺14]. Novel approaches employ propagating DWs [CKB⁺12, JKS⁺12, JSL⁺12] or the Spin Hall effect (SHE) [79, 80] for ultra-low power on-chip clocking, but especially for the last-mentioned approach much more research effort is inevitable.

1.3 Contribution of this work

This work started in 2009 at the NML research group at the Lehrstuhl für Technische Elektronik (LTE), when Becherer and collaborators from ND and the Institute for Nanoelectronics at TUM showed ordering of nanomagnets within patterned Co/Pt multilayer films by means of FIB irradiation. In their studies, they investigated ordering mechanisms in checkerboards and chains of magnets, but also fabricated hall-sensing devices for readout, current wires as electrical inputs, and performed substantiating micromagnetic simulations calibrated by experiments. The missing element and therefore the overall scope of this thesis was to embed well-directed logic functionality within the field-coupled magnets and experimentally demonstrate logic devices and circuits in magnetic media with PMA. Therefore, the following, essential steps have been contributed within this work:

- Set up of a magneto-optical microscope at LTE which is applicable to investigate the magnetic behavior of field-coupled nanostructures with PMA.
- Further development of a well-established manufacturing process of FIB-patterned multilayer films for the fabrication of partially irradiated magnets within the 100 nm-range.
- Implementation of directed signal flow within field-coupled nanomagnets by tuning of the magnetic anisotropy with partial FIB irradiation.
- Experimental demonstration of the first majority gate with PMA as universal logic device for pNML.
- Fabrication of the first fully functional 1-bit full adder circuit in NML.
- Experimental demonstration of threshold logic gate-based circuits in pNML based on the idea of Papp *et al.* from ND [PNC⁺14].
- Development of physics-based compact models of field-coupled magnets for the simulation and investigation of pNML logic devices and circuits.
- Development and demonstration of the domain wall gate, which is applicable for both signal routing in pNML circuits or as a stand-alone logic device.
- Development of an arithmetic logic unit, which is highly suitable as basic logic cell in systolic array-based pNML.

The achievements mentioned above also contributed to promote pNML as serious emerging beyond-CMOS technology, which finally led to the inclusion of pNML into the pioneering 2013 edition of the ITRS roadmap for emerging research devices [2] and the 2014 magnetism roadmap [64]. Both roadmaps are written by multiple experts and discuss current and future challenges within technology and promising research fields.

1.4 Outline of the thesis

The main scope of this thesis is introduce the reader to pNML and familiarize him with the basic working principles of pNML logic devices and circuits and the theory behind it. Thereby, the focus is on the experimental demonstration of logic operation within devices and circuits of field-coupled magnets. The thesis is organized as follows:

Section 2 introduces the basic theory of micromagnetics and the role of magnetic energies, the nucleation, propagation and pinning of domain walls as well as magnetization dynamics with focus on but not limited to magnetic multilayers.

Section 3 introduces the reader to magnetic metrology with focus on magneto-optical microscopy, which is required to understand and investigate the characteristics of magnetic nanostructures. The manufacturing process of the investigated, field-coupled nanomagnets made from Co/Pt multilayers is shown in section 4.

Section 5 introduces the fundamentals of pNML. Directed signal flow, logic operation and clocking of pNML are discussed and substantiated by experiments.

The application of the fundamental principles in order to provide logic devices is addressed in section 6. Basic logic gates (i.e. inverter and majority gates) and their interconnection are experimentally demonstrated.

Section 7 describes pNML circuits made of basic logic devices. Logic operation within pNML circuits and the application of threshold logic gates are exemplified by a 1-bit full adder circuit. Compact model simulations are used to investigate the potential of pNML circuits.

Architectures for pNML systems as well as methods for signal routing and processing of magnetic bitstreams are discussed in section 8. A simulated, pure magnetic arithmetic logic unit (ALU) finally demonstrates the promise of integrated pNML systems for next-generation computing.

The work closes with a summary of the thesis' results and a conclusion about further research requirements on pNML.

2 Basic Principles of pNML Magnetism

The focus of this engineering thesis is on the realization of digital logic circuits by using field-interacting nanomagnets with PMA. Therefore, mostly already known knowledge about a wide range of physical effects and magnetic properties is applied to *engineer* the nanomagnets conveniently in order to provide logic operation.

The basic theory and principles about pNML magnetism discussed in this section is therefore reduced to the main principles and equations required to understand the applied effects behind the realized logic system. For more information about the physical origin behind and the derivation of the final equations, the reader is kindly referred to the stated references.

There are numerous scientific books and papers dealing with the basic principles of magnetism, micromagnetism, magnetic domains, magnetic multilayers as well as appropriate metrology and simulation tools. The basic equations for micromagnetic energies, magnetization dynamics and domain theory presented in the following sections are based on [81–83].

2.1 Micromagnetism

Micromagnetism is the continuum theory of magnetic moments developed in the 1930s and 1940s to bridge the gap between the phenomenological Maxwell's theory and quantum theory [82]. Maxwell's theory of electromagnetic fields is valid for macroscopic dimensions and specifies material properties by global permeabilities and susceptibilities. By contrast, the quantum theory describes magnetic properties on the atomic level. The breakthrough towards a continuum theory of magnetism was achieved by Landau and Lifshitz in 1935, who gave a continuum expression for the exchange energy and a first interpretation of domain patterns [84]. Nowadays, the theory of micromagnetism is an efficient tool to describe magnetization processes, domain patterns as well as the characteristic switching properties.

2.1.1 Micromagnetic energies

The basic principle of micromagnetics is the minimization of the total energy of the magnetization vector [81]. Thereby, the torque on the local magnetization generated by related energy contributions and the formation of magnetic domains are a necessary consequence to reach the minimum energy level. Thus the following magnetization-dependent contributions to the total energy are the origin to describe both the magnetization dynamics and the domain theory.

Exchange energy

The exchange interaction is responsible for the establishment of magnetic ordering in magnetic materials. It describes a quantum effect between two contiguous spins \mathbf{S}_i and \mathbf{S}_j to align in a parallel magnetization direction. The exchange energy of a pair of spins is given by

$$E_{exchange}^{pair} = -2J_0 \mathbf{S}_i \cdot \mathbf{S}_j = -2J_0 \cdot S^2 \cos \phi_{i,j} \quad (2.1)$$

with the exchange constant J_0 and the spin $\mathbf{S}_{i,j} = S \mathbf{e}_{s_{i,j}}$ with the amplitude S and unit vector $\mathbf{e}_{s_{i,j}}$. The angle $\cos \phi_{i,j}$ is the angle between the spins \mathbf{S}_i and \mathbf{S}_j minimizing the exchange energy for parallel alignment of the spins $\phi_{i,j} = 0$ due to the minus sign in eq. 2.1. By using the unit magnetization vector $\mathbf{e}_m = \mathbf{e}_s$, the energy for a pair of spins can also be written in the form

$$E_{exchange}^{pair} = -2J_0 S^2 \mathbf{e}_{m_i} \cdot \mathbf{e}_{m_j} \quad (2.2)$$

where $\mathbf{e}_m = \mathbf{M}/M_s$ with the magnetization vector \mathbf{M} and the materials saturation magnetization M_s . For a bulk magnetic material with magnetization direction $\mathbf{e}_m(\mathbf{r})$ depending on the position \mathbf{r} , the exchange energy of a pair of spins is integrated over the volume V leading after some algebra to

$$E_{exchange} = A \int (\nabla \mathbf{e}_m(\mathbf{r}))^2 dV. \quad (2.3)$$

Thereby, the exchange stiffness A is a material constant depending on the crystal structure and the saturation magnetization [83]. It describes the strength of the magnetic coupling, and therefore the strength needed to deviate a spin from the direction of the exchange field. Hence, the exchange energy is minimized for all spins aligned in parallel $\nabla \mathbf{e}_m(\mathbf{r}) = 0$.

Anisotropy energy

The magnetic anisotropy depends on the relative direction of the magnetization to the crystal structure of the magnetic material. Depending on the orientation of the crystal, *moderate* or *high* magnetic fields are required to approach the saturation magnetization in the *easy-axis* or *hard-axis*. The associated anisotropy energy may originate from multiple reasons.

Uniaxial anisotropy The uniaxial anisotropy (or magnetocrystalline anisotropy) basically results from spin-orbit interactions and depends on the angle θ between the magnetization vector \mathbf{e}_m and the easy axis of the crystal:

$$E_{ani,u} = \int (K_{u1} \sin^2 \theta + K_{u2} \sin^4 \theta) dV = (K_{u1} \sin^2 \theta + K_{u2} \sin^4 \theta) \cdot V \quad (2.4)$$

with the uniaxial anisotropy constants K_{u1} and K_{u2} and the volume V of the magnetic material. Usually, $K_{u2} \ll K_{u1}$ is neglected by specifying the uniaxial anisotropy $K_u = K_{u1}$. The uniaxial anisotropy energy is minimized for $\theta \in \{0, \pi\}$ meaning the magnetization is aligned in parallel with the easy axis.

Surface and interface anisotropy For thin films and magnetic multilayers, the surface and interface anisotropy energy

$$E_{ani,s} = \int K_s [1 - (\mathbf{e}_m \cdot \mathbf{n})^2] dA \quad (2.5)$$

with the surface anisotropy constant K_s and the surface normal vector \mathbf{n} has to be taken into account. It occurs from the broken symmetry of the atoms at the surface [85] or the interfaces between ferromagnetic and non-magnetic media [81]. Those effects are negligible for ordinary bulk materials, but they become very important for thin films and magnetic multilayers. The surface and interface anisotropy energy is minimized if the magnetization vector \mathbf{e}_m is aligned parallel to the surface normal \mathbf{n} , i.e. perpendicular magnetization.

Magnetostatic energy

The magnetostatic energy originates from two different sources of magnetic fields, the externally applied magnetic field and the demagnetization field (or stray field) resulting from the magnetization \mathbf{M} .

Zeeman energy (external field energy) The energy generated by the interaction of the magnetization $\mathbf{M} = M_s \cdot \mathbf{e}_m$ with the external applied magnetic field \mathbf{H}_{ext} is called Zeeman energy, which is given by

$$E_{Zeeman} = -M_s \int \mathbf{H}_{ext} \cdot \mathbf{e}_m dV. \quad (2.6)$$

In order to minimize the Zeeman energy, the magnetization \mathbf{M} has to be aligned parallel to the direction of the external field.

Demagnetization energy (stray field energy) The demagnetization field (or stray field) is the magnetic field generated by the divergence of the magnetization \mathbf{M} itself:

$$\text{div } \mathbf{B} = \text{div } (\mu_0 \mathbf{H} + \mathbf{M}) = 0 \quad (2.7)$$

$$\Rightarrow \text{div } \mathbf{H}_{demag} = -\text{div } (\mathbf{M}/\mu_0) \quad (2.8)$$

with the magnetic flux density \mathbf{B} and the demagnetization field \mathbf{H}_{demag} . The according demagnetization energy is

$$E_{demag} = \frac{1}{2} \mu_0 \int_{allspace} \mathbf{H}_{demag}^2 dV = -\frac{1}{2} \int_{magnet} \mathbf{H}_{demag} \cdot \mathbf{M} dV. \quad (2.9)$$

The first integral extends over the whole space and is always positive, showing that the demagnetization energy is minimized for a minimum stray field \mathbf{H}_{demag} . The second one is only integrated over the sample volume which is much easier to evaluate.

Other sources of micromagnetic energies

Magnetoelastic and magnetostrictive energy Stress or strain from both externally applied sources (magnetoelastic) or generated by the material itself (magnetostrictive) introduce an energy which influences the total energy. The magnetoelastic energy E_{me} is an energetic contribution arising from external stress and its interaction with the magnetization. Magnetostriction is the effect of the change of dimensions of a ferromagnetic material during the process of magnetization due to the impact of magnetic exchange forces, which generate local stress and therefore contribute by the magnetostrictive energy E_{ms} .

Thermal energy Thermal energy plays a significant role in the behavior of magnetic materials. Temperature affects nearly all types of the micromagnetic energies mentioned above, as the saturation magnetization M_s , the exchange stiffness constant A or even the crystalline structure (due to lattice vibrations) are functions of the temperature. In micromagnetic simulations, the thermal energy is modeled by a stochastic field term $\mathbf{H}_{thermal}$, which is added to the effective field \mathbf{H}_{eff} (see section 2.1.2).

Total energy

Summing up all magnetization-dependent contributions mentioned above gives the total energy

$$E_{total} = \underbrace{E_{exchange}}_{\text{exchange interaction}} + \underbrace{E_{ani}}_{\text{anisotropy}} + \underbrace{E_{Zeeman} + E_{demag}}_{\text{magnetic fields}} + \underbrace{E_{me} + E_{ms}}_{\text{ext. and int. stress}}. \quad (2.10)$$

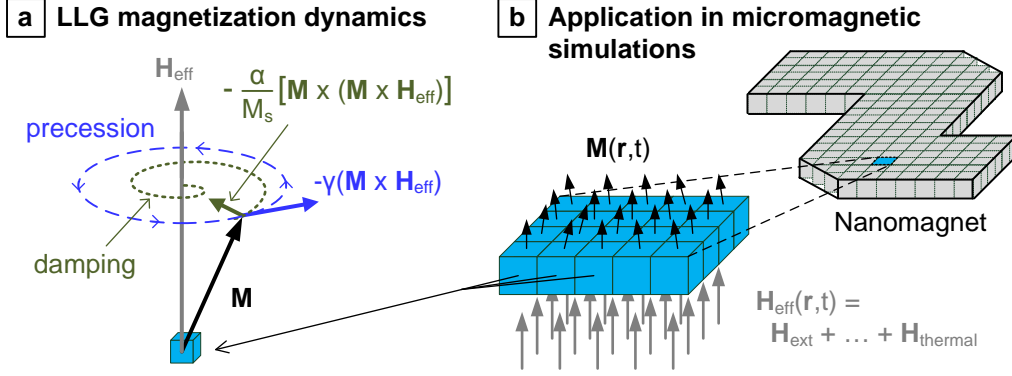


Figure 2.1: Magnetization dynamics and its application in micromagnetic simulations. The LLG-equation describes the motion of a magnetic moment \mathbf{M} in an applied magnetic field \mathbf{H}_{eff} (a). In micromagnetic simulations, the magnetic structure is discretized and the LLG is solved for each element (b).

The micromagnetic equations used in the following section 2.1.2 to describe the magnetization dynamics are based on the minimization of the total energy with respect to the unit magnetization vector $\mathbf{e}_m(\mathbf{r})$ [84, 86].

2.1.2 Magnetization dynamics

The Landau-Lifshitz-Gilbert (LLG) equation

A basic description of the time-dependent motion of a magnetic moment has been presented for the first time by Bloch in 1932 [87]. There, he considered the motion of an uncoupled and undamped magnetic moment. In 1935, Landau and Lifshitz published the Landau-Lifshitz-equation (LL-equation) for the motion of magnetic moments in an applied magnetic field (Fig. 2.1a) [84]. By transition from the dipole moment to the magnetization \mathbf{M} , the LL-equation describes the precession of the magnetization \mathbf{M} around an effective magnetic field \mathbf{H}_{eff} :

$$\frac{d\mathbf{M}(\mathbf{r}, t)}{dt} = -\gamma (\mathbf{M}(\mathbf{r}, t) \times \mathbf{H}_{eff}(\mathbf{r}, t)). \quad (2.11)$$

with the gyromagnetic ratio $\gamma = \mu_0 g \frac{\mu_B}{\hbar} = \mu_0 g \frac{e}{2m_e} \approx 2.2 \cdot 10^5 \frac{1}{T \cdot s}$ describing the ratio of magnetic moment and angular momentum with the gyromagnetic splitting factor g (g-factor, constant close to 2 for many ferromagnetic materials), the Bohr magneton μ_B , the reduced Planck constant \hbar , the elementary charge e and electron mass m_e .

In 1955, Gilbert and Kelly added the damping term to the LL-equation to also

describe strong damping in thin films (Fig. 2.1a) [88]. This finally resulted in the Landau-Lifshitz-Gilbert (LLG) equation, which is nowadays used to describe the magnetization dynamics:

$$\frac{d\mathbf{M}(\mathbf{r}, t)}{dt} = \underbrace{-\gamma \mathbf{M}(\mathbf{r}, t) \times \mathbf{H}_{eff}(\mathbf{r}, t)}_{\text{precession}} - \underbrace{\frac{\alpha}{M_s} \mathbf{M}(\mathbf{r}, t) \times \frac{d\mathbf{M}(\mathbf{r}, t)}{dt}}_{\text{damping}} \quad (2.12)$$

with the damping constant of the magnetization precession α . The effective field \mathbf{H}_{eff} is given by summing up all effective field components

$$\mathbf{H}_{eff} = \mathbf{H}_{ext} + \mathbf{H}_{demag} + \mathbf{H}_{ex} + \mathbf{H}_a + \mathbf{H}_{thermal}. \quad (2.13)$$

with the effective exchange field \mathbf{H}_{ex} due to exchange forces, the effective anisotropy field \mathbf{H}_a collecting all contributions from crystal and structural magnetic anisotropies and the thermal field $\mathbf{H}_{thermal}$ to model the thermal energy [50, 81, 89]. The thermal field is given by the stochastic term

$$\mathbf{H}_{thermal} = \frac{1}{\sqrt{V\Delta t}} \sqrt{\frac{2k_B T \alpha}{\mu_0 \gamma M_s}} \cdot \mathbf{g}(t) \quad (2.14)$$

with the Boltzmann constant k_B , the temperature T , the fixed simulation step time Δt applied in micromagnetic simulations and the Gaussian-distributed random vector $\mathbf{g}(t)$ to model the thermal noise [90]. Without the consideration of thermal energy, simulations are performed at $T = 0$ K and dynamic magnetization effects vanish.

Application in micromagnetic simulations

Usually, micromagnetic simulations are based on the minimization of the total energy in a magnetic system by solving the LLG equation. Therefore, first the material parameters (e.g. anisotropy K , saturation magnetization M_s , exchange stiffness A) and the geometry of the micromagnetic problem as well as the external field \mathbf{H}_{ext} or the simulation step time Δt are defined. Afterwards, the magnetic structure is discretized into finite elements in a three dimensional grid and the LLG equation is solved for each element minimizing the total energy (Fig. 2.1b). Such micromagnetic simulations enable to explore micromagnetic phenomena in two and three dimensional systems, analyze the static and dynamic magnetization behavior of magnetic nanostructures or verify and substantiate experimental or theoretic results. One of the most popular tools for the simulation of micromagnetic problems is the Object Oriented MicroMagnetic Framework (OOMMF) [91], a public domain micromagnetic simulator which is also used in this work.

2.2 Magnetic multilayers

Magnetic multilayers are stacks of ultra thin ferromagnetic (FM) layers separated by non-magnetic metall layers. As these individual layers become thinner, the impact of the surface and interface anisotropy (perpendicular contribution to the magnetic anisotropy, see sec. 2.1.1) raises significantly. Thereby, the easy-axis rotates from in-plane to perpendicular to the plane, which is usually referred to as perpendicular magnetic anisotropy (PMA) [92]. The individual magnetic layers interact via exchange coupling leading to FM or antiferromagnetic (AM) interlayer coupling, depending on the thickness of the non-magnetic layer [93].

2.2.1 Anisotropy in magnetic multilayers

Effective anisotropy

As already mentioned, the influences of the different anisotropy mechanisms discussed in sec. 2.1.1 are usually combined to a single anisotropy term, the so-called effective anisotropy. The anisotropy energy density in thin magnetic multilayer films is normally expressed in the general form

$$\epsilon_{ani} = K_{eff} \cdot \sin^2 \theta \quad (2.15)$$

with the effective anisotropy constant K_{eff} and the angle θ between the unit magnetization vector \mathbf{e}_m and the surface normal \mathbf{n} [94]. In the effective anisotropy, the contribution of all other anisotropy mechanisms such as magnetocrystalline anisotropy K_u , the shape anisotropy (magnetostatic energy by the demagnetization field) and the surface anisotropy K_s are considered¹:

$$K_{eff} = K_u - \frac{1}{2}\mu_0 M_s^2 + \frac{2K_s}{t_{layer}} \quad (2.16)$$

with the thickness t_{layer} of the FM layer. The first order term of the uniaxial anisotropy $K_u = K_{u1} \gg K_{u2}$ is in the range of $K_u = 10^3 \dots 10^5 \text{ J/m}^3$. The surface anisotropy constant is in the range of $|K_s| = 0.1 \dots 1.0 \cdot 10^{-3} \text{ J/m}^2$ and is therefore not negligible for magnetic thin films in the range of $t_{layer} \leq 1 \text{ nm}$. The factor of 2 in the surface anisotropy term is due to the fact that the magnetic layer is normally sandwiched between 2 non-magnetic layers [92].

Perpendicular magnetic anisotropy

For $K_{eff} > 0$ the anisotropy energy according to eq.2.15 is minimized for $\theta \in \{0, \pi\}$ meaning the magnetization is parallel to the surface normal. Hence, the easy axis is

¹Here, also the influence of magnetoelastic and magnetostrictive anisotropy can be considered by adding the corresponding anisotropy term, but their impact is assumed to be negligible for the utilized Co/Pt multilayer.

perpendicular to the plane and the magnetic thin film exhibits PMA. By contrast, for $K_{eff} < 0$ the easy axis lies in-plane and ϵ_{ani} is minimized for $\theta \in \{-\frac{\pi}{2}, \frac{\pi}{2}\}$. Accordingly, the general criteria for the anisotropy in a magnetic thin film are:

$$\text{perpendicular anisotropy (PMA)} : K_{eff} > 0 \quad (2.17)$$

$$\text{in-plane anisotropy} : K_{eff} \leq 0. \quad (2.18)$$

According to eq. 2.16, the corresponding critical film thickness t_{crit} for which the anisotropy changes from in-plane to perpendicular magnetization is

$$t_{crit} = -\frac{2K_s}{K_u - \frac{1}{2}\mu_0 M_s^2}. \quad (2.19)$$

For the Co/Pt multilayer stacks utilized in this work, the saturation magnetization of Co and the surface anisotropy constant of the Co/Pt interface are $M_{s,Co} = 1.4 \cdot 10^6$ A/m and $K_s = 1.15 \cdot 10^{-3}$ J/m², respectively [83, 95]. The uniaxial anisotropy K_u varies due to growth and texture of the Co/Pt multilayer. However, the effective anisotropy of the whole multilayer stack is in the range of $K_{eff,Co/Pt} = 2 \dots 3 \cdot 10^5$ J/m³ and therefore shows strong out-of-plane anisotropy.

2.2.2 Co/Pt multilayers for pNML

From a technological point of view, the magnetic anisotropy K_{eff} and the saturation magnetization M_s are the most important parameters in order to tailor the behavior of the interacting nanomagnets in pNML. Therefore, magnetic multilayers with PMA are highly suitable as both the anisotropy and the magnetic stray field can be adjusted by the composition of the multilayer stack.

The PMA can be tailored by varying the material of both the ferromagnetic (e.g. Fe, Co, Ni) and the non-magnetic layer (e.g. Pt, Cu, Au), the thickness of each layer, the number of multilayers and the crystal orientation [92, 96–98]. Thereby, the so-called seed layer, which is the buffer material between the substrate and the multilayer stack, induces the crystal orientation of the whole multilayer stack and therefore has strong impact on the magnetic anisotropy. Furthermore, the quality of the interfaces and the technological fabrication process (e.g. the deposition technique) are of great importance [92, 99, 100]. The magnetic stray field energy and therefore the interaction of the nanomagnets mainly depends on the saturation magnetization M_s and the volume of the magnetic material, according to eq. 2.9. In magnetic multilayers, the corresponding areal moment $M_s \cdot t_{mag} = M_{s,FM} \cdot t_{FM} \cdot N_{FM}$ can be easily adjusted by the layer thickness t_{FM} and the number N_{FM} of the magnetic layers.

This work employs Co/Pt multilayers to experimentally demonstrate the feasibility of logic operation in magnetic multilayers. In principle, nearly every magnetic thin film or multilayer material with PMA (e.g. Co/Ni, Co/Pd) can be used for

pNML as long as its anisotropy is tunable by FIB irradiation, which will be discussed in sec. 2.2.3. Therefore, the theoretical background as well as the principle ideas and the experimental techniques presented in this work are focused on but not limited to Co/Pt multilayers. However, Co/Pt has been the material of choice for this work for several reasons:

- Co/Pt multilayers are well-studied due to their application in magneto-optical recording media and hard drives for perpendicular magnetic recording [96, 98, 99, 101]. Both the general magnetization reversal [102–105] as well as the switching behavior by applying short field pulses [BKB⁺13],[106–108] have intensively been studied.
- Primary studies on pNML have been performed by investigating ordering phenomena in Co/Pt [61, 63]. Furthermore, the magnetic behavior of Co/Pt nanomagnets is well-understood to model their switching in micromagnetic simulations like OOMMF [62, 109].
- Co/Pt multilayers show strong perpendicular anisotropy, which can be well controlled by adjusting the number as well as the thickness of both the Co and the Pt layers [92, 96, 97, 99, 100, 110]. Another important role falls on the pressure during sputtering, which impacts the grain size and therefore influences the effective anisotropy [99, 111].
- Co shows a strong saturation magnetization of $M_{s,Co} = 1.4 \cdot 10^6$ A/m [112]. By stacking N layers of Co in a Co/Pt multilayer, the total areal magnetic moment $N \cdot t_{Co,layer} \cdot M_{s,Co}$ is heavily increased and therefore reliable interaction of field-coupled Co/Pt nanomagnets is achieved [SB13d].
- Just as the anisotropy, also the natural domain size is adjusted by the composition of the Co/Pt multilayer [93]. Co/Pt multilayers suitable for magnetic logic usually show domain sizes above 100 – 200 nm, which is sufficient to guarantee single-domain behavior of Co/Pt nanodots [26].
- One of the most important aspects is the possibility to tune the magnetic anisotropy by FIB irradiation. The irradiation of Co/Pt using focused Ga⁺ ion beams is well-controllable and has been the object of several fundamental studies [BKB⁺10],[113, 114].
- The fabrication of Co/Pt multilayers is comparatively well-known and covers a wide range of deposition techniques [92]. Magnetron sputtering offers reproducible homogeneous deposition over large areas and enables to tune the magnetic anisotropy by adjusting the sputtering parameters [99, 111, 115].

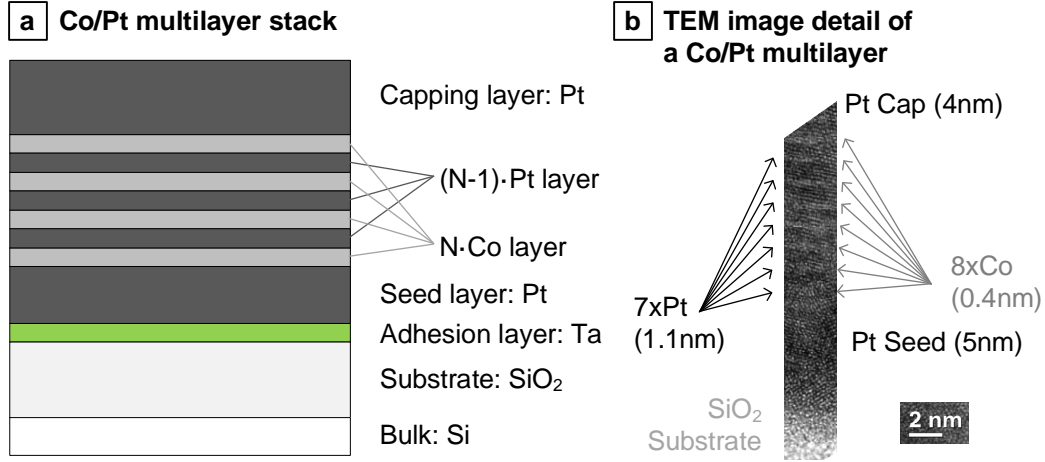


Figure 2.2: Sketch (a) and TEM image (b) of an as-grown Co/Pt multilayer stack.

- Co/Pt has also been the material of choice for magneto-optical recording media and shows a relatively strong magneto-optical Kerr effect (MOKE) [101, 116–118]. This is beneficial for the analysis of the magnetic behavior using magneto-optical microscopy (see sec. 3.1). Due to several advantages of optical analysis techniques (i.e. high-resolution, fast, contactless, easy sample preparation), MOKE microscopy of Co/Pt nanostructures is widely used in this work.

General structure of Co/Pt multilayers

The standard Co/Pt multilayer normally utilized in the experiments in this work is a $\text{Ta}_{2\text{nm}}\text{Pt}_{3\text{nm}}[\text{Co}_{0.8\text{nm}}\text{Pt}_{1\text{nm}}]_{\text{x}4}\text{Pt}_{3\text{nm}}$ stack as described below. Fig. 2.2 shows the a sketch of a common Co/Pt multilayer (a) and a transmission electron microscopy (TEM) image² of an as-grown $\text{Pt}_{5\text{nm}}[\text{Co}_{0.4\text{nm}}\text{Pt}_{1.1\text{nm}}]_{\text{x}8}\text{Pt}_{4\text{nm}}$ stack (b)³.

Substrate As already mentioned in sec. 1.1.1, one of the major requirements on emerging beyond-CMOS devices is the compatibility to CMOS and their fabrication process. Therefore, the Co/Pt multilayer stacks utilized for the experiments in this work are usually grown on a standard Silicium (Si) $\langle 100 \rangle$ wafer with a thermally oxidized SiO_2 film with a thickness of $t_{\text{SiO}_2} \approx 18 \text{ nm}$.

²The preparation of the TEM images by J. Kiermaier has been supported by the Notre Dame Integrated Imaging Facility (NDIIF), University of Notre Dame, Notre Dame, IN, USA.

³In earlier experiments, such different Co/Pt multilayer stacks with a smaller thickness but a higher number of the Co layers showing an equivalent magnetic moment but an increased effective anisotropy have been used.

Adhesion layer A thin adhesion layer of Tantalum (Ta) or Titanium (Ti) with a thickness of $t_{adhesion} = 1 \dots 2$ nm is required to increase the adhesion of the Co/Pt on the SiO₂ surface.

Seed layer The Pt seed layer induces the $\langle 111 \rangle$ texture on the consecutive Co layers [92]. The required thickness of the seed layer is $t_{seed} = 3 \dots 5$ nm in order to enforce the perpendicular anisotropy [110].

Co layer The ferromagnetic Co layers show perpendicular anisotropy induced by the Co/Pt interface up to a maximum thickness of $t_{Co} = 0.8$ nm, otherwise the magnetization turns in-plane [92, 96, 115]. In order to increase the total areal magnetic moment, usually $N = 4$ layers of Co separated by thin Pt layers are used increasing the total Co thickness to $t_{Co,total} = 3.2$ nm. A still higher amount of Co by further increasing the number of layers would increase the magnetic moment, but cause an undesired unsharp switching behavior as well as small domain sizes and constriction of the DW propagation.

Pt layer The Co layers are separated by thin Pt layers with a thickness of $t_{Pt} = 1.0$ nm. The Pt layers are thin enough to ensure ferromagnetic interlayer exchange coupling between the Co layers inducing parallel layer magnetization. At the same time, the Pt is thick enough to separate the Co layers and to renew $\langle 111 \rangle$ growth direction [97, 100].

Capping layer The capping layer or top layer prevents the magnetic material from oxidation. In order to sufficiently protect the Co and at the same time minimize the light absorption in magneto-optical measurement setups, the thickness of the Pt layer has been chosen to $t_{cap} = 3 \dots 5$ nm.

2.2.3 Anisotropy tuning by focused ion beam irradiation

As already discussed in sec. 2.2 the anisotropy of magnetic multilayers can be engineered by adjusting the number and thickness of each layer. However, for pNML it is mandatory to specifically reduce the anisotropy in a local spot in order to control the DW nucleation site (see sec. 2.3.2), [SB11a, SB12b].

The perpendicular anisotropy of magnetic thin films and magnetic multilayers strongly depends on the layer interfaces and the crystalline structure. Ion irradiation enables to modify structural properties due to collisional energy loss of the ions in the multilayer [119, 120]. Thereby, the magnetic material experiences irradiation-induced atom displacements (Fig. 2.3a). Short-range intermixing increases the roughness of the interfaces, whereas long-range mixing leads to the formation of alloys of the ferromagnetic and the non-magnetic material [121].

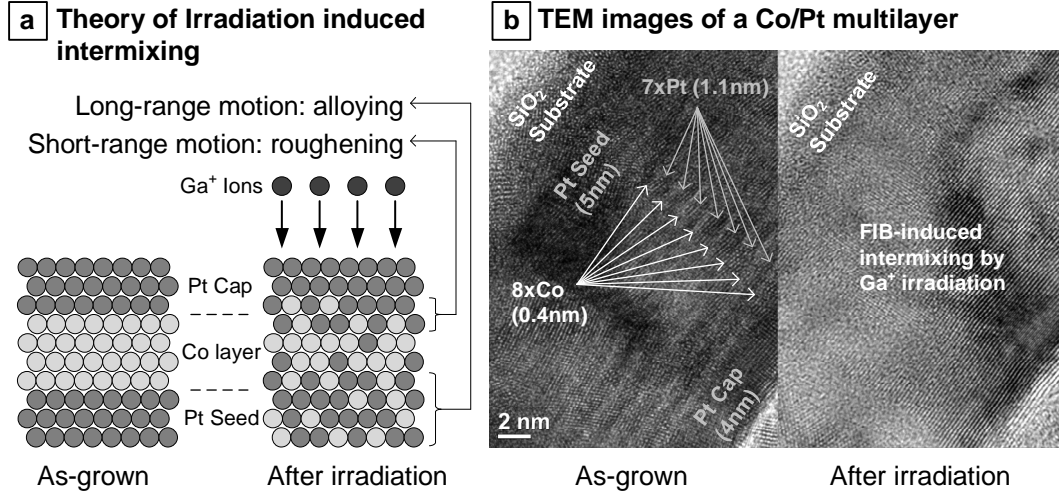


Figure 2.3: a) Irradiation-induced atom displacement after [121] leads to interface roughening (short-range motion) and alloying (long-ranged intermixing). b) TEM images of a Co/Pt multilayer stack as deposited and after Ga⁺ irradiation [SB12b].

Consequently, the interface anisotropy K_s favoring perpendicular magnetization direction is reduced. By contrast, the saturation magnetization M_s and therefore also the demagnetization energy remain constant. Therefore, the shape anisotropy ($-\frac{1}{2}\mu_0 M_s^2$) favoring in-plane magnetization becomes dominant according to eq. 2.16. As a consequence, the easy axis is reoriented from perpendicular orientation to in-plane orientation [114].

In principle, the influence of ion irradiation on the magnetic properties can be divided in three distinct regimes [113, 122, 123]:

- At low irradiation doses, the interface anisotropy is steadily reduced and therefore the coercivity decreases. However, the interface anisotropy still dominates the effective anisotropy and the magnetization remains perpendicular to the plane.
- At higher doses, the interface anisotropy drops by further intermixing of the interfaces and alloy formation. The effective anisotropy becomes negative due to the shape anisotropy and the easy axis reorientates from perpendicular to in-plane magnetization.
- If the irradiation dose is further increased, also the saturation magnetization is reduced and the film characteristic changes from ferromagnetic to paramagnetic.

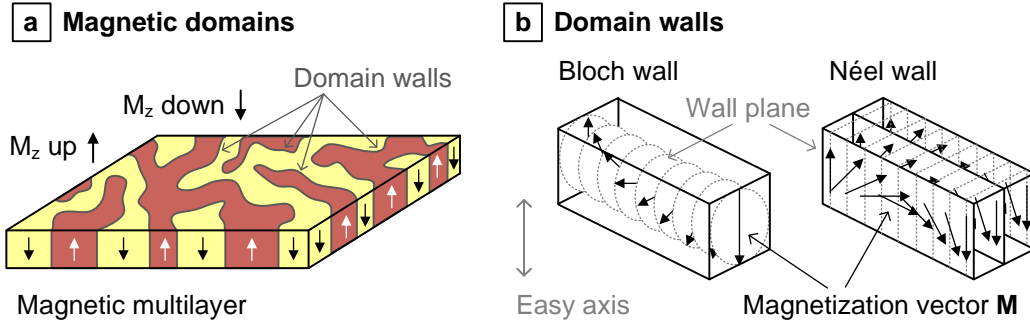


Figure 2.4: The magnetization tends to form domains separated by domain walls in order to minimize the total energy (a). The magnetization in DWs can rotate parallel (Bloch wall) or perpendicular (Néel wall) to the wall plane (b).

Focused ion beam irradiation enables to tailor the magnetic anisotropy in a distinct area. In the experiments the Co/Pt multilayers are irradiated using a 50 kV Ga^+ FIB system. Thereby, the ion-induced intermixing of Co/Pt interfaces leads to the formation of stable CoPt alloys with varying composition [113]. Fig. 2.3b shows TEM images⁴ of an asgrown (left) and an irradiated Co/Pt multilayer stack (right). During switching of magnetic multilayers by applying a magnetic field, the magnetization reversal is initiated in such spots with reduced anisotropy, as will be shown in the following section. Therefore, the specific reduction of the anisotropy in a local spot enables to control the switching behavior of the magnets in pNML.

2.3 Domain theory

In order to minimize the total energy, the magnetization tends to form regions with parallel magnetization to reduce the stray field energy. Such regions with approximately parallel magnetization direction are called *magnetic domains* and in principle, the total energy is reduced with an increasing number of domains (Fig. 2.4a). However, the transition regions between domains with different magnetization direction, so-called *domain walls* (DWs, Fig. 2.4b), increase both the exchange energy and the anisotropy energy. In the end, the magnetization forms a specific number of domains in order to minimize the total energy with respect to the applied field.

From the total energy (eq. 2.10), two important parameters can be derived to describe magnetic domains, the exchange length and the critical domain diameter [94]. The exchange length l_{exchange} is the characteristic length below which the

⁴by J. Kiermaier at NDIIF, University of Notre Dame.

exchange interaction dominates magnetostatic effects and is given by

$$l_{exchange} = \sqrt{\frac{2A}{\mu_0 M_s^2}} \approx 3 \text{ nm} \quad (2.20)$$

for Co/Pt using $A \approx 1.3 \cdot 10^{-11} \text{ J/m}$ and $M_{s,Co/Pt} = 7.2 \cdot 10^5 \text{ A/m}$. The critical domain diameter D_{crit} is the characteristic diameter of a small volume of magnetic material (single domain particle), above which the multidomain configuration is energetically more favorable compared to the single domain state. It is given by

$$D_{crit} = \frac{72\sqrt{AK_{eff}}}{\mu_0 M_s^2} \approx 200 \text{ nm} \quad (2.21)$$

for Co/Pt with $K_{eff} \approx 2.8 \cdot 10^5 \text{ J/m}^3$. Obviously, this parameter is very important for the stability of the Co/Pt magnets and therefore for the design of pNML gates and circuits.

2.3.1 Domain walls (DWs)

Domain walls form a continuous transition between two domains. Thereby, the magnetization transition from one domain to the opposite through a 180° wall rotation can occur in two main modes, namely parallel to the wall plane between the two domains or perpendicular to it. Such types of DWs are called *Bloch wall* or *Néel wall*, respectively (Fig. 2.4b). In principle, a Bloch wall shows less energy and is therefore the energetically preferred type of a DW. However, for small elements and thin magnetic films, the Néel wall becomes more favorable. At the edges of structured magnetic multilayers and thin films with PMA, normally a hybrid form between both wall types can be observed [82].

The exact width of a DW cannot be precisely defined, as the magnetization transition from one direction to the other is only approached asymptotically [83]. However, the characteristic DW width δ_w is usually defined by a tangential approximation leading to

$$\delta_w = \pi \sqrt{\frac{A}{K_{eff}}} \approx 20 \text{ nm} \quad (2.22)$$

for Co/Pt. Sometimes also the DW width parameter $\Delta = \sqrt{\frac{A}{K_{eff}}}$ is used in calculations. Another important parameter in the design of pNML gates is the DW energy density σ_w given by

$$\sigma_w = 4\sqrt{AK_{eff}}. \quad (2.23)$$

It remarkably influences the depinning behavior of a DW in the presence of geometric asymmetries [124]. Therefore the DW energy density is very important in

the design of artificial pinning sites to control the DW motion in magnetic nanowires [SB13c].

The generation and manipulation of DWs in magnetic nanostructures by magnetic fields is the basic approach of pNML. Please note, motion of magnetic domains comprises the generation and manipulation of DWs not only by magnetic fields, but also by e.g. electrical currents, voltages or stress. The theory and experimental work presented in this thesis is limited to the application of magnetic fields, but can be complemented by other effects.

The magnetization reversal in thin films and magnetic multilayers with PMA is dominated by DW nucleation and the subsequent DW propagation [125]. Thereby, the nucleation field H_{nuc} required to nucleate a DW and its propagation velocity v_{DW} under an applied field are crucial to describe and control the switching behavior of the magnets [126, 127]. Another aspect concerns the pinning and depinning of DWs at artificial energy barriers to control the DW motion in magnetic nanowires. Well-defined interaction of magnetic (stray) fields with magnetic DWs to control their nucleation and motion in magnetic nanowires is the key to enable logic operation. The following sections describe the nucleation, propagation and pinning of DWs with focus on magnetic multilayers.

2.3.2 Nucleation of DWs

DW nucleation covers the generation of new domains and the associated DWs. The initial magnetization reversal process in a small spot of a magnetic multilayer can be modeled by the magnetization reversal of a small particle [128]. For such small particles, the so-called Stoner–Wohlfarth model assumes coherent reversal of the particles magnetization under an applied field [129].

Stoner-Wohlfarth model

The Stoner-Wohlfarth model is a simple analytic model considering an uniformly magnetized ellipsoid with uniaxial anisotropy [83, 129]. By applying a magnetic field $\mathbf{H} = H \cdot \mathbf{e}_H$ with angle α to the anisotropy easy axis, the magnetization $\mathbf{M} = M_s \cdot \mathbf{e}_m$ is tilted from the easy axis by the angle θ (Fig. 2.5a). The total energy density ϵ_{tot} of such a single Stoner-Wohlfarth particle is given by

$$\epsilon_{tot} = K_u \sin^2 \theta - \mu_0 M_s H \cos(\alpha - \theta). \quad (2.24)$$

Consequently, the energy density is minimized for the case that the applied field \mathbf{H} and the magnetization \mathbf{M} are aligned parallel ($\alpha = 0$) on the easy axis ($\theta = 0$). However, more important is the minimum field required to saturate the magnetization in the hard axis ($\theta = \pi/2$) which is the most energetic magnetization

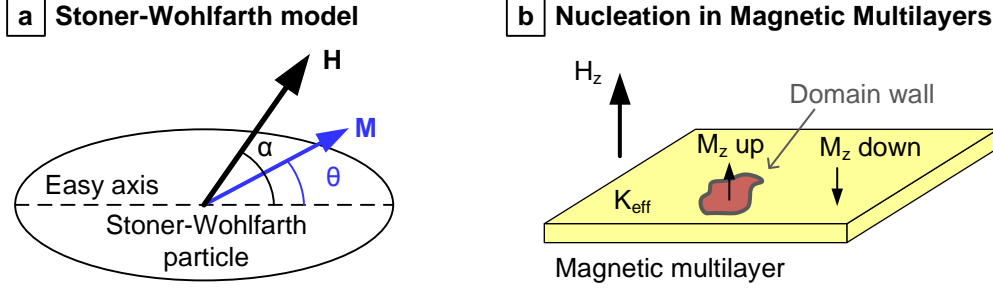


Figure 2.5: a) Stoner-Wohlfarth model: Applying a magnetic field \mathbf{H} with angle α tilts the magnetization \mathbf{M} from the easy axis by the angle θ . b) The domain wall nucleation in magnetic multilayers with PMA is a coherent reversal process which can be modeled using the Stoner-Wohlfarth model.

direction. It can be calculated by minimizing ϵ_{tot} ($\partial\epsilon_{tot}/\partial\theta = 0$) under the constraint $\theta = \pi/2$ [83]. The resulting field is the anisotropy field

$$H_{ani} = \frac{2K_u}{\mu_0 M_s}, \quad (2.25)$$

which is therefore also the maximum field needed to reverse the magnetization of the particle [81].

Nucleation in magnetic multilayers

In a magnetic multilayer film, the overall magnetization reversal is not coherent but governed by DW nucleation and following propagation through the entire magnetic structure. However, the DW nucleation is still a coherent reversal process which can be modeled using the Stoner-Wohlfarth model (Fig. 2.5b) [128]. The field required to reverse the magnetization of an area with effective anisotropy K_{eff} is given by the anisotropy field

$$H_{ani} = \frac{2K_{eff}}{\mu_0 M_s}. \quad (2.26)$$

Consequently, the DW nucleation event initializing the magnetization reversal in a magnetic material generally occurs in an area with lowest anisotropy. In an as-grown magnetic multilayer, such DW nucleation spots of weak anisotropy are usually randomly distributed due to crystal defects grown during the sputtering process [130, 131]. In order to control the DW nucleation and with it the magnetization reversal in magnetic nanostructures, one has to overcome the intrinsic anisotropy distribution.

The artificial, local decrease of the effective anisotropy by FIB irradiation is a

widely used approach to control the DW nucleation in multilayers and magnetic nanowires (e.g. [128, 132, 133]). Typically the entire side of a nanowire is irradiated to study DW pinning at anisotropy boundaries or to define the nucleation site in order to observe DW propagation in magnetic nanowires.

However, in pNML, the DW nucleation is controlled by the stray fields of surrounding input magnets [SB12a]. The stray field of those input magnets drops rapidly over distance and therefore the magnets have to be as close as possible to the nucleation site. In order to guarantee equal and distinct influence of the input stray fields of multiple magnets, the DW nucleation site in the nanowire has to be as small as possible. Therefore, the artificial anisotropy lowering by local FIB irradiation is concentrated on a tiny area creating an ANC for DWs, which enables to control the DW nucleation site and field [SB12b]. Note, that the artificial lowering of the anisotropy for DW nucleation also generates an anisotropy step from the irradiated to the non-irradiated area, which may influence the DW nucleation process (see sec. 2.3.4 and 2.3.5).

2.3.3 DW propagation

Propagation of DWs implies the motion of a DW and the associated expansion of the favored domain. Due to the influence of the applied field, the Zeeman energy E_{Zeeman} is minimized by aligning the magnetization \mathbf{M} parallel to the field \mathbf{H}_{ext} according to eq. 2.6 and hence by expanding the favored domain. The speed of the domain expansion and therefore the speed of the propagating DWs v_{DW} is the key parameter for magnetic devices based on DW motion, since it is the limiting factor for the operating speed of the device. In the simplest theoretical model, the DW velocity v_{DW} depends linearly on the applied field [134]:

$$v_{DW} = \mu_w H \quad (2.27)$$

with the domain wall mobility μ_w . However, in reality the DW velocity depends highly nonlinear on the applied field and eq. 2.27 is only valid for ideal ferromagnetic films without any defects and low magnetic fields below the so-called Walker field $H_w = 2\pi\alpha M_s$ [135, 136]. At low fields $H < H_w$, the DW shows a steady motion with an exact stationary-state solution to the LLG equation and the DW mobility $\mu_w (H < H_w) = \gamma\Delta/\alpha$ [134]. For higher fields $H \gg H_w$, the magnetization of the DW precesses continually and the DW alternates between the Néel and Bloch configuration leading to an oscillatory wall motion. In this precessional regime, the DW velocity is still proportional to the applied field, but with significantly reduced mobility $\mu_w (H \gg H_w) = \gamma\Delta/(\alpha + \alpha^{-1})$. In the intermediate regime, the DW velocity converges asymptotically from the steady motion to the regime of precession.

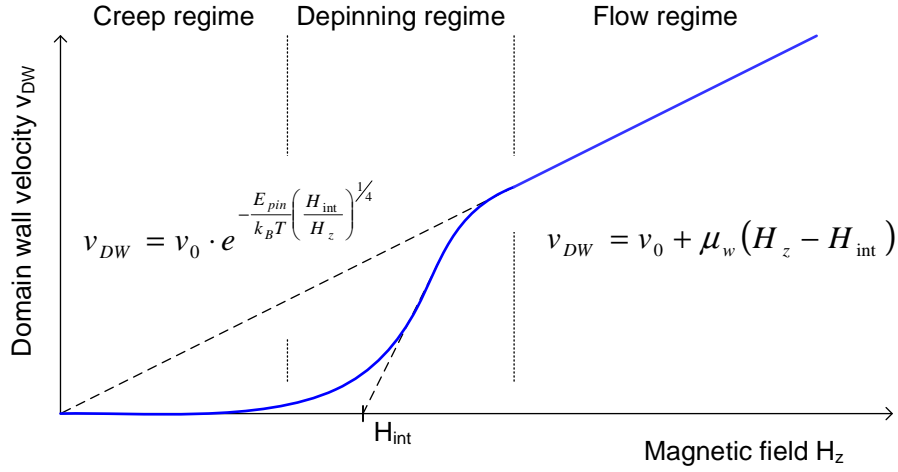


Figure 2.6: Domain wall velocity in magnetic multilayers with PMA versus the applied perpendicular field. Depending on the magnetic field H_z compared to the intrinsic pinning field H_{int} , the DW velocity v_{DW} is classified into three different regimes: the creep regime ($H_z \ll H_{int}$), the depinning regime ($H_z \approx H_{int}$) and the flow regime ($H_z \gg H_{int}$).

Propagation in thin films

In magnetic multilayer films with PMA, the DW motion is dominated by pinning due to small defects in the crystal structure [137, 138]. Here, the DW motion is modeled by a force (magnetic field H) driving a elastic 1D-interface (DW) through a 2D weakly disordered medium (multilayer film with crystal defects). Thereby, the DW velocity is classified into three different regimes depending on the magnetic field H_z compared to the intrinsic pinning field H_{int} , which is the field needed for DW depinning at zero temperature.

Creep regime

For small fields $H_z \ll H_{int}$, the DW depinning from defects is a thermally activated process [139]. The corresponding DW motion is also referred to as creep motion and the (average) DW velocity is described by

$$v_{DW}(H_z \ll H_{int}) \approx v_0 \cdot e^{-\frac{E_{pin}}{k_B T} \left(\frac{H_{int}}{H_z}\right)^{1/4}} \quad (2.28)$$

with the numerical prefactor v_0 and the disorder-induced pinning energy barrier E_{pin} . Velocities in the creep regime are very slow $v_{DW}(H_z \ll H_{int}) \ll 1$ m/s and would therefore strictly limit the device speed. However, the applied clocking field in pNML is usually much larger than the intrinsic pinning field and therefore the restriction in the creep regime is irrelevant for the operation of pNML.

Depinning regime

In the depinning regime, DW motion is still thermally activated, but the applied field H_z is already in the range of the intrinsic pinning field H_{int} . The velocity still increases exponentially with the applied field H_z and also strongly depends on the temperature T according to eq. 2.28 [140]. The depinning regime is also seen as smeared intermediate regime between creep motion and the following flow regime [141].

Flow regime

For high fields $H_z \gg H_{int}$ the disorder of the magnetic material becomes irrelevant and DW motion is governed by viscous flow dynamics [139, 142]. In the flow regime, the DW velocity depends again linear on the applied field corresponding to eq. 2.27 [126]:

$$v_{DW}(H_z \gg H_{int}) = v_0 + \mu_w (H_z - H_{int}). \quad (2.29)$$

The magnetic fields required to nucleate and depin a DW in a pNML logic gate are usually larger than the intrinsic pinning field $H_{nuc} > H_{int}$. Thus, pNML is operated in the flow regime showing DW velocities in the range of 20 – 50 m/s which are sufficient for operating frequencies in the 100 MHz range.

2.3.4 Pinning of DWs

Pinning and Depinning of DWs in magnetic nanowires is very important for the operation of pNML circuits. On the one hand, unintentional pinning due to defects in the magnetic material and the edge roughness of magnetic nanostructures decreases the average DW velocity [143]. This may lead to incomplete switching of a magnet causing critical errors in the logic computation in pNML. On the other hand, well-controlled pinning and depinning of propagating DWs allows to route the information flow in magnetic nanowires [SB13c]. This will enable to store, buffer, multiplex and synchronize magnetic information in complex pNML circuits [SB14c, SB14b]. In the following, two basic approaches to artificially pin propagating DWs are discussed.

Pinning by geometry deformation

Geometrical deformations in magnetic nanowires (e.g. notches) constitute energy barriers with a specific pinning potential for propagating DWs [143, 144]. The energy required to overcome the energy barrier of the geometrical deformation and depin the DW is supplied by the Zeeman energy. According to eq. 2.6, the

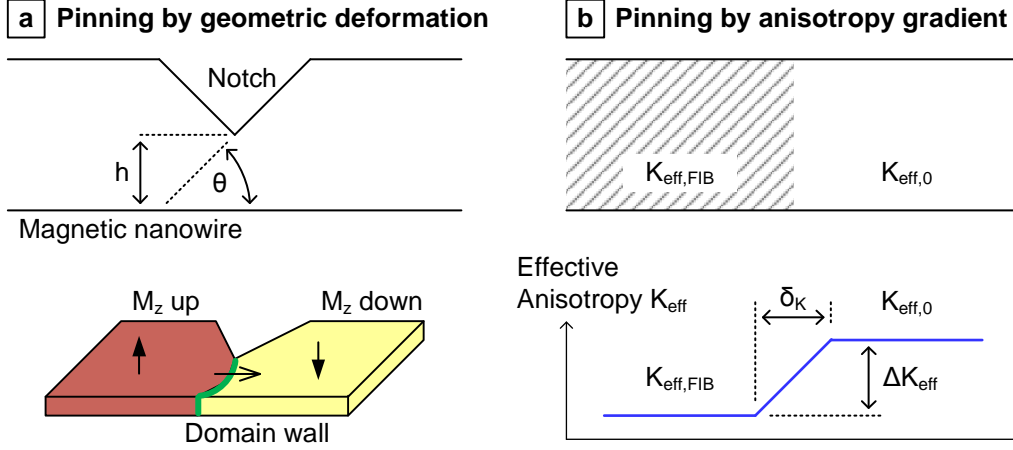


Figure 2.7: Domain wall pinning at geometric deformations (a) and anisotropy gradients (b). At a notch (a), the DW depinning field H_{depin} depends on the notch width h and the apex angle α . At an anisotropy gradient, the depinning field depends on the anisotropy step ΔK_{eff} and the width of the gradient δ_K .

Zeeman energy of the favored domain with area A_{domain} in a magnetic thin film with PMA under an applied, perpendicular field H_z is given by

$$E_{Zeeman} = -M_s H_z \cdot A_{domain} \cdot t_{layer}. \quad (2.30)$$

Thus, the perpendicular field H_z enforces the favored domain to expand its area A_{domain} in order to reduce its Zeeman energy. Simultaneously, the wall energy E_w itself has to be minimized:

$$E_w = \sigma_w \cdot t_{layer} \cdot l_w \quad (2.31)$$

with the length l_w of the domain wall. In order to depin from the geometrical deformation, the favored domain expands its area while minimizing its length. As a result, the DW is bent to an arc of circle (Fig. 2.7a).

For a single-sided notch in a magnetic nanowire, the depinning field H_{depin} , which is required to depin the DW, can be obtained from the competition between the Zeeman energy and the wall energy:

$$H_{depin} = H_{int} + \frac{\sigma_w \sin \alpha}{2M_s \left(h + \frac{1}{2} \cdot \delta_w \sin \alpha \right)} \approx H_{int} + \frac{\sigma_w \sin \alpha}{2M_s h}, \quad h \gg \delta_w \quad (2.32)$$

with the notch's apex angle α and the notch width h [124]. Similar to DW propagation in the creep regime, DW depinning from a notch is a thermally activated magnetization process. Therefore, the average DW depinning time, which is required to depin a DW from a notch with the depinning field H_{depin} under an

applied field H , is modeled by

$$t_{depin} = \tau_0 e^{\frac{M_s V_a}{k_B T} (H_{depin} - H)} \quad (2.33)$$

with the inverse of the attempt frequency $\tau_0 = f_0^{-1}$ and the activation volume V_a [124]. Obviously, the depinning field and time strongly depend on the shape of the geometrical deformation [145, 146]. Therefore the approach to control the signal flow by notches in magnetic nanowires is highly suitable for the application in pNML [SB14c].

Pinning by anisotropy gradient

Another approach to control the pinning and depinning of DWs is the local modification of the anisotropy, as a step in the anisotropy acts as an energy barrier for DWs [133, 147]. As already discussed in sec. 2.2.3, partial FIB irradiation locally reduces the anisotropy and therefore can be used to artificially pin propagating DWs. In the following applied model from [128], the PMA in a magnetic nanowire is reduced from $K_{eff,0}$ to $K_{eff,FIB}$ by FIB irradiation and the transition from $K_{eff,FIB}$ to $K_{eff,0}$ is a linear gradient with the length δ_K (Fig. 2.7b). If the DW is already nucleated in the irradiated area, the depinning field H_{depin} to inject the DW from the irradiated ($K_{eff,FIB}$) to the non-irradiated area ($K_{eff,0}$) is

$$H_{depin} = \frac{K_{eff,0} - K_{eff,FIB}}{2\mu_0 M_s} \frac{2\Delta}{\delta_K} \tanh \frac{\delta_K}{2\Delta}. \quad (2.34)$$

However, if the length of the anisotropy gradient is much smaller than the width of the DW ($\delta_K \ll \Delta$), the expression for the depinning field is simplified to

$$H_{depin} = \frac{K_{eff,0} - K_{eff,FIB}}{2\mu_0 M_s} = \frac{\Delta K_{eff}}{2\mu_0 M_s}. \quad (2.35)$$

If the irradiation dose is increased, the anisotropy of the irradiated area and therefore also the magnetization turn in-plane ($K_{eff,FIB} < 0$). Hence, the depinning field is limited to the nucleation field of a DW in an in-plane to out-of-plane interface, which is given by

$$H_{depin} = \frac{K_{eff,0}}{\mu_0 M_s}. \quad (2.36)$$

The combination of smooth and abrupt anisotropy gradients allows to control the DW propagation direction in an alternating, perpendicular field as demonstrated by [148]. However, the approach of local FIB irradiation to control the pinning of DWs in magnetic nanowires is not applicable in pNML. The technique of partial FIB irradiation is also used to fabricate the ANCs to control the DW nucleation in the magnets. Therefore, additional irradiated areas which are not controlled by the fringing fields of surrounding input magnets increase the risk of unintentional DW nucleation.

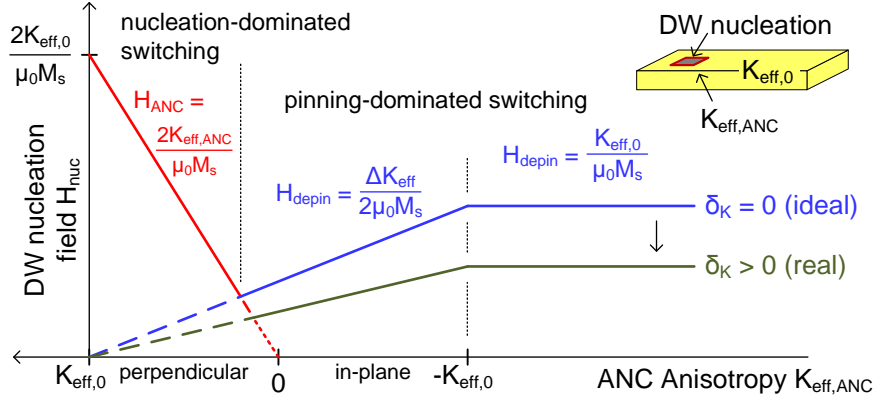


Figure 2.8: DW nucleation field H_{nuc} to nucleate a DW from the ANC into the non-irradiated area of a magnet. The magnetization reversal is either nucleation-dominated or pinning-dominated depending on the effective anisotropy $K_{eff,ANC}$ of the ANC fabricated by partial FIB irradiation.

2.3.5 DW nucleation from artificial nucleation centers

As already mentioned in sec. 2.3.2, the generation of ANC by local lowering the anisotropy with partial FIB irradiation also generates an anisotropy step from the irradiated to the non-irradiated area. Therefore, the field required to nucleate a DW from the ANC into the non-irradiated area, depends on both the anisotropy field to reverse the magnetization at the ANC H_{ANC} and the depinning field H_{depin} to overcome the anisotropy step (Fig. 2.8) [128]. Consequently, the nucleation field H_{nuc} , which is required to nucleate a DW into the non-irradiated area⁵, is

$$H_{nuc} = \max(H_{ANC}, H_{depin}). \quad (2.37)$$

Thereby, H_{ANC} and H_{depin} depend on the reduced anisotropy $K_{eff,ANC}$ at the ANC and the effective anisotropy $K_{eff,0}$ of the non-irradiated multilayer according to eqs. 2.26, 2.35 and 2.36. By applying eq. 2.37, the nucleation field can be determined to

$$H_{nuc} = \begin{cases} \frac{2}{\mu_0 M_s} K_{eff,ANC} & K_{eff,ANC} \geq \frac{1}{5} K_{eff,0} \\ \frac{1}{2\mu_0 M_s} (K_{eff,0} - K_{eff,ANC}) & \frac{1}{5} K_{eff,0} > K_{eff,ANC} > -K_{eff,0} \\ \frac{1}{\mu_0 M_s} K_{eff,0} & K_{eff,ANC} \leq -K_{eff,0} \end{cases} \quad (2.38)$$

as depicted in Fig. 2.8. In the first case, the anisotropy field H_{ANC} which is required to reverse the magnetization at the ANC still dominates the DW nucleation and therefore $H_{nuc} = H_{ANC} > H_{depin}$.

⁵In this work, the nucleation field H_{nuc} is referred to as the field, which is required to nucleate and eventually depin a DW into the non-irradiated area.

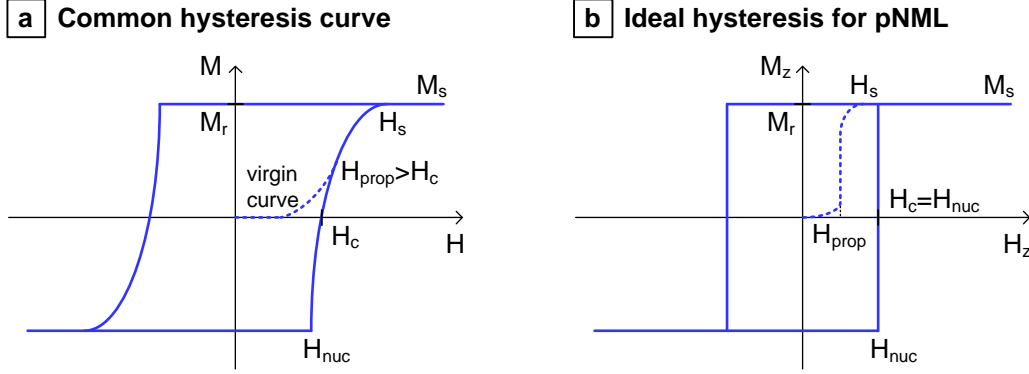


Figure 2.9: Hysteresis and corresponding virgin curves from the demagnetized state of a common magnetic multilayer film (a) and an ideal multilayer film for pNML (b).

In the second case, the anisotropy at the ANC is further reduced. Therefore, the anisotropy step ΔK_{eff} is increased, the DW is pinned at the anisotropy boundary and $H_{nuc} = H_{depin} > H_{ANC}$.

In the last case, when the anisotropy of the ANC is $K_{eff,ANC} \leq -K_{eff,0}$, the 90° DW is always present at the anisotropy boundary and the DW nucleation $H_{nuc} = H_{depin}$ is determined by the depinning field from in-plane to perpendicular anisotropy.

In this model, a sharp anisotropy gradient is assumed, which is of course an ideal model. In the experiments, a smooth anisotropy gradient will be present and the transitions between the nucleation regimes get smeared. Especially in the case of $K_{eff,ANC} < 0$, the real depinning field is significantly lower: $H_{depin,real} < \frac{K_{eff,0}}{\mu_0 M_s}$ (Fig. 2.8) [128].

2.4 Hysteresis curve

The hysteresis curve describes the non-linear, irreversible response of the magnetization \mathbf{M} of the magnetic material to an applied magnetic field \mathbf{H} . Fig. 2.9 shows the characteristic hysteresis curve of a magnetic multilayer film (a) which is exemplary discussed after [101] and an ideal hysteresis curve for pNML (b). Additionally, the virgin curve - the initial magnetization curve from the demagnetized state - is shown. In a certain manner, hysteresis measurement enables to partially determine the underlying magnetization dynamics in magnetic multilayers. In the following, the most significant characteristic parameters of the hysteresis curve are discussed.

Nucleation field H_{nuc}

The nucleation field H_{nuc} is the magnetic field required to reverse the magnetization in a small area in order to nucleate a DW. In theory, the nucleation field is equal to the anisotropy field $H_{nuc} = H_{ani} = \frac{2K_{eff}}{\mu_0 M_s}$. However, due to defects in the multilayer structure (locally reduced anisotropy K_{eff}) as well as thermal activation (see sec. 2.5), the nucleation field in magnetic multilayers is usually significantly decreased. In pNML, the DW is nucleated at an ANC and the nucleation field is given as described in sec. 2.3.5.

Propagation field H_{prop}

The magnetic field required to drive a DW through the magnetic material is called the propagation field H_{prop} . As already discussed in sec. 2.3.3, creep DW motion is observed even at low fields, but the DW velocity is rather slow and not applicable for pNML. Therefore, usually the intrinsic pinning field is referred to as propagation field $H_{prop} = H_{int}$. At the best, the propagation field is significantly smaller than the nucleation field ($H_{prop} < H_{nuc}$) in order to provide unimpeded DW propagation after nucleation. Thus, the shape of the hysteresis shows sharp switching particularly at the beginning of the magnetization reversal. However, the propagation field H_{prop} is still measurable in the virgin curve starting from the demagnetized state (cp. Fig. 2.9).

Coercive field H_c

The coercive field H_c also known as coercivity is the field required to demagnetize the sample and reverse the sign of the overall magnetization. For small DW propagation fields $H_{prop} < H_{nuc}$, the coercive field is usually equal to the nucleation field $H_c = H_{nuc}$. The coercivity is commonly used to describe the switching field of a magnetic structure.

Saturation field H_s

The saturation field H_s is required to saturate the magnetization of a magnetic material into the direction of the applied field. Depending on the composition of the magnetic multilayer, the saturation field may significantly exceed the coercivity, which is known as high-field irreversibility [149]. In an ideal case for pNML, the saturation field H_s and therefore also the propagation field H_{prop} are significantly smaller than the nucleation field ($H_{nuc} = H_c > H_s, H_{prop}$). In that case, the hysteresis shows sharp switching and the magnetization reversal is dominated by DW nucleation. The saturation field and the propagation field can still be measured in the virgin curve.

Saturation magnetization M_s

The saturation magnetization M_s is reached when the applied magnetic field is equal to the saturation field H_s . Thereby all magnetic moments are aligned in parallel to the applied field. Magneto-optical microscopy only offers to draw a limited conclusion about the absolute saturation magnetization, as the amplitude of the measured hysteresis depends on multiple criteria (e.g. reflectivity and Kerr rotation). Therefore, the hysteresis is usually depicted normalized to the saturation magnetization.

Remanence magnetization M_r

The remanence (magnetization) M_r is the remaining magnetization when the applied field is reduced to zero after saturation. At the best, the magnetization stays in the direction of the applied field and the remanence is equal to the saturation magnetization $M_r = M_s$. Full remanence is extremely important for pNML, where the magnetization has to remain aligned to ensure maximum coupling of interacting nanomagnets, even when the field is applied to the antiparallel direction. The ideal hysteresis for pNML shows a squared shape indicating sharp, nucleation-dominated switching ($H_{nuc} > H_{prop}, H_s$) and bistable, nonvolatile magnetization $M_r = M_s$ as shown in Fig. 2.9b.

2.5 Time-dependent magnetization dynamics

As already mentioned in sec. 2.1.1, thermal energy plays a significant role in magnetization dynamics. Néel and Brown showed, that the magnetization reversal of a small magnetic particle can be described by thermal activation over an energy barrier [150, 151]. Based on the Stoner-Wohlfarth model for the reversal of a small particle (see sec. 2.3.2), a simple model can be derived to describe the time-dependent coercivity by thermally assisted surmounting of an energy barrier, whose height is reduced by the applied field [152]:

$$E_{barrier} = K_{eff}V (1 - H/H_0)^2 \quad (2.39)$$

with the switching volume V of the particle [153]. Consequently, the coercive field at zero temperature

$$H_0 = \frac{2K_{eff}}{\mu_0 M_s} \quad (2.40)$$

is equivalent to the anisotropy field H_{ani} from the Stoner-Wohlfarth model (sec. 2.3.2) [152, 154]. The energy barrier is applied to a conventional Arrhenius model in order to describe the switching rate

$$r = f_0 e^{-\frac{E_{barrier}}{k_B T}} \quad (2.41)$$

with the attempt frequency f_0 , which is in the low GHz-range for single particles [155, 156] and discussed to be even higher for the thermal activation of domain walls [157]. By defining the coercivity $H_c(t)$ as the field, which is required to reverse the particle during the time t by a 50 % probability, one obtains

$$H_c(t) = H_0 \left[1 - \sqrt{\frac{k_B T}{K_{eff} V} \ln \left(\frac{f_0 t}{\ln 2} \right)} \right], \quad (2.42)$$

which is the classic Sharrock equation to determine the time dependent coercivity [152].

The Sharrock model can be also applied for the time-dependent DW nucleation in magnetic multilayers [156],[BKB⁺13]. Here, the energy term KV is usually replaced by the energy barrier at zero field $E_0 = K_{eff}V$ by substituting the switching volume with $V = \frac{2E_0}{\mu_0 M_s H_0}$ and using the anisotropy field $H_0 = \frac{2K_{eff}}{\mu_0 M_s}$ of eq. 2.40. Commonly, the energy barrier at zero field E_0 is specified in units of $k_B T$, leading to

$$E_{barrier} = E_0 \left(1 - \frac{H}{H_0} \right)^n \quad (2.43)$$

for the total energy barrier. The exponent n is in the range of $n = 1 \dots 2$ depending on the magnetization reversal (coherent rotation $n = 2$ or DW nucleation $n = 1$), but is influenced by temperature, DW pinning and the thickness of the magnetic material [156, 158].

During clocking in pNML, usually clocking field pulses with constant amplitude and pulse time are applied [SB13b, SB14b]. The according probability for DW nucleation in an applied field H during the time t can be described by using the Arrhenius model [153, 156]:

$$P_{nuc}(t, H) = 1 - \exp \left(-\frac{t}{\tau(H)} \right) \quad (2.44)$$

$$\tau(H) = f_0^{-1} \cdot \exp \left(\frac{E_0 \cdot \left(1 - \frac{H}{H_0} \right)^n}{k_B T} \right) \quad (2.45)$$

with the switching time constant $\tau(H) = 1/r$ as the inverse switching rate of eq. 2.41.

2.6 Magnetic fringing fields

Co/Pt nanomagnets in pNML interact by their fringing field (or coupling field, stray field) to perform logic operations. Naturally, the strength of the interaction depends on the magnetic material, the geometry and the distance between the coupled nanomagnets. In order to engineer the interaction between the magnets

as desired, numerical finite-element simulations are applied. Such simulations enable to pre-calculate the coupling field of a magnet depending on its magnetic material and geometry before fabrication.

2.6.1 Point-dipole approximation

The dipole field of a small magnetic element can be estimated using the well-known point-dipole approximation (e.g. [50, 83, 159]). A small magnetic element i with volume V_i , saturation magnetization M_s and magnetization direction \mathbf{e}_{m_i} possesses the magnetic moment

$$\mathbf{m}_i = M_s \cdot V_i \cdot \mathbf{e}_{m_i} \quad (2.46)$$

which is for an infinitesimal small volume V_i also referred to as *magnetic dipole*. The magnetic field generated by the magnetic moment \mathbf{m}_i is called *magnetic dipole field* [83]. It is calculated based on the Biot-Savart law, where a small volume δV with current density $\mathbf{j} = j \cdot \mathbf{e}_j$ generates the magnetic field

$$\delta \mathbf{H} = -\frac{1}{4\pi} \frac{\mathbf{r} \times \mathbf{j}}{r^3} \delta V \quad (2.47)$$

at the distance $\mathbf{r} = r \cdot \mathbf{e}_r$. According to Ampere's law, the magnetic moment \mathbf{m} generated by the current density $\mathbf{j}(\mathbf{r})$ at the point \mathbf{r} is

$$\mathbf{m} = \frac{1}{2} \int \mathbf{r} \times \mathbf{j}(\mathbf{r}) dV. \quad (2.48)$$

Assuming the magnetic dipole element as infinitesimal small current loop generating a magnetic moment \mathbf{m} finally gives the magnetic dipole field

$$\mathbf{H}(\mathbf{m}, \mathbf{r}) = \frac{1}{4\pi r^3} \left[3 \frac{(\mathbf{m} \cdot \mathbf{r}) \mathbf{r}}{r^2} - \mathbf{m} \right]. \quad (2.49)$$

The point-dipole approximation is also applicable to calculate the stray field of a small element with the magnetic moment \mathbf{m}_i according to eq. 2.46 as shown in Fig. 2.10a.

2.6.2 Coupling field of a Co/Pt nanomagnet

The coupling field of a Co/Pt nanomagnet is calculated by numerical finite element calculations using the point-dipole approximation discussed above. Therefore, the magnet is divided into small elements i with volume $V_i = d_x \cdot d_y \cdot d_z$ and the magnetic moment $\mathbf{m}_i = M_s \cdot V_i \cdot \mathbf{e}_{m_i}$ (Fig. 2.10b) [SB13d]. The saturation magnetization of the magnetic multilayer is calculated by

$$M_s = M_{s,Co} \cdot \frac{N \cdot t_{Co}}{t_{total}} \quad (2.50)$$

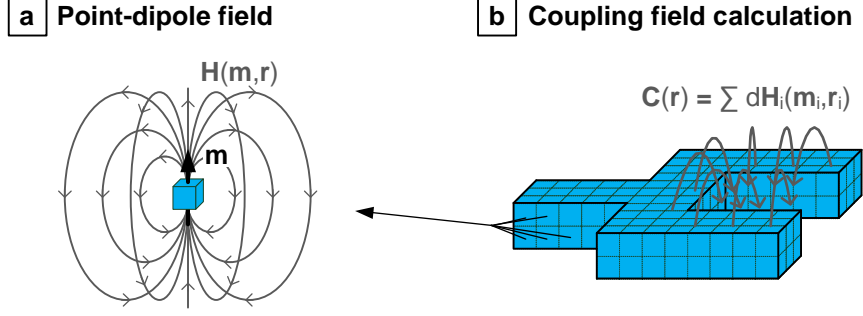


Figure 2.10: Strayfield $\mathbf{H}(\mathbf{m}, \mathbf{r})$ of a small magnetic volume using the point-dipole approximation (a). The coupling field $\mathbf{C}(\mathbf{r})$ of a nanomagnet is determined by numerical finite-element calculations (b).

with the number of Co layers N , the Co layer thickness t_{Co} and the total thickness t_{total} of the magnetic multilayer stack. The stray field contribution $d\mathbf{H}_i$ of each element i is estimated by the point-dipole approximation according to eq. 2.49:

$$d\mathbf{H}_i(\mathbf{m}_i, \mathbf{r}_i) = \frac{1}{4\pi r_i^3} \left[3 \frac{(\mathbf{m}_i \cdot \mathbf{r}_i) \mathbf{r}_i}{r_i^2} - \mathbf{m}_i \right]. \quad (2.51)$$

Finally, the coupling field \mathbf{C} of the whole Co/Pt nanomagnet is calculated by the superposition of the stray field $d\mathbf{H}_i$ of each element i [SB14b]:

$$\mathbf{C}(\mathbf{r}) = \sum_i d\mathbf{H}_i(\mathbf{m}_i, \mathbf{r}_i). \quad (2.52)$$

In 2D-pNML, the Co/Pt nanomagnets usually show perpendicular anisotropy $\mathbf{e}_m = \mathbf{e}_z$ and are fabricated on the same plane leading in good approximation to $\mathbf{r}_i = r_{i,x} \cdot \mathbf{e}_x + r_{i,y} \cdot \mathbf{e}_y$ and $r_{i,z} = 0$. Consequently, $\mathbf{m}_i \perp \mathbf{r}_i$ and therefore $\mathbf{m}_i \cdot \mathbf{r}_i = 0$. Hence, the point-dipole field of each element i of eq. 2.51 is simplified to

$$d\mathbf{H}_i(\mathbf{r}_i) = -\frac{M_s \cdot V_i}{4\pi r_i^3} \mathbf{e}_z. \quad (2.53)$$

and the coupling field calculation gives

$$\mathbf{C}(\mathbf{r}) = - \underbrace{\frac{M_s \cdot V}{4\pi} \sum_i \frac{1}{r_i^3}}_{\text{coupling strength } C(\mathbf{r})} \cdot \mathbf{e}_z = -C(\mathbf{r}) \cdot \mathbf{e}_z \quad (2.54)$$

assuming that the magnet is divided into equal elements with equal volume V . The negative sign indicates the antiparallel coupling of the nanomagnets.

3 Metrology of Magnetic Nanostructures

This section gives an overview of metrology of magnetic nanostructures with focus on magneto-optical microscopy. The set-up of an appropriate measurement system for the fast but accurate investigation and characterization of Co/Pt nanostructures has been one of the major mandatory aspects to realize pNML devices and circuits. Due to several general advantages of optical microscopy, one aspect of this thesis was the construction of a laser-scanning magneto-optical microscope, which in the following has been used for the major part of the experiments. Due to the success of the home-made laser microscope, another wide-field magneto-optical microscope providing fast magnetic imaging of structured surfaces has been set up to facilitate several experiments. Additionally, experiments have been supported by an enhanced magnetic force microscopy (MFM) [28] providing significantly increased lateral resolution (≈ 10 nm), but slow measurement times (sec. 3.2) .

3.1 Magneto-optical microscopy

Optical microscopy provides in general several advantages which are crucial for the multifarious investigation of Co/Pt nanostructures. Optical microscopy is

- fast,
- contactless (no sample disturbance),
- provides imaging with high lateral resolution,
- enables easy sample preparation, and
- has no impact on the sample characteristics (feedback prevention).

In order to exploit those benefits, two different magneto-optical microscopes based on the so-called MOKE have been set up and engineered at LTE particular for the measurement of Co/Pt multilayer films and nanostructures. The laser-scanning MOKE microscope (LMOKE) enables to scan the sample surface and measure the magnetic switching behavior by hysteresis measurements at each spot of the sample using a pulsed laser focused on a tiny spot. In a wide-field MOKE microscope

(WMOKE), the laser is replaced by a light-emitting diode (LED) illuminating a wide area and the reflecting light is detected by a camera, which allows fast imaging of magnetic domains on the structured sample surface. In the following, first the MOKE is described and afterwards the working principle of both MOKE microscopes is discussed in detail.

3.1.1 Magneto-optical Kerr effect (MOKE)

The discovery of the MOKE goes back to 1877, when J. Kerr investigated the rotation of the polarization of light by reflection from a magnetized surface [160]. Inspired by the discovery of the magneto-optical effect (or Faraday effect) by M. Faraday in 1846 [161], where the plane of polarization is rotated in a magnetic field, Kerr studied the polarization rotation by the reflection from the pole of a magnet. He finally found out, that:

"When plane-polarized light is reflected regularly from either pole of an electromagnet of iron, the plane of polarization is turned through a sensible angle in a direction contrary to the nominal direction of the magnetizing current; so that a true south pole of polished iron, acting as a reflector, turns the plane of polarization righthandedly." [160]

Consequently, the magnetization of a magnetic material like Co/Pt can be studied by analyzing the polarization of light reflected from the magnetic surface. In the following, an overview on the polarization of light and its modification by reflection at magnetized surfaces will be given. The description, equations and figures are based on [82, 162–164][Bre09].

Polarization of light

The general electromagnetic plane wave is described by

$$\mathbf{E}(\mathbf{r}, t) = \mathbf{E}_0 \exp[j(\mathbf{k} \cdot \mathbf{r} - \omega t + \varphi)] \quad (3.1)$$

with the complex electric field amplitude vector \mathbf{E}_0 , the wave (propagation) vector \mathbf{k} , the angular frequency ω and the phase shift φ . Thereby, the electric field $\mathbf{E}(\mathbf{r}, t)$ lies in the polarization plane which is perpendicular to the propagation vector \mathbf{k} (Fig. 3.1). Depending on the oscillation of $\mathbf{E}(\mathbf{r}, t)$ in the polarization plane, the wave is referred to as linear, circular or elliptic polarized wave.

Linear polarized wave In a linear polarized (LP) wave (Fig. 3.1a), the electric field $\mathbf{E}(\mathbf{r}, t)$ oscillates on a straight line which is rotated by the polarization angle Φ . Due to the principle of superposition, each wave $\mathbf{E}(\mathbf{r}, t)$ can be considered

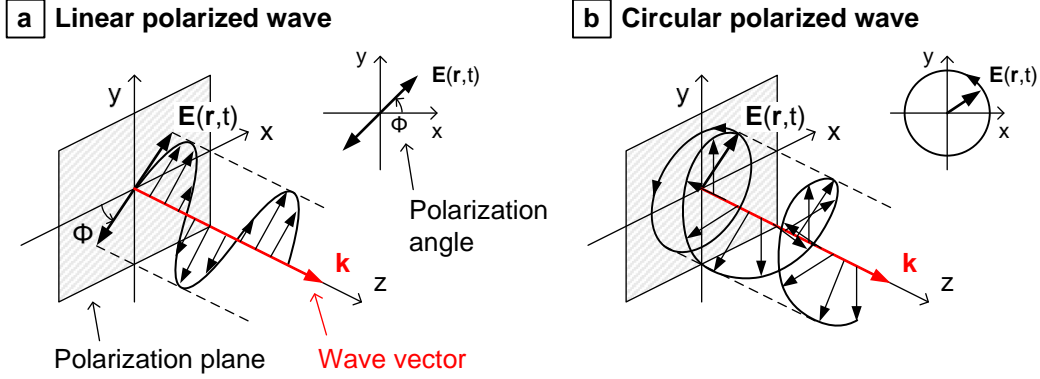


Figure 3.1: Sketch of a linear and a circular polarized propagating wave. For a linear polarized wave (a), the electric field $\mathbf{E}(\mathbf{r}, t)$ oscillates on a straight line in the polarization plane which is perpendicular to the propagation direction \mathbf{k} . For a circular polarized wave (b), the electric field $\mathbf{E}(\mathbf{r}, t)$ rotates in the polarization plane with constant amplitude.

as superposition of two linear polarized elementary waves \mathbf{E}_x and \mathbf{E}_y . Linear polarized waves can be substituted by two orthogonal linear polarized elementary waves with equal phase

$$\mathbf{E}_{LP} = \mathbf{E}_x + \mathbf{E}_y \text{ with } \varphi_x = \varphi_y. \quad (3.2)$$

The polarization angle of the corresponding, superposed wave \mathbf{E}_{LP} depends on the amplitudes of the elementary waves:

$$\tan \Phi = \frac{E_{0,y}}{E_{0,x}}. \quad (3.3)$$

Circular polarized wave In a circular polarized (CP) wave (Fig. 3.1b) $\mathbf{E}(\mathbf{r}, t)$ rotates around the propagation vector \mathbf{k} . Depending on the rotation direction, the wave is either right circularly polarized (RCP) or left circularly polarized (LCP). For the substitution of a circular polarized wave, the two linear polarized elementary waves show equal amplitudes, but the phase of one elementary wave is shifted by $\pm\pi/2$ compared to the other one:

$$\mathbf{E}_{CP} = \mathbf{E}_x + \mathbf{E}_y \text{ with } E_{0,x} = E_{0,y} \text{ and } \varphi_x = \varphi_y \pm \pi/2. \quad (3.4)$$

Depending on the sign of the phase shift $\Delta\varphi = \varphi_x - \varphi_y = \pm\pi/2$, the superposed wave \mathbf{E}_{CP} is either RCP (clockwise rotation) or LCP (counterclockwise rotation).

Elliptic polarized wave The most common description is the elliptic polarized (EP) wave, where $\mathbf{E}(\mathbf{r}, t)$ oscillates (clockwise or counterclockwise) on an ellipse

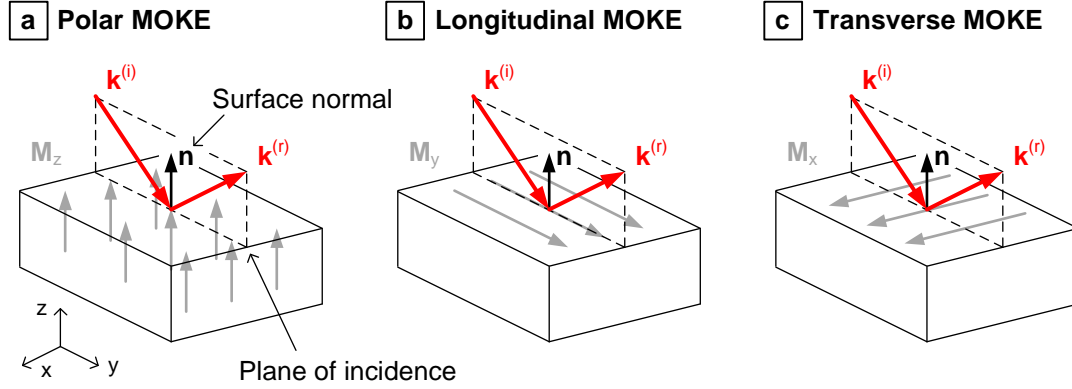


Figure 3.2: Various geometries of the magneto-optical Kerr effect. Depending on the orientation of the plane of incidence (= plane of the incident ($\mathbf{k}^{(i)}$) and reflected ($\mathbf{k}^{(r)}$) light wave), the direction of the sample magnetization \mathbf{M} and the the surface normal \mathbf{n} , the MOKE is referred to as polar ((a), $\mathbf{M} \parallel \mathbf{n}$), longitudinal ((b), $\mathbf{M} \perp \mathbf{n}$ and $\mathbf{M} \parallel$ plane of incidence) or transverse ((c), $\mathbf{M} \perp \mathbf{n}$ and $\mathbf{M} \perp$ plane of incidence).

which is rotated by the polarization angle Φ . For the substitution into elementary waves, neither the amplitudes $E_{0,x}$, $E_{0,y}$ nor the phase shift $\Delta\varphi$ between \mathbf{E}_x and \mathbf{E}_y are restricted. The corresponding polarization angle is

$$\tan 2\Phi = \frac{2E_{0,x}E_{0,y} \cos \Delta\varphi}{E_{0,x}^2 - E_{0,y}^2} \quad (3.5)$$

and the ellipticity $\epsilon_{\text{ell}} = \sqrt{a^2 - b^2}/a$ which describes the normalized ratio between the major (a) and the minor axis (b) of the ellipse ranging between 0 (ellipse is a circle) and 1 (ellipse is a straight line). Indeed, with the equations given above, one can imagine that the linear and the circular polarized wave are just special cases of an elliptic polarized wave.

Different modes of polarization rotation by reflection at magnetized surfaces

The MOKE is classified into three different modes are depending on the plane of incident light and the magnetization \mathbf{M} (Fig. 3.2). The plane of incidence is spanned by the incident wave $\mathbf{k}^{(i)}$ and reflected wave $\mathbf{k}^{(r)}$ and is in parallel to the normal \mathbf{n} of the magnetic surface.

- At the *polar MOKE* (Fig. 3.2a), the sample surface shows perpendicular magnetization which is in parallel to the sample surface $\mathbf{M} \parallel \mathbf{n}$.
- For the *longitudinal MOKE*, the magnetization \mathbf{M} lies in-plane $\mathbf{M} \perp \mathbf{n}$ and is parallel to the plane of incidence.

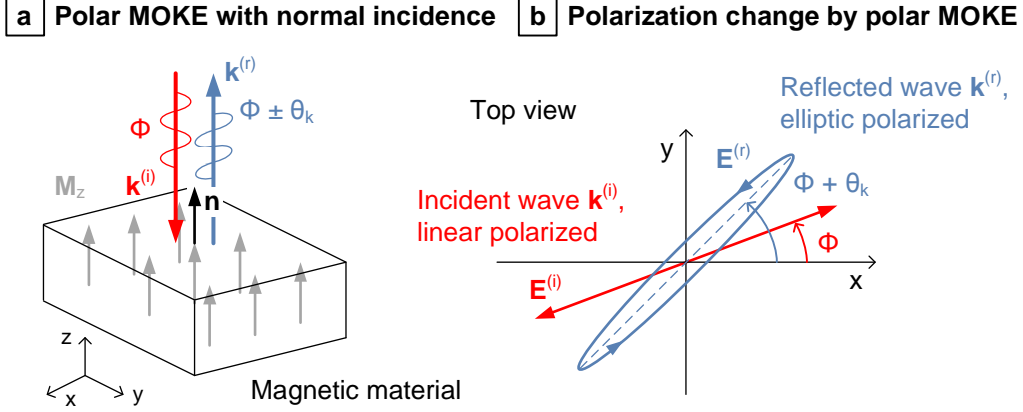


Figure 3.3: Polar magneto-optical Kerr effect. The vertical incident wave $\mathbf{k}^{(i)}$ is reflected at the surface of the perpendicular magnetized material (a). Thereby, the polarization of the reflected wave $\mathbf{k}^{(r)}$ is rotated by the Kerr angle θ_k and transformed to elliptic polarization (b).

- At the *transverse MOKE*, the magnetization \mathbf{M} is still in-plane $\mathbf{M} \perp \mathbf{n}$, but perpendicular to the plane of incidence.

As Co/Pt multilayers used in pNML exhibit PMA, the magneto-optical microscopes presented in sec. 3.1.2 and 3.1.3 are based on the polar MOKE. Therefore, in the following only the polar MOKE will be discussed.

Polar magneto-optical Kerr effect

Fig. 3.3 shows the geometry (a) and the corresponding polarization (b) for a normal incident, linear polarized wave which is reflected at the surface of a perpendicular magnetized medium. Due to the reflectivity of the metallic surface and the polar MOKE, the incident wave $\mathbf{k}^{(i)}$ is reflected at the surface and the polarization of the reflected wave $\mathbf{k}^{(r)}$ is rotated by the Kerr angle θ_k . Additionally, the polarization of the reflected wave is transformed to elliptic polarization. The sign of the polarization rotation by the Kerr angle θ_k thereby depends on the direction of the magnetization $\pm \mathbf{e}_z$. Hence, the magnetization of the magnetic medium can be determined using optical microscopy by analyzing the change of the polarization from the incident to the reflected wave. In the following, the polar MOKE will be discussed for a normal incident wave ($\mathbf{k}^{(i)} \parallel \mathbf{e}_z$), which is the simplest but also the most important situation. For more details about the MOKE with various geometries, the reader is kindly referred to [162, 164].

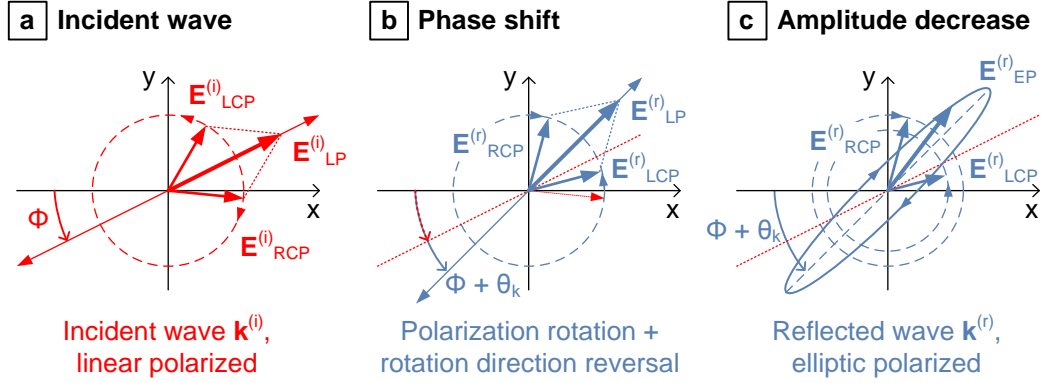


Figure 3.4: Origin of the magneto-optical Kerr effect. The linear polarized incident wave $\mathbf{k}^{(i)}$ is seen as superposition of two contrary circularly polarized waves (a). Due to a phase shift (b) and an amplitude change (c) between the superposed waves, the resulting polarization of the reflected wave $\mathbf{k}^{(i)}$ is elliptic and rotated by the Kerr angle θ_k .

Origin of the polar MOKE

For the understanding of the MOKE it is important to recognize that a linear polarized wave can also be substituted by two anticlockwise rotating circular polarized waves with equal amplitude [163]. According to Fig. 3.4a, the incident, linear polarized wave $\mathbf{E}_{LP}^{(i)}$ is expressed by the anticlockwise rotating circular polarized waves $\mathbf{E}_{RCP}^{(i)}$ and $\mathbf{E}_{LCP}^{(i)}$:

$$\mathbf{E}_{LP}^{(i)} = \mathbf{E}_{RCP}^{(i)} + \mathbf{E}_{LCP}^{(i)} \quad (3.6)$$

At the magnetic surface, both circular polarized waves are reflected but with different reflection coefficients depending on the direction of the magnetization \mathbf{M} and the polarization rotation direction (Fig. 3.4b,c). Additionally, the rotation direction is reversed at reflection at the surface ($\mathbf{E}_{RCP}^{(i)} \mapsto \mathbf{E}_{LCP}^{(r)}$). The reflected, elliptic polarized wave $\mathbf{E}_{EP}^{(r)}$ is then the superposition of the reflected, circular polarized waves:

$$\mathbf{E}_{LCP}^{(r)} = r_{RCP} \cdot \mathbf{E}_{RCP}^{(i)} \quad (3.7)$$

$$\mathbf{E}_{RCP}^{(r)} = r_{LCP} \cdot \mathbf{E}_{LCP}^{(i)} \quad (3.8)$$

$$\mathbf{E}_{EP}^{(r)} = \mathbf{E}_{LCP}^{(r)} + \mathbf{E}_{RCP}^{(r)} \quad (3.9)$$

The reflection coefficient $r_{RCP,LCP}$ for the RCP and the LCP wave is given by

$$r_{RCP,LCP} = \hat{r}_{RCP,LCP} \cdot e^{\varphi_{RCP,LCP}} = \frac{1 - n_{RCP,LCP}}{1 + n_{RCP,LCP}} \quad (3.10)$$

with the rotation-dependent amplitude reflection coefficient

$$\hat{r}_{RCP,LCP} = |r_{RCP,LCP}| = \left| \frac{1 - n_{RCP,LCP}}{1 + n_{RCP,LCP}} \right|, \quad (3.11)$$

the phase shift $\varphi_{RCP,LCP}$ with

$$\tan \varphi_{RCP,LCP} = \frac{\text{Im}(r_{RCP,LCP})}{\text{Re}(r_{RCP,LCP})} = \frac{\text{Im}\left(\frac{1 - n_{RCP,LCP}}{1 + n_{RCP,LCP}}\right)}{\text{Re}\left(\frac{1 - n_{RCP,LCP}}{1 + n_{RCP,LCP}}\right)}, \quad (3.12)$$

and the complex refractive index $n_{RCP,LCP}$ of the magnetic medium for the RCP and the LCP wave. By assuming an normal incident wave in z-direction ($\mathbf{k}^{(i)} \parallel \mathbf{e}_z$), the complex refractive index is

$$n_{RCP,LCP} = \sqrt{\varepsilon \pm j\varepsilon'} \quad (3.13)$$

with the magnetization-dependent, off-diagonal elements ε' (dielectric permittivity) of the dielectric tensor $\tilde{\varepsilon}$ of the magnetic medium:

$$\tilde{\varepsilon} = \begin{pmatrix} \varepsilon & \varepsilon' & 0 \\ -\varepsilon' & \varepsilon & 0 \\ 0 & 0 & \varepsilon \end{pmatrix}. \quad (3.14)$$

The ordinary interactions between light and magnetic medium are represented by the diagonal elements ε , whereas the magneto-optical activity is given by the off-diagonal elements ε' . Thereby, the sign from the off-diagonal elements directly depends on the direction of the magnetization:

$$\varepsilon'(\mathbf{M}) = -\varepsilon'(-\mathbf{M}). \quad (3.15)$$

For a non-magnetic, isotropic medium, the dielectric tensor is just $\tilde{\varepsilon} = \varepsilon \cdot \mathbf{1}$ with the identity matrix $\mathbf{1}$ and no off-diagonal elements.

According to eq. 3.10, the polarization rotation by the Kerr angle θ_k can be traced back to the phase shift between the RCP and the LCP wave (Fig. 3.4b):

$$\theta_k = \frac{1}{2}(\varphi_{LCP} - \varphi_{RCP}). \quad (3.16)$$

Therefore, the sign of the Kerr rotation depends directly on the magnetization \mathbf{M} according to eqs. 3.12, 3.13 and 3.15. The ellipticity ϵ_{ell} of the reflected wave depends on the different amplitude decreases given by the amplitude reflection coefficients (Fig. 3.4c):

$$\tan \epsilon_{ell} = \frac{\hat{r}_{RCP} - \hat{r}_{LCP}}{\hat{r}_{RCP} + \hat{r}_{LCP}}. \quad (3.17)$$

3.1.2 Laser-scanning Kerr microscopy (LMOKE)

In the laser-scanning MOKE microscope, the laser beam is focused on a tiny spot and the sample is mounted on a X-Y-scanner. Due to the MOKE, the polarization of the incident beam is rotated depending on the local magnetization. Therefore, the magnetic switching behavior can be measured in a certain spot by scanning the region of interest (ROI) of the sample surface and – after setting the desired coordinates – applying magnetic fields. Fig. 3.5 shows a sketch of the home-made LMOKE separated in an optical part (a) and an electronic part (b).

The set-up of the microscope is based on [165–167] and further inspired by [82, 162, 163]. The microscope has been developed with the support of several Diploma, Bachelor and Master theses [Bre09, Clo09, Neu09]. Integration of the pulse generator for on-chip coils is thanks to [BKB⁺13] and [Zie13]. In the following, the working principle of the MOKE will be discussed step-by-step beginning with the optical part and according to the optical path.

Optics

Laser A red laser diode with wave length $\lambda = 635\text{ nm}$ and a controllable light output power of $P_L = 0 \dots 4\text{ mW}$ is used as light source for the LMOKE. The laser diode is pulse modulated with a frequency of $f_{mod} = 100\text{ kHz}$ in order to increase the signal-to-noise ratio (SNR). The optical beam is reflected by a tiltable mirror which is used to adjust the laser beam on the optical axis of the subsequent optical components.

Lenses and aperture Two lenses and an adjustable aperture are used to adapt the diameter of the laser beam to the aperture of the objective lens. Additionally, the beam profile is modified by filtering the transverse laser modes generating a TEM_{00} profile (gaussian beam profile).

Polarizer The optical beam from the laser diode is partly linear polarized but with an insufficient polarization ratio. Therefore, a high-efficient *Glan-Thompson polarizer* with an extinction ratio of 1,000,000 : 1 (ratio between desired and undesired polarization direction) is used to induce the linear polarization. The polarizer is pivot-mounted along the optical axis in order to adjust the polarization angle Φ of the incident wave.

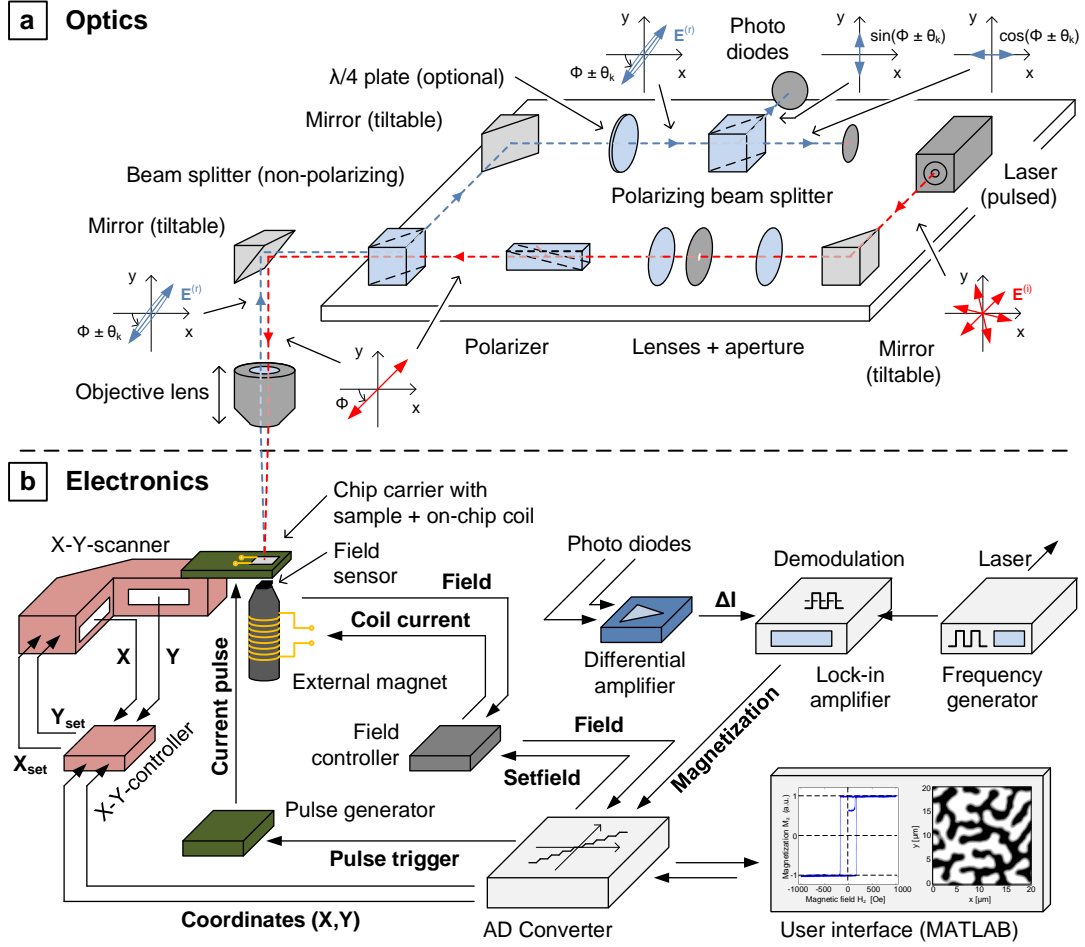


Figure 3.5: Sketch of the laser-scanning MOKE microscope consisting of an optical part (a) and an electronic part (b). The pulsed laser light is polarized and focused on the sample surface, where the polarization is rotated by the MOKE. The reflected beam is guided to the polarizing beam splitter, which separates the polarization into its x- and y-components. The corresponding differential currents generated by the photodiodes is amplified and demodulated in order to determine the magnetization. The sample is mounted on an X-Y-scanner to image the sample surface and measure the switching behavior in a certain spot. The X-Y-scanner and the applied magnetic field are controlled by feedback controllers, which can be set by an AD converter box connected to the computer. Additional sub- μ s field pulses can be applied through an on-chip coil supplied by a current pulse generator. The whole microscope is controlled through a MATLAB user interface.

Objective lens The linear polarized beam is guided through a non-polarizing beam splitter and a second tiltable mirror to the objective lens. The *Zeiss LD Epiplan 100x/0.75 HD DIC* objective provides a 100x optical magnification and has a long-working distance (LD) of 4 mm which enables an adequate design of the external magnet. The numerical aperture (NA) is $NA = 0.75$, which means that the corresponding Abbe diffraction limit of the LMOKE is $d_{min} = \lambda / (2NA) \approx 420 \text{ nm}$ [163]. The objective lens is movable in vertical z-direction by a micrometer screw and an additional piezo-electric actuator in order to focus the laser beam on the sample surface.

Reflection at sample surface After passing the objective lens, the optical beam is reflected at the sample surface and guided back through the objective. Due to the polar MOKE, the LP is rotated clockwise or counterclockwise by the Kerr angle $\pm\theta_k$ depending on the direction of the perpendicular magnetization $\pm\mathbf{M}_z$ at the sample surface. Additionally, the LP is transformed to EP (cp. sec. 3.1.1).

Wave plate (optional) The reflected beam is guided back through the objective lens, the non-polarizing beam splitter and a third tiltable mirror to an optional quarter wave plate. In principle, the $\lambda/4$ wave plate enables to correct the ellipticity or to rotate the polarization angle Φ by tilting the wave plate in a certain manner [163]. However, the ellipticity due to the MOKE is negligible and the optimal polarization angle $\Phi \approx 45^\circ$ in order to equally illuminate the photo diodes and maximize the contrast of the MOKE is already set by the pivot-mounted polarizer [Bre09].

Polarizing beam splitter The polarizing beam splitter is a high-efficient *Glan-Taylor polarizer* with an extinction ratio of 100,000:1 which splits the incoming wave into its elementary waves:

$$|\mathbf{E}_x^{(r)}| = |\mathbf{E}^{(r)}| \cdot \cos(\Phi \pm \theta_k), \quad (3.18)$$

$$|\mathbf{E}_y^{(r)}| = |\mathbf{E}^{(r)}| \cdot \sin(\Phi \pm \theta_k). \quad (3.19)$$

The generated elementary waves are guided to the photo diodes, whereas the horizontal polarized elementary wave $\mathbf{E}_x^{(r)}$ is transmitted through and the vertical polarized elementary wave $\mathbf{E}_y^{(r)}$ reflected by the polarizing beam splitter.

Photo diodes The elementary waves are guided to separated photo diodes which generate a photo current $I_{x,y}$ corresponding to the intensity of the incoming elementary waves:

$$I_{x,\pm} \propto |\mathbf{E}_x^{(r)}|^2 \propto \cos^2(\Phi \pm \theta_k), \quad (3.20)$$

$$I_{y,\pm} \propto |\mathbf{E}_y^{(r)}|^2 \propto \sin^2(\Phi \pm \theta_k). \quad (3.21)$$

Electronics

Differential amplifier and demodulation The (amplified) currents $I_{x,\pm}$, $I_{y,\pm}$ generated by the photo diodes are subtracted using a differential amplifier:

$$\Delta I_{\pm} = I_{x,\pm} - I_{y,\pm} \propto \cos^2(\Phi \pm \theta_k) - \sin^2(\Phi \pm \theta_k). \quad (3.22)$$

In order to optimize the measured contrast of the MOKE, the measured photo current difference ΔI_k between positive (ΔI_+) and negative (ΔI_-) polarization rotation has to be maximized:

$$\Delta I_k = \Delta I_+ - \Delta I_- \quad (3.23)$$

$$= [I_{x,+} - I_{y,+}] - [I_{x,-} - I_{y,-}] \quad (3.24)$$

$$\propto [\cos^2(\Phi + \theta_k) - \sin^2(\Phi + \theta_k)] - [\cos^2(\Phi - \theta_k) - \sin^2(\Phi - \theta_k)] \quad (3.25)$$

$$= 2 [\cos^2(\Phi + \theta_k) - \cos^2(\Phi - \theta_k)]. \quad (3.26)$$

It can be shown [Bre09], that this term is maximized for a polarization angle of the incident wave of $\Phi = 45^\circ$, which can be adjusted by the pivot-mounted polarizer. The corresponding measured contrast ΔI_k is then given by

$$\Delta I_k \propto \sin 2\theta_k. \quad (3.27)$$

Because of the small effect of the polarization rotation by the MOKE ($\theta_k \approx 0.2^\circ$), the laser beam is pulse modulated with a frequency of $f_{mod} = 100$ kHz. The pulse-amplitude modulation (PAM) enables to measure at a certain frequency level and therefore to reduce the noise (e.g. by daylight, power-line frequency) from the measurement signal and increase the SNR. The measurement bandwidth is controlled by the time constant of the demodulation filter from the lock-in amplifier.

Magnetic field generation Magnetic fields required to reverse the magnetization are provided by an external magnet, which allows for slow-growing fields with high amplitude. If high-frequency fields with moderate amplitude are required, a current pulse generator driving either a micro coil integrated in the chip carrier or an on-chip coil fabricated on the sample can be employed.

The external magnet is feedback-controlled by a proportional-integral-derivative (PID) controller with an audio amplifier to drive the electromagnet and a hall sensor to measure the actual field value. The external magnet provides magnetic fields up to $H_{ext,max} \approx 4$ kOe with about 1% accuracy. The reasonable upper limit for the field rate is about 5 kOe/s and field pulses are limited to $t_{pulse} > 10$ ms.

Shorter field pulses are provided by either a high-frequency micro coil integrated in the chip carrier ($1 \mu s < t_{pulse} < 10 \mu s$) or by on-chip coils ($50 \text{ ns} < t_{pulse} < 1 \mu s$) fabricated on the sample itself and bonded to the chip carrier (cp. sec. 4.5).

Both the micro coil and the on-chip coil are supplied by a pulse generator, which is controlled by the measurement setup [Zie13]. For both coils, the amplitude of the generated field is limited to $H_{pulse,max} \approx 1$ kOe. However, the field pulses generated by the micro coil or on-chip coil can be synchronized with the external magnet in order to enable constant fields with superposed field pulses. Table 3.1 summarizes the magnetic field generation provided for the measurements at LMOKE.

	External magnet	Micro coil	On-chip coil
Supplied by	Measurement setup + field controller	Chip carrier + pulse generator	On-chip + pulse generator
Pulse time	$t_{pulse} > 10$ ms	$1 \mu s < t_{pulse} < 10 \mu s$	50 ns $< t_{pulse} < 1 \mu s$
Amplitude	$H_{max} \approx 4$ kOe	$H_{max} \approx 1$ kOe	$H_{max} \approx 1$ kOe

Table 3.1: Magnetic fields provided by the measurement setup.

X-Y-scanner A feedback controlled X-Y-scanner is employed in order to image the sample surface and measure the magnetic behavior at a specific spot [Neu09]. For the LMOKE, a X-Y-scanner with piezo actuators to set the desired coordinates has been chosen for several reasons. The piezo actuators provide

- large scan range of up to $\approx 120 \mu m$,
- high spatial resolution of only a few nm,
- insensitivity to magnetic fields provided by the external magnet,
- no internal generation of magnetic fields,
- fast actuation in order to realize high scan repetition rates.

Fig. 3.6a shows the utilized X-Y-scanner. Two piezo actuators (one for each axis) are used to set the desired coordinates. The elongation of the piezo actuators is measured by two strain gauges in order to control the actual position with a PID controller. The X-Y-scanner provides a scan area of roughly $120 \mu m \cdot 120 \mu m$ with a spatial resolution of about 20 nm. The maximum scan repetition rate is about 30 Hz for each axis. Chip carriers with an embedded micro coil or bonded samples with on-chip coils can be mounted at the end of the piezo scanner in order to provide high-frequency magnetic field pulses (Fig. 3.6b).

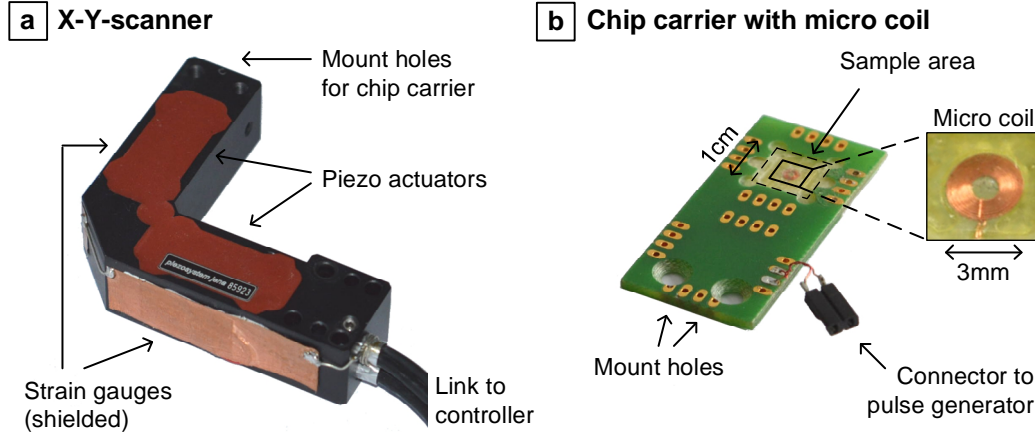


Figure 3.6: Feedback controlled X-Y-scanner at LMOKE used to image the sample surface and measure the magnetic behavior at a specific spot (a). Two piezo actuators set the desired coordinates which are controlled by two strain gauges. Adaptable chip carriers with an embedded micro coil (or bonded samples with on-chip coils) enable high-frequency magnetic field pulses (b).

A/D converter and user interface A USB data acquisition (DAQ) box is used for input and output of analog/digital signals to control the LMOKE. The DAQ box provides several analog input and output channels with 16 bit A/D converter for each channel as well as several digital ports used for triggering. Magnetic fields and X-Y-scanner coordinates are set with analog outputs and both the actual field value and the magnetization (demodulated current difference) are read in with analog inputs. A home-made user interface is provided in MATLAB to control the DAQ box at the computer, which is connected by universal serial bus (USB). The software provides script-based measurements as well as various options for advanced data processing like image shift correction algorithms or statistical evaluations.

3.1.3 Wide-field Kerr microscopy (WMOKE)

Laser-scanning Kerr microscopy as described above enables to image the sample surface by scanning with a focused laser beam. However, if the magnetic behavior is not of interest in only a tiny spot, but on a wide area, the laser-scanning technique becomes insufficient. On the one hand, the image recording time is limited by the X-Y-scanner to several seconds. On the other hand, the spatial resolution is reduced by the surface topography. In order to increase the speed of imaging and the spatial resolution, wide-field Kerr microscopy is applied [82]. In principle, the laser is replaced by an incoherent light source which allows to

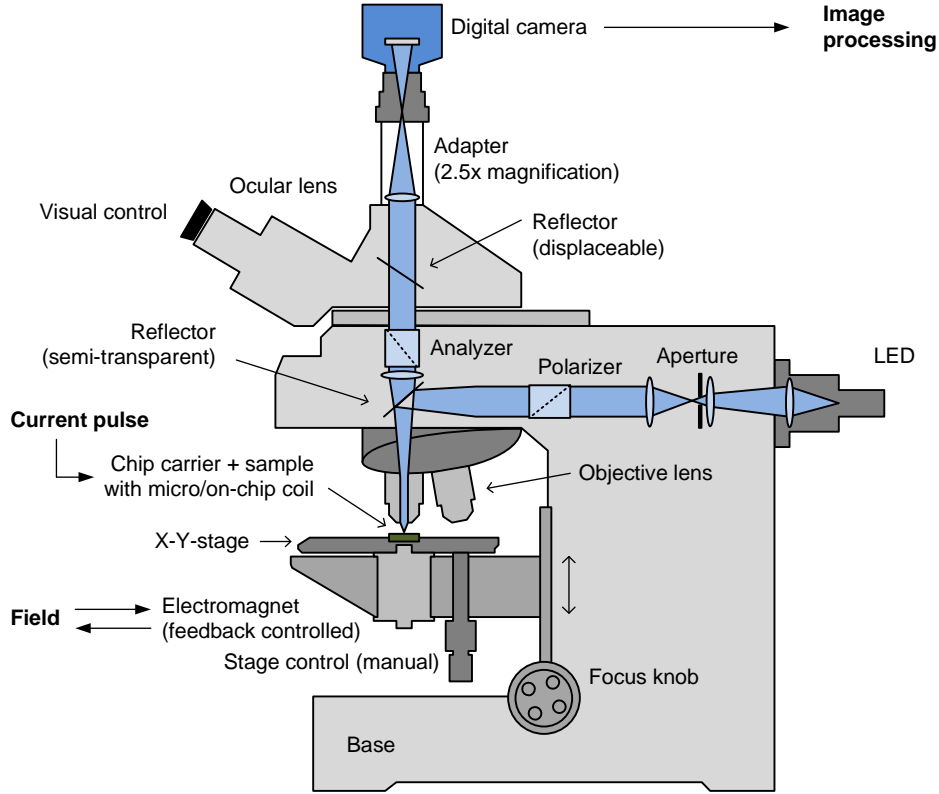


Figure 3.7: Sketch of the wide-field MOKE microscope based on a common optical microscope which is enhanced by two polarizers.

illuminate the sample surface homogeneously, and the photo diodes are substituted by a camera for imaging¹. Most suitably, a common optical microscope is enhanced by polarizing optical elements in order to sensitize the microscope to the MOKE.

WMOKE Setup

Fig. 3.7 shows a sketch of the setup of the WMOKE, which is based on a common optical microscope. A blue LED with a nominal wavelength of 470 nm and an integrated collimation lens is used for illumination. The optical beam is linear polarized with a high-grade Glan-Thompson polarizer and reflected by semi-transparent, non-polarizing reflector to the objective lens. Two different objectives are provided, one with a 20x magnification ($NA = 0.5$) which is used to navigate on the sample, and one with a 100x magnification ($NA = 0.9$) to maximize the spatial resolution ($d_{min} = \lambda / (2NA) \approx 260$ nm).

The focused light is reflected from the sample, which is mounted on a manually

¹Naturally, several additional lenses are required to focus the sample surface with the camera.

operated X-Y-stage for navigation. The X-Y-stage is adjustable in height to bring the sample into focus with the focus knob. Magnetic field generation is provided just as for the LMOKE by a feedback controlled electromagnet and/or current-driven micro or on-chip coils which are controlled via MATLAB.

The optical beam reflected from the sample surface exhibits a polarization rotation depending on the local magnetization $M_z(\mathbf{r})$ and passes the objective lens as well as the semi-transparent reflector. The analyzer is another high-grad polarizer which is tilted compared to the other polarizer by nearly 90° in order to maximize the magneto-optical contrast. A displaceable reflector guides the optical beam either to the camera or to the ocular lens for visual inspection.

The digital low-noise camera is mounted on a 2.5x magnifying adapter for further magnification and is connected via USB to import the recorded images to MATLAB. The charge-coupled device (CCD) sensor provides a resolution of 1392×1040 pixel with a dynamic range of 14 bit, which is required to image the magnetization due to the small polarization rotation of the MOKE. However, several steps of digital image processing are required to extract the magnetic information from the images recorded by the camera (see sec. 3.1.3). The size of each pixel is $6.45 \mu\text{m} \cdot 6.45 \mu\text{m}$, which (by using the 2.5x adapter and the 100x objective) corresponds to an areal resolution of $25.8 \text{ nm} \cdot 25.8 \text{ nm}$ on the sample surface.

Basic principles of magnetic imaging

The images recorded with the camera contain both information about the topography of the sample surface as well as magnetic information due to the polarizing optical elements. Indeed, in the original recorded image, the magnetic information is negligible compared to the topography due to the small impact of the MOKE on the polarization (cp. sec. 3.1.1). More precisely, the polarization rotation due to the MOKE changes the intensity in the recorded image only in bit number 8 or beyond. This means, by using an digital camera with a 10 bit A/D conversion for each pixel, only the 3 least significant bits contain the magnetic information. Consequently, a low-noise camera with an intensity depth of 12 or more bits is recommended to suitably image the magnetization. Additionally, image processing with several images recorded under different magnetization conditions is required to remove the topography information and generate pure "magnetic images". Fig. 3.8 illustrates the image processing for the reference image (a) and the magnetic image (b).

First of all a *reference image* is required, in which the magnetic information is removed and which hence only contains the surface topography (Fig. 3.8a). Therefore, two images are recorded: one image with all magnetic structures magnetized upwards (\mathbf{Im}_{up}) and the other one magnetized in opposite direction (\mathbf{Im}_{down}). In general, the images \mathbf{Im}_{rec} recorded from the camera and imported for image pro-

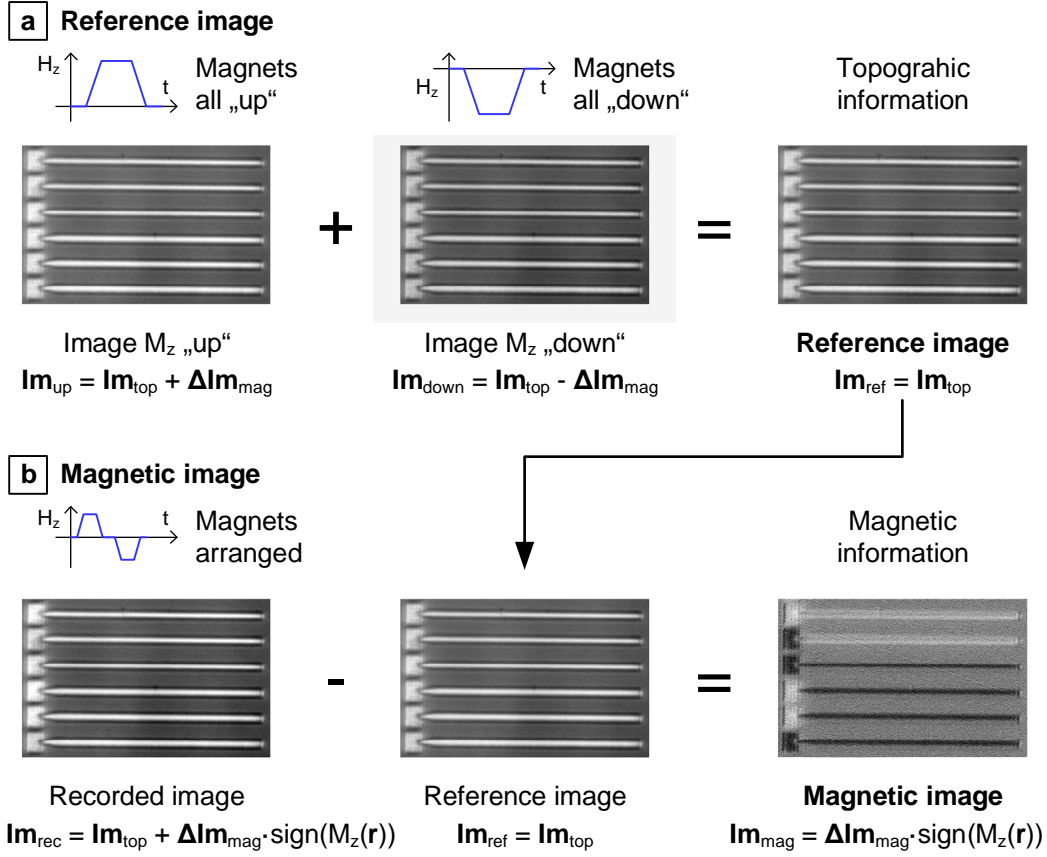


Figure 3.8: Image processing for the reference image (a) and the magnetic image (b) of magnetic nanowires after measuring by WMOKE.

processing are simple matrices with rows and columns corresponding to the resolution of the camera and containing data proportional to the local brightness. Due to the MOKE, the brightness of the magnetic structures is slightly in- or decreased depending on the local magnetization direction $M_z(\mathbf{r})$:

$$\mathbf{Im}_{rec} = \mathbf{Im}_{top} + \Delta\mathbf{Im}_{mag} \cdot \text{sign}(M_z(\mathbf{r})) \quad (3.28)$$

$$\Rightarrow \mathbf{Im}_{up} = \mathbf{Im}_{top} + \Delta\mathbf{Im}_{mag} \quad (3.29)$$

$$\mathbf{Im}_{down} = \mathbf{Im}_{top} - \Delta\mathbf{Im}_{mag} \quad (3.30)$$

with the image brightness due to the surface topography \mathbf{Im}_{top} which is superposed by the brightness change $\Delta\mathbf{Im}_{mag}$ depending on the magnetization $M_z(\mathbf{r})$. Consequently, the magnetic information is removed from the reference image by

simply adding the two images:

$$\mathbf{Im}_{ref} = 0.5 [\mathbf{Im}_{up} + \mathbf{Im}_{down}] \quad (3.31)$$

$$= 0.5 [\mathbf{Im}_{top} + \Delta\mathbf{Im}_{mag} + \mathbf{Im}_{top} - \Delta\mathbf{Im}_{mag}] \quad (3.32)$$

$$= \mathbf{Im}_{top}. \quad (3.33)$$

Afterwards, the reference image \mathbf{Im}_{ref} is subtracted from every further recorded image in order to remove the topography and visualize the magnetization in the *magnetic image* (Fig. 3.8b):

$$\mathbf{Im}_{mag} = \mathbf{Im}_{rec} - \mathbf{Im}_{ref} \quad (3.34)$$

$$= \mathbf{Im}_{top} + \Delta\mathbf{Im}_{mag} \cdot \text{sign}(M_z(\mathbf{r})) - \mathbf{Im}_{top} \quad (3.35)$$

$$= \Delta\mathbf{Im}_{mag} \cdot \text{sign}(M_z(\mathbf{r})). \quad (3.36)$$

The resulting magnetic image only shows the brightness change generated by the polarization rotation due to the influence of the local magnetization. But the image quality of the pure magnetic information is reduced by noise and a potential lateral image shift between the recorded images. Therefore, usually multiple images are recorded and processed for each magnetic image and reference image in order to reduce the noise [82]. The quality of the magnetic image (and the reference image) is further increased by correcting a potential lateral shift by adequate image processing algorithms, e.g. by correlation or fast Fourier transformation (FFT)-based algorithms.

3.2 Magnetic force microscopy (MFM)

The spatial resolution of magneto-optical microscopy is limited due to the wavelength λ of the light source and the corresponding diffraction limit to $d_{min} \approx 200 \text{ nm}$ [163]. However, if magnetic imaging with higher lateral resolution is required, usually MFM is applied [168].

3.2.1 Basic working principle of MFM

MFM is based on atomic force microscopy (AFM), which uses a movable cantilever with a tapered tip to scan the topography of the sample surface [169]. Usually, the cantilever is induced to oscillate with its resonance frequency, where both the amplitude and the phase of the oscillation is modified by the interaction of the tip with the sample surface by Van-der-Waals forces. Thereby, the deflection of the cantilever is measured with a laser beam, which is reflected from the cantilever to a position-sensitive 4-quadrant photo diode.

In a MFM, the tip is partially coated with a magnetic material in order to sensitize the tip to the magnetic stray fields of the measured structures [170, 171].

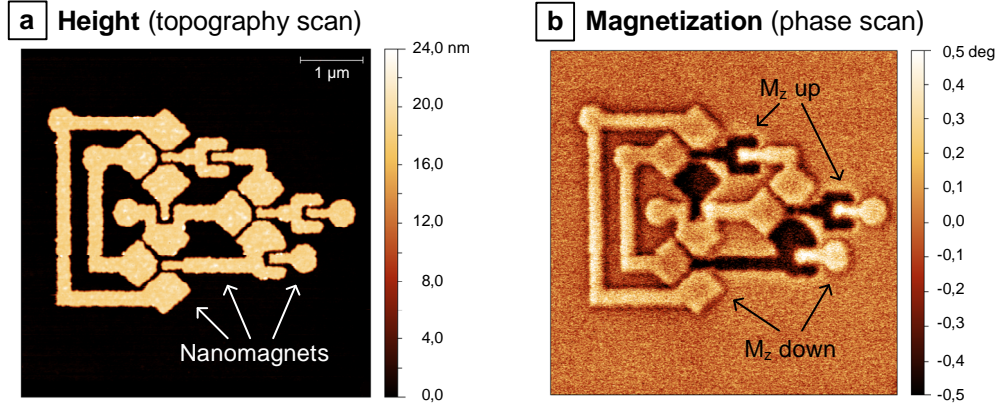


Figure 3.9: Height (a) and magnetization (b) of a magnetic full adder structure imaged by MFM.

Consequently, the lateral resolution of the MFM is only limited by the size of the magnetic tip, which is in the order of 20 nm. For magnetic imaging, first the topography is scanned in a line with the tip close to the surface ($h_{top} = 10 \dots 20$ nm), where atomic forces dominate the oscillation modification. Afterwards, the topography of the scanned line is retraced with a distinct distance ($h_{top} = 40 \dots 100$ nm) where the force of the magnetic stray fields dominate. Thereby, the phase of the cantilever oscillation is either in- or decreased ($|\Delta\varphi| < 1^\circ$) depending on the direction of the magnetic stray field which is generated by the local magnetization at the sample surface. The scan height of the tip is controlled by a z-piezo actuator and the sample surface is scanned line by line. Fig. 3.9 shows the height (a) and the magnetization (b) of a magnetic full adder structure measured by MFM. For a more detailed description of the working principle of modern MFM, the reader is referred to [26].

The MFM employed for this work provides a lateral resolution down to 10 nm, the vertical resolution to measure the height of the magnetic structures is below 1 nm. Additionally, MFM images provide a high contrast between different directions of magnetization. However, due to the scanning imaging technique line by line, the time for high quality imaging (resolution $> 512 \text{ pixel} \cdot 512 \text{ pixel}$, line scan frequency $\approx 1 \text{ Hz}$, measured area $5 \mu\text{m} \cdot 5 \mu\text{m}$) is restricted to more than 15 min per frame. Additionally, the maximal scan dimension is restricted to about $80 \mu\text{m} \cdot 80 \mu\text{m}$ [26]. Compared to wide-field Kerr microscopy, the application for MFM is mainly given for magnetic (and topographic) imaging of areas below $10 \mu\text{m} \cdot 10 \mu\text{m}$ with highest lateral resolution of 10 nm.

3.2.2 Extension by a 3D magnetic field module

The MFM setup was extended with a feedback controlled magnetic field module which provides user-definable 3D magnetic fields [KNB⁺11],[28]. Thereby, the challenging aspect was to provide high magnetic fields $|\mathbf{H}| = 1 \text{ kOe}$ in all directions without disturbing the scanning area of cantilever. The investigations by [KNB⁺11] finally led to a 3D magnetic field module consisting of 5 magnetic pole shanks (1 central pole shank for out-of-plane fields in z-direction, 2 shanks for each in-plane component in x-/y-direction), which are controlled by 5 coils and several field sensors. The magnetic field module provides homogeneous fields with a maximum amplitude of $H_{xy,max} = 1 \text{ kOe}$, $H_{z,max} = 1.5 \text{ kOe}$ and a settling time of 20 ms in an area of $100 \mu\text{m} \cdot 100 \mu\text{m}$, which is located 2 mm above the central pole. If faster magnetic field pulses in z-direction are required, both micro- or on-chip coils can be employed (see magnetic field generation in sec. 3.1.2).

3.3 Further magnetic metrology

Naturally, metrology of magnetic films and devices covers a much wider range than the techniques described in the sections above [24]. They all have their eligible field of application and experience specific attraction. Some of the measurement techniques which should be mentioned here are

- vibrating-sample magnetometry (VSM),
- superconducting quantum interference device (SQUID),
- extraordinary Hall effect (EHE) measurements,
- (Lorentz) transmission electron microscopy (TEM),
- scanning tunneling microscopy (STM), and
- photoemission electron microscopy (PEEM).

Some of the findings applied in this work (i.e. saturation magnetization M_s and effective anisotropy K_{eff} of Co/Pt multilayers) have been explored in former work using the techniques shortly described in the following [26, 28].

Vibrating-sample magnetometry: A VSM enables to measure quantitatively the total magnetization of a sample in a magnetic field [172, 173]. Therefore, the sample is mounted on a holder which is moved (vibrated) perpendicularly to the uniform magnetizing field. Several pickup coils located close to the vibrating sample enable to measure the voltage induced by the magnetization of the moving sample. The saturation magnetization can be determined from the total magnetization measured by VSM.

Extraordinary Hall effect measurements: In a EHE sensing device, the extraordinary (or anomalous) Hall resistivity, which directly depends on the magnetization M , is used to measure the hysteresis curve of magnetic films $> 1 \text{ cm}^2$ but also nanostructures $< 0.1 \mu\text{m}^2$ [109, 174, 175]. Therefore, the (Hall) voltage generated by the interaction of an applied sensing current and the samples magnetization is measured, which is possible in different sensing geometries (e.g. conventional hall crossbar [BKB⁺10] or split-current geometry [KBJ⁺11]. EHE sensing enables to determine the effective anisotropy K_{eff} by rotating the sample in a magnetic field during measurements.

4 Fabrication Technology

The development and optimization of the manufacturing process for partial irradiated Co/Pt nanostructures has been - besides the set up of the magneto-optical microscope - one of the major challenging aspects of this thesis. Naturally, there are many approaches to the fabrication of magnetic nanostructures [24]. However, this section describes the final, up-to-date most suitable fabrication process at LTE for pNML devices and circuits based on Co/Pt multilayers as shown in Fig 4.1.

First, the Si wafer¹ is cleaned and a thin SiO₂ layer is grown on the substrate for electrical isolation (a). Afterwards, the Co/Pt multilayer is deposited by RF magnetron sputtering (b). In a third step, the multilayer film is patterned into isolated Co/Pt nanomagnets using FIB lithography and Argon (Ar) ion beam etching (c). Finally, the ANC's of the magnets are generated by partial FIB irradiation (d). Afterwards, potential on-chip coils and/or electrical contacts can be fabricated by optical lithography (e). In the following, the fabrication steps of the manufacturing process are discussed in more detail.

4.1 Sample preparation

The first step of the manufacturing process to fabricate the Co/Pt nanomagnets is the cleaning of the Si wafer (Fig. 4.1a). First, the wafer is placed into an acetone bath and thereafter into an isopropanol bath to remove the protecting photoresist, which was required to protect the wafer during dicing into the 1 cm × 1 cm pieces. Afterwards, the Si wafer is cleaned using the RCA standard clean, which consists of a RCA1 (NH₄OH + H₂O₂ + H₂O) bath to remove organic substances, an hydrofluoric acid (HF) dip (HF + H₂O) to remove the thin native oxid layer and a subsequent RCA2 (HCl + H₂O₂ + H₂O) bath to remove the remaining inorganic contaminants [176]. Afterwards, the Si wafer is thermally oxidized (dry oxidation) for 15 minutes at 1000 °C to grow an 18 nm thin SiO₂ layer, which is required for isolation of electrical contacts and on-chip coils.

¹The Co/Pt nanomagnets are usually fabricated on a common, undoped Si wafer, but can be fabricated on a wide range of potential substrates.

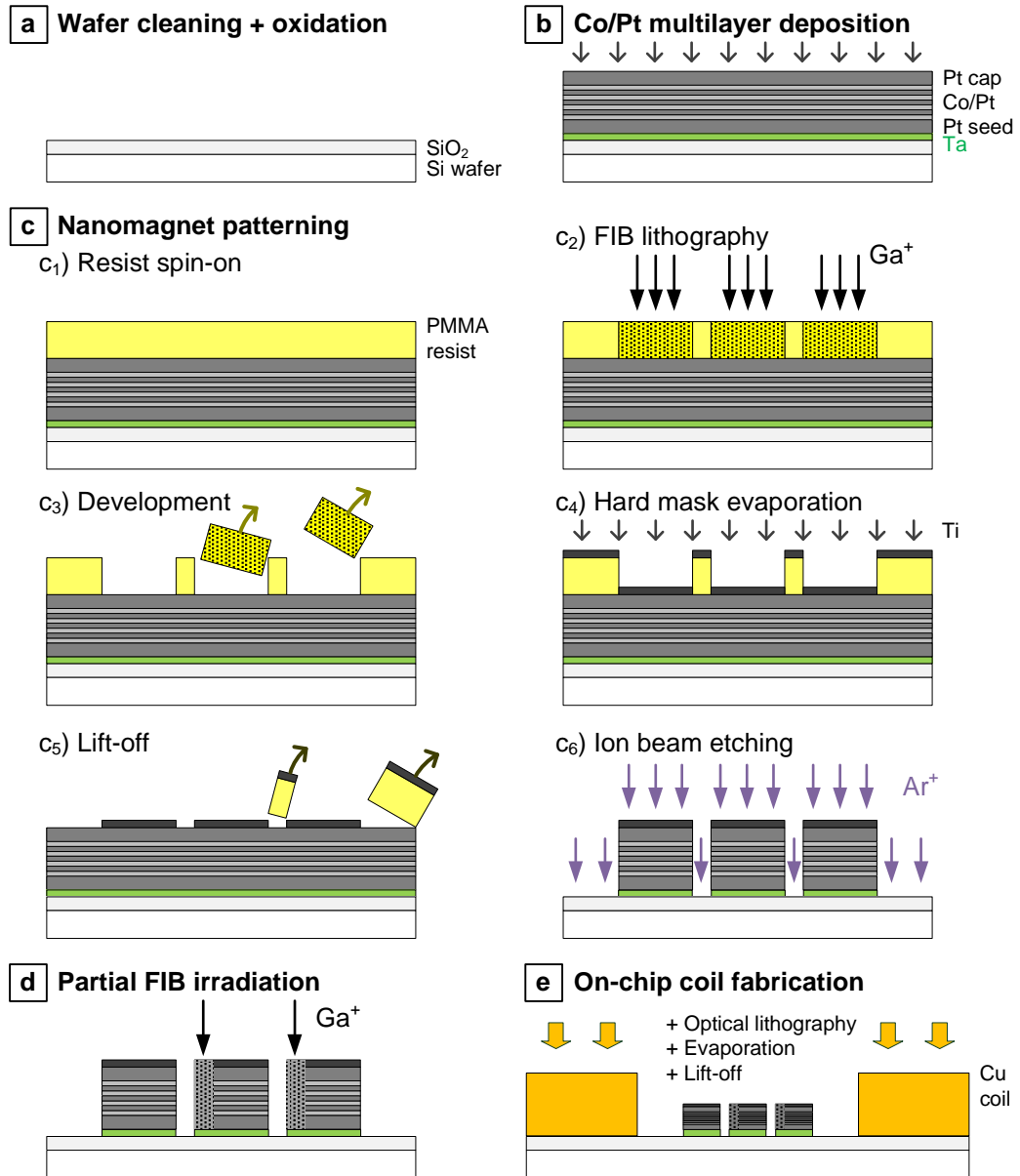


Figure 4.1: Manufacturing process of pNML devices consisting of Co/Pt nanomagnets with ANC and on-chip coils.

4.2 Co/Pt multilayer deposition

The Co/Pt multilayer films fabricated in this work are deposited by RF magnetron sputtering (Fig. 4.1b). Compared to other deposition techniques like molecular beam epitaxy (MBE), laser ablation and electrodeposition, sputtering provides reproducible deposition of magnetic multilayers with large homogeneity and less pinholes [92]. In order to enable the deposition of high quality multilayers providing the advantages mentioned before, the background (initial) vacuum pressure has to be in the range of $10^{-7} \dots 10^{-9}$ mbar and the sputter gas (inert gas) at a pressure around 10^{-3} mbar. As already mentioned in sec. 2.2.2, the Ar pressure, which is the sputter gas for the utilized Co/Pt multilayers, has a significant influence on the magnetic behavior of the multilayer. We found, that the Ar pressure should be as low as possible to fabricate Co/Pt multilayers with the desired characteristics of sharp switching and adequate domain sizes [Che10]. Table 4.1 shows an overview of the sputtering parameters for a $\text{Ta}_{2\text{nm}}\text{Pt}_{3\text{nm}}[\text{Co}_{0.8\text{nm}}\text{Pt}_{1.0\text{nm}}]_{\times 4}\text{Pt}_{3\text{nm}}$ stack. Fig. 4.2 shows the corresponding hysteresis curve (a) and the magnetic do-

Layer	Material	Quantity	Thickness	Ar Pressure
Adhesion layer	Ta	1	2 nm	2 μ bar
Seed layer	Pt	1	3 nm	2 μ bar
Multilayer	Co	N = 4	0.8 nm	4.5 μ bar
	Pt	(N-1) = 3	1.0 nm	2 μ bar
Capping layer	Pt	1	3 nm	2 μ bar

Table 4.1: Sputtering parameters for a conventional Co/Pt multilayer film.

main (b) of the sputtered $\text{Ta}_{2\text{nm}}\text{Pt}_{3\text{nm}}[\text{Co}_{0.8\text{nm}}\text{Pt}_{1.0\text{nm}}]_{\times 4}\text{Pt}_{3\text{nm}}$ multilayer stack measured by MOKE. The Co/Pt film shows the desired switching characteristics (cp. sec. 2.4) of sharp, nucleation-dominated switching with $H_{nuc} > H_{prop}$, H_s and full remanence $M_r = M_s$ (Fig. 4.2a). We measured a nucleation field of $H_{nuc} = 165$ Oe from the common hysteresis curve and a propagation field of $H_{prop} = 140$ Oe as well as a saturation field of $H_s \approx 145$ Oe from the virgin curve. The natural domain size is measured after demagnetization of the sample leading to adequate domain sizes with a diameter of $d \approx 1.5 \mu\text{m}$ (Fig. 4.2b), which enables single domain Co/Pt nanomagnets with a width $w < 1.5 \mu\text{m}$. During prior experiments in collaboration with ND, the effective anisotropy and the saturation magnetization of the whole Co/Pt multilayer stack have been determined to $K_{eff} \approx 2.5 \cdot 10^5 \text{ J/m}^3$ and $M_s \approx 7.2 \cdot 10^5 \text{ A/m}$, respectively.

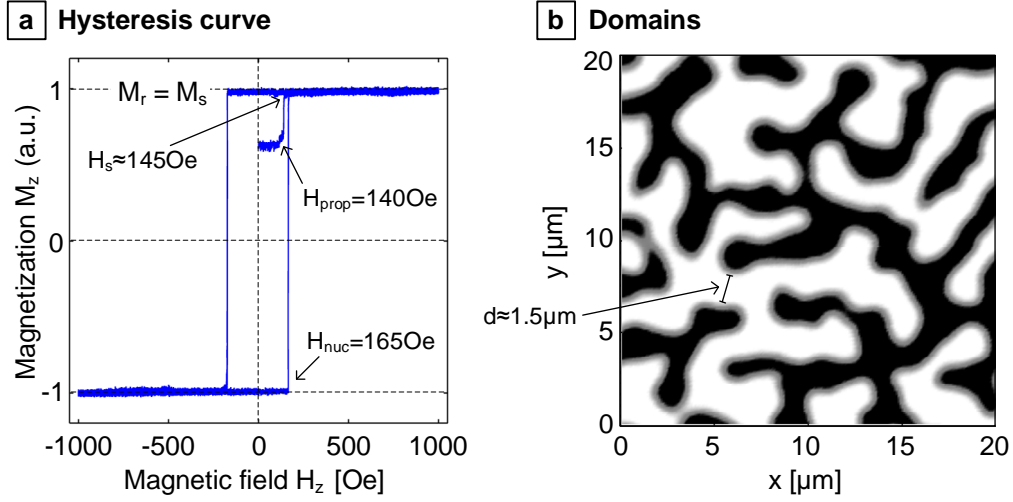


Figure 4.2: Hysteresis curve (a) and magnetic domains (b) of an as-grown $\text{Ta}_{2\text{nm}}\text{Pt}_{3\text{nm}}[\text{Co}_{0.8\text{nm}}\text{Pt}_{1.0\text{nm}}]_{\times 4}\text{Pt}_{3\text{nm}}$ multilayer stack measured by LMOKE.

4.3 Patterning of Co/Pt nanomagnets

The next fabrication step is the patterning of the Co/Pt multilayer film into isolated Co/Pt islands (Fig. 4.1c). Primarily, the sample is baked out on a hotplate at 100°C for 30 minutes in order to remove adsorbed water from the surface and increase the adhesion of the photoresist. Afterwards, a Polymethylmethacrylate (PMMA) e-beam photoresist is spun on for 30 s at $\approx 1800 \text{ min}^{-1}$ resulting in a 60 nm thick resist (Fig. 4.1c₁). The sample is immediately prebaked for 90 s at 100°C to remove the solvents.

4.3.1 FIB lithography

Due to the availability of an adequate 50 kV Ga^+ FIB system and the possibility of direct lithography irradiation (DLI) – the generation of ANCs during lithography, see sec. 4.4 – the patterning process is done using FIB lithography. Therefore, the PMMA resist on the sample surface is specifically exposed to radiation according to the layout mask with a dose of $4 \cdot 10^{12} \frac{\text{ions}}{\text{cm}^2}$ (Fig. 4.1c₂ and 4.3a). Due to the thickness of the photoresist, the Ga^+ ions are slowed down due to scattering and do not affect the magnetic behavior of the underlying Co/Pt multilayer [26]. The ion-irradiation exposed PMMA is wet-chemically developed for 15 s in a Methylisobutylketon (MIBK) dilution. Afterwards, the sample is dipped in Isopropanol for 30 s to stop the development and flushed in water for 180 s to dissolve the exposed and developed areas (Fig. 4.1c₃). The ion-irradiation dose as well as

the development time have been optimized to minimize both the feature size (i.e. the distance between adjacent magnets) and the edge roughness of the patterned nanomagnets.

4.3.2 Hard mask evaporation & lift-off

After the lithography step, the sample is again baked out on a hotplate at 100 °C for 30 min to increase the adhesion of the hard mask. A 5 nm thick Ti layer is deposited on the patterned photoresist by physical vapor deposition (PVD) using e-beam evaporation (Fig. 4.1c₄). The thickness of the hard mask is chosen to be thick enough to resist the ion beam etching but thin enough to not disturb magneto-optical measurements. The sample is placed for 10 min into an ultrasonic bath of a 75 °C warmed-up N-Methylpyrrolidone (NMP) solvent to lift-off the remaining resist with the overlying Ti layer (Fig. 4.1c₅).

4.3.3 Ion beam etching

In the last patterning step, the multilayer film is structured into isolated Co/Pt nanomagnets by ion beam etching (IBE). Therefore, the sample is exposed to a homogeneous Ar ion beam for ≈ 8 min in order to mill the Co/Pt multilayer film which is not protected by the evaporated Ti hard mask (Fig. 4.1c₆). Fig. 4.3 shows the lithography mask of several pNML full adder circuits (a) as well as the corresponding microscope (b) and scanning electron microscope (SEM) images (c,d) after patterning. The width of the magnets is ≈ 120 nm with a minimum distance of ≈ 15 nm. The structured Co/Pt magnets map the lithography mask very well.

After etching, it is recommended to deposit a 3 nm thick Pt layer on top of the patterned nanomagnets by sputtering in order to prevent the uncovered Co layers at the edges of the patterned nanomagnets from oxidation. However, if electrical contacts or on-chip coils are required, this step should be omitted or followed by deposition of an insulating layer to avoid short circuits.

4.4 Partial FIB irradiation

Partial FIB irradiation to generate ANCs in Co/Pt nanomagnets is the most important but also the most critical fabrication step in the manufacturing process. The location of the ANCs decides about the direction of the signal flow in pNML devices and circuits [SB11a],[EBK⁺12]. Therefore, the Co/Pt nanomagnets are specifically irradiated by focused Gallium (Ga) ion irradiation with doses of $1 \dots 10 \cdot 10^{13} \frac{\text{ions}}{\text{cm}^2}$ (Fig. 4.1d) [SB12b]. Thereby, the anisotropy is locally reduced depending on the applied irradiation dose (cp. sec. 2.2.3). The reduction of the

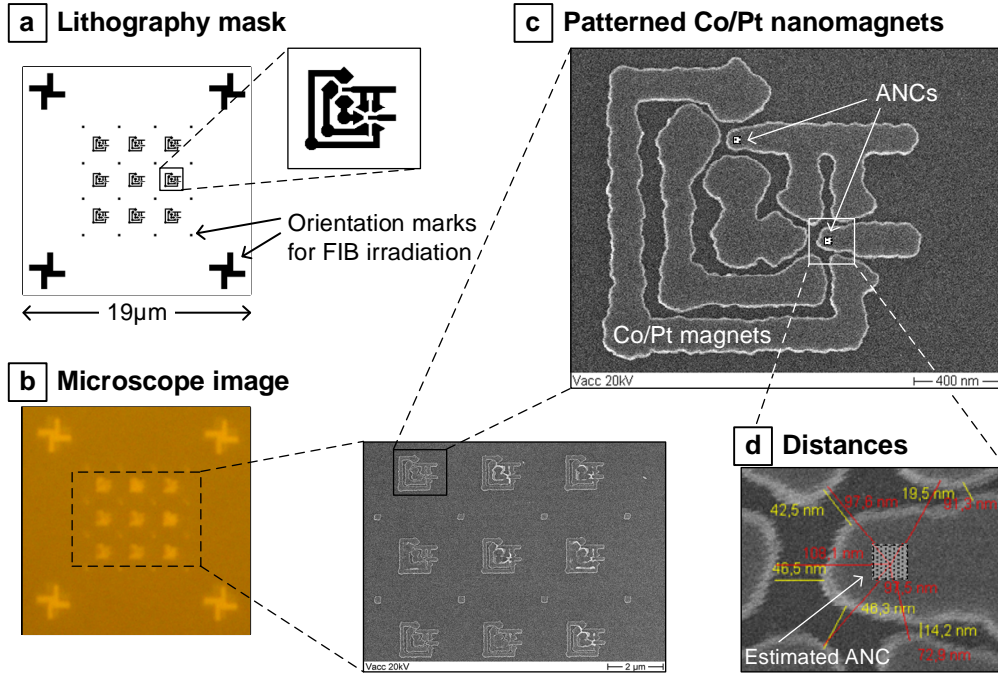


Figure 4.3: Lithography mask (a), corresponding microscope (b) and SEM images (c,d) of patterned pNML full adder circuits.

effective anisotropy by ion-induced intermixing of the Co and Pt layers generates the ANCs required to control the DW nucleation and therefore the signal flow in the field-coupled nanomagnets [SB11a, SB12b].

However, even small misalignments of the ANC in the 10 nm-range lead to unbalanced input coupling fields, which causes malfunctioning of pNML gates and circuits [SB12a]. In order to avoid such misalignments, the ANCs can be already fabricated during the FIB lithography step in the patterning process by DLI. Due to the usage of the positive mode PMMA resist, the magnets are fabricated exactly at that position where the photoresist is irradiated before (cp. Fig. 4.1 c₂ and c₆). If the irradiation dose is locally increased during the lithography step, the PMMA is already specifically milled and the Ga ions may penetrate in the underlying Co/Pt multilayer. Therefore, the partial irradiation is applied directly after the lithography step by another irradiation mask. Our experiments showed, that approximately an increase by a factor of ten for the irradiation dose is required to achieve reasonable results. Note, the DLI technique is limited to devices > 100 nm width as the additional irradiation also increases the area of the lithographic irradiation due to ion backscattering.

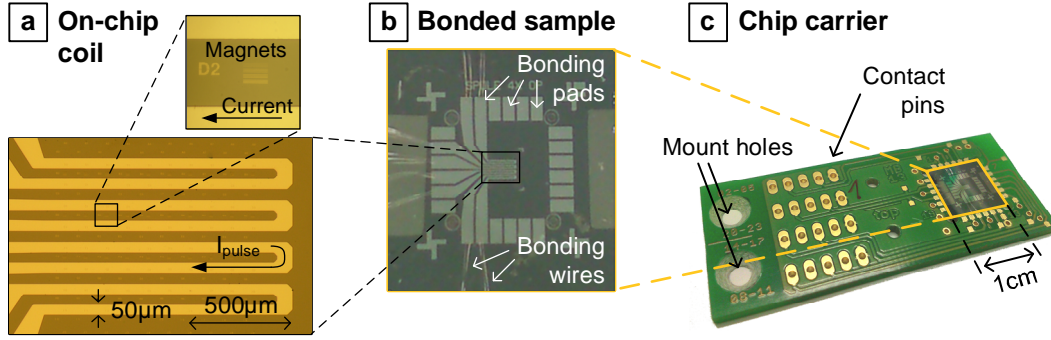


Figure 4.4: Sample with on-chip coil bonded on a chip carrier: a) Evaporated on-chip coil providing sub- μ s field pulses by current pulses. b) Die photo of the sample showing the on-chip coil with the connected bonding pads and bonding wires. c) The sample is bonded on a chip carrier which can be mounted into the measurement setups.

4.5 On-chip coil fabrication

The magnet integrated in the measurement setups which provide the magnetic fields in the experiments are limited to field pulses in the 10 ms range. If sub- μ s field pulses are required, it is mandatory to fabricate on-chip coils on the sample, which enable field pulses from 10 μ s down to 100 ns [BKB⁺13]. The on-chip coils are fabricated by optical lithography using an 2 μ m thick negative tone photoresist, which is required to generate an adequate undercut. After developing the resist, a $\text{Ti}_{3\text{nm}}\text{Cu}_{500\text{nm}}\text{Ti}_{3\text{nm}}\text{Al}_{150\text{nm}}$ metal stack is evaporated by e-beam PVD. The Ti layers are required to increase the adhesion of the conducting Copper (Cu) coil, whereas the Aluminium (Al) layer is required for bonding. After lift-off in a NMP ultrasonic bath, the sample is bonded on a chip carrier which can be connected to current pulse-generating circuits [Zie13]. Fig. 4.4 shows the evaporated on-chip coil (a), which is bonded through several bonding pads (b) on a chip carrier (c).

5 Fundamentals of pNML

The key challenge of pNML is to engineer the nanomagnets to such an extent that their well-controlled interaction enables logic computation in arrays of such magnets. Therefore, the switching behavior of the nanomagnets is specifically manipulated by local FIB irradiation in order to control the DW nucleation process by the fringing fields of further close-by magnets. Fig. 5.1 shows the fundamentals of logic operation in pNML. FIB irradiation generates ANC's to control the DW nucleation site. Thereby, the PMA is locally reduced and the switching field of the magnet is decreased from the intrinsic switching field $H_{c,0}$ to the coercivity H_c (Fig. 5.1a).

Due to the location of the ANC, only the left neighbor I_1 influences the switching process of the central magnet I_z . The distance to the right neighbor I_2 is too large in order to significantly influence the ANC. Depending on the magnetization state M_1 , DW nucleation is either supported or prevented by the coupling field C . Consequently, the hysteresis of the central magnet is shifted to left or right. (Fig. 5.1b).

An alternating clocking field with adequate amplitude H_{clock} will force the central magnet to switch to the antiparallel state compared to M_1 due to the antiferromagnetic coupling (Fig. 5.1c). Thereby, range of adequate clocking field amplitudes for correct switching of the magnets to their desired states, is narrowed by both thermally-induced and fabrication-dependent switching field distributions (SFDs). The remaining window of usable clocking field amplitudes is known as *clocking window* ΔH_{clock} , which naturally should be as large as possible to provide reliable logic operation of pNML circuits.

Appropriate arrangement of the input magnets around the output magnet enables logic operation in pNML logic gates (Fig. 5.1d). Thereby, the clocking field switches the output magnet O antiparallel compared to the (weighted) input majority due to the influence of their coupling fields C_i .

In the following, the basic principles of pNML mentioned above will be discussed step-by-step substantiated by experimental results.

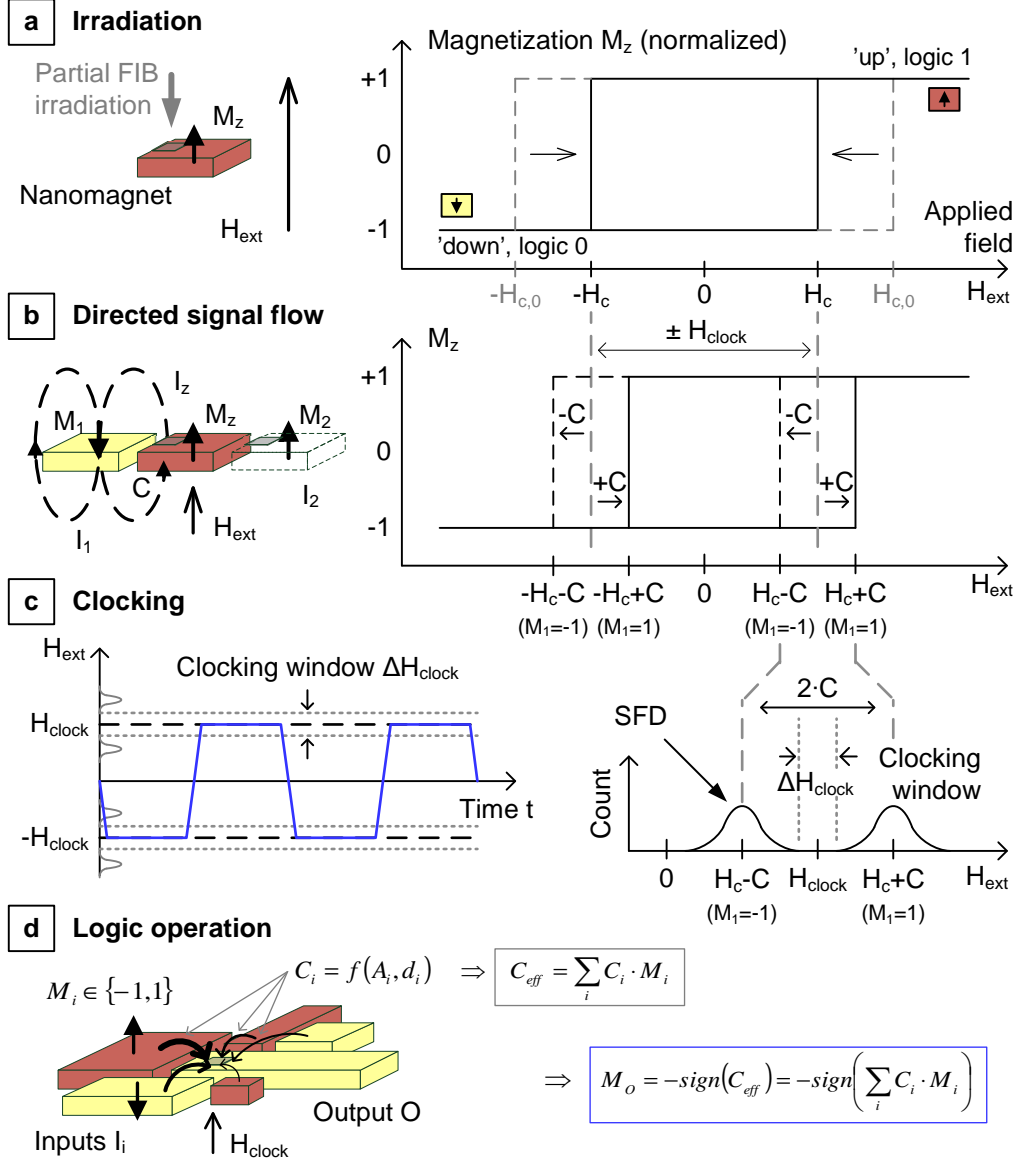


Figure 5.1: Fundamentals of logic operation in pNML. Partial FIB irradiation locally reduces the PMA and creates an ANC to control the DW nucleation (a). Thereby, the switching field of the magnet is decreased from $H_{c,0}$ to H_c . The coupling field C of the left neighbor I_1 influences the DW nucleation of the central magnet I_z and therefore shifts its hysteresis to left or right (b). A clocking field with adequate amplitude will switch M_z antiparallel to M_1 (c). Several input magnets I_i acting on one single output magnet O by their geometry-dependent coupling field C_i enable logic operation in pNML logic gates (d).

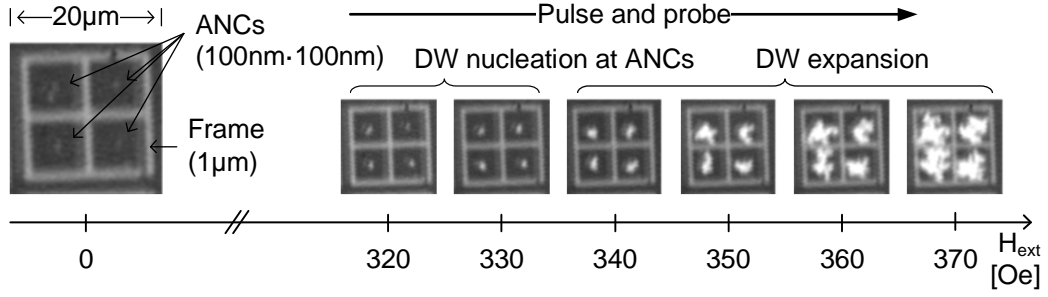


Figure 5.2: Magnetization reversal in a magnetic multilayer film with ANC generated by high ion dose irradiation. By applying an adequate field, the DWs are nucleated at the ANCs and afterwards, with further increasing field, depinned to expand through the non-irradiated multilayer film. The visible frames used for orientation are fabricated by low ion dose irradiation.

5.1 Partial irradiation

The fabrication of ANCs is the major challenge to provide logic computation within field-coupled magnets. Partial FIB irradiation intermixes the Co/Pt multilayers and therefore locally reduces the PMA of the magnets (sec. 2.2.3). As the field-induced DW nucleation is always initiated at the spot with lowest anisotropy, the FIB-induced ANCs dominate the magnetization reversal process and therefore render the film-inherent anisotropy distribution ineffective. For logic operation, the DW nucleation at the ANCs is supported or prevented by the coupling fields of the surrounding magnets. Hence, the well-controlled fabrication of ANCs at user-defined positions is indispensable in order to program logic functionality in arrays of field-coupled magnets.

5.1.1 Fabrication of ANCs in magnetic multilayers

In a first experiment, an as-grown $[\text{Co}_{0.3\text{nm}}/\text{Pt}_{1.1\text{nm}}]_{\times 8}$ multilayer film was partially irradiated in four spots of each $100\text{ nm} \cdot 100\text{ nm}$ size using a high dose of $1 \cdot 10^{17}$ ions/cm² in order to demonstrate the feasibility of FIB-induced fabrication of ANCs ([Fla11], cp. Fig. 5.2). Additionally, four $8\mu\text{m} \cdot 8\mu\text{m}$ frames were irradiated in the multilayer film around the ANCs by low ion dose irradiation ($1 \cdot 10^{13}$ ions/cm²) to visualize the area of interest by the reduced anisotropy in the LMOKE images. The irradiation dose of the frames is rather small so that the ANCs still dominate the DW nucleation. A common pulse and probe approach was applied in the measurements, where for each imaging step, first a magnetic field pulse is applied and afterwards the sample surface is imaged in remanence by LMOKE.

Fig. 5.2 shows the measurement results of the partially irradiated Co/Pt multilayer film. The ANC and the frames are apparent in the images as the anisotropy is reduced (magnetization lies in-plane at zero field) and the surface is roughened by the ion irradiation. By applying a moderate magnetic field of $H_{ext} = 330$ Oe, the magnetization reversal is initiated at the ANC and the DWs nucleated as expected. Note, the DW nucleation is initiated in each frame at the same field, which indicates that besides the DW nucleation field H_{nuc} itself also its distribution due to fabrication variations is comparatively small. With further increasing field, the DWs are depinned from the ANC and propagate through the non-irradiated multilayer film.

These first experiments prove the feasibility of ANCs fabrication in magnetic multilayers with PMA by partial FIB irradiation. However, in order to realize logic operation in pNML, the generation and characterization of ANCs in isolated Co/Pt nanomagnets is essential.

5.1.2 Application of ANCs to Co/Pt nanomagnets

In the following, the concept of local high-ion dose irradiation of magnetic multilayers is transferred to isolated nanomagnets etched of an Co/Pt multilayer film. In the experiment, $\text{Pt}_{4\text{nm}}[\text{Co}_{0.4\text{nm}}/\text{Pt}_{1.1\text{nm}}]_{\times 8}\text{Pt}_{4\text{nm}}$ magnets (anisotropy $K_{eff} \approx 2.8 \cdot 10^5 \text{ J/m}^3$) are partially irradiated using a 50 kV Ga^+ FIB in order to investigate the coercivity drop by local lowering of the anisotropy. In the experiment, the coercivity of the as-grown and the FIB irradiated magnets is determined by hysteresis measurements using LMOKE.

Fig. 5.3a shows an SEM image of a $500 \text{ nm} \cdot 500 \text{ nm}$ Co/Pt nanomagnet which was partially irradiated on an $100 \text{ nm} \cdot 100 \text{ nm}$ area with a dose of $1 \cdot 10^{13} \text{ ions/cm}^2$. The ANC is visible in the SEM image due to the surface roughening of the FIB irradiation. Fig. 5.3b shows the measured hysteresis curve before (blue solid line) and after irradiation (red dashed line) of the magnet. Due to the anisotropy reduction at the ANC, the coercivity has dropped from $H_{c,0} = 4.3 \text{ kOe}$ for the non-irradiated magnet to $H_c = 1.95 \text{ kOe}$ after irradiation. For another magnet, the coercivity is even further reduced by increasing the dose to $5 \cdot 10^{13} \text{ ions/cm}^2$ (black dotted line). Hence, the first requirement of the pNML fundamentals is fulfilled (cp. Fig. 5.1a).

5.1.3 Characteristics of FIB-induced ANCs

In order to optimize partial FIB irradiation for the application in pNML, the characteristics of the ANCs depending on size and dose of the local irradiation are essential. In terms of scaling and low-power operation of pNML, both the size of the ANC as well as the resulting coercivity of the irradiated nanomagnets should be as low as possible. Therefore, isolated Co/Pt magnets of $500 \cdot 500 \text{ nm}^2$

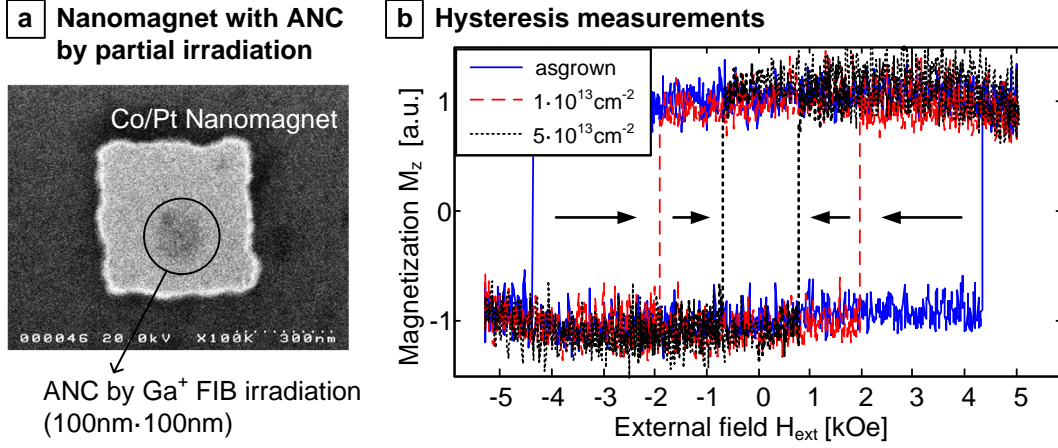


Figure 5.3: Partial irradiation of a Co/Pt magnet. The generation of ANCs by local ion irradiation roughens the surface as indicated in the SEM image (a). Hysteresis curves measured by LMOKE show, that the coercivity of non-irradiated magnets (blue solid line) is steadily reduced with increasing irradiation dose (red dashed line and black dotted line) (b).

to $1 \cdot 1 \mu\text{m}^2$ size are irradiated with varying areal size ($10 \cdot 10 \text{ nm}^2$ to $50 \cdot 50 \text{ nm}^2$) and dose ($8 \cdot 10^{12} \dots 1 \cdot 10^{14} \text{ ions/cm}^2$) to investigate the SFD of the nucleation field at ANCs [SB12b],[Hue11, Sch12]. Fig. 5.4 shows the measured coercivity of the magnets, which exhibit a strong dependency on both the irradiation area and dose.

The effect of the areal dose can be explained by the beam profile of the FIB. The beam diameter is considerably larger than the scanning step size (10 nm) during the irradiation process, which leads to an overlap of irradiated spots. Consequently, the number of ions is locally increased for larger irradiation areas and therefore the anisotropy is further decreased in the irradiation center.

The influence of the irradiation dose is explained by the nucleation-pinning-model derived from [128]. The two regimes of nucleation-dominated switching at moderate doses and pinning-dominated switching for high doses as predicted by theory in sec. 2.3.5 can be clearly separated within each irradiation size:

- For very low doses, the coercivity remains at the switching field of the non-irradiated nanomagnets of $H_{c,0} \approx 4 \text{ kOe}$ indicating the dominant influence of the film-inherent anisotropy distribution: $H_{nuc} = H_{c,0} < H_{ANC}$. Those intrinsic nucleation centers dominate until the magnet has been irradiated with a minimum number of ions required to generate an area with lower anisotropy (=ANC) than the as-grown anisotropy distribution.
- With further increasing dose, the anisotropy at the ANC is continuously reduced and the switching process is nucleation-dominated. The anisotropy

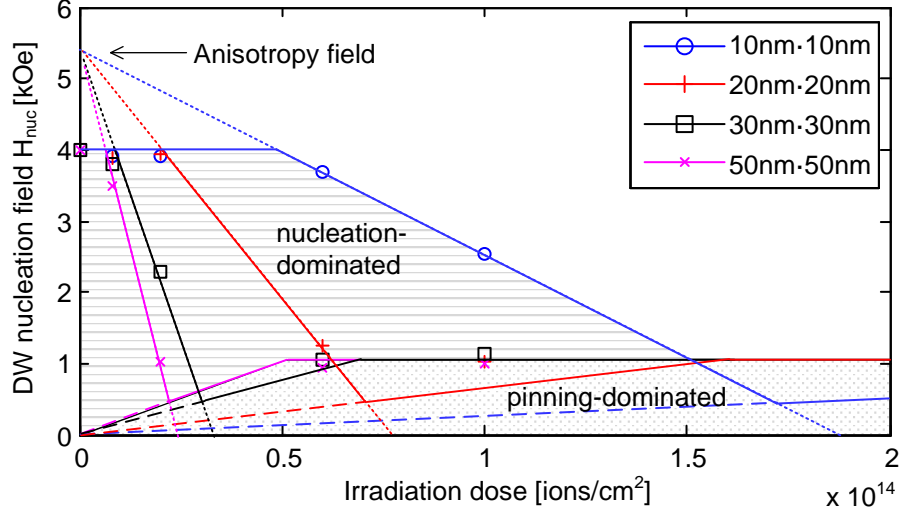


Figure 5.4: Experimental results for the DW nucleation field H_{nuc} depending on dose and size of partial FIB irradiation. The measured nucleation field (markers) is modified depending on the irradiation dose according to the theory of nucleation- and pinning-dominated switching (fitted lines, cp. sec. 2.3.5). A minimum dose is required to overcome the intrinsic SFD of the non-irradiated magnets by the anisotropy field of the ANC.

field at the ANC is lower than the film-inherent anisotropy distribution, but still above the depinning field of the anisotropy step from the ANC to the non-irradiated area: $H_{nuc} = H_{ANC} > H_{depin}$. The dotted lines cross on the y-axis (zero dose \equiv no defects) at $H_0(T) \approx 5.4$ kOe, which is supposed to be the anisotropy field of a defect-free magnet of the utilized 8 ML stack under measurement conditions (anisotropy $K_{eff} \approx 2.8 \cdot 10^5$ J/m³, room temperature $T = 300$ K, sweep rate of external field $R = 5$ kOe/s) [SB12b],[152].

- The coercivity drops with increasing dose until the depinning field of the anisotropy step dominates the anisotropy field: $H_{nuc} = H_{depin} > H_{ANC}$. In the pinning-dominated area, the nucleation field again rises slightly with increasing dose and remains constant at $H_c \approx 1$ kOe for very high irradiation doses. Due to the Gaussian beam profile of the FIB system, the anisotropy step is not sharp but smeared and therefore the high-dose nucleation field is lower than the theoretical limit of $0.5 \cdot H_{c,0}(T)$ (cp. sec. 2.3.5).

Another important aspect is the SFD of the nucleation field, as variations dramatically reduce the clocking window for adequate amplitudes of the clocking field. Therefore, also the standard deviation (SD) of the nucleation field is determined within multiple dots. In the experiment, six dots for each irradiation dose have

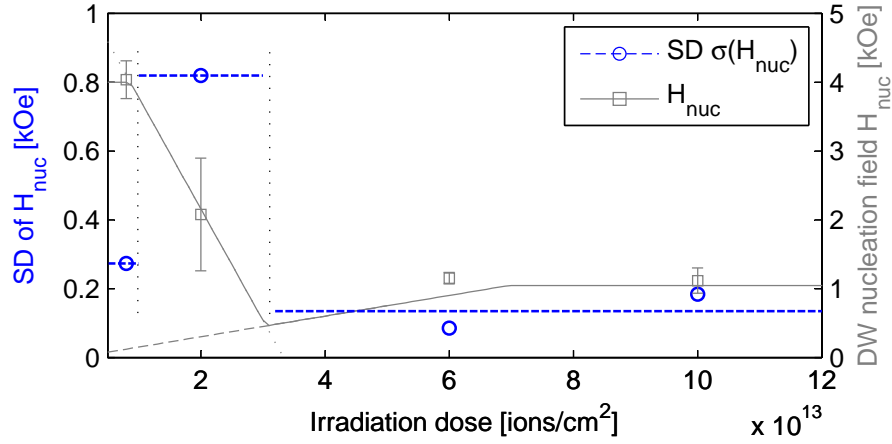


Figure 5.5: SFD of the nucleation field H_{nuc} depending on the irradiation dose of the ANC. The SD of the nucleation field H_{nuc} changes significantly from the intrinsic to the nucleation-dominated and the pinning-dominated switching regime.

been investigated. Fig. 5.5 shows the measurement results for the SD σ_{nuc} of the nucleation field H_{nuc} depending on the irradiation dose of the ANC exemplarily for the $30\text{ nm} \cdot 30\text{ nm}$ irradiation. Additionally, the nucleation field H_{nuc} with error-bars corresponding to the SD is shown in gray in the background to visualize the intrinsic, the nucleation-dominated and the pinning-dominated switching regime.

- For low ion doses ($8 \cdot 10^{12}\text{ ions/cm}^2$) the switching is still dominated by the film-inherent anisotropy distribution showing a moderate SD for the nucleation field of $\sigma_{nuc} = 270\text{ Oe}$.
- In the nucleation-dominated switching regime, the SD is dramatically increased to $\sigma_{nuc} = 810\text{ Oe}$. This makes absolutely sense, as the anisotropy reduction by FIB irradiation is a somehow stochastic process. Low doses of $2 \cdot 10^{13}\text{ ions/cm}^2$ corresponds to only 180 ions on the whole irradiation area of $30 \cdot 30\text{ nm}^2$. Consequently, even small variations of the irradiation dose come along with large switching field variations.
- If the irradiation dose is further increased to the pinning-dominated switching regime, the anisotropy step from the ANC to the non-irradiated area is the limiting factor. Here, the anisotropy in the ANC is already in-plane ($K_{eff} < 0$) and therefore variations of the nucleation field mainly arise from variations of the anisotropy step (i.e. step height and width). In the experiments, a SD of $\sigma_{nuc} = 80 \dots 180\text{ Oe}$ for the pinning-dominated regime has been found, which is the lowest SD of all switching regimes.

The observed behavior of a switching regime-dependent SFD has been monitored for all investigated irradiation areas substantiating the underlying explanations provided above. In order to minimize both the nucleation field H_{nuc} and its SD σ_{nuc} , the irradiation dose has to be adjusted with respect to the size of the ANC and the magnetic material itself. Accordingly, the pinning-dominated switching regime close to the transition region from nucleation- to pinning-dominated switching is favored for DW nucleation at the ANC. As the determination of this optimal dose is very challenging (and time-consuming) to determine for each structure, usually quite high irradiation doses are applied in most of the following experiments. Here, the generated ANCs are in the pinning-dominated regime showing low variations, but moderate switching fields.

5.2 Directed signal flow

The fundamental principle of pNML is controlling the switching of a magnet by the coupling field of adjacent magnets in order to provide logic operation and directed signal flow in arrays of field-coupled magnets. Depending on the magnetization state of the input magnets, their coupling fields either support or prevent the clocking field-induced DW nucleation at the ANC of the output magnet. By contrast, feedback from the output magnet on the input magnets has to be prevented.

In order to prove the fundamental principle of directed signal flow, a chain of three magnets with the two inputs I_1 and I_2 and the central output O was investigated (Fig. 5.6a) [SB11a]. By irradiating the output O on the left side, its switching behavior should be only manipulated by the state of I_1 due to its coupling field C_1 . The input I_2 is too far away in order to influence the ANC of output O significantly. The $[\text{Co}_{0.4\text{nm}}/\text{Pt}_{1.1\text{nm}}]_{\times 8}$ magnets with a size of $1 \cdot 1 \mu\text{m}^2$ each are separated by a 100 nm gap. The middle magnet is irradiated on an area of $100 \cdot 100 \text{ nm}^2$ with a dose of $1 \cdot 10^{13} \text{ ions/cm}^2$ on the left side. The coercivities of the non-irradiated input magnets are $H_{c,I_1} = 3.9 \text{ kOe}$ for input I_1 , and $H_{c,I_2} = 2.2 \text{ kOe}$ for I_2 , which are different due to inherent anisotropy variations. The switching field of the partial irradiated output O is decreased to $H_{c,O} = 1.5 \text{ kOe}$ due to the anisotropy reduction at the ANC (Fig. 5.6b).

Due to the significant difference of the switching fields of I_1 and I_2 , each input configuration can be set by corresponding external fields. For example, first a negative field pulse with $H_{ext} = -4.5 \text{ kOe}$ sets I_1 to the down state and second a positive pulse with $H_{ext} = 2.5 \text{ kOe}$ sets I_2 upwards. Afterwards, the SFD of the partial irradiated output O is investigated by hysteresis measurements.

In order to determine the influence of the input magnets on the output O , its SFD is measured for all 4 possible input configurations. In the experiment, first the desired input configuration of I_1 and I_2 is set by external fields. Second, the

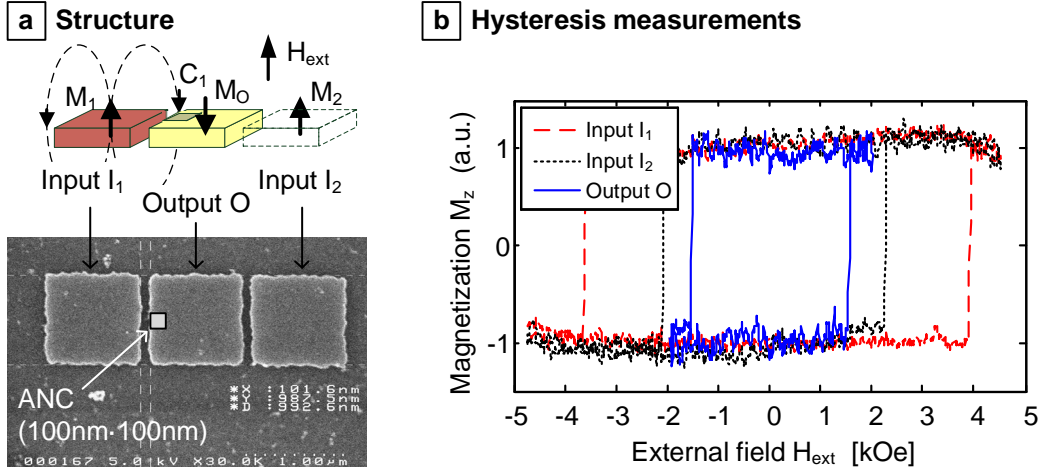


Figure 5.6: Device under test to prove the fundamental principle of directed signal flow. a) In a chain of three magnets with the two inputs I_1 and I_2 , the central output magnet O is partially irradiated on the left side. Therefore, its switching behavior is only dependent on the state of I_1 . b) Hysteresis curves reveal different switching fields of all magnets, which enables to first set the desired input configuration of I_1 and I_2 and afterwards measure the corresponding SFD of the partial irradiated output magnet O .

SFD of the output O is measured by $N = 100$ hysteresis curves using the LMOKE. Thereby, the external field is ramped with a sweep rate of 1 kOe/s within a range of ± 2 kOe to not affect the states of I_1 and I_2 . Afterwards, the hysteresis curves are analyzed in 20 Oe steps in order to determine the SFD of the output.

Fig. 5.7 shows the measured output SFDs depending on the configuration of the input magnets. The SFD is only shifted by the coupling field C_1 of the input I_1 next to the ANC. Depending on the magnetization state of I_1 , the SFD is shifted by $C_1 = \pm 45$ Oe. If I_1 is up (red lines), the coupling field C_1 is subtracted from the external field and hence the SFD is shifted to the right by 45 Oe. If the input I_1 is in the downstate (orange lines), the SFD is shifted to the left by -45 Oe.

By contrast, the magnetization state of the input I_2 (solid lines: $I_2 \downarrow$, dotted lines: $I_2 \uparrow$) has no remarkable impact on the output. As expected, the distance of the input I_2 is too large so that its coupling field has less influence on the DW nucleation at the ANC.

The experiment was repeated for two further chains with three magnets in order to confirm the results. Both times, the switching behavior of the output was only influenced by the neighbor next to the ANC, whereas the neighbor next to the non-irradiated side had negligible influence.

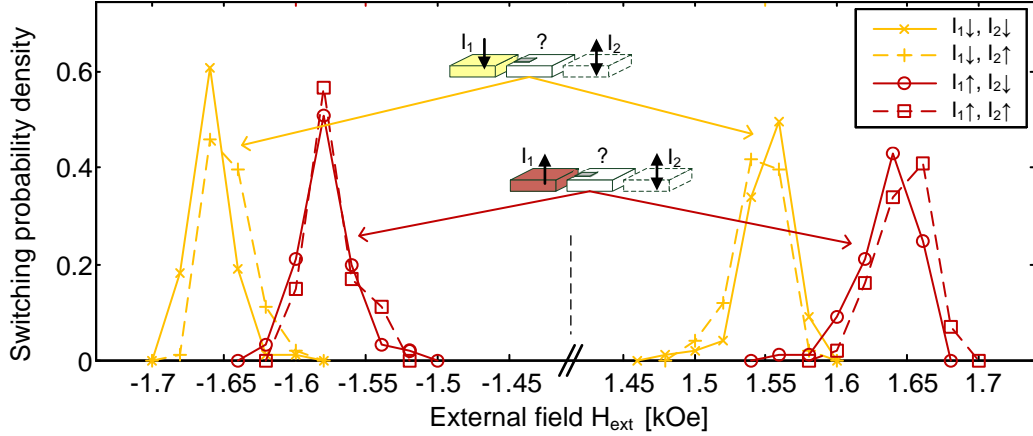


Figure 5.7: Demonstration of directed signal flow in a chain of three magnets. The central output magnet O is partially irradiated on the left side, therefore its SFD is shifted depending on the magnetization state of the input I_1 due to its coupling field C_1 . The input I_2 is too far away in order to influence the ANC of output O significantly.

The measurement results prove the fundamental principle of directed signal flow by controlling the DW nucleation at the ANC of one magnet by the coupling field of adjacent magnets as postulated at the beginning of this chapter. An applied clocking field with adequate amplitude will switch the partial irradiated magnet antiparallel compared to the magnetization of the neighbor next to the irradiated area.

The invented and demonstrated technique of directed signal flow by local high ion dose irradiation has in the following been applied in multiple applications in both experiment and simulation. Chains consisting of several partial irradiated magnets are perfectly ordered and the signal is transferred through the entire chain as demonstrated by [EBK⁺12, KBE⁺13a]. Furthermore, the ANC fabrication has been successfully applied to logic gates [SB12a], circuits [SB13b, SB14a], [JWR⁺12, PNC⁺14] and even in 3D-integrated pNML [KBE⁺13b, EBK⁺14, EBZ⁺14].

5.3 Clocking and speed

In order to perform logic operations and propagate magnetic information through arrays of field-coupled magnets, a pulsed clocking field with adequate amplitude is applied. Thereby, the magnets are ordered step by step according to the alternating clocking field [EBK⁺12, KBE⁺13a]. In other words, the clocking field acts as both internal clock and power supply. Thereby, both the clocking field amplitude H_{clock} and the pulse time t_{clock} have to be adapted (Fig. 5.8).

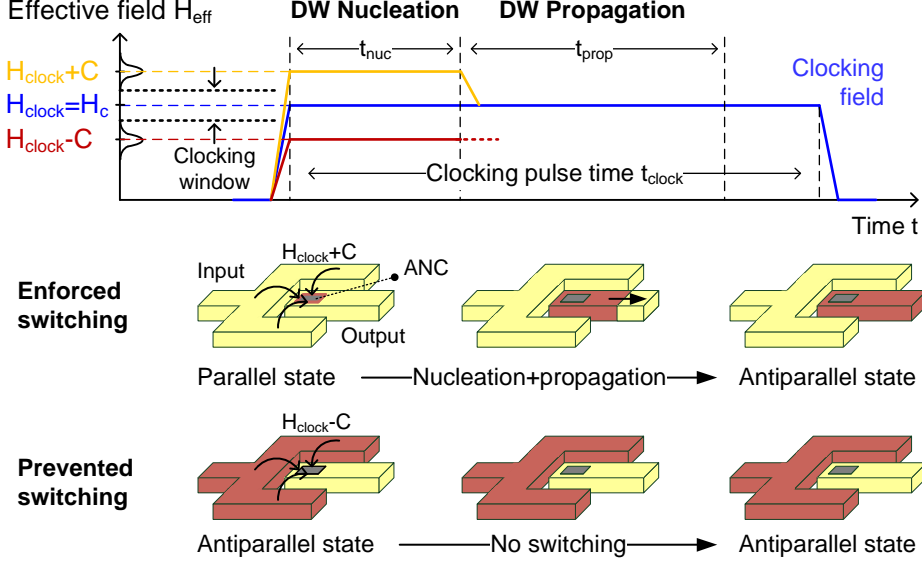


Figure 5.8: Switching process of field-coupled magnets. The clocking field-induced DW nucleation at the ANC is enforced or prevented by the input coupling field C . After nucleation in the nucleation time t_{nuc} , the clocking field drives the DW through the entire magnet in the propagation time t_{prop} . In order to provide reliable operation, both the amplitude H_{clock} and the required pulse time t_{clock} have to be chosen adequately.

- On the one hand, the clocking field reduces the energy barrier for DW nucleation at the ANC, which is in turn supported or prevented by the coupling field C of the surrounding input magnet. Here, an appropriate amplitude H_{clock} is required in order to adequately reduce the energy barrier, so that the coupling field C is sufficient to enforce or prevent the DW nucleation depending on the input state. Thereby, the clocking window is reduced by both the thermally induced and the fabrication-dependent SFD. Clocking field amplitudes exceeding or falling below the clocking window will cause erroneous switching of the magnets.
- On the other hand, the clocking field is required to drive the nucleated DW through the output magnet in order to completely reverse it. Thereby, both the DW nucleation time t_{nuc} and the propagation time t_{prop} have to be taken into account [SB14d]. If the clocking field pulse time t_{clock} is too short, some magnets will not be completely reversed and the propagating DWs will get stuck. In the next (opposite) clocking pulse, such DWs will move backwards and the magnets will be switched back. If the clocking pulse is too long, the clocking frequency of the entire circuit is reduced.

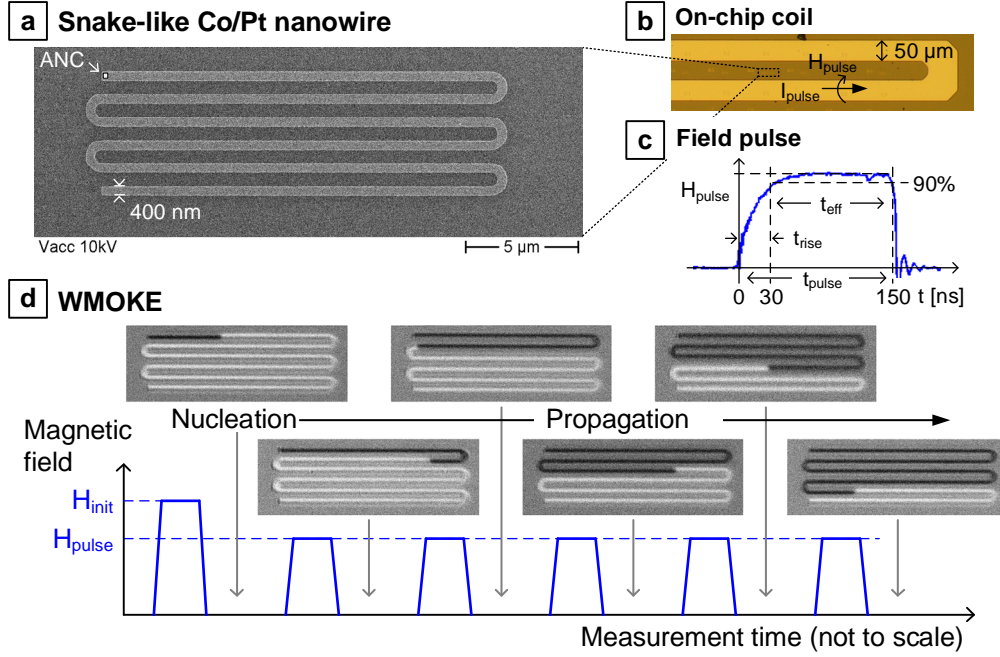


Figure 5.9: Snake-like Co/Pt nanowire to measure the DW velocity. a) SEM image. b) Optical micrograph with on-chip coil to generate magnetic field pulses. c) Field pulse H_{pulse} corresponding to the measured current pulse I_{pulse} applied through the on-chip coil. d) WMOKE images to determine the DW propagation length l_{prop} after each field pulse.

The field pulse amplitude and time required to nucleate a DW can not be handled independently, as the DW nucleation probability depends on both the effective field pulse amplitude and time (cp. sec. 2.5) [BKB⁺13]. Hence, both the DW propagation speed (DW velocity v_{DW}) and the nucleation probability P_{nuc} have to be investigated in order to determine the propagation time t_{prop} , the nucleation time t_{nuc} and the required field amplitude H_{clock} .

5.3.1 DW velocity

After DW nucleation at the ANC by the effective field H_{eff} , the DW is propagated through the magnet by the applied clocking field. According to the theory derived in sec. 2.3.3, the DW propagation velocity v_{DW} is classified into three different regimes (creep, depinning and flow regime), which depend on the relation between the applied field amplitude H_{clock} and the intrinsic pinning field H_{int} . Thereby, the DW speed for a given amplitude is approximately constant over time. Hence,

the DW propagation time t_{prop} in a magnet with length l_{mag} is given by:

$$t_{prop} = \frac{l_{mag}}{v_{DW}(H_{clock})}. \quad (5.1)$$

In the experiment, the DW velocity $v_{DW}(H_{clock})$ is determined in Co/Pt nanowires by applying single field pulses with different amplitudes H_{pulse} and measuring the propagated distance l_{prop} after each pulse (Fig. 5.9)[SB14d],[Mit12]. The 400 nm wide snake-like $[\text{Co}_{0.8\text{nm}}\text{Pt}_{1.0\text{nm}}]_{\times 4}$ nanowires are partially irradiated ($40 \cdot 40 \text{ nm}^2$, areal dose $5 \cdot 10^{13} \frac{\text{ions}}{\text{cm}^2}$) at one end to control the DW nucleation (a). An on-chip coil is used to generate magnetic field pulses with a pulse time $t_{pulse} = 150 \text{ ns}$ with different amplitudes H_{pulse} (b). Due to a field rise time of $t_{rise} \approx 30 \text{ ns}$, the effective field pulse time $H_{pulse} \geq 0.9 \cdot H_{clock}$ is reduced to $t_{eff} = 120 \text{ ns}$ (c).

First, a high field pulse is required to nucleate the DW at the ANC. Afterwards, several field pulses with the desired field pulse amplitude H_{pulse} are applied and the propagated distance of the DW is measured after each pulse by WMOKE (d). The field-dependent DW velocity in the snake-like nanowire is then calculated by

$$v_{DW}(H_{pulse}) = \frac{l_{prop}(H_{pulse})}{t_{eff}}. \quad (5.2)$$

Fig. 5.10 shows the measurement results ($N(H_{pulse}) = 50$) depending on the applied field pulse amplitude H_{pulse} . The DW velocity v_{DW} can be clearly separated into the characteristic propagation regimes according to [139] (see sec. 2.3.3). The corresponding intrinsic pinning field is determined to $H_{int} = 170 \text{ Oe}$.

- In the creep regime ($H_{pulse} \ll H_{int}$), the DW motion is dominated by depinning from energy barriers (defects, edge roughness) due to thermal activation. However, no DW propagation has been observed during the experiments for field pulse amplitudes below $H_{pulse,min} = 220 \text{ Oe}$ for the utilized 120 ns-field pulses.
- In the depinning regime ($H_{pulse} \approx H_{int}$), DW motion is still thermally activated, but field pulse amplitude H_{pulse} are already sufficient to propagate the DW through the nanowire. According to eq. 2.28, the velocity increases exponentially with the applied field H_{pulse} as fitted by the dashed line:

$$v_{DW}(H_{pulse} \approx H_{int}) = v_0 \cdot e^{-\frac{E_{pin}}{k_B T} \left(\frac{H_{int}}{H_{pulse}} \right)^{\frac{1}{4}}} \quad (5.3)$$

with the non-meaningful, numerical prefactor $v_0 = 1.14 \cdot 10^6 \text{ m/s}$ and the pinning energy barrier $E_{pin} = 12.1 \text{ k}_B \text{ T}$, induced by both crystal defects and edge roughness of the nanowire. Significant variations of the DW velocity decreasing with increasing field amplitude confirm on the one hand the theory

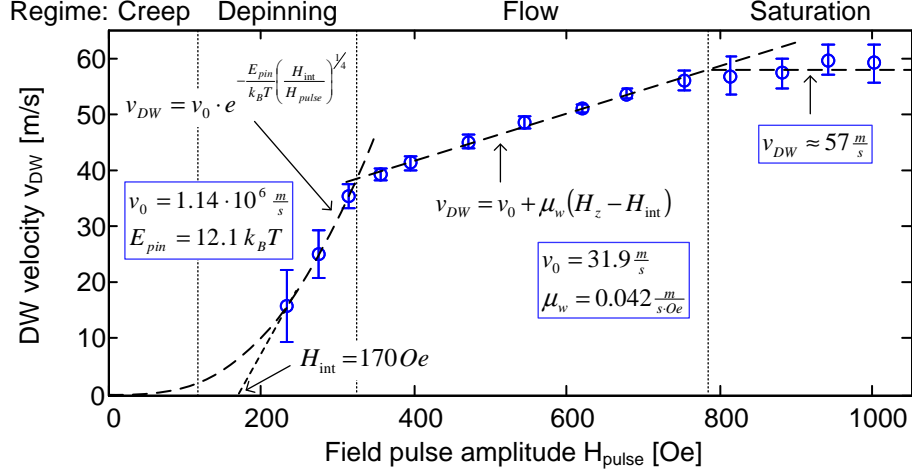


Figure 5.10: Domain wall velocity v_{DW} depending on the field pulse amplitude H_{pulse} measured in the snake-like Co/Pt nanowire. The measured DW velocity (blue markers, errorbars = standard deviation, $N = 50$) features the characteristic DW motion regimes fitted by the corresponding theory (dashed lines).

of DW motion by thermal activation, on the other hand they substantiate the depinning regime to be the smeared intermediate regime between the creep and the flow regime.

- In the flow regime ($H_{pulse} \gg H_{int}$) DW motion is governed by viscous flow dynamics. Thus, the DW velocity depends linear on the applied field corresponding to eq. 2.29 and variations ($\sigma_{v_{DW}} < 1 \text{ m/s}$) are reduced to a minimum:

$$v_{DW}(H_{pulse} \gg H_{int}) = v_0 + \mu_w (H_{pulse} - H_{int}) \quad (5.4)$$

with the numerical prefactor $v_0 = 31.9 \text{ m/s}$ and the domain wall mobility $\mu_w = 0.042 \text{ m/sOe}$ as relevant fitting parameters.

The saturation effect at $v_{DW,sat} \approx 57 \text{ m/s}$ for pulse amplitudes $H_{pulse} > 750 \text{ Oe}$ is not finally resolved, but may be traced backed to limitations of the measurement system (pulse generator, [Zie13]) or the utilized multilayer stack.

5.3.2 DW nucleation probability

The probability P_{nuc} for DW nucleation at the ANC by an magnetic field pulse with amplitude H_{pulse} and effective pulse time t_{eff} is modeled by an Arrhenius

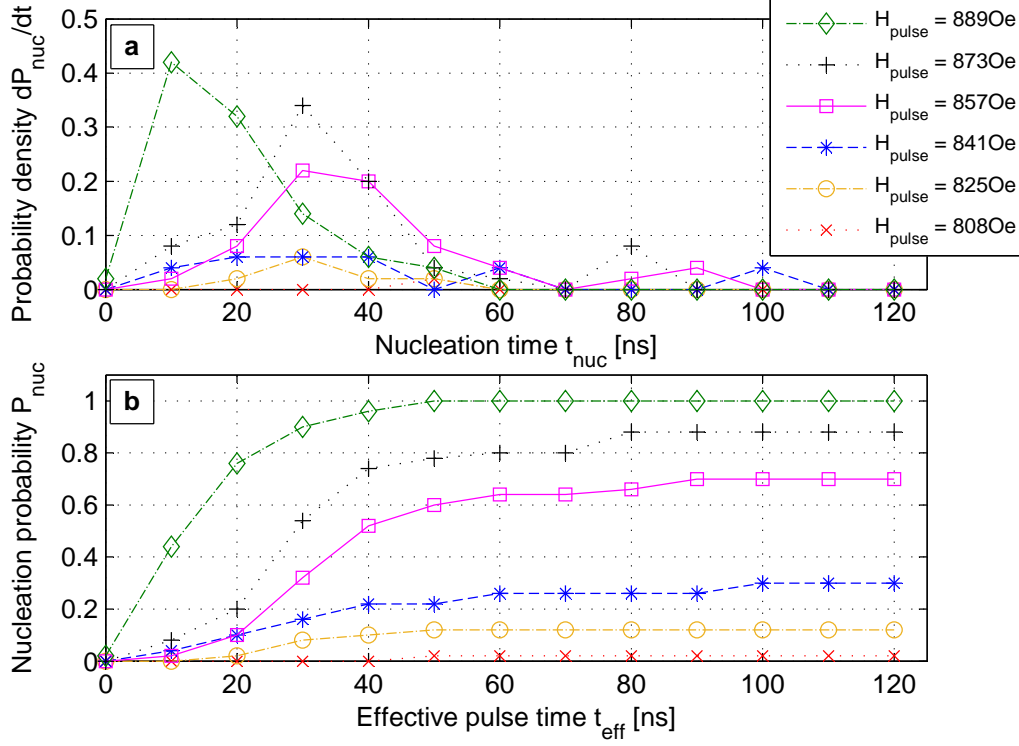


Figure 5.11: DW nucleation probability depending on the applied field pulse time and amplitude. With increasing amplitude H_{pulse} , the DW nucleation time t_{nuc} is decreased (nucleation probability density dP_{nuc}/dt is shifted to shorter times, (a)), and the overall nucleation probability for the whole pulse time t_{eff} is increased (cumulative nucleation probability P_{nuc} raises, (b)).

switching model according to eq. 2.44:

$$P_{nuc}(t_{eff}, H_{pulse}) = 1 - \exp(-t_{eff}/\tau(H_{pulse})) \quad (5.5)$$

$$\tau(H_{pulse}) = f_0^{-1} \cdot \exp\left(\frac{E_0 \cdot (1 - \frac{H_{pulse}}{H_0})^2}{k_B T}\right) \quad (5.6)$$

In order to determine the time-dependent DW nucleation probability by experiment, primarily the DW nucleation probability density dP_{nuc}/dt is investigated by measuring the distribution of the field-dependent DW nucleation time $t_{nuc}(H_{pulse})$ within several repeated measures ($N(H_{pulse}) = 50$). In the following experiment, the DW nucleation time was measured in a 400 nm wide $[\text{Co}_{0.8\text{nm}}\text{Pt}_{1.0\text{nm}}]_{\times 4}$ nanowire with ANC for different field amplitudes H_{pulse} .

Therefore, the nanowire is first saturated to the down state by several negative field pulses. Afterwards, one single positive field pulse ($t_{eff} = 120$ ns) with the

amplitude H_{pulse} is applied and the propagated distance l_{prop} of the DW is measured by WMOKE. The time needed to propagate the DW through the distance l_{prop} is given by $t_{prop} = l_{prop}/v_{DW}(H_{pulse})$. Accordingly, the remaining field pulse time was required to nucleate the DW at the ANC:

$$t_{nuc} = t_{eff} - t_{prop} = t_{eff} - \frac{l_{prop}}{v_{DW}(H_{pulse})}. \quad (5.7)$$

Afterwards, the corresponding nucleation probability P_{nuc} is determined by integration over the measured probability density of the DW nucleation time.

Fig. 5.11 shows the measurement results for the nucleation probability density dP_{nuc}/dt (a) versus the nucleation time t_{nuc} and the cumulative nucleation probability P_{nuc} (b) depending on the effective pulse time t_{eff} for different field amplitudes H_{pulse} . The DW nucleation time is significantly reduced for increasing field amplitudes H_{pulse} :

- For high field amplitudes of $H_{pulse} = 889$ Oe, the peak of the measured probability density is shifted to only 10 ns and the DW is nucleated for sure during the first 50 ns of the field pulse: $t_{nuc}(H_{pulse} = 889 \text{ Oe}) \leq 50$ ns.
- If the amplitude is decreased by just 16 Oe, the peak of the DW nucleation time already increases to 30 ns and the DW nucleation probability is reduced to $P_{nuc}(H_{pulse} = 873 \text{ Oe}) = 0.88$.
- If the field pulse amplitude is further decreased to $H_{pulse} = 808$ Oe, only one nucleation event has been observed during 50 experiments, whereas none was measured for fields below 800 Oe.

Hence, a difference of $\Delta H_{pulse} = 90$ Oe is sufficient to prevent or guarantee DW nucleation at the ANC in the investigated Co/Pt nanowire during an effective pulse time of $t_{eff} = 120$ ns.

In order to compare the measurement results to the employed model, the structure- and material-dependent parameters E_0 (energy barrier at zero field) and H_0 (coercive field at zero temperature) for the switching probability have to be determined. Therefore, the model of eq. 5.5 is calibrated to the experimental results of the total nucleation probability $P_{nuc}(H_{pulse}, t_{eff} = 90 \text{ ns})$ by using a least-square algorithm (Fig. 5.12a). Hereby, we determined $E_0 = 187 k_B T$ and $H_0 = 1027$ Oe by using an attempt frequency of $f_0 = 1.2$ GHz.

The calibrated nucleation probability model is evaluated by comparing simulation (lines) and experiment (marker) of the time-dependent DW nucleation probability $P_{nuc}(t_{eff}, H_{pulse})$ at the ANC (Fig. 5.12b). Notably, both the shape as well as the nucleation probability level of the experimental data are mapped very well by the applied model. Therefore, the obtained results prove the validity of the model for dynamic simulations, but also the experimental method to determine the field-dependent DW nucleation time.

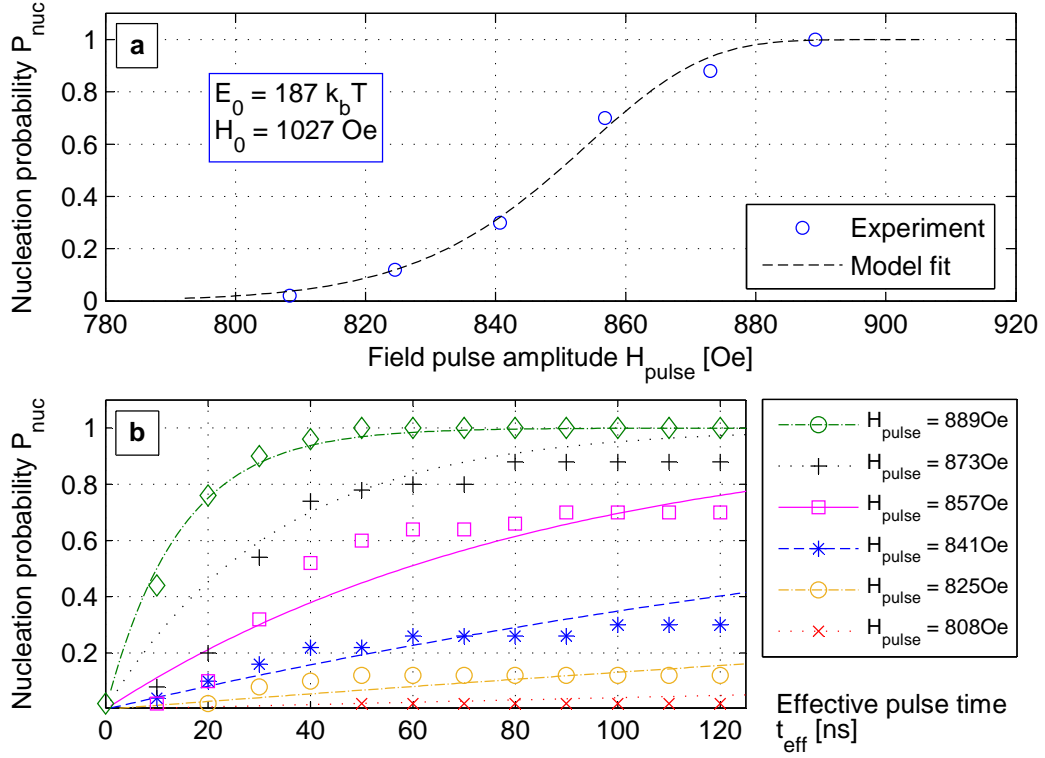


Figure 5.12: Evaluation of the DW nucleation model by calibration and comparison to experimental results. a) The model is fitted to the measured nucleation probability $P_{nuc}(H_{pulse}, t_{eff} = 90 \text{ ns})$ to determine the model parameters E_0 and H_0 . b) Comparison between the calibrated model (lines) and the measurement results (markers) for the nucleation probability P_{nuc} depending on the effective field pulse amplitude t_{eff} (bottom).

5.3.3 Influence of field-coupling

In order to achieve directed signal flow, the DW nucleation at the ANC of one magnet is controlled by the coupling field of an adjacent input magnet (see Fig. 5.8). Thereby, the effective field acting on the ANC is given by the superposition of the clocking field H_{clock} and the coupling field C of the input with magnetization state M_{in} :

$$H_{eff} = H_{clock} - C \cdot M_{in}. \quad (5.8)$$

Hence, the energy barrier for DW nucleation $E_{barrier}$ according to eq. 2.39 is in- or decreased depending on the input state M_{in} . The corresponding DW nucleation probability $P_{nuc}(t_{eff}, H_{eff})$ according to eq. 5.5 is shifted by the coupling field C . Thereby, the strength of the coupling field C is crucial for the reliability of the inverter structure.

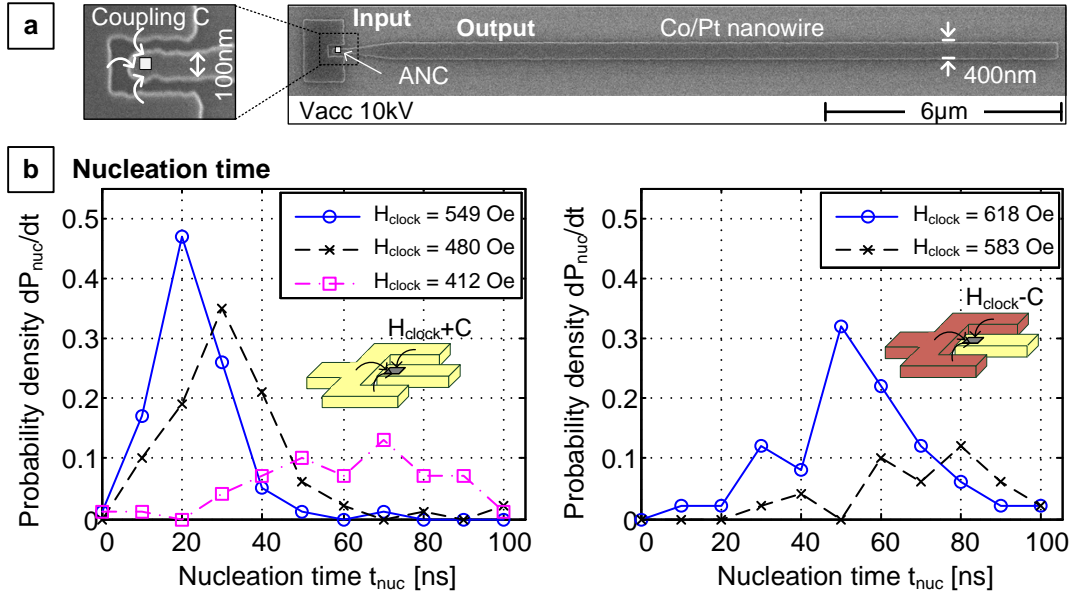


Figure 5.13: Influence of the coupling field on the DW nucleation time in a pNML inverter structure. a) SEM image of the investigated structure with an input magnet acting on an output nanowire by its coupling field C . b) Measured DW nucleation probability density depending on the applied field H_{clock} and the input state.

On the one hand, when the output magnet is parallel to the input, DW nucleation is supported by the coupling field C . In terms of clocking, the DW has to be nucleated at the ANC during the nucleation time t_{nuc} to provide sufficient field pulse time to propagate the DW through the entire magnet:

$$P_{nuc}(t_{nuc}, H_{clock} + C) \rightarrow 1 \quad (5.9)$$

On the other hand, when the output magnet is already in the antiparallel state, DW nucleation is impeded by the input coupling field C . In order to prevent computing errors the DW nucleation has to be suppressed during the whole clocking pulse time t_{clock} :

$$P_{nuc}(t_{clock}, H_{clock} - C) \rightarrow 0 \quad (5.10)$$

Obviously, the DW nucleation probability P_{nuc} and therefore the reliability of the pNML inverter strongly depends on the strength of the coupling field C , but also the applied clocking pulse time t_{clock} and the field amplitude H_{clock} .

In order to determine the influence of the coupling field on the DW nucleation time t_{nuc} and the nucleation probability P_{nuc} , an inverter structure with a fork-like input magnet and an output nanowire is investigated (Fig. 5.13a) [SB15b]. The 18 μ m long and 400 nm wide output nanowire is tapered to 100 nm at the input

side in order to increase the input coupling field C (see sec. 6.1.2). The ANC at the tip of the output nanowire provides controlled DW nucleation. In the experiment, first the input magnet is set by externally applied fields and afterwards the DW nucleation time is measured according to eq. 5.7 by applying $t_{eff} = 100$ ns field pulses through an on-chip coil. Fig. 5.13b shows the measured distributions of the DW nucleation time depending on the applied field pulse amplitude for parallel (left) and antiparallel switching (right).

- For the parallel case ($M_{in} = -1$, left), the input coupling field C is added to the applied field amplitude H_{clock} and therefore supports the DW nucleation from the ANC ($H_{eff} = H_{clock} + C$). In the experiment, the mean DW nucleation time is reduced to $\overline{t_{nuc}}(H_{clock} = 549 \text{ Oe}) = 20$ ns.
- In the antiparallel case ($M_{in} = 1$, right), the effective field acting on the ANC is decreased ($H_{eff} = H_{clock} - C$) and DW nucleation is impeded. Also with high field amplitudes of $H_{clock} = 618$ Oe, the mean DW nucleation time is still $\overline{t_{nuc}}(H_{clock} = 618 \text{ Oe}) \approx 50$ ns. For an amplitude of $H_{clock} = 549$ Oe, any nucleation event hasn't been observed in the antiparallel case.

Fig. 5.14a shows the nucleation probability P_{nuc} depending on the applied field amplitude H_{clock} for both input configurations. Experimental results (marker) are fitted by the Arrhenius model (lines) $P_{nuc}(t_{eff} = 100 \text{ ns}, H_{clock} \pm C)$ in order to determine the energy barrier at zero field $E_0 = 117 \text{ k}_B\text{T}$, the coercive field at zero temperature $H_0 = 650$ Oe and the input coupling field $C = 90$ Oe. The probability functions are shifted due to the supporting (parallel) or impeding (antiparallel) effect of the coupling field C on the DW nucleation.

The most suitable clocking field amplitude H_{clock} can be determined by minimizing the error rate

$$e = 1 - P_{nuc}(t_{nuc}, H_{clock} + C) \cdot [1 - P_{nuc}(t_{clock}, H_{clock} - C)] \quad (5.11)$$

with respect to the conditions of eqn. 5.9 and 5.10 derived above. Fig. 5.14b shows the simulation results for the corresponding error rate e depending on the clocking field amplitude H_{clock} for different permitted nucleation times $t_{nuc} = t_{eff} - t_{prop}$. The ideal clocking amplitude increases with decreasing nucleation time (stronger field $H_{eff} \equiv$ faster DW nucleation), but has to be adapted depending on the required DW propagation time for complete magnetization reversal according to eq. 5.1. Therewith, sufficient error rates below $e < 10^{-6}$ can be achieved for the studied inverter structure. Obviously, the error rate can be further reduced by increasing the coupling field C .

The results show, that the DW nucleation time t_{nuc} , the coupling field C as well as the pulse time t_{clock} and the amplitude H_{clock} of the applied clocking field are crucial for reliable operation of pNML logic gates. In order to determine

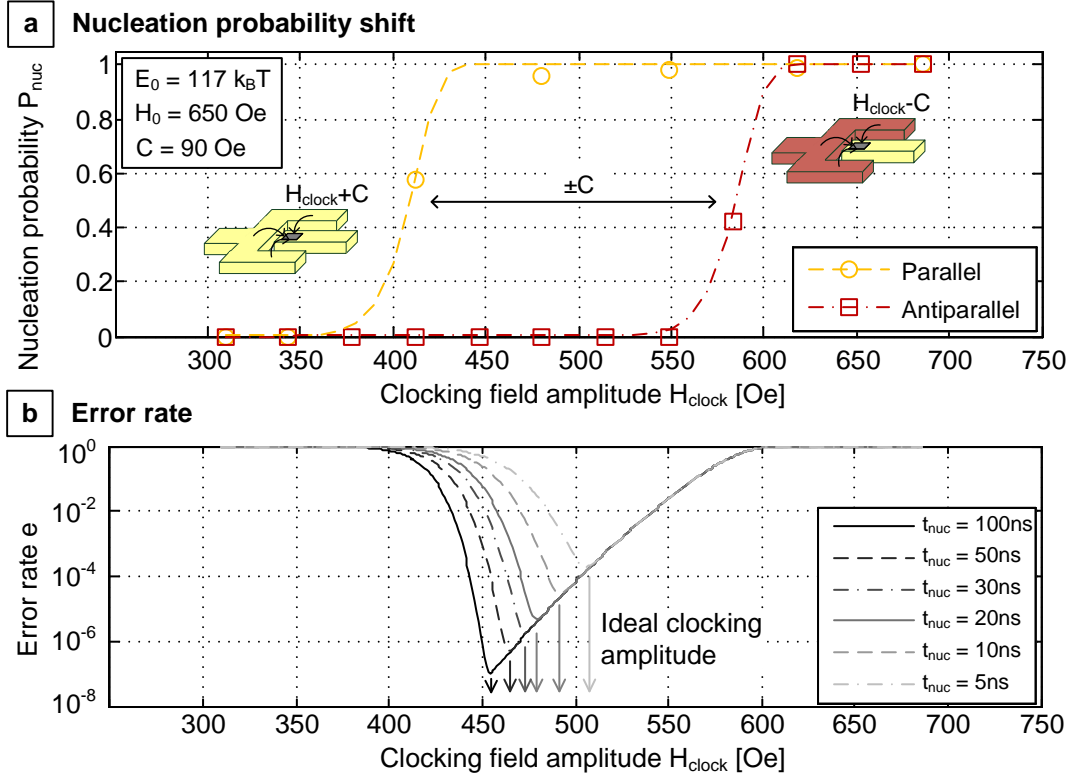


Figure 5.14: Clocking of a pNML inverter structure. a) The nucleation probability is shifted due to the coupling field C of the input. b) The error rate e can be minimized by adapting the clocking field amplitude with respect to the desired nucleation time t_{nuc} .

the necessary clocking frequency and amplitude of a pNML circuit, the time for DW nucleation has to be taken into account. Thereby, the nucleation time is considerably affected by the strength of the coupling field. This is crucial for the design and clocking of pNML circuitry.

5.4 Logic operation

Logic operation in pNML is provided by adequate arrangement of the magnets in combination with the specific fabrication of ANC. Thereby, the coupling fields of the inputs, which surround the ANC of the output, manipulate the clocking field-induced DW nucleation (cp. sec. 5.2). The effective field H_{eff} acting on the ANC is given by the superposition of the clocking field H_{clock} and the coupling fields C_i

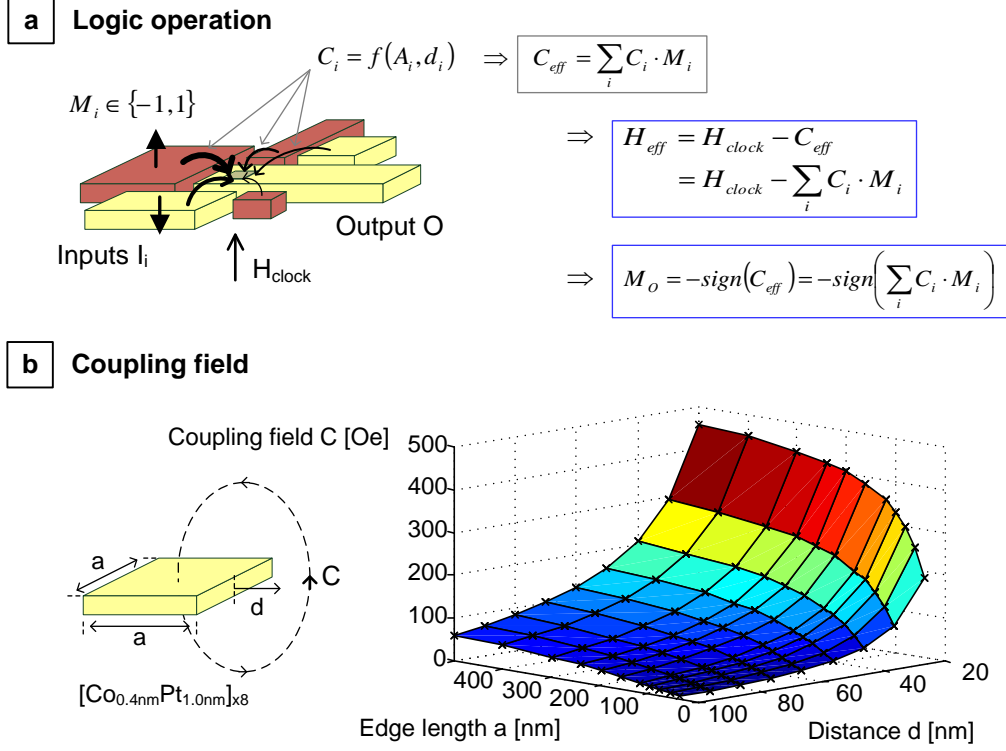


Figure 5.15: Logic operation in pNML by utilizing the interaction of field-coupled magnets. a) The input coupling fields C_i are a nonlinear function of the input size A_i and the distance d_i to the output ANC. This results in an effective coupling field C_{eff} , which enforces or prevents the clocking field-induced DW nucleation at the ANC. b) Simulated coupling field of a squared Co/Pt magnet depending on its edge length a and the distance d . The coupling field scales by $C \propto A^{n_1}/d^{n_2}$ with $A = a^2$, $n_1 \approx 0.2$ and $n_2 \approx 1.4$ according to eq. 5.13.

of the input magnets $i \in \mathbb{N}$ with magnetization $M_i \in \{-1, 1\}$ (Fig. 5.15a):

$$H_{eff} = H_{clock} - \sum_i C_i \cdot M_i. \quad (5.12)$$

Thereby, the coupling field $C_i = f(A_i, d_i)$ of each input magnet is a nonlinear function of the input size A_i (and shape) and its distance d_i to the ANC of the output. It approximately scales by

$$C_i \propto \frac{A_i^{n_1}}{d_i^{n_2}} \quad (5.13)$$

with the geometry-dependent exponents n_1 and n_2 which are in the range of $0 < n_1 \leq 1$ and $1 < n_2 \leq 3$ [SB13d, SB14a]. The exact strength of coupling

field can be determined by numerical finite elements calculations as described in sec. 2.6.

Fig. 5.15b shows the simulation results for a squared $[\text{Co}_{0.4\text{nm}}\text{Pt}_{1.0\text{nm}}]_{\text{x}8}$ magnet depending on the edge length $a = \sqrt{A}$ and the distance d measured from the mid of the edge. The coupling field scales with $C \propto A^{n_1}/d^{n_2}$ with $n_1 \approx 0.2$ and $n_2 \approx 1.4$ for the simulated squared geometry. Even for small magnets $< 100 \cdot 100 \text{ nm}^2$, sufficient coupling $C > 100 \text{ Oe}$ is achieved by reducing the distance to the ANC to $d < 30 \text{ nm}$, which is very desirable in terms of scaling. The coupling field can be further increased by changing the input shape from squared magnets to e.g. fork-like structures for inverters [KBE⁺13a],[177]. In general, it is fair to say that the more 'input material' is as close as possible to the ANC, the higher is the resulting coupling field.

By applying an adequate clocking field amplitude H_{clock} (cp. sec. 5.3), the output magnet is forced to switch to the direction of the superposed clocking fields acting on the ANC:

$$M_{\text{out}} = -\text{sign} \left(\sum_i C_i \cdot M_i \right). \quad (5.14)$$

To ensure distinct switching of the output, the effective coupling field C_{eff} acting on the ANC has to be non-zero:

$$C_{\text{eff}} = \sum_i C_i \cdot M_i \neq 0. \quad (5.15)$$

Additionally, the thermally-induced SFD which reduces the available clocking window has to be taken into account in order to provide reliable switching.

Usually, the layout of the logic gate is chosen to provide equal coupling fields $C_i = C$ for all input magnets. Hence, the output is switched to the antiparallel state compared to the input majority:

$$M_{\text{out}} = -\text{sign} \left(\sum_i M_i \right). \quad (5.16)$$

Here, an odd number of inputs $i \in \{1, 3, 5, \dots\}$ has to be employed in order to ensure a definite output state after clocking. However, equal weights of the input coupling fields is not compulsory, as it opens up new possibilities in the circuit design, e.g. for threshold gate-based circuitry (cp. sec. 7.2).

6 Basic pNML Devices

Logic computing in conventional digital circuits is mostly based on the Boolean operators NOT, NAND and NOR [21]. Thereby, the bistable, computational variable is binary-coded with 0 or 1 depending on its state. For example, in digital CMOS circuits, the voltage levels V_{DD} (high) and V_{SS} (low) are encoded with logic '1' and logic '0'. Such digital circuits perform logic operation in logic gates, which are connected by wires.

Also in pNML, the bistable, perpendicular magnetization direction $M_z = \pm M_s \cdot e_z$ utilized as state variable is binary-coded. A magnetization pointing in negative z-direction is encoded with logic '0', whereas the magnetization in positive z-direction is encoded with a logic '1'. The interaction of the field-coupled nanomagnets is then used to perform Boolean logic operations in pNML devices and circuits.

In principle, logic operation in pNML is performed using two basic logic devices: The inverter structure, which provides the Boolean NOT function, and the majority gate, which provides the universal majority decision that can be programmed to the NAND/NOR functionality. Such pNML logic gates are interconnected by magnetic nanowires to transmit the magnetic signal from one output to the inputs of one or more subsequent gates.

In the following, first the basic logic elements inverter and majority gate will be discussed. Afterwards, magnetic nanowires and fanout structures used as interconnects from gate to gate are introduced.

6.1 Inverter

6.1.1 Basic principle

The inverter basically consists of two antiferromagnetically coupled nanomagnets to invert the signal from the input magnet I to the output magnet O (Fig. 6.1a). A FIB-fabricated ANC at the edge close to the input I sensitizes the output O to the input coupling field C . Depending on the input state, the DW nucleation at the output's ANC is either supported or prevented by the coupling field C . After clocking, the output O is aligned antiparallel to the input I and therefore provides the basic Boolean NOT-function:

$$O = \text{NOT}(I) = \bar{I}. \quad (6.1)$$

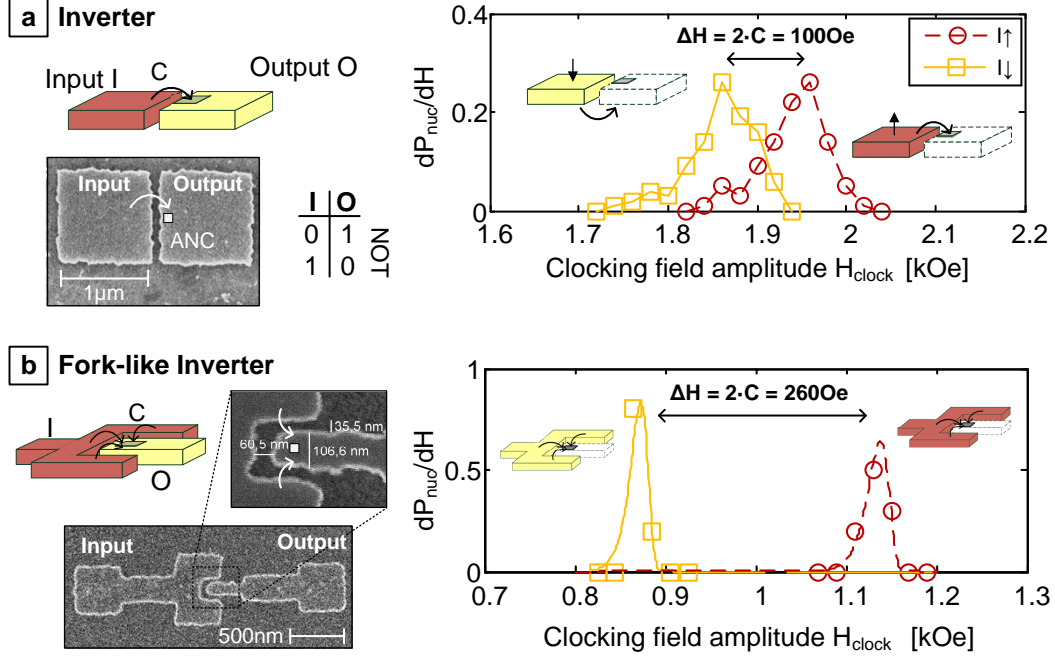


Figure 6.1: Inverter structure and comparison between square magnets and fork-like design. In general, the DW nucleation at the output magnet O is supported or prevented by the input coupling field. Depending on the input state, the nucleation probability density dP_{nuc}/dH is therefore shifted by $\pm C$. The strength of the coupling field is significantly increased by changing the shape from square magnets (a) to a fork-like structure and reducing the distance between the magnets (b).

In a first experiment, we investigated an inverter structure with two field-coupled square magnets according to Fig 6.1a [SB13d]. The size of the $[\text{Co}_{0.4\text{nm}}\text{Pt}_{1.1\text{nm}}]_{\text{x}8}$ magnets is $1 \cdot 1 \mu\text{m}^2$ and the distance between them is about 100 nm. The ANC is about $100 \cdot 100 \text{ nm}^2$ in size and located as close to the edge as possible. Numerical finite-element calculations predict a coupling field of $C = 50 \text{ Oe}$ for the given structure.

In our experiment, we measured the coercivity of the output magnet within 200 hysteresis curves in order to determine its SFD for each input state. Depending on the input I , the output SFD is shifted by $\Delta H = \pm C$ due to the influence of the coupling field C . The measurement results are also shown in Fig. 6.1a. The shift between the two measured SFDs is $\Delta H = 2 \cdot C \approx 100 \text{ Oe}$, which means that the strength of the coupling field is $C \approx 50 \text{ Oe}$ as expected.

However, the two SFDs overlap, which means there is no remaining clocking window with adequate field amplitudes for reliable switching. Hence, significant switching errors may appear during clocking, which has also been identified within

the experiments on an inverter chain with squared magnets by [EBK⁺12].

6.1.2 Improvement of field-interaction

In order to minimize erroneous switching, the two SFDs have to be separated by increasing the input coupling field. Therefore, several options are available:

1. **Increasing the size A** of the input magnet will enhance the coupling field, but also the size of the inverter structure. In addition, the coupling field is only scaled by $C \propto A^{n_1}$ with $n_1 \leq 1$ according to eq. 5.13. Hence, this approach is not sufficient in terms of both scaling and efficiency.
2. **Reducing the distance d** between input magnet and ANC of the output is an adequate instrument to reduce the error rate. According to eq. 5.13, the coupling field scales with $C \propto 1/d^{n_2}$ with $1 < n_2 \leq 3$. Hence, reducing the gap between the magnets is very suitable to increase their interaction. But note, scaling the gap is not trivial, as it requires lithographic improvements in the manufacturing process.
3. **Changing the shape** of the magnets enables to enclose more material of the input magnet around the ANC of the output magnet, which will in turn significantly increase the coupling field strength. Due to the shape-independent anisotropy of the nanomagnets, this is the simplest approach to increase the field-coupling.

So in order to increase the coupling field, both the manufacturing process and the shape of the magnets have to be improved.

In terms of manufacturing, the hard mask fabrication process has been changed from a wet-chemical Cr etching step to Ti evaporation + lift-off as described in sec. 4. Together with an improvement of the FIB lithography parameters (resist thickness, FIB dwell time, development parameters), the minimum distance between the magnets could be reduced from 100 nm to about 25 nm. But note, this does not mean that the coupling is increased by a factor of 4, because the distance to the ANC is decisive for the coupling strength.

The coupling field is further improved by changing the shape of the magnets from square dots to a fork-like structure (Fig. 6.1b). Therefore, the shape of the output magnet is changed to a tapered nanowire with the ANC located right at its tip. The input surrounds the tip of the output in a fork-like shape to enclose the input magnet to the ANC. This idea has also been proposed in [177], but they did not combine this approach with the technique of artificially reducing the anisotropy to control the nucleation site.

In a first experiment, we used a fork-like input magnet with a 200 nm wide output nanowire, which is tapered to 100 nm at the interaction area with the ANC

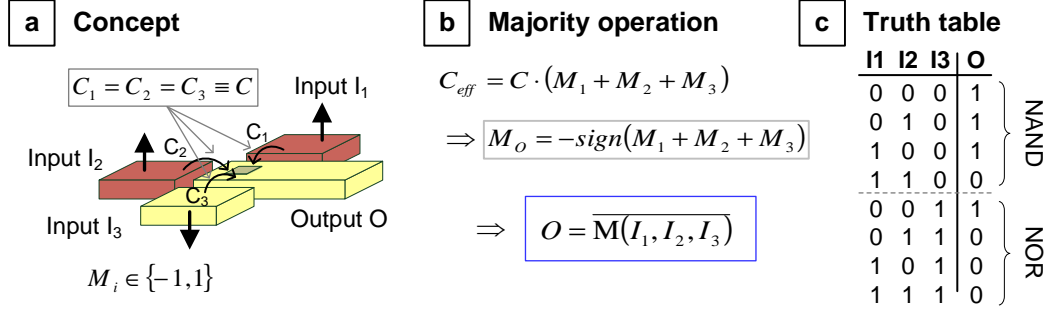


Figure 6.2: Concept of the majority logic gate for pNML. Three inputs $I_{1,2,3}$ with equal coupling fields $C_i = C$ act on the ANC of the output O (a). Due to similar coupling field strengths, the output is ordered antiparallel to the input majority, which is expressed by the majority operator M (b). According to the truth table (c), the majority gate can be programmed to NAND or NOR functionality by fixing e.g. input I_3 .

(Fig. 6.1b). The SFD of the output wire is measured depending on the input state by probing the DW nucleation field during $N = 10$ hysteresis curves. Depending on the state of the input magnet, the nucleation probability density dP_{nuc}/dH is shifted by $C = \pm 130$ Oe. The SFDs are clearly separated and hence, reliable logic operation in the inverter is feasible.

In summary, the enhancements in both the manufacturing process and the design of the magnets have been very successful in order to improve logic operation in pNML devices. For the inverter structures (fork-like versus square magnets inverter) investigated above, the coupling field has been improved by a factor of 2.6. At the same time, the computing area has been reduced by a factor of 8 from $2\mu\text{m}^2$ (2 square magnets) to $\approx 0.25\mu\text{m}^2$ (fork area, cp. Fig. 6.1). In further experiments, reliable signal propagation in an inverter chain using fork-like magnets has been successfully proven [KBE⁺13a].

6.2 Majority gate

The majority gate is the universal computing device for logic operation in NML. Its working principle for perpendicular, field-coupled logic has been introduced in 2002 by [50]. The pNML majority gate contains three input magnets I_1 , I_2 and I_3 with magnetization $M_i \in \{-1, 1\}$ coupled to the output O (Fig. 6.2a).

6.2.1 Concept

The layout of the majority gate is chosen to provide equal input coupling fields $C_1 = C_2 = C_3 \equiv C$ acting on the ANC. According to eq. 5.16, the output is

therefore switched antiparallel compared to the input majority (Fig. 6.2b):

$$M_{out} = -\text{sign}(M_1 + M_2 + M_3). \quad (6.2)$$

The majority logic operation is described by the majority operator \mathbb{M} , given by

$$\mathbb{M}(X_1, \dots, X_i, \dots, X_n) = \begin{cases} 1 & \sum X_i > n/2 \\ 0 & \sum X_i < n/2 \end{cases} \quad (6.3)$$

with $X_i \in \{0, 1\}$ and the odd number of inputs $n = 2k + 1$, $k \in \mathbb{N}$ to prevent undetermined states [Yil10]. For $n = 3$, eq. 6.3 can be rewritten to [178]:

$$\mathbb{M}(X_1, X_2, X_3) = X_1 \cdot X_2 + X_1 \cdot X_3 + X_2 \cdot X_3. \quad (6.4)$$

For a three input majority gate, the logic operation is therefore written by:

$$O = \overline{\mathbb{M}(I_1, I_2, I_3)} = \overline{I_1 \cdot I_2 + I_1 \cdot I_3 + I_2 \cdot I_3}. \quad (6.5)$$

This universal majority decision can be applied to a wide range of applications as will be demonstrated in the following chapter 7.

According to the truth table (Fig. 6.2c), the majority decision can be programmed to the NAND or NOR function by keeping one input at a fixed state [SB12a],[KBE⁺13b]. For example, if the input I_3 is fixed to logic '0', the majority gate operates as NAND gate for the inputs I_1 and I_2 . By contrast, the NOR function of I_1 and I_2 is applied if the input I_3 is kept at logic '1'. Furthermore, the gate may be degraded to an inverter (NOT gate) by fixing two inputs to opposed direction so that their coupling fields cancel each other (e.g. $I_2 = 0$ and $I_3 = 1$). Hence,

$$O = \begin{cases} \text{NAND}(I_1, I_2) & I_3 = 1, \\ \text{NOR}(I_1, I_2) & I_3 = 0, \\ \text{NOT}(I_1) & I_2 \neq I_3. \end{cases} \quad (6.6)$$

6.2.2 Experimental demonstration

The experimental demonstration of the first majority gate with PMA in 2012 is one of the milestones in the development of pNML [SB12a]. Fig. 6.3 shows the lithography mask (b) and the SEM image of the fabricated structure (c). The symmetric geometry provides the required equal coupling fields $C_1 = C_2 = C_3$ in the central area between of the input magnets I_1 , I_2 and I_3 . The output magnet O is extended into this area by a small tip which provides the ANC for DW nucleation.

The majority gate was fabricated from a $[\text{Co}_{0.4\text{nm}}, \text{Pt}_{1.0\text{nm}}]_{\times 8}$ multilayer stack and provides large pads which are required for hysteresis measurements using the

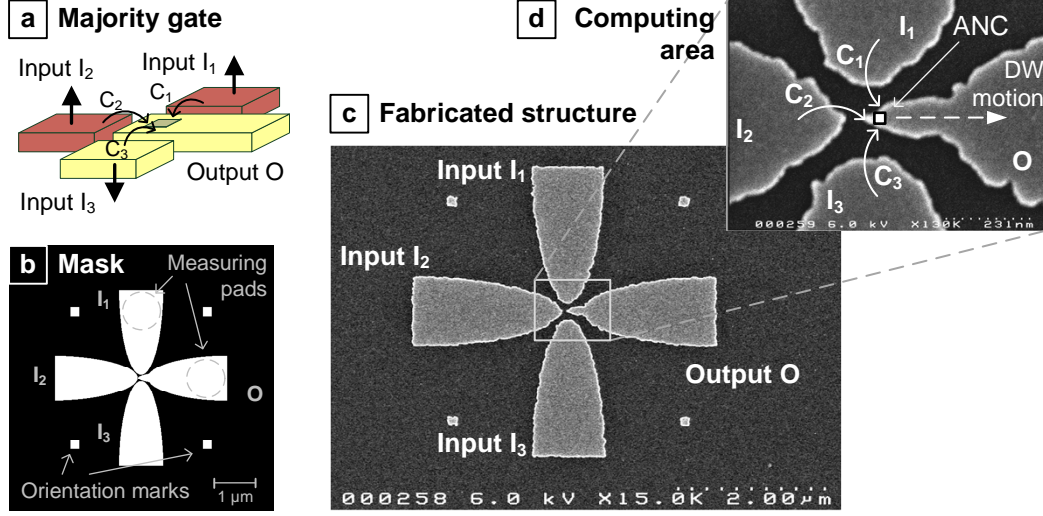


Figure 6.3: Majority gate for perpendicular Nanomagnetic Logic. a) Principle structure b) Mask for lithography process with pads for LMOKE measurements and orientation marks for ANC alignment. c) Fabricated structure showing three inputs I_1 , I_2 and I_3 and the partial irradiated output magnet O . d) Computing area of the majority gate: The DW nucleation at the ANC is influenced by the input coupling fields C_1 , C_2 and C_3 .

LMOKE. Of course, they increase the size of the majority gate, but micromagnetic and numerical simulations show, that only the computing area ($\approx 1 \cdot 1 \mu\text{m}^2$, Fig. 6.3d) is required for logic operation [SB12a]. Small orientation marks enable to accurately locate the ANC at the tip of the output magnet by partial FIB irradiation on an area of $20 \text{ nm} \cdot 20 \text{ nm}$ using a dose of $1 \cdot 10^{14} \text{ ions/cm}^2$. The central position of the ANC ensures equal influence of each input.

In the experiment, the input magnets are set to the desired input configuration $I_1 I_2 I_3$ by externally applied field pulses. Therefore, first the coercivity of the as-grown input magnets was measured by LMOKE to $H_{c,I1} = 4.8 \text{ kOe}$, $H_{c,I2} = 4.9 \text{ kOe}$ and $H_{c,I3} = 5.4 \text{ kOe}$. Consequently, the desired configuration is set by corresponding field pulses with adequate amplitude and, if necessary, verified by MFM. Afterwards, the nucleation field H_{nuc} of the output O is measured by LMOKE hysteresis measurements ($R = 1 \text{ kOe/s}$, $H_{max} = 2 \text{ kOe}$) without affecting the prior set input configuration. In the experiment, $N = 10$ hysteresis curves have been measured and analyzed for each input configuration $I_1 I_2 I_3$ in order to determine the input-dependent nucleation probability $P_{nuc}(I_1 I_2 I_3)$ of the output. Fig. 6.4 shows the measured DW nucleation probability P_{nuc} (6.4a) and the corresponding probability density dP_{nuc}/dH (6.4b) versus the applied clocking field amplitude H_{clock} depending on the input configuration $I_1 I_2 I_3$.

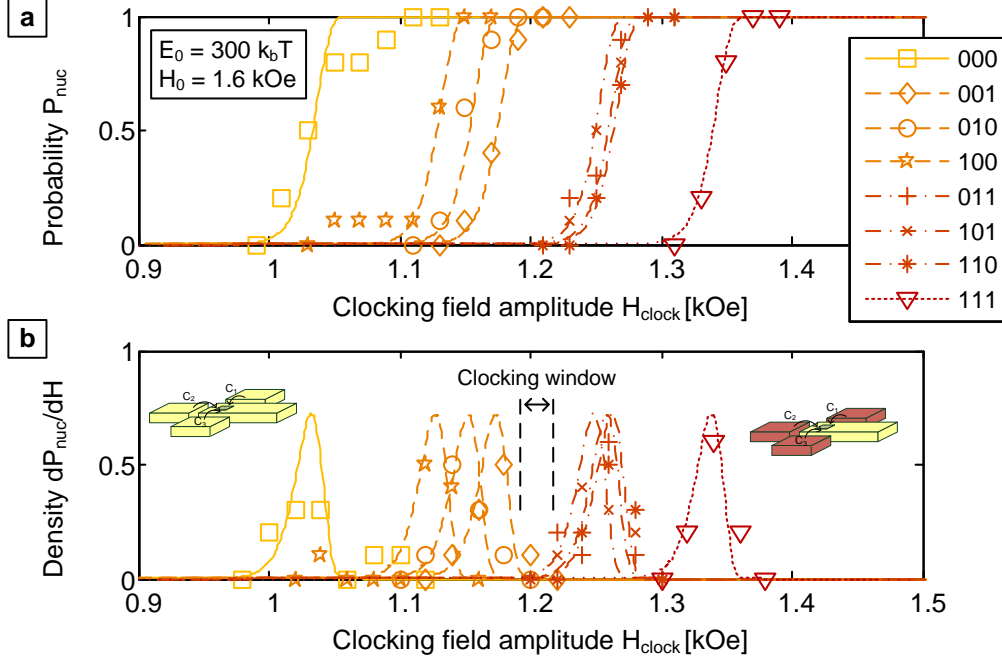


Figure 6.4: Switching characteristics of the pNML majority gate. The DW nucleation probability P_{nuc} (a) and the corresponding probability density dP_{nuc}/dH (b) is shifted depending on the input configuration $I_1I_2I_3$. The calibrated DW nucleation model (lines) is in very good agreement with the experimental results (marker).

Due to the influence of the input coupling fields on the ANC, the DW nucleation is supported or impeded and the corresponding DW nucleation probability (density) is shifted to left or right. Thereby, the effective field acting on the gate's ANC is given by

$$H_{eff} = H_{clock} - (C_1 \cdot M_1 + C_2 \cdot M_2 + C_3 \cdot M_3) = H_{clock} - \underbrace{C \cdot \sum M_i}_{C_{eff}}. \quad (6.7)$$

The nucleation probability model (lines) according to eq. 2.44 matches the measurement results (markers) by using energy barrier parameters $E_0 = 300 \text{ k}_B\text{T}$ and $H_0 = 1.6 \text{ kOe}$, an effective pulse time of $t_{eff} \approx \frac{H_{max}}{2R} = 1 \text{ s}$ and the effective field H_{eff} of eq. 6.7. The virgin output nucleation field $H_{nuc,0}$ for DW nucleation without the influence of any input magnet is calculated (according to [BKB⁺13] and eq. 2.42) to

$$H_{nuc,0} = H_0 \left[1 - \sqrt{\frac{k_B T}{E_0} \ln \left(\frac{f_0 t_{eff}}{\ln 2} \right)} \right] = 1.2 \text{ kOe}. \quad (6.8)$$

Obviously, the measured (and simulated) nucleation probability P_{nuc} (or probability density dP_{nuc}/dH , respectively) can be clearly separated in 4 specifiable areas corresponding to the number of inputs magnetized up or down:

1. For the input configuration 000 all input magnets are in the down state and therefore support the nucleation of the up domain by their coupling fields. Hence, the effective coupling field $C_{eff} = -C_1 - C_2 - C_3 = -3C$ is maximized and the DW nucleation is shifted to $H_{nuc}(000) = 1.03 \text{ kOe} \approx H_{nuc,0} - 3C$.
2. When one input magnet is in the up state (configurations 001, 010, 100), the DW nucleation is shifted to left by only $C_{eff} = -C$ as two coupling fields cancel out each other. The corresponding measured DW nucleation field is $H_{nuc}(001, 010, 100) = 1.15 \text{ kOe} \approx H_{nuc,0} - C$.
3. Two magnets upwards (configurations 011, 101, 110) already induce a positive, effective coupling field $C_{eff} = +C$ which increases the DW nucleation field to $H_{nuc}(011, 101, 110) = 1.26 \text{ kOe} \approx H_{nuc,0} + C$.
4. Finally, when all magnets are in the up state (111), the DW nucleation is maximally impeded by $C_{eff} = +3C$ and the corresponding DW nucleation field is shifted to $H_{nuc}(111) = 1.34 \text{ kOe} \approx H_{nuc,0} + 3C$.

Naturally, the classification in those 4 areas is only possible if similar coupling fields $C_1 \approx C_2 \approx C_3$ are provided by the majority gate.

The adequate amplitude of the clocking field in order to switch the output magnet antiparallel to the input majority is estimated from Fig. 6.4b to $H_{clock} = 1.2 \text{ kOe}$, which is of course equal to the calculated virgin DW nucleation field $H_{nuc,0}$. The detailed calculation of each coupling field C_i and the favorable clocking field amplitude H_{clock} is shown in the following section.

The remaining clocking window ($\approx 20 \text{ Oe}$) identified in Fig. 6.4b enables error free logic operation of the majority gate. Fig. 6.5 shows an AFM image (a) and the measured MFM images of the majority gate after clocking (b) by using the designated clocking field amplitude H_{clock} . The output magnet is ordered in the correct state antiparallel to the input majority for all input configurations $I_1 I_2 I_3$. Due to the reversal mechanism of propagating DWs, the output of the majority gate can be connected to inputs of subsequent devices by using magnetic interconnects (sec. 6.3), which is crucial for the necessary concatenation of logic devices (cp. sec. 1.1.1). In summary, the results prove correct logic operation and experimentally demonstrate the functionality of the pNML majority gate.

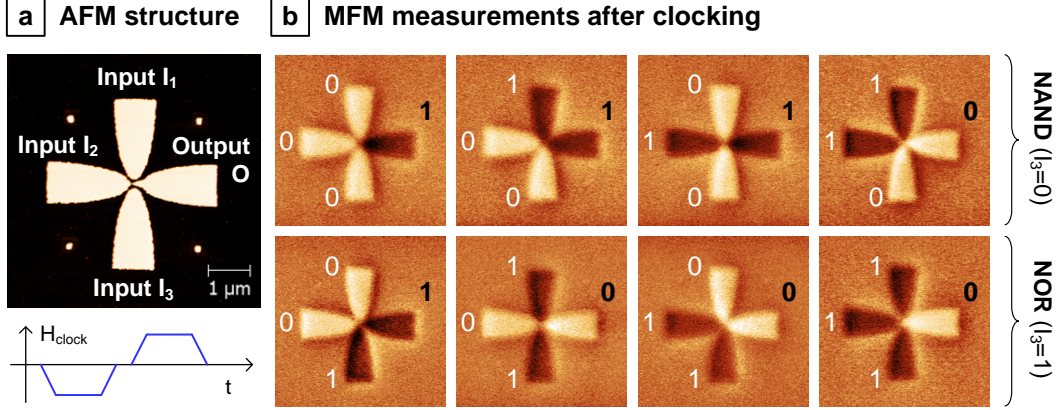


Figure 6.5: Experimental demonstration of the majority gate. a) Structure of the gate measured by AFM. b) MFM images showing the magnetization state of the clocked majority gate. For each input configuration, the output magnet is aligned antiparallel to the input majority [SB12a].

6.2.3 Advanced calculations

Clocking field amplitude

The measured DW nucleation probability functions can be used to calculate the most suitable clocking field amplitude as well as the exact coupling field of each input. Therefore, the DW nucleation field $H_{nuc}(I_1 I_2 I_3)$ of each input configuration is defined as the field needed for the nucleation probability $P_{nuc}(I_1 I_2 I_3) = 0.5$ according to eq. 2.42:

$$H_{nuc}(I_1 I_2 I_3) = H_{clock}|_{(P_{nuc}(I_1 I_2 I_3)=0.5)}. \quad (6.9)$$

Tab. 6.1 shows the measured DW nucleation fields $H_{nuc}(I_1 I_2 I_3)$ for both magnetization changes from up to down ($1 \rightarrow 0$) and from down to up ($0 \rightarrow 1$)¹. According to eq. 6.7, the DW nucleation field for a given input configuration is given by the virgin nucleation field $H_{nuc,0}$, which is modified by the superposing coupling fields:

$$H_{nuc}(I_1 I_2 I_3) = H_{nuc,0} - (C_1 \cdot M_1 + C_2 \cdot M_2 + C_3 \cdot M_3). \quad (6.10)$$

Accordingly, the overall mean of all eight measured positive or negative DW nucleation fields $\pm H_{nuc}(I_1 I_2 I_3)$ gives the pure DW nucleation field, which is in turn (according to eqn. 6.10 and 6.9 by using $M_i = 0$) also the optimal clocking field amplitude:

$$\pm H_{clock,opt} = \pm H_{nuc,0} = \frac{1}{8} \sum \pm H_{nuc}(I_1 I_2 I_3) = \dots = \pm 1.2 \text{ kOe}. \quad (6.11)$$

¹Please note, the measured values slightly differ from [SB12a] due to the different analysis method (nucleation probability model vs. mean of SFD)

Input configuration			Output characteristics		
I_1	I_2	I_3	$H_{nuc}(1 \rightarrow 0)$	$H_{nuc}(0 \rightarrow 1)$	Clocked state
0	0	0	−1.34 kOe	1.03 kOe	1
0	0	1	−1.26 kOe	1.17 kOe	1
0	1	0	−1.27 kOe	1.15 kOe	1
1	0	0	−1.26 kOe	1.13 kOe	1
0	1	1	−1.15 kOe	1.26 kOe	0
1	0	1	−1.15 kOe	1.25 kOe	0
1	1	0	−1.16 kOe	1.26 kOe	0
1	1	1	−1.05 kOe	1.34 kOe	0
Clocking field amplitude:			−1.2 kOe	1.2 kOe	

Table 6.1: Measured DW nucleation field H_{nuc} of the majority gate depending on the input configuration.

The result is equal to the virgin nucleation field calculated with the Sharrock model in eq. 6.8. Hence, this is the most favorable clocking field amplitude in order to switch the output to the antiparallel state compared to the input majority.

Coupling fields

Furthermore, also the coupling field strength C_i of each input I_i can be calculated from the experimentally determined DW nucleation fields $H_{nuc}(I_1 I_2 I_3)$ [SB12a, EBZ⁺14]. Due to the influence of the coupling field C_i , the DW nucleation is shifted by $\pm C_i$. Hence, the difference between the mean of the nucleation fields $\overline{H_{nuc}}(I_i = 1)$, where the corresponding input I_i is up and the mean $\overline{H_{nuc}}(I_i = 0)$, where I_i is down, is two times the coupling field according to eq. 6.10:

$$C_i = \frac{1}{2} [\overline{H_{nuc}}(I_i = 1) - \overline{H_{nuc}}(I_i = 0)] \quad (6.12)$$

$$= \frac{1}{8} \left[\sum H_{nuc}(I_i = 1) - \sum H_{nuc}(I_i = 0) \right]. \quad (6.13)$$

By using both the negative and positive measured nucleation fields of Tab. 6.1 and averaging the results, the coupling fields are calculated to $C_1 = 48$ Oe, $C_2 = 50$ Oe and $C_3 = 54$ Oe for the inputs I_1 , I_2 and I_3 , respectively. The calculated coupling fields are slightly different among each other, which may depend on the minor

number of measured hysteresis loops per configuration ($N = 10$), or on a small misalignment of the ANC during fabrication as discussed below. However, the coupling fields are in an adequate range and error free operation is achievable as shown in the experiment.

Margins for correct operation

As previously discussed in sec. 5.4, the coupling field drops over distance with $C \propto 1/d^{n_2}$ and a misalignment of the ANC would therefore degrade the functionality of the majority gate. For example, a misalignment in the direction to I_3 will increase the coupling field C_3 and at the same time reduce C_1 of input I_1 . Accordingly, the required shift of the DW nucleation probability in order to provide the clocking window is reduced for certain input configurations. Hence, the corresponding SFDs may overlap and the operational reliability of the gate is decreased.

In order to define the margins for the ANC alignment, the area of the output magnet, where an appropriate clocking window is provided by the input coupling fields, has to be determined. Therefore, primarily the geometry of the computing area of the majority gate is extracted from the lithography mask of the manufacturing process (Fig. 6.6a).

Afterwards, the corresponding input coupling fields $C_i(x, y)$ are simulated by numerical finite element calculations as described in sec. 2.6.2. Then, the effective coupling field is calculated for each input configuration $I_1I_2I_3$:

$$C_{eff}^{I_1I_2I_3}(x, y) = C_1(x, y) \cdot M_1 + C_2(x, y) \cdot M_2 + C_3(x, y) \cdot M_3. \quad (6.14)$$

The area of proper ANC positioning and the corresponding clocking window margin ΔH_{clock} are then determined by evaluating the sign and the strength of the effective coupling field $C_{eff}^{I_1I_2I_3}(x, y)$. The overlap of all computed areas within the output magnet area for each input configuration finally gives the area of proper ANC positioning for different remaining clocking margins.

Fig. 6.6b shows the simulation results for the clocking window margin ΔH_{clock} depending on the misalignment $(\Delta x_{ANC}, \Delta y_{ANC})$ of the ANC from the favored position where $C_1(x, y) = C_2(x, y) = C_3(x, y)$. Note, that these calculations do not include the reduction of the clocking window due to the thermally induced SFD. Additionally, the size of the ANC itself has to be considered.

An adequate clocking window is therefore only assured as long as the misalignment of the ANC is below $\Delta x_{ANC}, \Delta y_{ANC} < 10 \text{ nm}$. Further Monte-Carlo simulations show, that the error rate for logic computation significantly increases with decreasing accuracy of the ANC alignment [SB12a].

However, a mask alignment accuracy less than 10 nm is technically feasible in common manufacturing technology provided by modern semiconductor facilities.

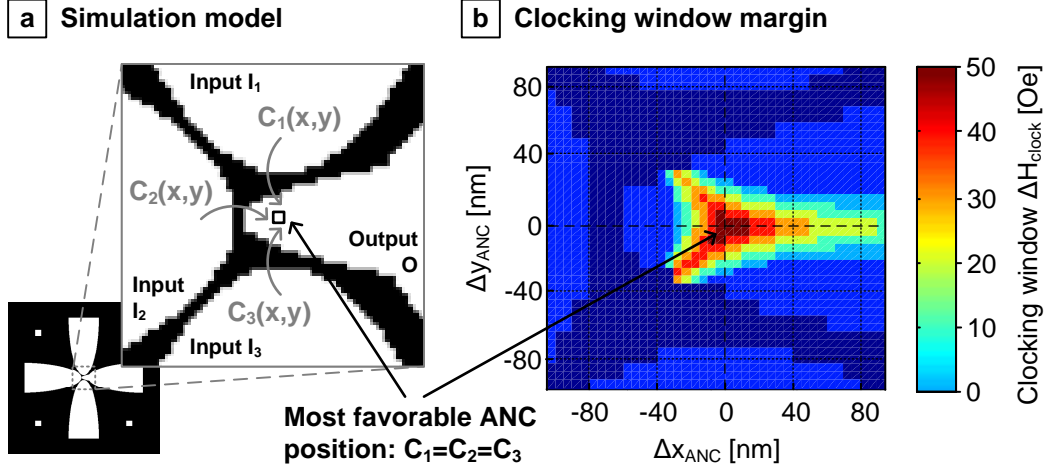


Figure 6.6: Margins for correct logic operation of the majority gate. a) Simulation model for coupling field calculations extracted from the lithography mask. b) Correct operation of the majority gate significantly depends on the location of the ANC. Small misalignments from the ideal position ($C_1 = C_2 = C_3$) dramatically reduce the remaining clocking window ΔH_{clock} (simulated without thermal noise).

6.3 Magnetic interconnects

Usually, multiple logic gates (inverters and majority gates) are linked and combined into a logic unit which provides specific arithmetic functions, such as adders or XOR gates. Therefore, both the logic gates within a logic unit as well as several logic units have to be interconnected with each other. Until now, circuits in NML usually used inverter chains to "transport" magnetic information (Fig. 6.7). But obviously, inverter chains made of several field-coupled nanomagnets are very insufficient in terms of area, speed and operational reliability [SB11c],[90]. By contrast, pNML provides a very efficient way of signal propagation between logic gates/units via magnetic nanowires, which have been introduced during this work for the first time [Lun11].

6.3.1 Magnetic nanowires

Due to the shape-independent anisotropy of the pNML magnets, magnetic nanowires are highly suitable to interconnect multiple logic gates/units with each other in pNML circuits. Therefore, the output of one logic gate is elongated and connected with one (or more) input(s) of subsequent logic gates (Fig. 6.7a).

Once the DW is nucleated at the ANC in the previous gate, the magnetic DW is driven through the nanowire by the applied clocking field to set the input of the

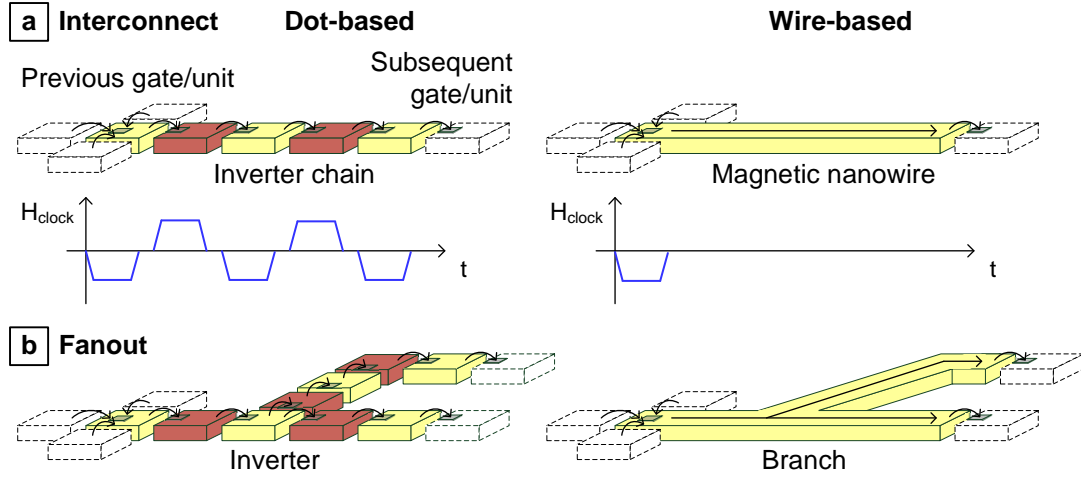


Figure 6.7: Magnetic interconnects in pNML circuitry. a) Dot-based interconnects use inverter chains to transport information between logic gates/units. Thereby, the magnetic signal is transported through the chain according to the applied clocking field. Wire-based interconnects use elongated nanowires to propagate DWs within only one clocking pulse. b) Fanout structures provide the signal from the output of one logic gate for two or more inputs of subsequent gates/units. Here, branches are applied to split propagating DWs for two (or more) nanowires.

subsequent gate. Thereby, the edge roughness, the length of the nanowire and the speed of the propagating DW are the most important design parameters.

Influence of edge roughness

Ideally, there is no effect of the width of the nanowire on the DW motion. But, as already mentioned in sec. 2.3.4, considerable edge roughness of the nanowire provides pinning sites with a specific pinning potential for the propagating DWs [143] (Fig. 6.8a). Therefore, the DW propagation field is significantly increased according to eq. 2.32:

$$H_{\text{wire}} = H_{\text{int}} + \frac{\sigma_w \sin \alpha}{2M_s h_{\text{wire}}}. \quad (6.15)$$

However, as long as the wire depinning field H_{wire} is well below the DW nucleation field H_{nuc} of the corresponding logic gate, the pinning effect vanishes and the DW propagates unimpeded through the nanowire. But, with an decreasing nanowire width h_{wire} , the wire depinning field increases significantly and therefore the required field to propagate the DW to the output of the nanowire:

$$H_{\text{out}} = \max(H_{\text{nuc}}, H_{\text{wire}}). \quad (6.16)$$

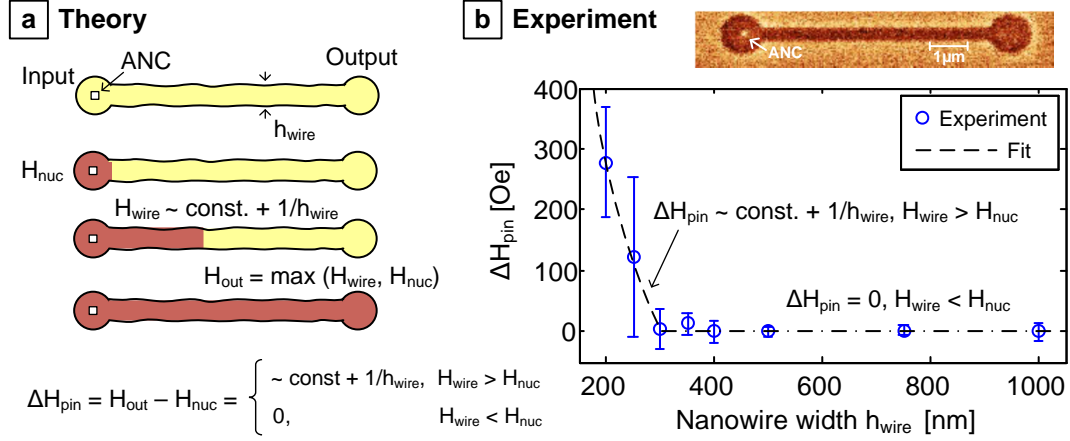


Figure 6.8: Theory and experiment on the DW motion in magnetic nanowires. a) The DW is nucleated at the ANC and propagates through the nanowire. Due to edge roughness, the DW may get pinned by the depinning field $H_{wire} \propto \text{const.} + 1/h_{wire}$. The output switching field H_{out} is therefore the maximum of nucleation and depinning field. b) In the experiment, the difference ΔH_{pin} between nucleation field H_{nuc} and output field H_{out} is measured depending on the nanowire width ($N = 4$, errorbars = standard deviation).

In our experiment, we measured the difference $\Delta H_{pin} = H_{out} - H_{nuc}$ between the output field H_{out} and the DW nucleation field H_{nuc} for various $[\text{Co}_{0.4}\text{nmPt}_{1.1}\text{nm}]_{\times 5}$ nanowires. The nanowires fabricated using a chemical wet etching process to structure the Cr hard mask show significant edge roughness along the nanowires. Depending on the width of the nanowire h_{wire} , either the nucleation field H_{nuc} or the wire depinning field H_{wire} dominates the output field. According to eq. 6.16, the measured difference between input and output is

$$\Delta H_{pin} = \begin{cases} H_{wire} - H_{nuc}, & H_{wire} \geq H_{nuc} \\ 0, & H_{wire} < H_{nuc} \end{cases} \quad (6.17)$$

$$= \begin{cases} H_{int} - H_{nuc} + \frac{\sigma_w \sin \alpha}{2M_s h_{wire}} \propto \text{const.} + \frac{1}{h_{wire}}, & H_{wire} \geq H_{nuc} \\ 0, & H_{wire} < H_{nuc} \end{cases} \quad (6.18)$$

Fig. 6.8b shows the measurement results for nanowires with varying widths of $h_{wire} = 200 \text{ nm} \dots 1000 \text{ nm}$ and $N = 4$ wires per width. The DW propagates unimpeded through the nanowires as long as its width is above 300 nm. For smaller nanowires, the wire depinning field caused by edge roughness increases according to eq. 6.15 and a significant difference ΔH_{pin} is measurable.

By contrast, no relevant effect of the curvature radius in bended nanowires has been identified, which means that even sharp turns are applicable [Lun11].

However, by changing the fabrication process from a wet-chemical Cr etching step to Ti evaporation + lift-off as described in sec. 4, also the edge roughness is decreased remarkably and unimpeded DW propagation is provided also in only 100 nm wide nanowires.

Timing

According to eq. 5.1, the propagation time $t_{prop} = l_{wire}/v_{DW}$ corresponding to the length of the nanowire (magnet) l_{wire} determines the minimum clocking pulse time $t_{clock} = t_{nuc} + t_{prop}$. Due to the homogeneous clocking field, the maximum clocking frequency of the whole logic circuit is given by $f_{max} = 1/2t_{clock}$. If the length of the nanowire exceeds the maximum length which is reversible with desired clocking frequency, the insertion of several (N) inverters in the interconnecting nanowire is advisable. But of course, this will also delay the signal transportation through the interconnect by $N/2$ clocking cycles.

However, this may also be favored when magnetic signals have to be delayed, e.g. in terms of signal synchronization within or between logic units. Additionally, the field-driven DW motion in the interconnecting nanowires can be used for signal routing by so-called DW gates, which enable the synchronization and buffering of magnetic signals in pNML circuits (see sec. 8.3).

6.3.2 Fanout structures

Fanout structures are used to provide the signal from the output of one logic gate for two or more inputs of subsequent gates or readout devices. Generally, such structures are essential for the signal routing in any complex logic circuit. In in-plane NML, the signal from an inverter chain for signal transmission is therefore decoupled by further dots [179]. Also in NML with perpendicular anisotropy, signals have been branched by decoupling through additional magnets [63].

However, the application of magnetic nanowires as interconnects opens up a simple, but very efficient method to split the signal information. Branches integrated in the interconnecting nanowires split a propagating, incoming DW into two (or more) independent DWs, which in turn propagate to subsequent structures through continuing nanowires (Fig. 6.9a). Obviously, this approach is very efficient in terms of area and speed, as the DW is split and propagated during one single clocking field pulse.

However, one detail to be considered is the potential depinning field from the branch H_{branch} . Naturally, branches in magnetic nanowires are geometric deformations which constitute a specific pinning potential. In order to split the DW in the branch, first the length of the DW is increased which in turn increases the corresponding DW energy E_{DW} according to eq. 2.31. Hence, the depinning field

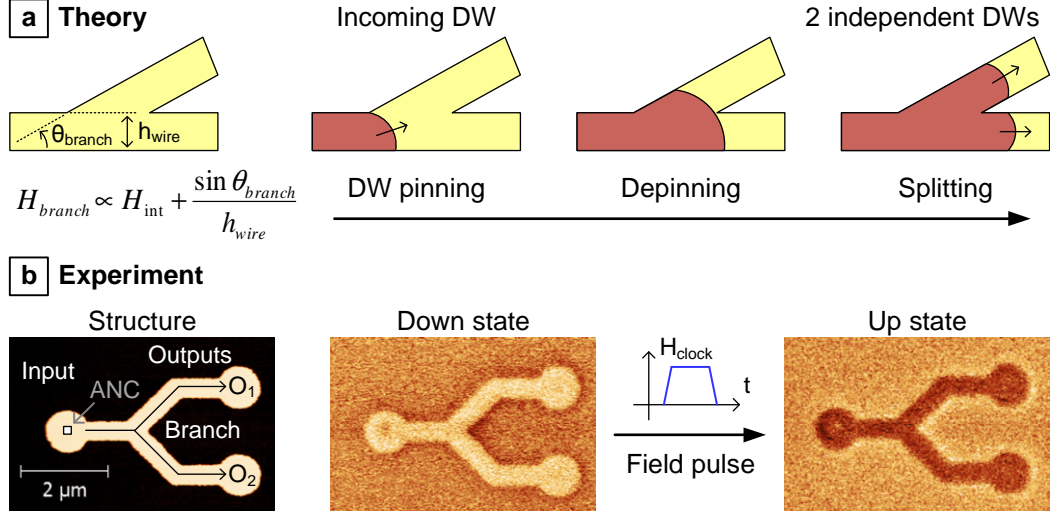


Figure 6.9: Theory and experimental demonstration of a fanout structure. a) The incoming DW is pinned at the branch by the depinning field H_{branch} . After depinning, the DW is split into two independent DWs which in the following propagate through the subsequent nanowires. b) In the experiment, the DW is nucleated at the ANC of the input side. After one single field pulse, the DW is nucleated and propagates through the entire structure without pinning.

H_{branch} corresponds to the depinning field from a notch according to eq. 2.32:

$$H_{branch} = H_{int} + \frac{\sigma_w \sin \theta_{branch}}{2M_s h_{wire}} \quad (6.19)$$

with the apex angle of the branch in the nanowire θ_{branch} and the wire width h_{wire} . Obviously, the depinning field in the fanout structure can be designed by the geometry of the branch according to eq. 6.19. However, usually the branch depinning field H_{branch} is negligible as it is well below the DW nucleation field H_{nuc} at the ANC.

In the experiment (Fig. 6.9b), a fanout structure with one input and two output nanowires (width $h_{wire} = 500 \text{ nm}$) made of a $[\text{Co}_{0.4\text{nm}}\text{Pt}_{1.1\text{nm}}]_{\times 5}$ multilayer stack has been fabricated [SB12b]. The input side is partially irradiated with a dose of $1 \cdot 10^{14} \text{ ions/cm}^2$ in order to determine the DW nucleation site. Small pads are used to measure the switching field at both input and output wires by LMOKE. Hysteresis measurements show a nucleation for DW injection at the input side of $H_{nuc} = 930 \text{ Oe}$ and switching fields of the output nanowires of $H_{c,O1} = 940 \text{ Oe}$ and $H_{c,O2} = 943 \text{ Oe}$, respectively [SB12b]. They match very well the nucleation field $H_{nuc} \approx H_{c,O1} \approx H_{c,O2}$, which indicates unimpeded DW propagation through the branch and therefore $H_{branch} < H_{nuc}$.

In a second experiment, we first saturated the fanout to the down state and afterwards applied one single 10 ms field pulse with $H_{clock} = 1$ kOe amplitude. MFM measurements show, that the DW nucleates at the input and propagates through the entire structure without pinning.

Further measurements on several structures with various nanowire widths and geometries confirm the results [Lun11]. Hence, the application of magnetic nanowires as interconnects and fanouts is favorable for pNML circuitry.

7 pNML Circuitry

The fundamentals and basic pNML devices, which were presented and demonstrated in the previous sections 5 and 6, enable the implementation of complex nonvolatile logic circuits based on field-coupled nanomagnets. Most CMOS logic circuits are based on the conventional boolean operations (NOT, NAND, NOR), which of course may be directly implemented in pNML by inverter structures and majority gate programmed to NAND or NOR.

However, the majority gate provides much more logic functionality by using the universal majority decision. Therefore, both the functional analysis of logic operations as well as the layout synthesis for majority-based logic is required. This enables to dramatically reduce the circuit complexity and hence improve logic circuits in terms of area, speed and power.

In the following sections, first a 1-bit full adder circuit based on basic pNML devices is presented and logic operation is experimentally demonstrated. Second, majority gates are extended to threshold gates by weighting the input coupling fields due to size and distance of the input magnets. This enables to even more reduce the circuit complexity and therefore further improve area, speed and power, as will be shown for the 1-bit full adder circuit.

7.1 1-bit full adder

The 1-bit full adder is one of the standard logic circuits used to demonstrate and benchmark logic operation of emerging devices [21]. Hence, the demonstration of the 1-bit full adder function is one of the milestones for beyond-CMOS devices and therefore also used to demonstrate the feasibility of pNML circuitry.

7.1.1 Signal analysis and model synthesis

The implementation of the 1-bit full adder circuit for field-coupled computing goes back to the first implementations investigated for QCA [178]. There, the full adder circuit using the majority operator for the first time was implemented in QCA, which is in a way the "ancestor" of pNML. Fig. 7.1a shows their published schematic, where they used 5 majority gates and 3 inverters connected by chains of QCA cells, which is in a sense the application of the standard 1-bit full adder

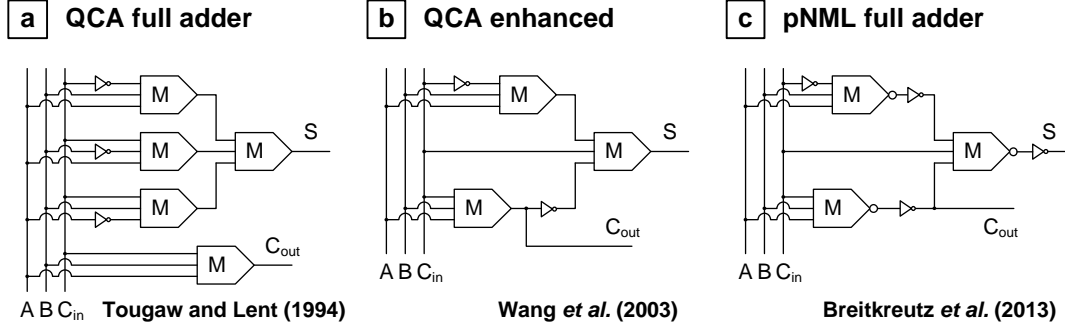


Figure 7.1: Schematics of majority logic gate-based 1-bit full adder circuits. a) Original schematics published by [178] for QCA using 5 majority gates and 3 inverters. b) Enhanced QCA design by [180] with only 3 gates and 2 inverters. c) Full adder schematics of Wang *et al.* [180] adapted to pNML by [SB13b] using 3 inverting pNML majority gates and 4 inverters.

operation based on $\text{NOT}(\bar{X})$, $\text{AND}(\cdot)$ and $\text{OR}(+)$ operations:

$$S = A \cdot B \cdot C_{in} + \bar{A} \cdot \bar{B} \cdot C_{in} + \bar{A} \cdot B \cdot \bar{C}_{in} + A \cdot \bar{B} \cdot \bar{C}_{in} \quad (7.1)$$

$$= \mathbb{M} [\mathbb{M} (\bar{A}, B, C_{in}), \mathbb{M} (A, \bar{B}, C_{in}), \mathbb{M} (A, B, \bar{C}_{in})], \quad (7.2)$$

$$C_{out} = A \cdot B + A \cdot C_{in} + B \cdot C_{in} \quad (7.3)$$

$$= \mathbb{M} (A, B, C_{in}) \quad (7.4)$$

with the inputs A , B and carry-in $C_{in} \in \{0, 1\}$, the output bits sum S and carry-out C_{out} .

The full adder design of Tougaw and Lent [178] has been further developed by Wang *et al.* [180], who transformed the QCA addition algorithm to:

$$S = \mathbb{M} [\bar{C}_{out}, C_{in}, \mathbb{M} (A, B, \bar{C}_{in})], \quad (7.5)$$

$$C_{out} = \mathbb{M} (A, B, C_{in}). \quad (7.6)$$

Accordingly, their proposed adder design features only 3 majority gates and 2 inverters (Fig. 7.1b). In comparison to standard CMOS circuits, which use – depending on the implementation form – about 28 transistors for the full adder operation [181], this impressively demonstrates the benefit of the universal majority decision for logic circuitry. The first iNML implementation of the full adder design of Wang *et al.* was shown by [182], but however, error free operation could not be proven due to the sensibility of iNML to fabrication variations and thermal noise [90].

Majority gates in pNML generally switch the output **antiparallel** to the input majority due to the antiferromagnetic coupling between the magnets:

$$O = \overline{\mathbb{M}} (I_1, I_2, I_3) \equiv \overline{\mathbb{M}} (I_1, I_2, I_3). \quad (7.7)$$

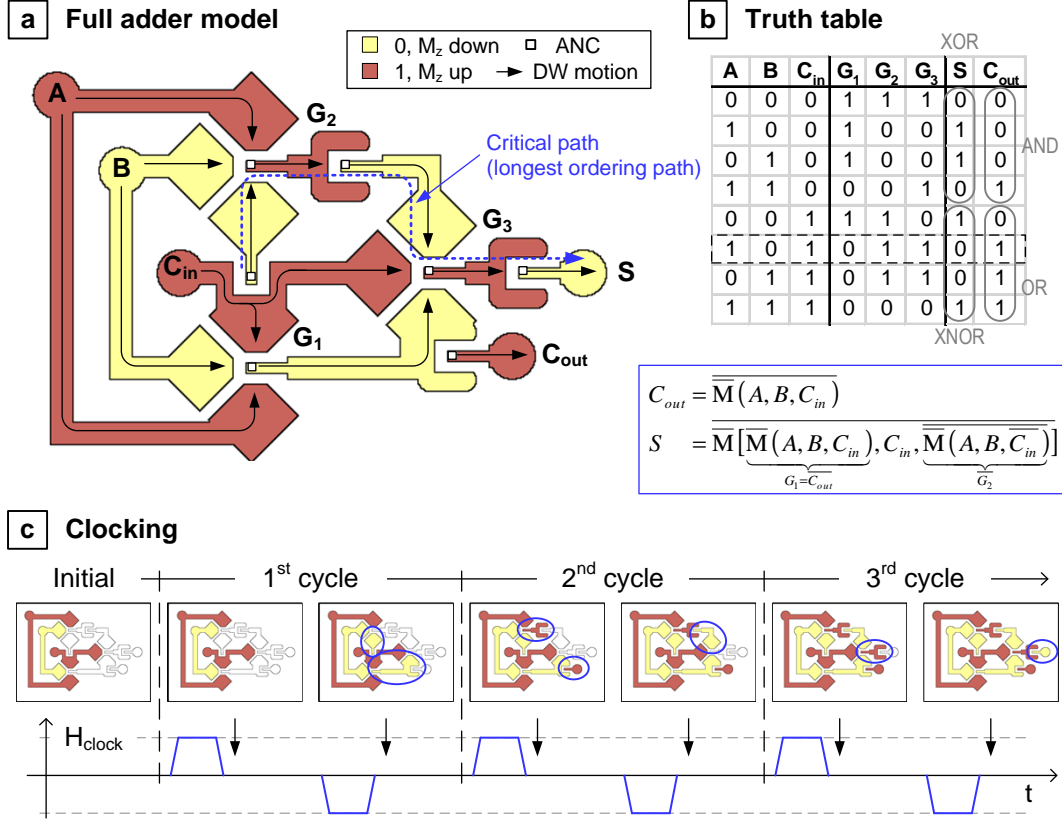


Figure 7.2: Model of the pNML 1-bit full adder circuit. a) Layout based on the schematics of Fig. 7.1c using 3 majority gates and 4 inverters. b) Corresponding truth table and logic function based on pNML majority gates. c) The magnets are ordered stepwise according to the alternating clocking field.

Of course, this implies additional inverters and changes in the design of the 3-gate adder of Wang *et al.* for the implementation in pNML. More precisely, the output of each majority gate needs to be additionally inverted, but the inverter for the computation of $\overline{C_{out}}$ becomes redundant (Fig. 7.1c). In summary, 3 majority gates and 4 inverters are required for the pNML full adder [Yil10, Hil12], [SB13b]:

$$S = \overline{M}[\overline{M}(A, B, C_{in}), C_{in}, \overline{M}(A, B, \overline{C_{in}})], \quad (7.8)$$

$$C_{out} = \overline{M}(A, B, C_{in}). \quad (7.9)$$

Fig. 7.2a shows the corresponding layout of the full adder circuit with input magnets A , B and carry-in C_{in} and the output magnets sum S and carry-out C_{out} . The majority gates and inverter devices are interconnected by magnetic nanowires.

7.1.2 Signal propagation and clocking

According to the truth table (Fig. 7.2b), the carry-in C_{in} programs the majority gate G_1 to $G_1(C_{in} = 0) = \text{NAND}(A, B)$ or $G_1(C_{in} = 1) = \text{NOR}(A, B)$ in order to compute the carry-out C_{out} by an additional inverter. Here, the great benefit of the universal majority decision is applied for calculation of C_{out} .

The sum is $S(C_{in} = 0) = \text{XOR}(A, B)$ and $S(C_{in} = 1) = \text{XNOR}(A, B)$. It is computed by the inverted NAND/NOR function of the negated carry-out $\overline{C_{out}} = G_1$ and the inverted majority of $\mathbb{M}(A, B, \overline{C_{in}}) = G_2$. Here, the NAND or NOR functionality is again programmed by the carry-in C_{in} .

Logic operation is provided by applying an alternating clocking field with adequate amplitude. Here, the magnets are ordered stepwise according to the clocking field [EBK⁺12, KBE⁺13a],[SB13b].

Correct ordering of the first computing magnet G_1 and $\overline{C_{in}}$ requires one full clocking cycle, as their final state depends on the input configuration of A , B and C_{in} . Afterwards, the signal propagates by 2 magnets per cycle [28]. The critical path (longest ordering path) of the investigated full adder structure is $N_{path} = 5$ magnets long, which means that correct computation of sum S and carry-out C_{out} is only assured after $N_{clock} = \frac{N_{path}+1}{2} = 3$ clocking cycles.

Thereby, the signal propagation in the full adder is as follows (Fig. 7.2c):

- During the first clocking cycle, the output of the gate G_1 and the inverted carry-in $\overline{C_{in}}$ required for the computation of G_2 are set to their desired state.
- The second clocking cycle sets the carry-out C_{out} and both the gate G_2 and its negation $\overline{G_2}$. Only now, the correct state of all inputs of gate G_3 required for the computation of the sum S is guaranteed.
- Finally, the third cycle sets the output of G_3 as well as the following inverter to compute the sum S .

Meanwhile, magnets which are not just yet finally computed, may flip a number of times during clocking, whereas already ordered magnets must not switch in order to provide correct logic operation. Note, the sum S and the carry-out C_{out} may serve as input magnets for subsequent logic units. Clocking experiments on the fabricated full adder circuit have shown, that especially the sum flips several times during the first 2 clocking cycles. Hence, some sort of signal buffering is required in more complex circuits to provide constant inputs for interconnected logic units, as will be discussed in sec. 8.2.

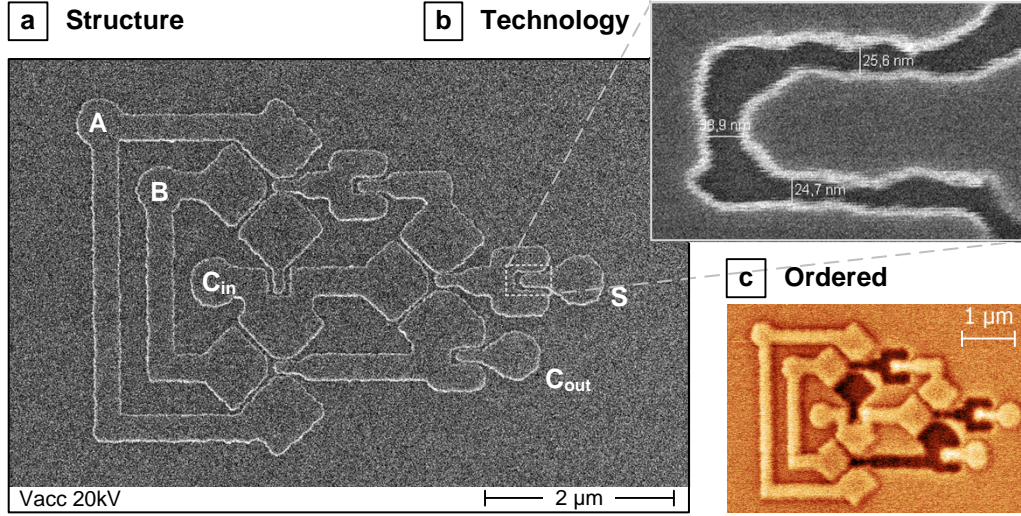


Figure 7.3: 1-bit full adder circuit fabricated in the experiments. a) SEM image of the fabricated structure. b) The gap between the magnets is about 25...40 nm. c) MFM image showing the correctly ordered magnetization states of the demagnetized structure.

7.1.3 Experiment

Structure

Fig. 7.3a shows a SEM image of the fabricated structure, which is based on the pNML full adder model of Fig. 7.2a [SB13b]. The 200 nm wide $[\text{Co}_{0.8\text{nm}}\text{Pt}_{1.0\text{nm}}]_{\times 4}$ magnets are fabricated as described in sec. 4 (ANCs: $60 \cdot 60 \text{ nm}^2$, $2.8 \cdot 10^{13} \frac{\text{ions}}{\text{cm}^2}$). The size of the full structure is about $5 \cdot 3.4 \mu\text{m}^2$, the gap between the magnets is approximately 25...40 nm (Fig. 7.3b).

Method

The non-irradiated input magnets A , B and carry-in C_{in} are switched by high external fields around 3 kOe in order to set the desired input configuration. The mean DW nucleation at the ANC of the irradiated computing magnets is at about 560 Oe, which is also the amplitude of the clocking field. Measurements are performed with MFM, the 3D field module generates clocking field pulses in the $t_{\text{clock}} = 100 \text{ ms}$ range.

Fig. 7.4a shows the clocking scheme and the corresponding signal propagation through the circuit to demonstrate the functionality of the full adder. Before applying the clocking field, first the input magnets A , B and carry-in C_{in} are set by initial field pulses to the desired input configuration. The computing magnets are set to the up state by a positive pulse of $H_{\text{clock}} = 1 \text{ kOe}$ (init), and afterwards

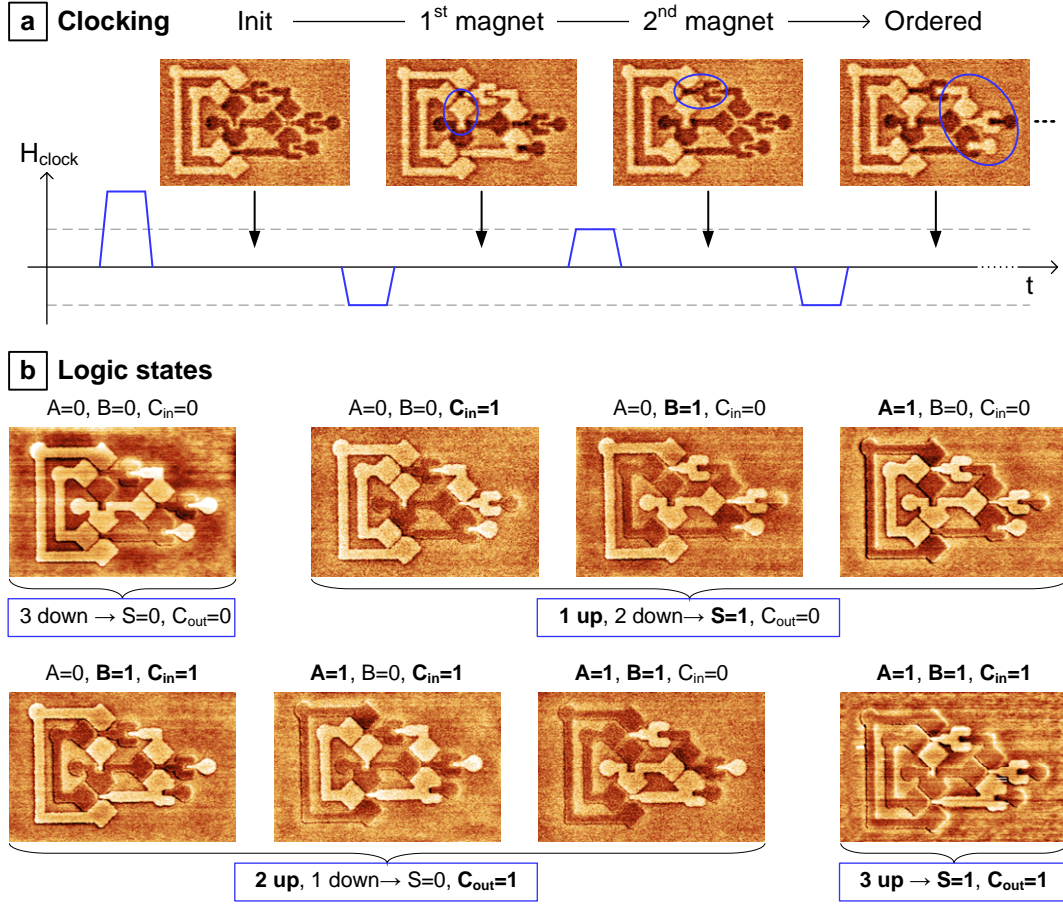


Figure 7.4: Clocking and logic operation of the investigated 1-bit full adder circuit. a) After initialization (set inputs, all other magnets up state), the structure is ordered stepwise according to the clocking field. b) MFM images demonstrate correct logic operation.

ordered stepwise according to the alternating clocking field. MFM images after each clocking field pulse indicate the stepwise signal propagation through the structure.

In the experiment, the structure is already ordered after 3 clocking pulses and the outputs sum S and carry-out C_{out} show the correct state¹. As discussed above (sec. 7.1.2), complete ordering may occur earlier as denoted for the critical path, but the correct state of the output magnets can only be guaranteed after 3 complete clocking cycles.

¹Computing errors may occur during clocking due to fabrication variations and thermally induced SFDs of the computing magnets.

Results

The experiment has been performed for all possible input configurations in order to demonstrate the functionality of the pNML full adder. Fig. 7.4b shows the MFM images of a full adder after clocking for each input pattern of A , B and C_{in} . The magnets are successfully ordered and the output magnets sum S and carry-out C_{out} show the correct result of the adding operation for each case.

Please note, that it was not possible to clock the full adder with a constant clocking field amplitude for each input pattern. Fabrication variations within the ANCs of the magnets in combination with the switching probability density of each ANC dispersed the clocking window and necessitated to slightly adapt the clocking field amplitude in several cases [SB13b].

In comparison to the iNML full adder of [182], the pNML full adder is potentially slower due to different clocking concepts (iNML: single in-plane field pulse, pNML: alternating field pulses) and has a larger footprint ($17\mu\text{m}^2$ vs. $2.3\mu\text{m}^2$). However, the application of TLGs in pNML significantly reduces the circuit size and improves the speed as will be demonstrated in the following section. To our knowledge, this 1-bit full adder is the first reported and at the same time the still most complex NML circuit demonstrating correct logic operation compared to all other experimental work about NML logic circuits published so far.

Meanwhile, also a lot of research about investigating the properties and benefit of pNML circuitry by simulation has been published. Recent work about conventional circuits like XOR gates [JWR⁺12] or 3D-integrated full adder circuits [183], but also about systolic architectures, e.g. for pattern matching hardware [184], demonstrate the promise of pNML for future, beyond-CMOS circuit technology.

7.2 Threshold logic gate-based pNML

The pNML working principle of coupling field-induced DW nucleation at the ANC for logic operation does not limit the number and weight of inputs for majority gates, as proposed by [PNC⁺14]. In general, the application of so-called threshold logic gates enables the reduction of both complexity and footprint of logic circuits [27]. Advantageously, the implementation of TLGs in pNML is very convenient by adjusting the input number and their coupling fields within the majority logic gates [SB14a],[PNC⁺14].

This section describes the basic principle of threshold logic and its application to pNML. Finally, a TLG-based 1-bit full adder is investigated and compared to the full adder circuit presented in the previous section.

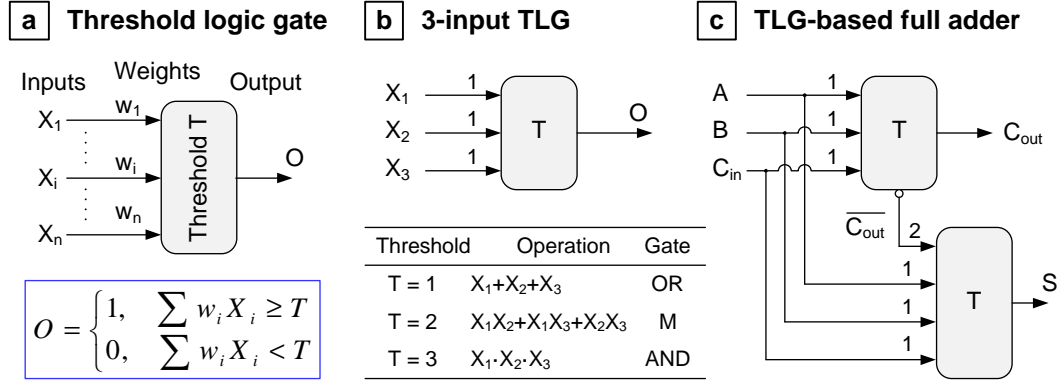


Figure 7.5: Basic principle of threshold logic and TLG-based full adder circuit. a) Threshold logic gate: The weighted input sum $\sum w_i X_i$ is compared to a threshold T to determine the output O . b) The 3-input TLG is programmed to the OR-, Majority- or AND-function by the threshold T . c) TLG-based full adder circuit using only 2 TLGs and one inverter.

7.2.1 Threshold Logic

Threshold logic has been an active research field for non-conventional logic circuitry in the late 1960's and early 70's (e.g. [27, 185, 186]) in order to reduce the circuit complexity and improve both power and speed of ICs. Fig. 7.5a shows the schematic and the basic principle of a TLG. Binary inputs X_i are weighted and their sum is compared to a reference (threshold T) in order to determine a binary output O :

$$O(X_1, \dots, X_i, \dots, X_n) = \begin{cases} 1 & \sum_i w_i X_i \geq T \\ 0 & \sum_i w_i X_i < T \end{cases} \quad (7.10)$$

with w_i as the weight of input $X_i \in \{0, 1\}$. Thereby, the function of the TLG can be programmed by both the input weights w_i and the reference threshold T . For instance, Fig. 7.5b shows the schematic of a TLG with three inputs $X_{1,2,3}$ with equal weights $w_i = 1$. Depending on the threshold T , the 3-input gate can be programmed to the OR ($T = 1$), Majority ($T = 2$) or AND ($T = 3$) function demonstrating the flexibility of these gates. Moreover, the functionality and applicability of such TLGs is significantly improved by increasing the number of inputs and adjusting the input weights [27].

The versatility of TLGs enables a significant reduction of the circuit complexity. Fig. 7.5c shows the threshold gate-realization of a 1-bit full adder circuit as proposed by [27]. Only 2 TLGs (and one inverter) are required for operation:

- The 3-input TLG provides equal weights $w_i = 1$ and is programmed to the

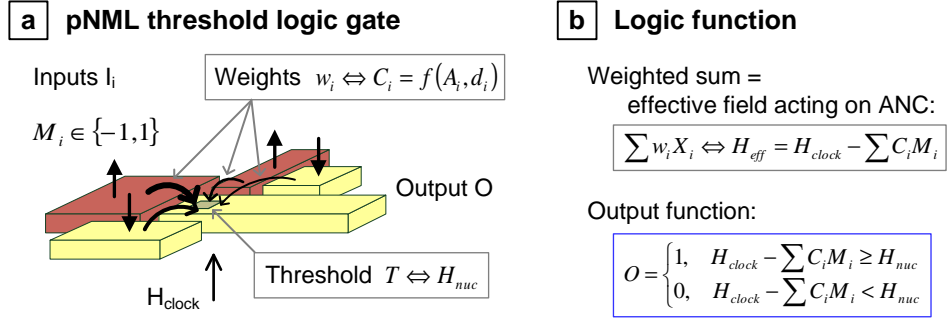


Figure 7.6: Equivalent of a threshold logic gate in pNML. a) The coupling fields C_i correspond to the input weights w_i whereas the threshold T is represented by the DW nucleation field H_{nuc} . b) The weighted input sum $\sum w_i X_i$ is given by effective field H_{eff} acting on the ANC.

majority function (threshold $T = 2$) in order to compute the carry out:

$$C_{out} = \mathbb{M}(A, B, C_{in}). \quad (7.11)$$

- The inverted carry-out C_{out} is double-weighted ($w_{\overline{C_{out}}} = 2$) in the 4-input TLG, which is also programmed to the majority function by $T = 3$. The remaining inputs A , B and C_{in} provide equal weights $w_A = w_B = w_{C_{in}} = 1$ in order to compute the resulting sum:

$$S = \mathbb{M}(A, B, C_{in}, 2\overline{C_{out}}). \quad (7.12)$$

The improvement of the full adder design from 3 majority gates and 2 inverters of conventional majority gate-based computing (Wang *et al.* [180]) to only 2 TLGs and 1 inverter for the TLG-based adder demonstrates the potential of TLG-based circuitry. However, the implementation of TLGs in conventional CMOS technology is not beneficial as several additional components are required in order to program the input weights and the reference threshold.

7.2.2 Threshold logic gates in pNML

By contrast, pNML logic gates provide input weighting and threshold switching by nature through the coupling fields and the DW nucleation field. Fig. 7.6 shows the equivalent representation of a TLG in pNML. The weight w_i of each input I_i in a pNML TLG corresponds to the coupling field C_i , which is predefined during fabrication and can be engineered by size and distance of each input to the ANC of the output magnet. Here, the antiferromagnetic coupling of the magnets has to be considered.

With respect to the clocking field, the effective field $H_{eff} = H_{clock} - \sum_i C_i M_i$

which acts on output ANC corresponds to the weighted input sum $\sum_i w_i X_i$. The reference threshold T for switching of the output O is determined by the DW nucleation field H_{nuc} at the ANC. According to eq. 7.10, the output function of a pNML TLG is then given by

$$O(I_1, \dots, I_i, \dots, I_n) = \begin{cases} 1, & H_{clock} - \sum_i C_i M_i \geq H_{nuc} \\ 0, & H_{clock} - \sum_i C_i M_i < H_{nuc} \end{cases} \quad (7.13)$$

with input $I_i \in \{0, 1\}$ and its corresponding magnetization $M_i \in \{-1, 1\}$. By applying the adequate clocking field amplitude $H_{clock} = H_{nuc}$, the output O is finally given by

$$O(I_1, \dots, I_i, \dots, I_n) = \begin{cases} 1, & \sum_i C_i M_i \leq 0 \\ 0, & \sum_i C_i M_i > 0. \end{cases} \quad (7.14)$$

In principle, logic functionality of TLGs in pNML is not limited in terms of number of inputs and input weights. In other words, the 3-input majority gate is just a special case of a TLG with 3 inputs and equal weights. But note, both fabrication variations (e.g. misalignment of the ANC) and thermally induced DW nucleation probabilities have to be considered in order to provide correct logic operation, which therefore limits the variety of TLG-based pNML.

7.2.3 TLG-based 1-bit full adder

Model

The application of threshold logic to pNML has been proposed for the first time by Papp *et al.* [PNC⁺14]. In their paper, the TLG-based full adder model of [27] was adapted for perpendicular NML by using only 2 TLGs and inverted outputs \bar{S} and \bar{C}_{out} .

Fig. 7.7a shows the schematic of the TLG-based full adder circuit implemented by [PNC⁺14]. Here, Papp *et al.* [PNC⁺14] took advantage of the inverted outputs of pNML logic gates and therefore avoided any additional inverters². Naturally, this reduces both size and delay of the logic circuit. Finally, they implemented their full adder circuit in micromagnetic simulations and proved correct logic operation. The first logic gate to compute the inverted carry-out \bar{C}_{out} is a standard pNML majority gate with 3 inputs A , B and C_{in} and equal weights $w_A = w_B = w_{C_{in}}$. The inverted sum \bar{S} is provided by a 4-input majority gate, in which the inverted carry-out \bar{C}_{out} is double-weighted compared to the remaining inputs: $w_{\bar{C}_{out}} = 2 \cdot w_{A,B,C_{in}}$.

²The full adder outputs carry-out C_{out} and sum S are inverted in this structure, but can be easily inverted for subsequent circuits by antiferromagnetic field-coupling or – if necessary – by 2 additional inverter structures.

TLG-based 1-bit full adder in pNML

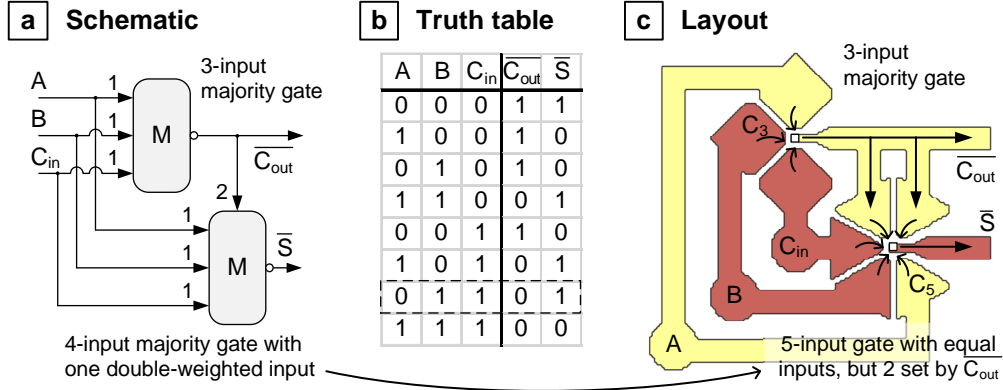


Figure 7.7: TLG-based 1-bit full adder circuit in pNML. a) Schematic from [PNC⁺14] using a 3-input majority gate for the inverted carry-out $\overline{C_{out}}$ and a 4-input majority gate with double-weighted $\overline{C_{out}}$ to compute the sum \overline{S} . b) Corresponding truth table. c) Layout for the experimental TLG-based pNML full adder. The 4-input gate is implemented by using a 5-input gate with 2 inputs set by $\overline{C_{out}}$.

Fig. 7.7b shows the corresponding truth table of the TLG-based pNML full adder. In the original paper [PNC⁺14], the shape of the 4-input gate has been engineered in order to adjust the coupling field $C_{\overline{C_{out}}}$. However, in semiconductor technology it is more common to fabricate structures with equal sizes and distances. Consequently, the 4-input gate to compute the sum \overline{S} is replaced in the experiments by a 5-input majority gate with equal inputs, but with 2 inputs set by $\overline{C_{out}}$. The remaining inputs are set by A , B and C_{in} , respectively. Fig. 7.7c shows the adapted layout for the experimental demonstration of the TLG-based full adder.

Experiment

Fig. 7.8a shows a SEM image of the fabricated 1-bit full adder circuit (nanomagnets: $\text{Ta}_{1\text{nm}}\text{Pt}_{3\text{nm}}[\text{Co}_{0.8\text{nm}}\text{Pt}_{1\text{nm}}]_{x4}\text{Pt}_{3\text{nm}}$, ANCs: $20 \cdot 20 \text{ nm}^2$, $2 \cdot 10^{13} \frac{\text{ions}}{\text{cm}^2}$) [SB14a]. The symmetric majority gates feature comparable input sizes within each gate in order to provide equal coupling fields C_3 and C_5 within the 3-input gate and the 5-input gate, respectively. The circuit footprint is $1.5 \cdot 1.3 \mu\text{m}^2 = 1.95 \mu\text{m}^2$, the width of the magnets is $\approx 120 \text{ nm}$ and the gap between inputs and outputs is $\approx 20 \dots 40 \text{ nm}$. But note, the distance from the input magnets to the ANC is significantly larger in the range of $\approx 70 \dots 100 \text{ nm}$, which decreases the coupling fields as discussed later in the analysis. The computing magnets $\overline{C_{out}}$ and \overline{S} show slightly different DW nucleation fields of $H_{nuc, \overline{C_{out}}} \approx 630 \text{ Oe}$ and $H_{nuc, \overline{S}} \approx 620 \text{ Oe}$. In the experiment (Fig. 7.8b), first the desired input pattern of A , B and C_{in}

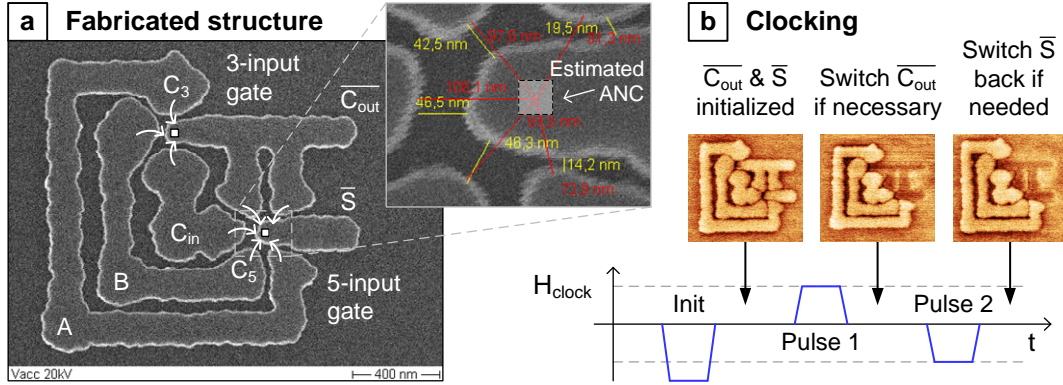


Figure 7.8: Experiment on the fabricated TLG-based 1-bit full adder circuit. a) SEM image of the fabricated structure with the 3-input gate (coupling field C_3 for each input) to compute $\overline{C_{out}}$ and the 5-input gate (coupling C_5) for the sum \overline{S} . b) $\overline{C_{out}}$ and \overline{S} are initialized (may be up or down) with a high field pulse. Afterwards, $\overline{C_{out}}$ and \overline{S} are switched to the correct state during at most 2 clocking field pulses.

is set by appropriate field pulses above 1.5 kOe. Second, the computing magnets are set to the initial state (Init) using a moderate field pulse of $H_{clock} = 1$ kOe. Afterwards, the clocking field with an amplitude of $H_{clock} = 620$ Oe is applied for logic computation. Thereby, $\overline{C_{out}}$ and \overline{S} are sequentially ordered within 2 alternating clocking field pulses. The first pulse (Pulse 1), switches $\overline{C_{out}}$ to its designated state. The second pulse (Pulse 2) switches \overline{S} back to the correct state if needed. So in summary, only $1\frac{1}{2}$ clocking cycles are required for operation. As shown in Fig. 7.8b, the output magnets may already be switched to the correct state before, which naturally depends on the applied input pattern. But, correct logic computation is only guaranteed after $1\frac{1}{2}$ clocking cycles.

During the experiment, the ordering process of the nanomagnets was verified by MFM after each clocking field pulse [SB14a]. Fig. 7.9 shows the MFM images of the ordered full adder after clocking. The carry-out $\overline{C_{out}}$ and sum \overline{S} are correctly aligned for each input pattern of A , B , and C_{in} . The results prove correct logic operation of the investigated 1-bit full adder and demonstrate the feasibility of TLG-based pNML.

Analysis

In the experiment, the applied clocking field had to be adapted for input patterns with one input up: $(ABC_{in}) \in \{100, 010, 001\} \rightarrow (\overline{C_{out}}\overline{S}) = \{10\}$ [SB14a]. Here, the second clocking field pulse had to be slightly reduced to 600 Oe in order to not switch the sum \overline{S} back to the up state. Therefore, two different (or

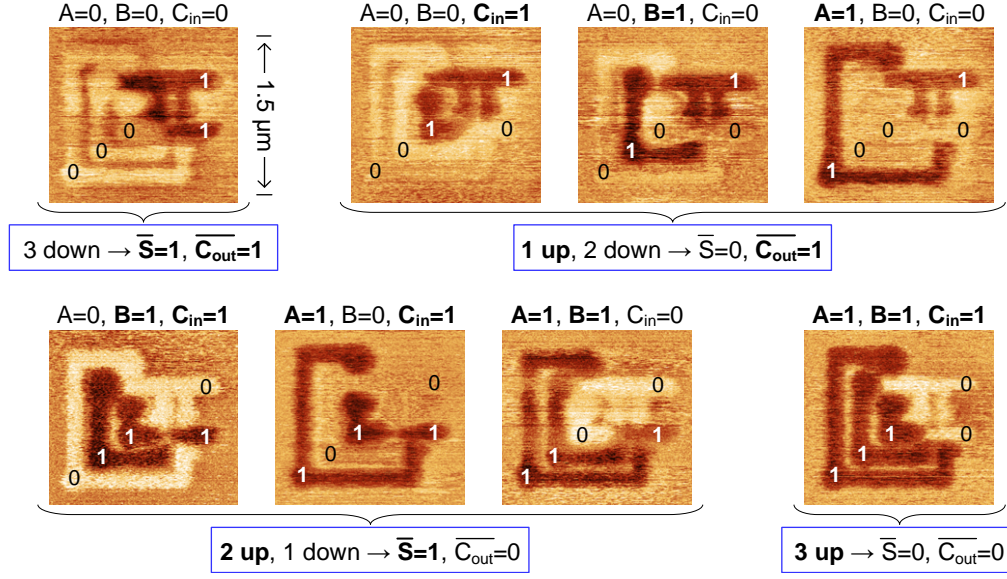


Figure 7.9: Logic operation of the TLG-based 1-bit full adder. MFM images show correct ordering after clocking with 2 field pulses. Carry-out $\overline{C_{out}}$ and sum \overline{S} are successfully computed for each input pattern A, B, C_{in} .

combined) reasons are imaginable:

1. **Unequal coupling fields $C_{out} \neq 2C_{A,B,C_{in}}$:** As already discussed in sec. 6.2.3, margins of the ANC alignment for correct operation of a majority gate are very restricted ($\Delta x_{ANC}, \Delta y_{ANC} < 10$ nm). Hence, a small shift of the ANC from \overline{S} in the order of $10 \dots 20$ nm off the input $\overline{C_{out}}$ would decrease the required, stabilizing effect of the coupling field of $\overline{C_{out}}$ during the second pulse.
2. **Undersized coupling fields C_5 :** Small input coupling fields lead to a minor shift of the DW nucleation field at the ANC and hence to an overlap of the corresponding SFDs. Consequently, the clocking window vanishes and erroneous computing occurs for several input patterns.

The first potential reason cannot be investigated as the location of the ANC is not visible in both SEM and MFM images. But however, Fig. 7.8a indicates that distances to the ANC may vary between $70 \text{ nm} \dots 100 \text{ nm}$ by estimating the location of the ANC from the lithography masks. Accordingly this would lead to unequal coupling fields in the 5-input gate.

For the second reason, the input coupling fields of the 5-input gate cannot be determined by measuring the SFDs via LMOKE, because not all possible input configurations can be set as also $\overline{C_{out}} = f(A, B, C_{in})$. But, the coupling fields

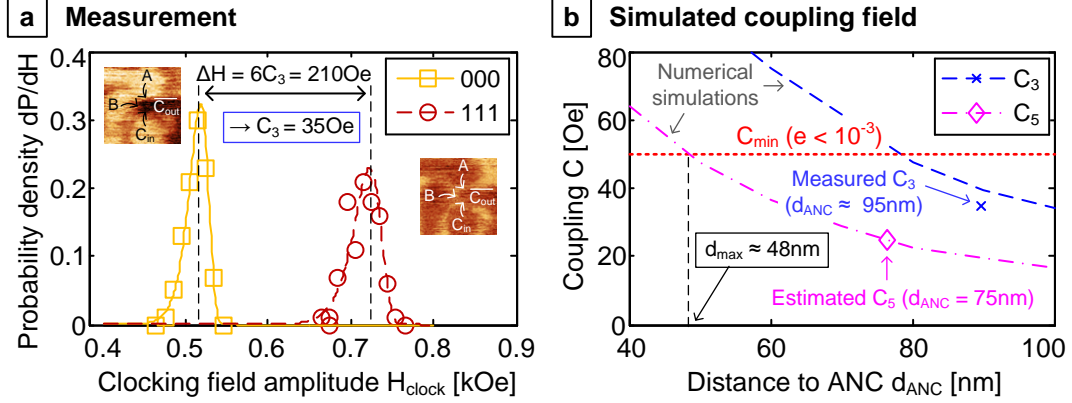


Figure 7.10: Measurement and simulation of the coupling fields of the TLG-based full adder. a) The measured nucleation probability density ($N = 100$) of $\overline{C_{out}}$ is shifted by the $\pm 3C_3$ for the investigated input patterns 000 and 111. b) Simulations using compact models show, that a coupling field of at least $C_{min} = 50$ Oe is required for reliable logic operation (error rate $e < 10^{-3}$).

C_3 of the 3-input gate can be measured and compared to numerical simulations. Afterwards, also the coupling C_5 of the 5-input gate can be estimated by numerical simulations.

Fig. 7.10a shows the measured SFDs of $\overline{C_{out}}$ at the 3-input gate for the 000 and the 111 input patterns. By assuming equal coupling fields $C_A = C_B = C_{C_{in}} = C_3$, the measured gap between both SFDs is $\Delta H = 6 \cdot C_3 = 210$ Oe and hence, the 3-input gate coupling is $C_3 = 35$ Oe. The measured value for C_3 is in good agreement to the calculations using numerical simulations. Fig. 7.10b shows the calculated coupling fields based on the lithography mask depending on the distance to the ANC d_{ANC} . By estimating the distance d_{ANC} from the SEM images from Fig. 7.8a, the resulting coupling field for the 5-input gate would be $C_5 (d_{ANC} \approx 75 \text{ nm}) = 25$ Oe.

Naturally, this value is way too small for reliable logic operation. Simulations based on calibrated compact models show, that the coupling field of each input has to be increased to at least $C_{min} = 50$ Oe in order to reduce the error rate of a pNML logic gate below $e < 10^{-3}$ (e.g. [SB11d, SB13d]). As already mentioned, the input coupling fields can be dramatically increased by reducing the distance to the ANC, as also shown in Fig. 7.10b. Consequently, the gate's input distances to the ANC has to be reduced below $d_{max}(C_5) \approx 48 \text{ nm}$ and $d_{max}(C_3) \approx 80 \text{ nm}$ for the given $[\text{Co}_{0.8\text{nm}}\text{Pt}_{1\text{nm}}]_{\times 4}$ magnets to provide definite and reliable logic computation. However, such dimensions are feasible in modern manufacturing technology.

Compared to 3 majority gate-implementation of the full adder (sec. 7.1), the circuit footprint is reduced by a factor of 8.7 from $17 \mu\text{m}^2$ to $1.95 \mu\text{m}^2$. At the

same time, the delay is reduced by a factor of 3 due to shorter magnets (factor of 1.5) and a shorter critical path ($1\frac{1}{2}$ clocking cycles instead of 3).

The computational throughput as common measure quantifying logic operations per area and second [21], is therefore increased by a factor of 26! In summary, the experimental results impressively substantiate the promise of TLG-based pNML as emerging beyond-CMOS technology.

7.3 Simulation of pNML circuitry

The demonstrated TLG-based full adder is further investigated by simulation in order to specify the potential of pNML circuitry in terms of progressive scaling, clocking speed enhancements and material improvements. Compact modeling of pNML is applied to simulate the circuit behavior and determine the operational reliability, i.e. the error rate.

7.3.1 Compact modeling

Micromagnetic modeling tools based on the (time-intensive) evaluation of the LLG-equation with high spatial resolution like OOMMF (cp. sec. 2.1.2) are highly suitable for the exploration of micromagnetic phenomena, but they are not capable for simulations of large circuits or extensive parameter investigations. By contrast, physical-based compact models provide fast simulation times and at the same time accurately mimic the switching behavior of nanomagnets with PMA [SB14b, SB13d].

More precisely, they enable to simulate the field-induced DW nucleation from ANC's within field-coupled magnets. Therefore, it is required to

1. calculate the geometry- and material-dependent coupling field strength of each input magnet on the ANC's, and
2. determine characteristic parameters for DW nucleation at the ANC, i.e. the energy barrier at zero field E_0 and the coercive field at zero temperature H_0 ,

prior to the simulation. Afterwards, within each time step of the simulation, the compact models need to

3. calculate the effective field acting on the ANC of each output depending on the current input configuration and the applied clocking field,
4. evaluate the resulting DW nucleation probability at the ANC, and
5. finally set the corresponding magnetization of the magnets.

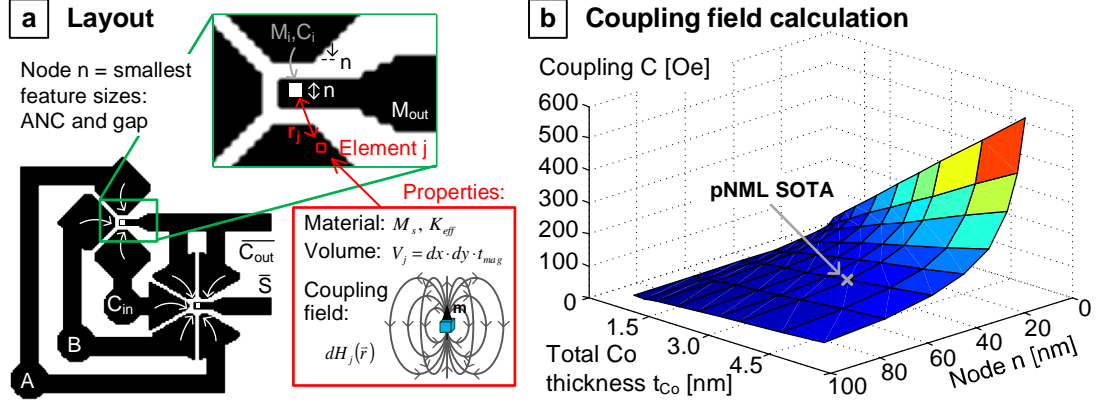


Figure 7.11: Coupling field calculation for compact modeling of pNML circuitry. a) The circuit layout is discretized in small elements j to calculate the coupling fields $\mathbf{C}_i(\mathbf{r}) = \sum d\mathbf{H}_j(m_j, \mathbf{r}_j)$. b) Input coupling strength of a 3-input majority gate depending on the technology node n and the total Co thickness t_{Co} .

In the following, the details of the compact models are discussed exemplary for the investigated TLG-based full adder.

Coupling field calculation

The coupling fields of each magnet are determined as described in sec. 2.6. Therefore, the layout mask of the circuit is discretized in small elements j with volume $V_j = dx \cdot dy \cdot t_{mag}$ and magnetic moment $m_j = M_s \cdot V_j$ (Fig. 7.11a). The stray field $d\mathbf{H}_j(m_j, \mathbf{r}_j)$ of each element j is then calculated by the point-dipole approximation using eq. 2.51. The coupling field $\mathbf{C}_i(\mathbf{r})$ of each magnet i results from the stray field superposition of the corresponding elements j according to eq. 2.52:

$$\mathbf{C}_i(\mathbf{r}) = \sum_j d\mathbf{H}_j(\mathbf{m}_j, \mathbf{r}_j) \quad (7.15)$$

Afterwards, the coupling field strength $C_i(\mathbf{r}_{ANC})$ acting on the output ANC is determined depending on its position \mathbf{r}_{ANC} . Here, also fabrication-dependent variations $\sigma_{\mathbf{r}_{ANC}}$ of the ANC position can be considered.

The corresponding technology node n for fabrication of the simulated full adder is given by the smallest feature size, i.e. the distance between the magnets and the size of the ANC. Fig. 7.11b shows the resulting input coupling field strength of the 3-input majority gate of the full adder depending on the technology node n and the total Co thickness $t_{Co,tot}$. It increases linearly with the Co thickness due to the higher magnetic moment and by $C_i \propto \frac{1}{n}$ with the technology node due to the smaller distance. The state-of-the-art (SOTA)-point marked in the

diagram illustrates the potential to increase the coupling by progressive scaling of the devices.

ANC parameters and clocking field

In order to determine the energy barrier for DW nucleation from the ANC (see eq. 2.43), the characteristic parameters $E_{0,ANC}$ and $H_{0,ANC}$ are calculated depending on the material parameters, i.e. the effective anisotropy K_{eff} , the saturation magnetization M_s and nucleation volume V_{ANC} .

Thereby, an optimal FIB irradiation lowering the anisotropy in the ANC to $K_{ANC} = \frac{1}{5}K_{eff}$ is assumed (eq. 2.38). Hence, switching of the magnets is assumed to be nucleation-dominated (not pinning-dominated by the anisotropy gradient). The resulting coercive field at zero temperature at the ANC is

$$H_{0,ANC} = \frac{2K_{ANC}}{\mu_0 M_s} = \frac{0.4 \cdot K_{eff}}{\mu_0 M_s} \quad (7.16)$$

according to eq. 2.40. The corresponding energy barrier at zero field is given by

$$E_{0,ANC} = K_{ANC}V_{ANC} = \frac{1}{5} \cdot K_{eff}V_{ANC}. \quad (7.17)$$

In both characteristic parameters, fabrication-dependent material variations, i.e. of the anisotropy K_{eff} , the lowering of K_{eff} at the ANC (factor $\frac{1}{5}$), the saturation magnetization M_s and the size of the ANC V_{ANC} , can be considered.

The resulting, optimal field amplitude for clocking of the circuit is calculated by the Sharrock equation (eq. 2.42):

$$H_{clockamp}(t_{clock}) = H_{0,ANC} \left[1 - \sqrt{\frac{k_B T}{E_{0,ANC}} \ln \left(\frac{f_0 t_{clock}}{\ln 2} \right)} \right], \quad (7.18)$$

with the field pulse time t_{clock} corresponding to the desired clocking frequency $f_{clock} = \frac{1}{2t_{clock}}$.

Effective field calculation

During the simulation, the effective field acting on each ANC has to be determined within each time step (Fig. 7.12a). Therefore, the resulting effective field $H_{eff}(t)$ within each model is calculated by

$$H_{eff}(t) = H_{clock}(t) - \sum C_i M_i(t) \quad (7.19)$$

with the time-dependent clocking field $H_{clock}(t)$ and the current input states $M_i(t) \in \{-1, 1\}$. Here, also the rise-time of the clocking field has to be considered.

Within each time step, additional noise can be added to the clocking field amplitude (σ_{noise} , e.g. to include noise of the clock generating ICs) and to the coupling fields (σ_C , e.g. to recognize field-induced tilting and magnetization precession).

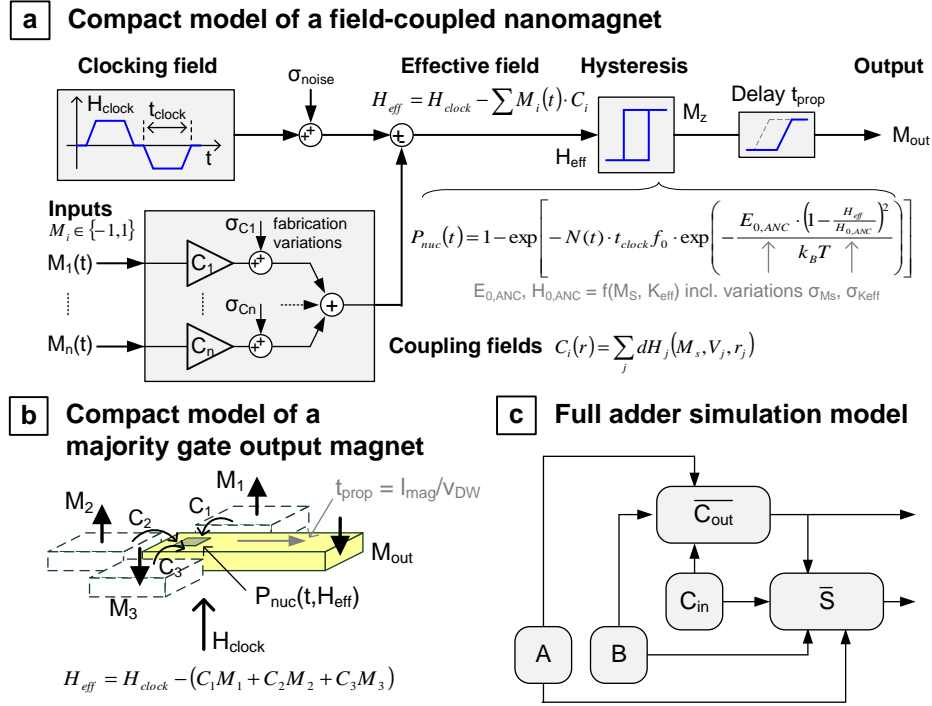


Figure 7.12: Compact modeling of pNML circuitry. a) The compact models calculate the effective field H_{eff} depending on the clocking field H_{clock} and the sum of the coupling fields $\sum M_i C_i$ to determine the nucleation probability P_{nuc} to switch the magnet. b) Corresponding compact model for the output magnet of a 3-input majority gate. c) Simulation model of the TLG-based 1-bit full adder.

DW nucleation probability evaluation

The evaluation of the resulting DW nucleation probability is based on the current effective field H_{eff} (Fig. 7.12a). Therefore, the DW nucleation probability within the current clocking field pulse is calculated according to the Arrhenius model of eq. 2.44:

$$P_{nuc}(t) = 1 - \exp \left[-N(t) t_{clock} f_0 \cdot \exp \left(-\frac{E_{0,ANC} \cdot \left(1 - \frac{H_{eff}(t)}{H_{0,ANC}}\right)^2}{k_B T} \right) \right] \quad (7.20)$$

with $N(t) \in [0, 1]$ evaluating the actual duration of the current field pulse. The final decision about the magnetization reversal is then evaluated by comparison of a random number $R(t) \in [0, 1]$ with the previously calculated DW nucleation probability $P_{nuc}(t)$ within each time step.

Magnetization reversal

After positive evaluation of the DW nucleation within one time step, the output magnetization $M_{out}(t) \in \{-1, 1\}$ is switched according to the current clocking field direction. Here, also a switching delay of

$$t_{switch} = \frac{l_{magnet}}{v_{DW}(H_{clock})} = t_{prop} \quad (7.21)$$

corresponding to the magnet length l_{magnet} and the DW velocity $v_{DW}(H_{clock})$ can be considered.

The equivalent to the compact model of an majority gate output magnet is shown in Fig. 7.12b. For the simulation of the full adder circuit, the individual compact models of the magnets are linked according to the circuit layout (Fig. 7.12c). In the following, the described compact models are used to investigate the potential of the TLG-based 1-bit full adder of sec. 7.2.3 with respect to scaling, clocking speed and material improvements.

7.3.2 Potential of pNML

Beside the quantitative physical measures area, power and delay, the operational reliability (i.e. the error rate) is one of the most important characteristics of ICs. In order to investigate the future potential of pNML circuitry, the error rate e of the TLG-based 1-bit full adder circuit is simulated depending on the

- technology node n ([90 nm ... 7 nm]),
- clocking frequency f_{clock} ([50 kHz ... 1 GHz]),
- effective anisotropy K_{eff} ($[0.5 \dots 2.5 \cdot 10^5 \text{ J/m}^3]$), and
- total Co thickness $t_{Co,tot}$ ($[0.5 \dots 5 \text{ nm}]$, \propto magnetic moment of the material).

For each parameter configuration ($n, f_{clock}, K_{eff}, t_{Co,tot}$), the coupling fields C_i of each nanomagnet and the characteristic parameters for DW nucleation E_0 and H_0 are calculated as described in the previous section. In the simulation, the error rate e is simulated within $N = 10^5$ runs for each possible configuration of the investigated parameters.

Within each run, a random input pattern (A, B, C_{in}) is applied and the circuit is clocked using the optimal clocking field amplitude according to eq. 7.18. Afterwards, potential errors are detected by evaluating the generated output patterns ($\bar{S}, \overline{C_{out}}$) of each run. In summary, $N_{total} = 5 \cdot 10^8$ simulation runs have been performed. Fig. 7.13 shows the compact model simulation results based on the SOTA pNML ($n \approx 32 \text{ nm}$, $f_{clock} = 5 \text{ MHz}$, $K_{eff} = 2.0 \cdot 10^5 \text{ J/m}^3$, $t_{Co,tot} = 3 \text{ nm}$).

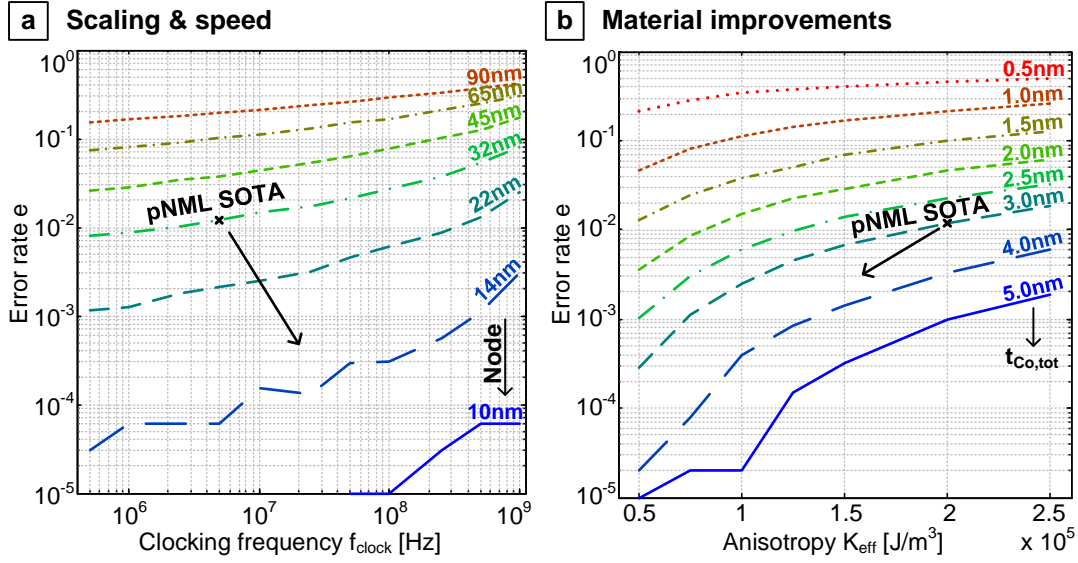


Figure 7.13: Simulated error rate of the TLG-based 1-bit full adder. a) Progressive scaling according to the technology node n enables to reduce the error rate e despite of increasing the clocking frequency f_{clock} . b) Material improvements, i.e. reducing the effective anisotropy K_{eff} and increasing the magnetic moment (here the total Co thickness $t_{\text{Co,tot}}$), enable to further reduce the error rate e .

Scaling and clocking speed

Fig. 7.13a shows the dependency of the error rate e on the technology node n versus the applied clocking frequency f_{clock} .

As expected, the error rate decreases significantly for improving nodes due to the increase of the coupling fields (cp. Fig. 7.11b). This is very beneficial with respect to the requested scalability of beyond-CMOS devices [21]. For the 7 nm-node, no erroneous switching has been observed for the whole investigated frequency range. For further scaling, one has to keep in mind that exchange coupling between spins of neighboring magnets arises for gaps below < 7 nm.

In terms of speed, the error rate increases for higher clocking frequencies due to the broadening of the time-dependent DW nucleation probability. However, increasing the clocking frequency is technically feasible by at the same time improving technology node. As already mentioned, the propagation time $t_{\text{prop}} = \frac{l_{\text{magnet}}}{v_{\text{DW}}(H_{\text{clock}})}$ required to propagate the DW through the magnets has to be considered. For a clocking frequency of $f_{\text{clock}} = 100$ MHz, the maximum magnet length is only $l_{\text{magnet}} = \frac{v_{\text{DW}}(H_{\text{clock}}) \approx 50 \text{ m/s}}{2f_{\text{clock}}} \approx 250$ nm. Consequently, the circuit design has to be adapted to reduce the DW propagation length for higher clocking frequencies.

Material improvements

Much potential is given by material improvements, as depicted in Fig. 7.13b. On the one hand, enhancing the areal magnetic moment $M_s \cdot t_{mag}$ (e.g. by increasing the total Co thickness $t_{Co,tot}$) increases the coupling strength and therefore reduces the error rate e . On the other hand, reducing the effective anisotropy K_{eff} narrows the nucleation probability density, which in turn leads to less erroneous switching. Furthermore, a reduction of K_{eff} decreases the characteristic parameters E_0 and H_0 , and therefore also the required clocking field amplitude $H_{clockamp}$ according to eq. 7.18. Hence, also the power consumption of the clocking structure $P_{clock} \propto H_{clockamp}^2$ is significantly reduced.

Note, the material parameters effective anisotropy K_{eff} and areal magnetic moment $M_s \cdot t_{mag}$ cannot be modified arbitrarily. The effective anisotropy K_{eff} can be tuned in magnetic multilayers by changing material, number, and thickness of the individual layers (according to eq. 2.16). But, thick magnetic layers – as required for high magnetic moments – may tilt the anisotropy from perpendicular to in-plane. Furthermore, the thermal stability limit of the nanomagnets $E_{0,limit} \approx 40 \text{ k}_B\text{T}$ has to be considered.

In summary, the presented compact model simulations provide far-reaching investigations within field-coupled magnets based on well-known physical models. They enable fast and extensive simulations of complex pNML circuits and systems with respect to e.g. circuit geometries, material properties, fabrication variations, clocking speed, noise and temperature.

The compact model simulations specify significant potential for pNML by conventional scaling and material improvements.

Advancing the technology node reduces the circuit area and in addition increases the operational reliability. At the same time, it enables to increase the clocking frequency (shorter magnets) and reduce the corresponding delay.

Material improvements enable more reliable logic computation and lower clocking field amplitudes, which significantly decreases the power consumption of the circuit. Furthermore, they may lead to faster DW velocities, which in turn enables to increase the clocking frequency.

8 Towards pNML Systems

In general, logic computing systems process bit streams with multiple bits and consist of concatenated logic gates and units. The bit streams are first loaded from memory, then processed and afterwards stored back to memory (von-Neumann architecture). Thereby, signals are transmitted, synchronized and buffered to facilitate complex logic circuitry.

Also in pNML, such aspects are of great importance in order to realize complex systems. The inherent nonvolatility of the magnets and the pipelined signal processing according to the clocking field makes pNML suitable to a wide range of architectures and signal processing.

8.1 Architecture

In addition to general Boolean logic circuits organized in common von-Neumann architectures, NML is highly applicable for systolic architectures [187, 188]. Here, signals are pipelined successively through many processing elements (logic units) with different or similar logic functionality. General criteria for systolic architectures are the multiple use of each input data, extensive concurrency, only a few types of logic cells, as well as simple and regular data / control flow. Hence, systolic architectures are beneficial to any regular arithmetic problem such as [188]:

- Signal and image processing (e.g. filtering, discrete Fourier transformation (DFT), convolution),
- Matrix arithmetic (e.g. matrix and vector multiplication, decomposition),
- Pattern matching or language recognition.

In recent years, research on NML (and QCA) systems has been extended to systolic architectures [66, 187, 189] and Programmable Logic Arrays (PLAs) [190, 191]. The working principle of field-coupled computing and inherently pipelined logic operation using simple majority gates maps extremely well to systolic architectures. Furthermore, runtime-programmable majority gates (e.g. by inplane fields [KBE⁺13b] or 3D majority gates [EBZ⁺14]) enable to implement Field-Programmable Gate Array (FPGA) functionality into pNML systems.

Fig. 8.1a shows a sketch of a proposed pNML architecture based on a systolic

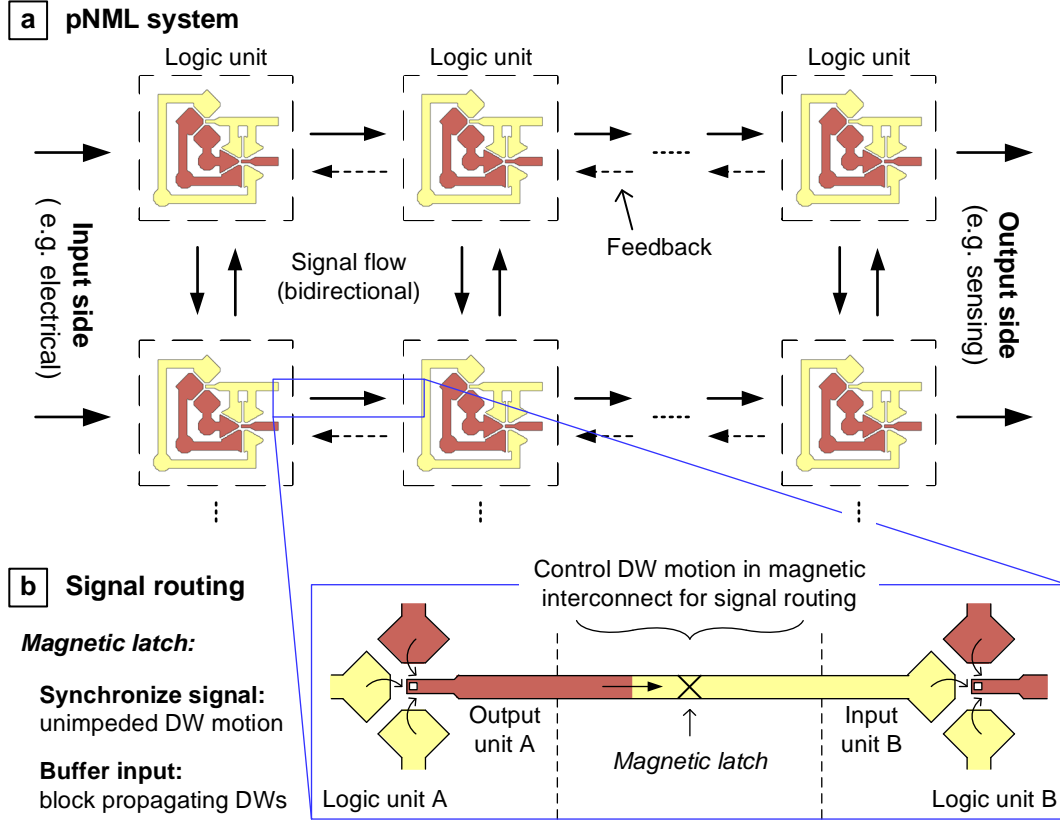


Figure 8.1: PNML system based on a systolic array. a) Input patterns are pipelined through several processing logic units (sketched in a simplified manner), which are interconnected by magnetic nanowires. b) The signal flow between logic units is directed by magnetic latches, which control the DW motion through the nanowires.

array. Several processing logic units, which provide minor logic operations, are arranged in an array and interconnected by magnetic nanowires. Thereby, feedback loops and bidirectional signal flow are feasible.

Input patterns and bit streams from magnetic or electrical inputs are pipelined through the logic array. Here, an arithmetic logic unit (ALU) based on an TLG-based 1-bit full adder as shown in sec. 8.5 is highly suitable as basic logic cell. It can be programmed to the AND, OR, XOR, PAR (=XNOR), ADD or SUB operation during runtime in order to provide the favored logic operation. Hence, also the whole systolic array could be adapted to the required function. The resulting output patterns are sensed or stored into memory.

Signal routing between the logic units is one of the most important aspects in order to provide correct logic operation. Therefore, some kind of *magnetic latch* is required to control the signal flow within the interconnects (Fig. 8.1b).

8.2 Signal routing

In CMOS, signals are commonly buffered and synchronized by latches according to the internal clock. Also in pNML systems, magnetic signals have to be synchronized, routed, and buffered between logic units.

Usually, logic operations are not limited to single bit operations. Common applications (e.g. matrix arithmetic or image processing) require logic circuits which provide multiple bit operations, e.g. 32-bit adders [21]. In order to be classified as proper emerging beyond-CMOS technology, processing of magnetic bit streams is also required in pNML systems.

Another important aspect of signal routing to be mentioned here is the crossing of magnetic signals. One promising approach is to detour signals through additional functional layers as proposed for QCA by [192].

Analog to CMOS, where wires are crossed within multiple metal layers, magnetic information in pNML can be transferred through multiple functional layers stacked upon each other [EKB⁺13]. Magnetic vias, which exploit the 3-dimensional nature of coupling fields to transfer magnetic signals between multiple functional layer, are used to provide unimpeded DW motion through super-imposed, crossed magnetic nanowires [EBK⁺14].

8.2.1 Processing of magnetic bit streams

Consecutive information (the next bit) can be injected in an inverter chain at the earliest every second clocking cycle [KBE⁺13a],[28, 184]. Therefore, it is favorable that each logic unit processes information within 2 clocking cycles in order to maximize the data throughput of a pNML system.

Meanwhile, the corresponding input magnets of each logic unit have to be kept constant. Though, the logic units output magnets – which act as inputs for subsequent units – may flip several times during logic computation, as already depicted in sec. 7.1.2. Hence, controllable, magnetic latches between logic units to buffer domains and control the signal flow are required.

Compact model simulations [SB14b] have shown, that it is not necessary to allow one additional cycle for signal transfer after processing. Due to the asynchronous switching of up- and down-states according to the alternating clocking field, new input bits for the next bit operation can already be set within the ongoing second processing clocking cycle, while the current outputs are still computed:

- During the first clocking cycle, the input magnets are fixed (buffered) and logic operation is computed within the first logic gates of a logic unit. Thereby, the current bit propagates at least 2 magnets further, which is the required interspace to inject a new bit without erasing the previous one [KBE⁺13a].

- In the second cycle, the final output signals are computed and transferred to the subsequent logic unit. In the meantime, signals from the previous logic unit are also transferred and the new input bits for the next bit operation are already set.

Naturally, the logic cells have to be designed in an appropriate way to enable this 2-clocking-cycle information processing.

Usually, output magnets are connected to input magnets of subsequent logic units by magnetic nanowires. Thereby, the signal is transferred from output to input within one single clocking pulse without delaying the logic computation. Favorably, the needed signal routing device (magnetic latch) does not additionally delay the overall signal flow.

In summary, this means that a controllable device is required, which

1. blocks the signal flow within magnetic interconnects for one (optional also more) clocking cycles to buffer the currently processed input bits,
2. provides signal transfer during the next full clocking cycle (transfer period, one pulse each for up- and down-domains), and
3. does not delay the signal flow between the logic units during the transfer period.

Thereby, the footprint of the device should be as small as possible, whereas switching between blocking and transfer period is controllable by user-defined actions.

8.2.2 Controlled DW motion

One promising approach to meets such requirements, is to control the DW motion through the magnetic interconnects (cp. Fig. 8.1b). On the one hand, when DW motion is blocked, the domain at the end of the wire (=input for subsequent gate) is buffered due to the nonvolatile character of the magnets. On the other hand, during the transfer period, the field-driven DWs propagate unimpeded through the interconnects and signals are synchronized within several wires.

In principle, various approaches based on different physical effects can be applied to manipulate the DW propagation in magnetic nanowires:

1. Anisotropy variations (e.g. by local FIB irradiation [147, 148]) generate anisotropy steps which induce a depinning field for DWs (see sec.2.3.4). But, the local decrease of the anisotropy may also generate ANCs leading to erroneous DW nucleation and is therefore not applicable to control the DW motion in pNML.

2. Geometric pinning sites (e.g. notches [124] or vertical indents [193]) increase the DW depinning field without generating ANC's (see sec. 2.3.4). Thereby the depinning field is adjusted by the geometry of the pinning site. However, local manipulation on the corresponding energy barrier is necessary to control the DW pinning.
3. Field or current pulses drive DWs through magnetic nanowires depending on their direction and amplitude [140]. However, current pulses through the nanowires feature very high current densities and necessitate electrical contacts for each nanowire. Field pulses are not limited to the area of interest and superpose with the global clocking field, which may also influence the DW nucleation at the ANC's.
4. Voltage-controlled DW trapping [194, 195] provides real-time control of the DW motion, but sustained voltages increase the power consumption and again electrical contacts for each wire are required. Furthermore, the applicability in nanowires made from magnetic multilayers is still questionable.
5. Local coupling fields of nearby magnets manipulate the DW motion in a nanowire, as shown for Py wires using a close-by Supermalloy bar [196]. However, in PMA materials the coupling field locally changes the effective field and therefore just slightly manipulates the DW propagation speed.
6. Branches in Py nanowires (T-shape structure) modify the necessary DW propagation field and therefore enable to block DWs as shown by [197]. However, in this way the approach is not applicable to pNML, as branches are used for fanout structures and DWs in PMA materials exhibit a different pinning behavior.

Individually, none of the presented approaches is sufficient to control the DW motion in the magnetic interconnects. However, in combination, the 2. and 5. approach provide the requested characteristics as independently investigated for Py wires by [198]. The effect of coupling fields on notches is a promising approach to control the DW motion in PMA nanowires.

8.3 Domain wall gate (DWG)

In a *domain wall gate (DWG)*, propagating DWs are pinned in notches, whose energy barrier is modified by local coupling fields of nearby *gate* magnets [SB13c, SB14c]. Direct control on the DW motion through the DWG enables to modify the signal flow in the interconnects and therefore facilitates signal routing in pNML systems.

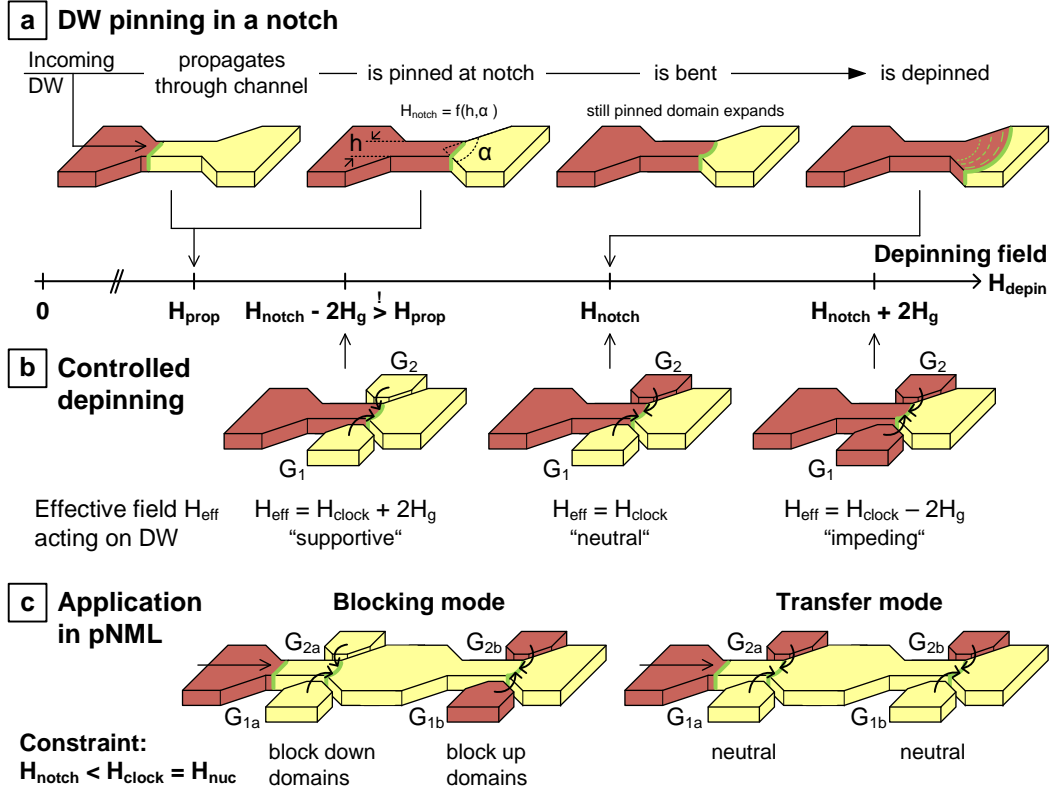


Figure 8.2: Working principle of a domain wall gate. Propagating DWs are pinned at the channel end, whose depinning field H_{notch} depends on its geometry (a). To control the DW motion, coupling fields of surrounding gate magnets in- or decrease the effective field and therefore modify the required clocking field amplitude to depin the DW (b). For application in pNML, two DWGs are necessary to control the signal flow independently of the incoming DW (c).

8.3.1 Working principle

As already mentioned in sec. 2.3.4, notches in magnetic nanowires constitute pinning sites with a specific depinning field required to depin the DW. Thereby, the depinning field H_{notch} depends on the notch shape and the magnetic material. In a DWG, the notch is elongated to a channel in which the nanowire width h_{wire} is reduced to the channel width h (Fig. 8.2a). By applying a perpendicular field $H_z > H_{prop}$, the incoming, field-driven DW will propagate unimpeded through the channel. At the end of the channel, the width is increased to the nanowire width under an apex angle α . Due to the corresponding energy barrier, the DW is pinned at the notch and bent to an arc of circle in order to reduce the Zeeman energy. According to eq. 2.32, the effective field required to depin the DW from

the notch is given by

$$H_{notch} = H_{int} + \frac{\sigma_w \sin(\alpha/2)}{M_s \cdot (h + \delta_w \sin(\alpha/2))}. \quad (8.1)$$

To control the DW depinning from the notch, two gate magnets G_1 and G_2 with magnetization state $M_{g1,g2} \in \{-1, 1\}$ are located close to the channel (Fig. 8.2b). The gate coupling fields $H_{g1} = H_{g2} = H_g$ superpose with the applied clocking field H_{clock} and therefore in- or decrease the effective field H_{eff} acting on the pinned DW depending on gate states:

$$H_{eff} = H_{clock} - H_g (M_{g1} + M_{g2}). \quad (8.2)$$

Accordingly, the required clocking field amplitude to depin the DW is

$$H_{depin} = \pm H_{notch} \pm H_g (M_{g1} + M_{g2}). \quad (8.3)$$

Naturally, the pinning behavior depends on the expanding domain. Up-domains are supported by down-gates and blocked by up-gates and vice versa. In the following, only the case of an expanding up-domain (positive perpendicular field) is discussed, which can be transferred to down-domains by negotiating the corresponding signs. According to eq. 8.3, three different gate configurations have to be considered (see Fig. 8.2b):

- $G_1 = G_2 = 0$ ($M_{g1} = M_{g2} = -1$): When both gates are down, the effective field is increased by $2H_g$ and the DW depinning field H_{depin} is reduced to $H_{notch} - 2H_g$. Hence, depinning of an up domain is supported by the gate magnets. Note, the clocking field amplitude to depin the DW has to be larger than the required DW propagation field: $H_{depin} > H_{prop}$.
- $G_1 \neq G_2$ ($M_{g1} \neq M_{g2}$): The coupling fields of antiparallel gates more or less cancel out each other and therefore do not affect the DW depinning: $H_{eff} = H_{clock}$ and $H_{depin} = H_{notch}$.
- $G_1 = G_2 = 1$ ($M_{g1} = M_{g2} = 1$): Both gates up reduce the effective field to $H_{clock} - 2H_g$ and therefore increase the depinning field to $H_{notch} + 2H_g$.

Obviously, two connected DWGs are necessary to control the signal flow in pNML independently of the propagating DW. For application in pNML systems, the notch depinning field and the gate fields have to be adapted to the DW nucleation field in the logic gates:

$$H_{notch} - 2H_g < H_{nuc} < H_{notch} + 2H_g. \quad (8.4)$$

In other words, the DW has to be depinned by the amplitude of the clocking field $H_{clock} = H_{nuc}$ (see eq. 6.11) when the gates support the depinning and vice versa.

Accordingly, for the antiparallel case ($G_1 \neq G_2$), the notch of a DWG can be designed to let every nucleated DW propagate through ($H_{notch} < H_{nuc}$), or block every DW-type ($H_{notch} > H_{nuc}$) with the limitation of $H_g > 0.5 |H_{nuc} - H_{notch}|$.

Fig. 8.2c shows the DWGs arranged in series¹ for the case of $H_{notch} < H_{nuc}$.

In blocking mode, the gate magnets of the first DWG are down ($G_{1a} = G_{2a} = 0$) and those of the second one are up ($G_{1b} = G_{2b} = 1$). Hence, each DWG blocks one type of DW and therefore no DW passes the double-DWG structure. In transfer mode, both DWGs are set to antiparallel state ($G_{1a} \neq G_{2a}$ and $G_{1b} \neq G_{2b}$) to let any DW pass due to $H_{notch} < H_{clock} = H_{nuc}$.

Naturally, the gate magnets have to be controlled appropriately in order to determine the operating mode of the DWGs. In a pNML system, the gates are set by further magnetic or electrical input structures or connected to magnetic nanowires.

In summary, a double-DWG structure provides the requested characteristics and enables signal routing, buffering and synchronization in complex pNML systems.

8.3.2 Micromagnetic simulation

In order to confirm the working principle of the DWG derived in 8.3.1, micromagnetic simulations using the Object Oriented MicroMagnetic Framework (OOMMF) [91] are performed (Fig. 8.3). Therefore, a DWG composed of Co/Pt ($M_s = 7.2 \cdot 10^5$ A/m, $K = 4.3 \cdot 10^5$ J/m³, $A = 1.3 \cdot 10^{-11}$ J/m) with two gate magnets G_1 and G_2 is simulated. The 200 nm wide nanowire is reduced to $h = 40$ nm in the $l = 300$ nm long channel. The apex angle of the notch is $\alpha = 90^\circ$ and the distance between gates and channel is $d = 30$ nm (Fig. 8.3a). According to eq. 8.1, the corresponding theoretical depinning field is $H_{notch} \approx 820$ Oe.

In the simulation, an up-domain is injected on the input side and the DW is propagated through the structure by a stepwise increasing perpendicular field H_z ($\Delta H_z = 20$ Oe). Fig. 8.3b shows the simulation results for the nanowire magnetization M_z versus the perpendicular field H_z depending on the state of the gate magnets.

For each gate configuration, the DW propagates through the channel at small fields $H_z < 250$ Oe. The channel propagation fields are slightly different due to the influence of the gate fringing fields on the effective field. At the end of the channel the DW is pinned due to the energy barrier of the notch. As expected, the still pinned DW expands and is bent to an arc of circle with increasing field H_z . When the applied field reaches the depinning field H_{depin} , the DW is depinned and propagates unimpeded through the output nanowire.

Thereby, the corresponding depinning field is modified by the gate coupling fields, which locally in- or decrease the effective field according to eq. 8.2:

¹Parallel arrangement of the DWGs is also feasible when using $H_{notch} > H_{nuc}$.

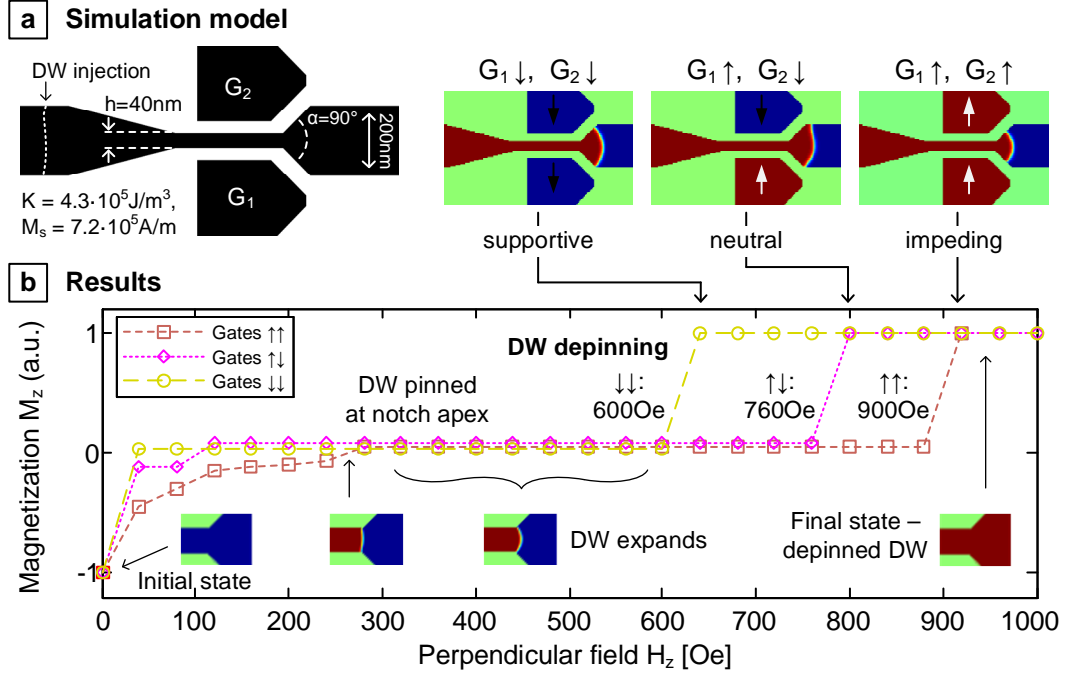


Figure 8.3: Micromagnetic simulation of a DWG. a) Geometry and magnetic constants of the simulation model. DWs are injected on the left side of the nanowire. b) Simulation results show, that the DW depinning field is modified by the applied gate configuration.

- $G_1 = G_2 = 0$: Both gates down increase the effective field by $2H_g$ and therefore lower the DW depinning field to $H_{depin}(\downarrow\downarrow) = 600\text{ Oe}$.
- $G_1 \neq G_2$: For the antiparallel gate configuration, the coupling fields cancel out each other and the DW is depinned at the notch pinning field $H_{depin}(\uparrow\downarrow) = 760\text{ Oe} \approx H_{\text{notch}}$.
- $G_1 = G_2 = 1$: Up gates impede the depinning of the expanding up domain until the applied field H_z reaches the depinning field $H_{depin}(\uparrow\uparrow) = 900\text{ Oe}$.

The pure DW depinning field of the notch can be calculated according to eq. 8.3 to $H_{\text{notch}} = 0.5(H_{depin}(\uparrow\uparrow) + H_{depin}(\downarrow\downarrow)) = 750\text{ Oe}$ and is close to the expected depinning field of 820 Oe from theory. The corresponding strength of the gate fields is $H_g = 0.25(H_{depin}(\uparrow\uparrow) - H_{depin}(\downarrow\downarrow)) = 75\text{ Oe}$.

The results of the performed micromagnetic simulations illustrate the expected behavior of the DW at the notch and the working principle of the DWG, which are both demonstrated by experiment in the following sections.

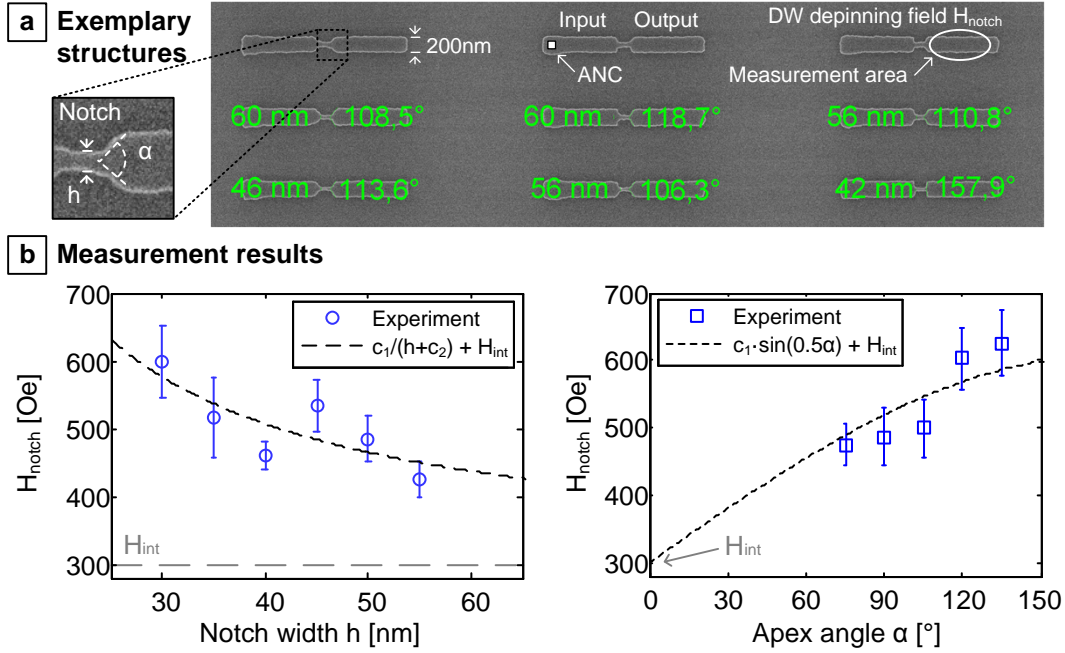


Figure 8.4: Experiment on notches in magnetic nanowires. a) SEM image of exemplary nanowires with notches showing varying channel widths h and apex angles α . ANCs are used to inject DWs at the input side, whereas the depinning field is measured on the output side by WMOKE. b) Measurement results reveal the expected behavior of the depinning field on the notch geometry (error bars = standard error of mean).

8.3.3 Notches in magnetic nanowires

First, the DW pinning in notches of magnetic nanowires with PMA is studied by experiment [SB13c]. Therefore, 200 nm wide $[\text{Co}_{0.8\text{nm}}\text{Pt}_{1\text{nm}}]_{\times 4}$ nanowires featuring notches with varying widths h and apex angles α are investigated. Fig. 8.4a shows several exemplary structures. DWs are nucleated at the ANCs on the input side ($H_{nuc} \approx 400$ Oe) and pinned at the end of the channel. With increasing field, the DWs are depinned again and propagate to the output, where the corresponding depinning field H_{notch} is measured by WMOKE.

The experimental results are shown in Fig. 8.4b. The measured depinning field H_{notch} is in good agreement with the theory according to eq. 8.1 and scales with $H_{notch} \propto \frac{c_1}{h+c_2} + H_{int}$ depending on the notch width h (left). The depinning field shows a strong increase for small notch widths $h < 40$ nm. For different apex angles α (right), the depinning field is $H_{notch} \propto c_1 \sin \frac{\alpha}{2} + H_{int}$ and also matches the theoretical behavior.

The corresponding error bars show the measured standard error of the mean, which

is moderately distributed due to non-sharp edges of the fabricated structures. Furthermore, the plotted results are averaged over multiple angles or widths. The intrinsic pinning field $H_{int} \approx 300$ Oe has been measured in further experiments. The results show that the depinning field of the notch can be adjusted by its geometry, but accurate fabrication is required to reduce variations. However, they are sufficient to pin propagating DWs in DWGs in order to control the signal flow.

8.3.4 Experimental demonstration of the DWG

Structure

A DWG (Fig. 8.5a) fabricated from a $[\text{Co}_{0.8\text{nm}}\text{Pt}_{1\text{nm}}]_{\times 4}$ multilayer stack with $M_s = 7.2 \cdot 10^5$ A/m and $K_{eff} \approx 2.5 \cdot 10^5$ J/m³ is investigated to demonstrate the working principle of field-coupled control of the DW motion [SB14c]. An applied perpendicular field nucleates a DW at the ANC and drives it through the input nanowire into the channel. Thereby, the 200 nm wide nanowire is reduced to $h \approx 40$ nm in the channel, the apex angle on the output side is $\alpha \approx 90^\circ$. The field-driven DW is pinned at the notch apex, whose depinning field is modified by the close-by gate magnets G_1 and G_2 ($d \approx 30$ nm). Numerical calculations predict coupling fields of $H_g = 60$ Oe for each gate magnet. With increasing field, the DW is depinned and propagates through the output nanowire.

Method

In the experiment, LMOKE is used to measure the DW nucleation (probability) at the input and the DW depinning (probability) at the output nanowire. Fig. 8.5b shows exemplary hysteresis curves of the DW nucleation at the input nanowire (solid line) and the DW motion through the output nanowire (dashed lines). The DW is nucleated at $H_{nuc} \approx 0.4$ kOe, whereas depinning from the notch varies in the range of $H_{depin} \approx 0.5 \dots 0.9$ kOe depending on the configuration of the gate magnets. Thereby, the output hysteresis curve is shifted to the right with an increasing number of up-gates.

In order to determine the DW nucleation / depinning probability densities, the following experiment is repeated several times ($N = 50$) for each gate configuration:

- First, the gate configuration is set by initial perpendicular field pulses and verified by MFM.
- Afterwards, the nanowire is set to the down-state by a negative field pulse of $H_{init} = -1$ kOe.

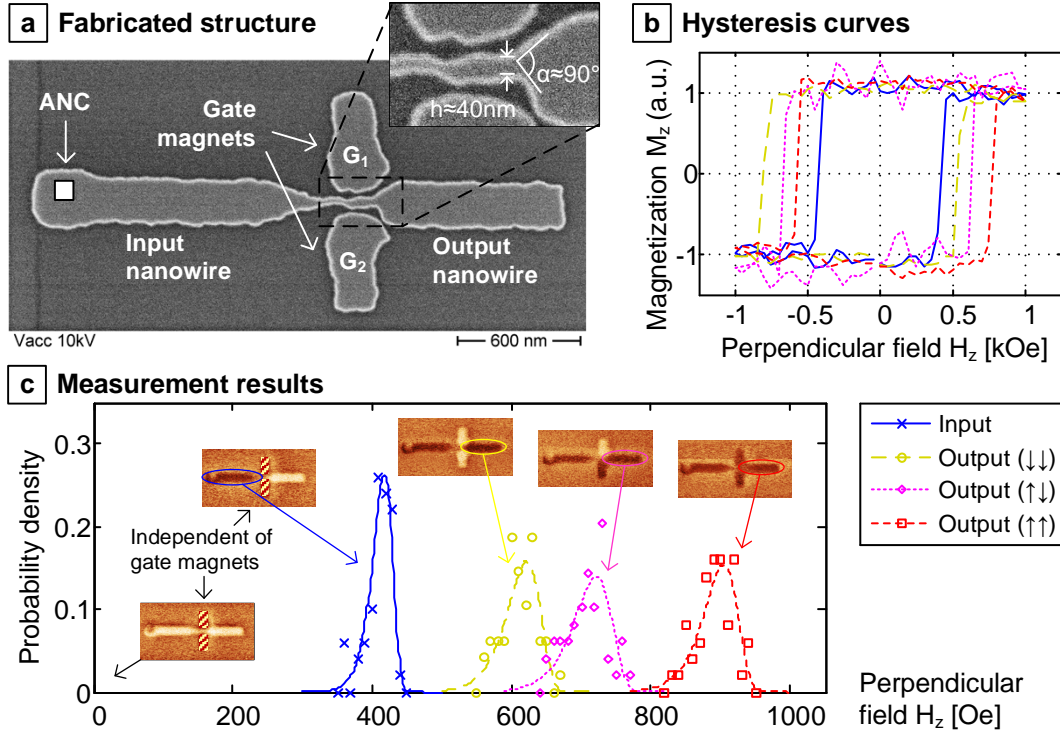


Figure 8.5: Experimental demonstration of the domain wall gate. a) Fabricated structure. b) Hysteresis curves of input and output for different states of the gate magnets. c) Measured probability densities of DW nucleation at the input side and the DW depinning field depending on the gate configuration.

- Finally, the magnetic field H_z is ramped from 0 to $H_{max} = 1$ kOe (rate $R = 2$ kOe/s) to measure the DW nucleation field H_{nuc} at the input or the depinning field H_{depin} at the output, respectively.

Results

Fig. 8.5c shows the measured probability densities for DW nucleation on the input side (blue solid line) and the DW depinning field of the DWG (dashed lines) for different gate configurations as well as the corresponding MFM images:

- **Nucleation:** DWs are nucleated at $H_{nuc} = 410$ Oe at the ANC on the input side independently of the gate states.
- **Depinning:** The nucleated DWs propagate through the channel and are pinned at the end for all gate configurations. The corresponding depinning field varies due to the influence of the coupling fields on the energy barrier:

Parameters	Simulation		Experiment	
Anisotropy	$K = 4.3 \cdot 10^5 \text{ J/m}^3$		$K_{eff} \approx 2.5 \cdot 10^5 \text{ J/m}^3$	
Magnetization	$M_s = 7.2 \cdot 10^5 \text{ A/m}$		$M_s \approx 7.2 \cdot 10^5 \text{ A/m}$	
Notch width	$h = 40 \text{ nm}$		$h \approx 40 \text{ nm}$	
Apex angle	$\alpha = 90^\circ$		$\alpha \approx 90^\circ$	
Results	Simulation	(Theory)	Experiment	(Theory)
Depinning field H_{notch}	750 Oe	(820 Oe)	760 Oe	(1.5 kOe)
Gate fields H_g	75 Oe	(—)	90 Oe / 50 Oe	(60 Oe)

Table 8.1: Summary of theoretical, simulation and experimental results of the domain wall gate.

- : $G_1 \downarrow, G_2 \downarrow$: If both gate magnets are down, the expanding up-domain is supported by the gate fields and the DW depinning field is reduced to $H_{depin}(\downarrow\downarrow) = 620 \text{ Oe}$.
- : $G_1 \downarrow, G_2 \uparrow$: With both gates up, the depinning field is increased and the DW is blocked until the applied field reaches $H_{depin}(\uparrow\uparrow) = 900 \text{ Oe}$.
- : $G_1 \downarrow, G_2 \uparrow$: In the antiparallel case (neutral state), the gate fields cancel out each other and the DW is depinned at $H_{depin}(\uparrow\downarrow) = 720 \text{ Oe}$.

Analysis

The pure depinning field of the notch without any gate influence is calculated by $H_{notch} = 0.5 (H_{depin}(\downarrow\downarrow) + H_{depin}(\uparrow\uparrow)) = 760 \text{ Oe}$, which is far away from the theoretical value of $H_{notch} = 1.5 \text{ kOe}$ using eq. 8.1 ($H_{int} = 300 \text{ Oe}$). Presumably, the depinning field is significantly lowered by the non-sharp edges of the notch. According to eq. 8.3, the coupling fields are determined to $H_{g1} = 90 \text{ Oe}$ for gate G_1 and $H_{g2} = 50 \text{ Oe}$ for gate G_2 , respectively. The difference is assumed to occur due to the asymmetry of the notch (cp. Fig. 8.5a) and the coupling field gradient within the notch for antiparallel gates. Hence, also the depinning field in neutral (antiparallel) state $H_{depin}(\uparrow\downarrow) = 720 \text{ Oe}$ differs significantly from the expected field (= pure notch depinning field) of $H_{notch} \approx 760 \text{ Oe}$.

However, the measurement results demonstrate control of DW pinning in a notch by the magnetization state of close-by gate magnets and are in good agreement with the micromagnetic simulations. Tab.8.1 shows a summary of theoretical, simulated and experimental results of the DWG.

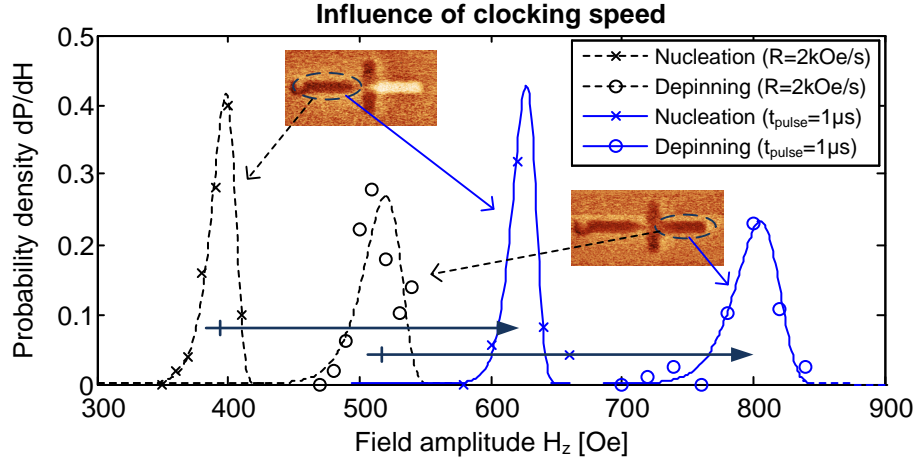


Figure 8.6: Influence of the clocking speed on a DWG. Both DW nucleation and depinning fields are increased for when changing from slowly ramped fields ($R = 2 \text{ kOe/s}$) to short field pulses $t_{\text{pulse}} = 1 \mu\text{s}$.

Speed

Naturally, for application in high-frequency clocked pNML systems also correct operation of the DWG on fast time scales is required. Therefore, the experiment shown above is partly repeated for another DWG ($h = 44 \text{ nm}$, $\alpha \approx 100^\circ$) using field pulses in the μs -range [SB13c].

Both the DW nucleation and the DW depinning from a notch are thermally activated processes and the corresponding field amplitudes increase for shorter timescales as discussed in secs. 2.3.4 and 2.5. Fig. 8.6 shows the influence of the clocking speed on DW nucleation and depinning fields in a DWG (both gates up). When the applied field amplitude H_z is ramped slowly ($R = 2 \text{ kOe/s}$), the DW is nucleated at the ANC at $H_{\text{nuc,ramped}} = 400 \text{ Oe}$ and pinned in the notch up to $H_{\text{depin,ramped}} = 520 \text{ Oe}$. By applying short pulses (as preferred for clocking) with a pulse time of $t_{\text{pulse}} = 1 \mu\text{s}$, both the DW nucleation ($H_{\text{nuc,pulsed}} = 640 \text{ Oe}$) and the DW depinning ($H_{\text{depin,pulsed}} = 820 \text{ Oe}$) probability densities are shifted to significantly higher field amplitudes. However, both nucleation and depinning fields are increased in the same way ($\frac{H_{\text{nuc,pulsed}}}{H_{\text{nuc,ramped}}} \approx \frac{H_{\text{depin,pulsed}}}{H_{\text{depin,ramped}}} \approx 1.6$) and the still DWG operates reliable in the MHz-range. As the DW velocity v_{DW} also increases for higher field amplitudes, the device speed is also increased.

The experiments successfully demonstrate the working principle of the DWG. For application in pNML, the nucleation field H_{nuc} and the notch depinning field H_{notch} have to be matched as shown in [SB13c]. Accordingly, double-DWG structures enable to control the signal flow within pNML systems.

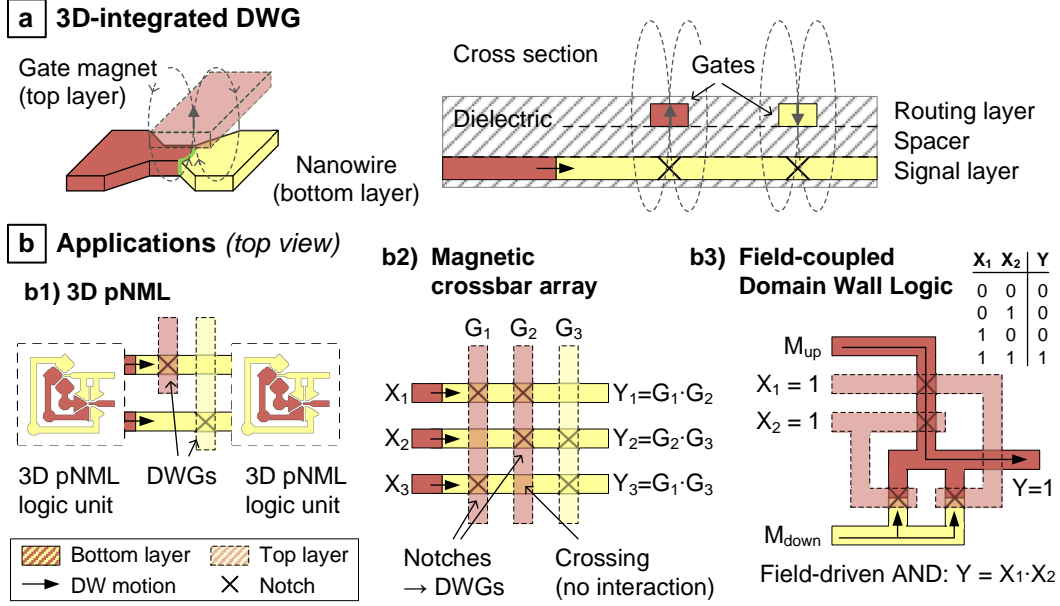


Figure 8.7: 3D integration of a DWG and possible applications. a) 3-dimensional coupling fields enable to place the gate magnet (routing layer) above the notch to control the DW motion in the nanowire (signal layer). b) Possible applications include signal routing in 3D pNML (1), non-volatile, pure magnetic crossbar arrays (2) or Field-coupled Domain Wall Logic providing CMOS-like gate structures (3).

8.3.5 3D integration and applications

The 3-dimensional character of the gate coupling field enables 3D integration of a DWG [SB13c, SB15a],[Hib12]. 2D-embedded DWGs hold limited use for high-density applications, because several crossings and magnetic vias [EBK⁺14] are required to connect the gates in integrated pNML circuits. By contrast, 3D integration of a DWG enables the separation of the controlling routing layer and the logic processing signal layer.

Working principle

In a 3D DWG, the gate magnet to control the DW pinning is located directly above (or underneath) the notch (Fig. 8.7a). Propagating DWs through a nanowire, which is located in the signal layer, are pinned at the notch of the DWG according to eq. 8.1. The corresponding depinning field is in- or decreased by the (in this case) ferromagnetically acting coupling field of the gate magnet in the routing layer:

$$H_{depin} = H_{notch} - H_g M_g. \quad (8.5)$$

Thereby, the gate field strength H_g depends on the size of the gate, the lateral alignment of the structures and the vertical distance to the notch [SB13c, SB15a]. The two functional layers are separated by a thin dielectric ($\approx 40 \dots 60$ nm), which may be spun-on and hardened using e.g. hydrogen silsesquioxane (HSQ), [EKB⁺13] or deposited and planarized by chemical mechanical polishing (CMP). For correct operation in pNML systems, this spacer layer has to be thin enough to provide sufficient coupling field strengths at notches and ANC's of 3D majority gates, but thick enough to enable unimpeded signal crossing [EBK⁺14, EBZ⁺14]. First fundamental studies prove the working principle of 3D-integrated DWGs [Hib12] and have recently been published in [SB15a]. They also indicate several, significant benefits of 3D-integrated DWGs:

- **Reduced footprint:** Arranging the gate directly below or above the notch, enables to reduce the channel length and redundantizes the area required for the gate magnets beside the notch. Probably, the footprint can be reduced to $F^2 < 0.01 \mu\text{m}^2$ by using a gate magnet $< 50 \cdot 100 \text{ nm}^2$, which is sufficient to control the DW motion in a 50 nm-wide nanowire (channel length 100 nm).
- **Increased control:** A reduced distance between gate and notch increases the gate field significantly. Numerical simulations show, that the gate field is increased up to $H_g = 200 \text{ Oe}$ while still providing a sufficient thickness of the spacer layer [SB13c].
- **Higher operating speed:** Shorter channel lengths reduce the DW propagation time and therefore increase the device speed. Reduced dimension smaller than 100 nm length enable transition times $t = \frac{l_{\text{channel}}}{v_{\text{DW}}} < 5 \text{ ns}$ shifting the operating frequency well above 100 MHz-border.
- **Reduced circuit complexity:** Separation of signal and routing layer makes several crossing structures and magnetic vias become redundant and therefore reduces both complexity and footprint of the circuit.

Applications

3D DWGs are very promising to control the signal flow between the logic units in (3D) pNML systems (Fig. 8.7b₁). Compared to their 2D version, they provide reduced circuit complexity and footprint with simultaneously increased speed. Naturally, again multiple 3D DWGs are required for adequate signal routing in each interconnect.

Due to the uniformity of input, output and gate, each output nanowire can act as input or gate for one or more subsequent DWGs. The concatenation of multiple DWGs enables a wide range of DW-based circuits, such as magnetic crossbar arrays (Fig. 8.7b₂). Here, each input wire X_i contains several notches controlled

by the gates $G_1 \dots G_n$. Simple crossings do not influence the DW motion. The resulting output function Y_i reminds to an AND-structure and depends on the existence of potential pinning sites and the state of the gate array.

A completely new approach is Field-coupled Domain Wall Logic (FDWL) [Hib12]. Here, the combination of multiple 3D DWGs in series and in parallel provides logic functionality in CMOS-like Boolean gate structures (Fig. 8.7b₃). Regions of up- and down-magnetization M_{up} and M_{down} are used analogous to V_{DD} and V_{SS} in CMOS circuits to switch the output Y depending on the input gate configuration $X_1 \dots X_n$. The resulting output Y can serve as input gate for subsequent structures by using magnetic vias to transfer the signal to the routing layer. Furthermore, pNML and FDWL can be combined to enhance the functionality of a logic system.

8.4 Alternative concepts for signal routing

The DWGs demonstrated in the previous sections enable direct control of the DW motion in magnetic interconnects of pNML systems. However, the alternation between blocking and transfer period requires an additional control unit to switch the corresponding gate magnets to the proper states (cp. sec. 8.3.1). Furthermore, two connected DWGs are necessary to control the signal flow independently from the incoming signals. Consequently, there is some potential to further improve signal buffering and synchronization in pNML systems.

Necessarily, DWs propagating through the interconnects have to be blocked for signal buffering during the blocking period, and let through for synchronization during the transfer period. In the concept illustrated in Fig. 8.8, DWs are blocked in notches, whose energy barrier can be reduced with local in-plane fields to let the DWs propagate through. The in-plane field pulses are generated by current pulses through subjacent current wires and synchronized with the clocking field to control the signal flow.

Designing the depinning field of the notch to $H_{notch} > H_{clock} = H_{nuc}$ will block every propagating DW in the interconnects and buffer inputs of subsequent logic units. The additional energy required to overcome the energy barrier of the notches during the transfer period is supplied by in-plane field pulses H_{sync} . Thereby, the resulting depinning field $H_{depin} < H_{clock}$ is reduced independently of the expanding domain.

The in-plane field pulses are generated by short current pulses I_{sync} through current wires, which are buried in the substrate and lie just below the notches. It is important that the field pulses are limited to the area of interest and do not modify the nucleation fields in the nearby logic gates. Here, an architecture based on systolic arrays turns out to be very beneficial (cp. Fig. 8.8). Yoke-like claddings of the wires are suitable to reduce the required current density and the corresponding

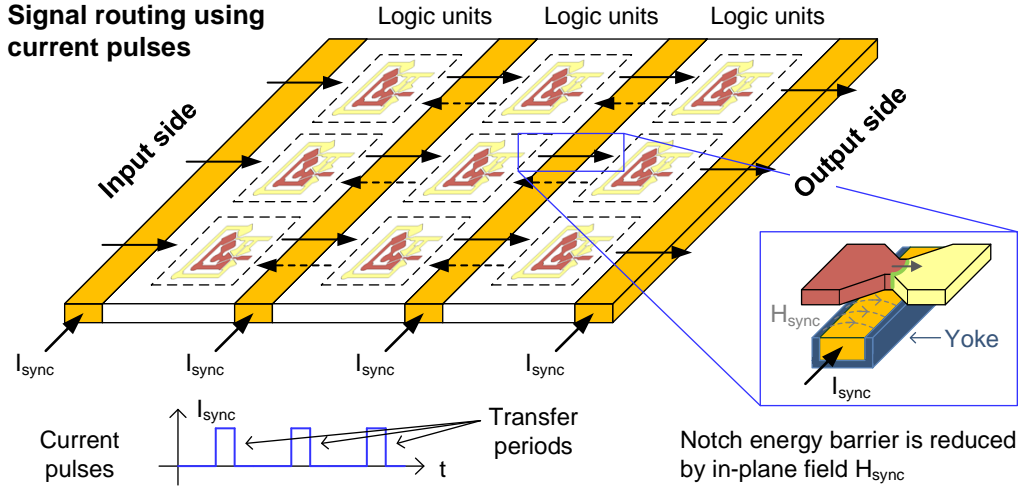


Figure 8.8: Alternative concept for signal routing in pNML. Current pulses I_{sync} through buried wires generate in-plane fields H_{sync} , which reduce the energy barrier of the notch and therefore the DW depinning field.

power losses [199, 200]. Obviously, such a signal routing concept

- is independent of the signals themselves,
- significantly reduces the circuit complexity,
- enables simple signal control (current pulses every second clocking cycle),
- provides minor area overhead, and
- is comparatively easy to fabricate.

Potentially, the controlled DW depinning could also be supplied by the SHE [79, 201, 202]. Current pulses through small Pt wires < 100 nm, arranged as in Fig. 8.8 but contacted to the notches, could detach the pinned DWs. This would further reduce both footprint and energy consumption, but more engineering is necessary in this recent field of research.

8.5 Arithmetic logic unit (ALU)

The TLG-based 1-bit full adder structure as demonstrated in sec. 7.2.3 can be used as processing unit for further logic and boolean operations [SB14b]. Fig. 8.9a shows the schematic of a pure magnetic ALU, where the full adder structure as central element is extended by two inverters to implement the non-inverted outputs C_{out} and S .

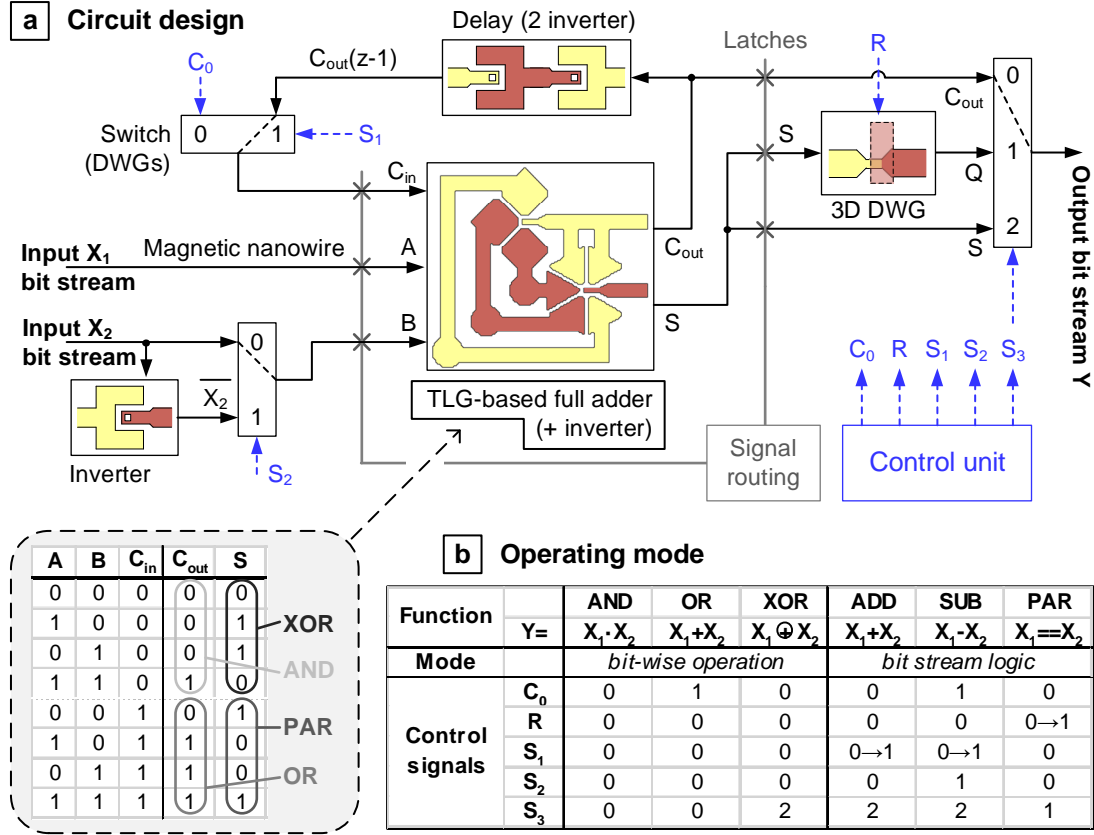


Figure 8.9: Arithmetic Logic Unit in pNML. a) Schematic of the circuit design based on a TLG-based full adder. The input bit streams X_1 and X_2 are processed through the adder and an optional 3D DWG to generate the output stream Y . Signal routing is provided by latches (i.e. controlled DW pinning at notches). b) Switches (e.g. based on DWGs) are set by a control unit to program the operating mode of the ALU.

8.5.1 Working principle

The input bit streams X_1 and X_2 are processed through the adder and an optional 3D DWG to generate the output stream Y . Thereby, the inputs are set bit-wise every second clocking cycle starting with the least significant bit (LSB) and ending with the most significant bit (MSB) of each bit stream.

Operating modes

According to its truth table (Fig. 8.9a bottom left), the inputs A and B are bit-wise processed with the AND, OR, XOR function or tested on parity (PAR) depending on the state of the carry-in C_{in} and the evaluated output (C_{out} or S).

The carry-out C_{out} is fed back through a delay using two inverters ($\hat{=}$ one clocking cycle) and a controllable switch to the carry-in C_{in} . Accordingly, the ALU provides the addition (ADD) or subtraction (SUB) of two bit streams X_1 and X_2 . As customary, the bit stream X_2 has to be inverted by an additional inverter and increased by 1 ($C_{in}(0) = 1$) for the subtraction of two bit streams $X_1 - X_2$.

For parity check of whole bit streams (e.g. for sample recognition), a simple 3D DWG with a gate set to up-state is used as magnetic latch². Once the currently processed bits of X_1 and X_2 differ, the sum S is 1 and the latch output Q is irreversibly set to 1. Consequently, only the MSB decides about the parity of the whole bit streams (0 = equal, 1 = unequal). The latch output Q can be reset by the input R of the control unit.

In summary, the ALU provides bit-wise Boolean AND, OR or XOR operation and ADD, SUB or PAR on open-end bit streams.

Control unit

Three controllable switches S_1 , S_2 and S_3 are required to program the operating mode of the ALU. According to Fig. 8.9b they control the (initial) carry-in C_{in} to program the function of the adder, invert the bit stream X_2 for subtraction and direct the correct signal (C_{out} , Q or S) to the output Y of the ALU.

In principle, such switches can be realized by using a fan-in (multiple inputs guided to one output) with a double-DWG structure for each input to set the switch.

The switches S_1 , S_2 and S_3 are set by a control unit, which also sets the (initial) carry-in C_{in} and resets the 3D DWG output by R .

Signal routing

A signal routing unit controls the DW motion in the magnetic interconnects. The junctions (marked by an X) are controlled to conduct any magnetic signal every second clocking cycle for signal buffering and synchronizations. Therefore, double-DWG structures as shown in sec. 8.3.1 or one of the alternative concepts outlined in sec. 8.4 are feasible.

8.5.2 Simulation

The working principle of the ALU is demonstrated by compact model simulations. Thereby, the magnets of the ALU are modeled by their switching behavior according to the DW nucleation probability model (cp. sec. 2.5) and their interaction by their coupling field (sec. 2.6) as shown in [SB14c]. The simulation results are shown in Fig. 8.10.

²By contrast to the ALU of [SB14b], the two majority gates of the RS latch have been replaced by a 3D DWG to increase the operating speed.

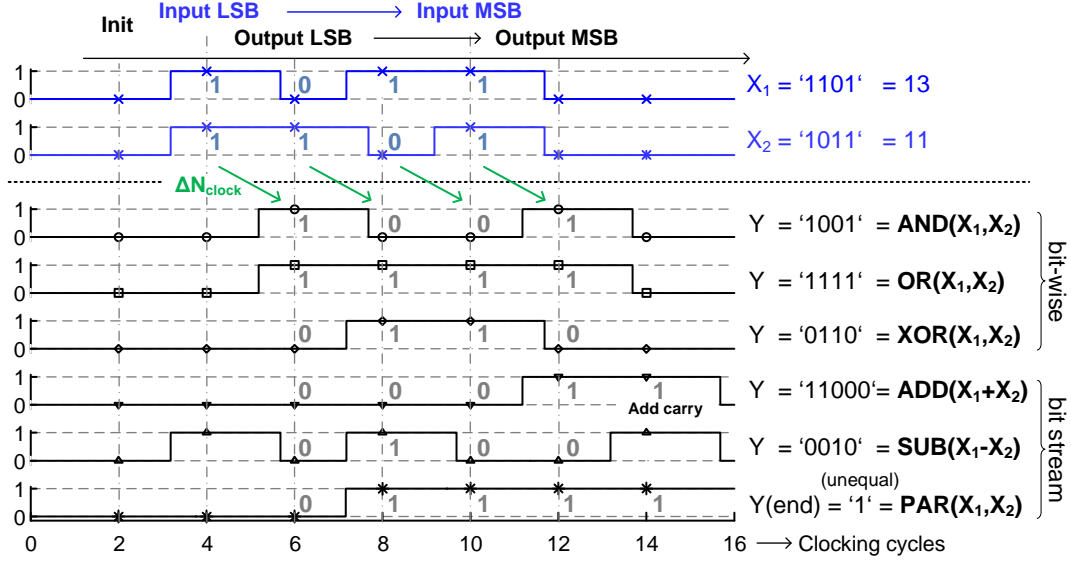


Figure 8.10: Simulation results for processing two 4-bit streams depending on the operating mode of the ALU. Correct logic operation is provided in each operating mode, whereas the processing delay of the ALU is $\Delta N_{clock} = 2$ clocking cycles as desired.

Two exemplary bit streams $X_1 = '1101'$ and $X_2 = '1011'$ are processed through the ALU, which is programmed to the corresponding operating mode by the control unit. Note, control signals (i.e. R and S_1) can change from the initial clocking cycle to the remaining ones (i.e. from zero to one: $0 \rightarrow 1$, cp. Fig. 8.9b) to provide correct functionality.

An initial clocking phase consisting of almost two clocking cycles with $X_1 = X_2 = 0$ and $C_{in}(0) = R = S_1 = S_2 = S_3 = 0$ is needed to reset the ALU. Afterwards, the inputs bits are set every second clocking cycle starting with the LSB of each bit stream X_1 and X_2 .

The output stream Y is delayed for only favorable $\Delta N_{clock} = 2$ clocking cycles (cp. sec. 8.2.1) and shows correct logic computation in each programmed operating mode. The input bit streams $X_1 = '1101'$ and $X_2 = '1011'$ are bit-wise AND-, OR- or XOR-operated, or stream-wise added (ADD), subtracted (SUB), or tested on parity (PAR).

Furthermore, correct operation of the ALU has been confirmed in additional simulations with different input patterns. In summary, the simulation results successfully demonstrate the functionality of the presented pure-magnetic ALU.

8.5.3 Application in pNML systems

The ALU is highly suitable as basic logic cell in systolic arrays. As required, it inherently provides

- several types of minor logic operations (AND, OR, XOR, PAR, ADD, SUB),
- runtime-programmability,
- bit-wise and open-end bit stream processing,
- minimum signal delay (2 clocking cycles), and
- simple and regular signal and control flow.

The application in systolic architectures with multiple, interconnected ALUs as logic units according to Fig. 8.1 enables extensive parallel computing. Thereby, it still provides typical characteristics of pNML, such as

- low-power computing with zero leakage,
- high-density, 3D integration,
- non-volatility and radiation hardness.

Furthermore, it meets the requirements on emerging beyond-CMOS technologies ([21], cp. sec. 1.1.1) like room temperature operation, scalability or CMOS compatibility. Therefore, systolic pNML systems based on ALU cells are very beneficial for highly-demanded arithmetic computing problems as image processing, signal filtering, DFT, matrix arithmetic or pattern matching.

9 Conclusion

Summary

In the present work, the theory, fabrication and fundamentals of pNML logic devices are introduced. Basic computing gates are investigated and digital logic circuits are demonstrated by experiment. Compact model simulations indicate the potential of pNML and outline the promise of pNML systems.

Within this work, a laser-scanning and a wide-field magneto-optical microscope were built up, which enable extensive measurements on field-coupled nanomagnets with perpendicular magnetic anisotropy (PMA). The development of suitable measurement techniques provides deeper insight in the switching characteristics of the investigated nanomagnets and enables fast imaging of magnetized surfaces and magnetic states. High lateral resolutions (< 300 nm), easy sample preparation, accurate magnetic fields (both slowly ramped or pulsed in the sub- μ s-range) and fast measurement times of the magneto-optical microscopes are key features for their use in almost all experiments performed in this work.

Partial focused ion beam (FIB) irradiation of isolated Co/Pt multilayer islands generating so-called artificial nucleation centers (ANCs) was invented and investigated in this work to specifically control the domain wall (DW) nucleation in the magnets. Experimental results are analyzed and are found to be in very good agreement with the theory. Based on irradiation-induced ANCs, directed signal flow within field-coupled magnets is proven by experiment for the first time. The demonstrated technique is the basis for a multitude of applications in both experiment and simulation. Time-dependent characteristics for DW nucleation from ANCs are studied and are in very good agreement with the theory. Requirements on the clocking field in order to perform logic operations are discussed.

Logic information processing is provided by clocking field-induced DW nucleation from ANCs, which is controlled via field-coupling by the magnetization states of the surrounding input magnets. A majority gate with perpendicular anisotropy as universal logic device in pNML is demonstrated by experiment for the first time. In combination with an inverter structure, it provides the basic Boolean functions (NOT, AND, OR). Magnetic nanowires and fanout structures employed as interconnects between subsequent logic gates are investigated to provide unimpeded signal transport (i.e. DW propagation).

A 1-bit full adder circuit built from the basic logic elements majority gate, inverter, nanowire and fanout is shown in order to demonstrate the feasibility of complex

pNML circuitry. To our best knowledge, this is the most complex circuit, which is up-to-date successfully demonstrated by experiment in NML. Correct operation is proven by magnetic force microscopy (MFM) for all possible input patterns of the adder circuit.

Threshold logic is applied to pNML to reduce the circuit size and complexity. A threshold logic gate (TLG)-based 1-bit full adder $< 2 \mu\text{m}^2$ using a novel 5-input gate is experimentally demonstrated. The fabricated circuit consists of only 2 majority gates with in total only 5 magnets (3 inputs, 2 output) and shows reliable operation.

Physical-based compact modeling of field-coupled magnets is introduced in order to specify the characteristics of pNML circuitry and enable simulation-based circuit design. The provided compact models enable to simulate the circuit behavior depending on the magnet geometry, magnetic material, technology node, irradiation spots, fabrication variations, clocking speed, temperature and noise. In the simulations, the potential of the TLG-based full adder is analyzed in terms of progressive scaling, clocking speed and material improvements. The results show that scaling increases the operational reliability (error rate $e < 10^{-4}$) and enables to increase the clocking speed to the +100 MHz-range. Material improvements allow to reduce the clocking power consumption and to significantly decrease the error rate.

An outlook to integrated pNML systems is given discussing several important aspects like suitable architectures, signal routing concepts and processing of magnetic bit streams. Systolic architectures based on interconnected logic units with minor logic functionality and massively parallel information processing are found to be very beneficial for pNML. Signal routing concepts for systolic arrays to control the signal flow between the logic units are discussed. Simulations and experiments show that domain wall gates as invented in this work enable to control the DW motion within magnetic nanowires in order to direct the signal flow in pNML systems. Finally, an arithmetic logic unit (ALU) based on the findings gathered within this work is presented and investigated by simulation. Signal routing concepts are applied to an extended TLG-based 1-bit full adder (core of the ALU) in order to program the logic operation on two magnetic bit streams. The ALU provides bit-wise AND, OR, XOR functionality as well as the addition, subtraction or parity check of open-end bit streams and is therefore highly suitable as runtime-programmable logic unit in systolic pNML systems.

Future perspective

The experiments performed in this work and summarized above demonstrate, that in principle pNML meets all the requirements on emerging beyond-CMOS devices as requested (sec. 1.1.1, [21]). However, to compete with CMOS and other emerging technologies, a lot of further research and engineering on pNML is essential.

Compact model simulations show that pNML features much room for improvement of common physical measures (area, power, speed) and the logic reliability (error rate) by continued engineering. Progressive scaling of pNML devices decreases the circuit footprint and at the same time increases the coupling fields. Consequently, the error rate is significantly reduced and the clocking speed can be increased due to the shorter magnet size. Novel materials with lower effective anisotropy, but equivalent (or even higher) areal magnetic moment (e.g. Co/Ni or CoFeB multilayers) enable to further improve the characteristics of pNML. They provide reduced switching fields and narrower nucleation probability densities, which in turn may reduce both the clocking power consumption and the error rate. Probably higher DW propagation speeds will enable to increase the clocking frequency.

One of the major challenges is to reduce the fabrication-dependent switching field distribution (SFD) among the ANC's, which currently limit to further increase the number of devices per circuit in a manner analogous to Moore's law. Therefore, different ANC fabrication processes using lighter-ion irradiation (e.g. by Helium (He) FIB systems [203]), ion implantation or even replacing conventional ANC's by shape-induced nucleation sites [204], are promising approaches.

3D integration of pNML is very promising in order to reduce the circuit footprint, the clocking power consumption and the circuit complexity [EBZ⁺14]. Magnetic vias and 3D majority gates provide interconnect-free signal transmission and processing within multiple functional layers. The expansion of systolic arrays of pNML into the 3rd dimension will further improve its applicability and attractiveness to widely-used, regular arithmetic processing tasks. Finally, I/O devices, clocking structures and signal routing concepts should be integrated in a stack of functional layers of 3D pNML.

Several beneficial key features (i.e. high-density 3D integration, majority voting, non-volatility, no interconnects, zero leakage) indicate pNML as highly competitive in terms of area and power consumption. In order to compare the performance of pNML with other emerging beyond-CMOS device candidates, benchmarking of integrated pNML circuits is required [21]. Therefore, layouts and characteristics of essential pNML logic elements and circuits have to be further investigated and evaluated in terms of area, power and delay.

In summary, the present work is the first extensively investigating the fundamentals of pNML and demonstrating their application in basic logic elements, standard logic circuits and signal routing devices. The fundamentals demonstrated in this work are the basis for a wide-range of logic operation in field-coupled, perpendicular magnetic media. The results pave the way for the development of 3D-integrated pNML systems based on systolic arrays, which are very promising as co-processing units for specific computing tasks in hybrid CMOS/pNML ICs.

Acronyms

AFM	atomic force microscopy
Al	Aluminium
ALU	arithmetic logic unit
AM	antiferromagnetic
ANC	artificial nucleation center
Ar	Argon
CCD	charge-coupled device
CMOS	complementary metal-oxide semiconductor
CMP	chemical mechanical polishing
Co	Cobalt
CP	circular polarized
Cu	Copper
DAQ	data acquisition
DFT	discrete Fourier transformation
DLI	direct lithography irradiation
DTPL	Domain-tip Propagation Logic
DW	domain wall
DWG	domain wall gate
DWL	Domain Wall Logic
EHE	extraordinary Hall effect
EP	elliptic polarized
ERD	Emerging Research Devices
FDWL	Field-coupled Domain Wall Logic
FET	field effect transistor
FFT	fast Fourier transformation
FIB	focused ion beam
FM	ferromagnetic

FPGA	Field-Programmable Gate Array
Ga	Gallium
GMR	giant magnetoresistance
He	Helium
HF	hydrofluoric acid
HSQ	hydrogen silsesquioxane
IBE	ion beam etching
ICs	integrated circuits
IEEE	Institute of Electrical and Electronics Engineers
iNML	in-plane Nanomagnetic Logic
ITRS	International Technology Roadmap for Semiconductors
LCP	left circularly polarized
LD	long-working distance
LED	light-emitting diode
LLG	Landau-Lifshitz-Gilbert
LMOKE	laser-scanning MOKE microscope
LP	linear polarized
LSB	least significant bit
LTE	Lehrstuhl für Technische Elektronik
MBE	molecular beam epitaxy
MFM	magnetic force microscopy
MIBK	Methylisobutylketon
MOKE	magneto-optical Kerr effect
MOSFET	metal-oxide semiconductor field effect transistor
MQCA	Magnetic Quantum Cellular Automata
MSB	most significant bit
MTJ	magnetic tunnel junction
NA	numerical aperture
ND	University of Notre Dame
NEMS	Nano-Electro-Mechanical switches

NML	Nanomagnetic Logic
NMP	N-Methylpyrrolidone
OOMMF	Object Oriented MicroMagnetic Framework
PAM	pulse-amplitude modulation
PEEM	photoemission electron microscopy
PID	proportional-integral-derivative
PLA	Programmable Logic Array
PMA	perpendicular magnetic anisotropy
PML	Perpendicular Magnetic Logic
PMMA	Polymethylmethacrylate
pNML	perpendicular Nanomagnetic Logic
Pt	Platinum
PVD	physical vapor deposition
Py	Permalloy
QCA	Quantum Cellular Automata
RCP	right circularly polarized
RF	radio frequency
ROI	region of interest
RT	room temperature
SD	standard deviation
SEM	scanning electron microscope
SFD	switching field distribution
SHE	Spin Hall effect
Si	Silicium
SNR	signal-to-noise ratio
SOTA	state-of-the-art
SQUID	superconducting quantum interference device
STM	scanning tunneling microscopy
STO	Spin Torque Oscillator
STT	spin transfer torque
Ta	Tantalum

Acronyms

TEM	transmission electron microscopy
Ti	Titanium
TL	Threshold Logic
TLG	threshold logic gate
TMR	tunnel magnetoresistive
TUM	Technische Universität München
USB	universal serial bus
VSM	vibrating-sample magnetometry
WMOKE	wide-field MOKE microscope

List of Symbols

A	exchange stiffness (material constant) [J/m]
A_x	area of element x, e.g. of a domain
α	damping constant (material constant)
α_x	angle of element x, e.g. apex angle of a notch
B	magnetic flux density
C (r)	magnetic coupling field
C	coupling field strength
C_{eff}	effective coupling field strength
D_{crit}	critical single domain diameter
d	distance, length, diameter
d_{min}	diffraction limit
Δ	domain wall width parameter
ΔH_{clock}	range of the clocking window
Δt	step time (simulation)
δ_k	width of the anisotropy gradient
δ_w	domain wall width
E_0	energy barrier at zero field
E ₀	complex electric field amplitude vector
E_{ani}	anisotropy energy
$E_{ani,s}$	surface (and interface) anisotropy energy
$E_{ani,u}$	uniaxial anisotropy energy
$E_{barrier}$	energy barrier
E_{demag}	demagnetization energy (or stray field energy)
$E_{exchange}$	exchange energy
E_{me}	magnetoelastic energy (due to external stress)
E_{ms}	magnetostrictive stress energy
E_{pin}	pinning energy barrier

List of Symbols

$E_{thermal}$	thermal energy
E_{total}	total energy
$\mathbf{E}(\mathbf{r}, t)$	electric field vector
E_{Zeeman}	Zeeman energy (or external field energy)
e	elementary charge $e = 1.602 \cdot 10^{-19}$ C
e	error rate
\mathbf{e}_j	unit current density vector
\mathbf{e}_m	unit magnetization vector
\mathbf{e}_s	spin unit vector
\mathbf{e}_z	unit vector (in z-direction)
$\tilde{\epsilon}$	dielectric tensor
ϵ_{ani}	anisotropy energy density
ϵ_{ell}	ellipticity
ϵ_{tot}	total energy density
ϵ	dielectric permittivity
f_0	attempt frequency f_0
f_{clock}	clocking frequency
g	gyromagnetic splitting factor g (g-factor, constant close to 2)
$\mathbf{g}(t)$	Gaussian-distributed random vector
γ	gyromagnetic ratio (constant): ratio between a magnetic dipole moment and its angular momentum
\mathbf{H}	magnetic field
H_0	coercive field at zero temperature
H	magnetic field amplitude
\mathbf{H}_a	effective anisotropy field
H_{ANC}	anisotropy field of the ANC
H_{ani}	anisotropy field
H_c	coercive field or coercivity
H_{clock}	clocking field amplitude
\mathbf{H}_{demag}	demagnetization field (or stray field)
H_{depin}	depinning field
\mathbf{H}_{eff}	effective field

\mathbf{H}_{ex}	effective exchange field
\mathbf{H}_{ext}	external magnetic field
H_{int}	intrinsic pinning field
H_{notch}	depinning field of a notch
H_{nuc}	nucleation field
H_{prop}	propagation field
H_{pulse}	field pulse amplitude
H_s	saturation field
$\mathbf{H}_{thermal}$	thermal field (stochastic)
H_w	Walker field
H_z	perpendicular magnetic field
h_x	width of the element x, e.g. notch or nanowire
\hbar	reduced Planck constant $\hbar = 1.055 \cdot 10^{-34}$ Js
I	current
\mathbf{Im}_{mag}	magnetic image
\mathbf{Im}_{ref}	reference image
J_0	exchange constant between contiguous spins
\mathbf{j}	current density vector
j	current density
K_{eff}	effective anisotropy constant [J/m ³]
K_s	surface anisotropy constant [J/m ²]
$K_{u1,2}$	uniaxial anisotropy constant [J/m ³]
\mathbf{k}	wave (propagation) vector
k_B	Boltzmann constant $k_B = 1.381 \cdot 10^{-23}$ J/K
$l_{exchange}$	exchange length
l_{mag}	length of a magnet
l_{prop}	propagated distance of a DW
λ	wave length
\mathbf{M}	magnetization vector $\mathbf{M} = M_s \cdot \mathbf{e}_m$
M	magnetization
\mathbb{M}	majority operator
M_r	remanence magnetization

List of Symbols

M_s	saturation magnetization [A/m]
M_z	perpendicular magnetization
m_e	electron mass $m_e = 9.109 \cdot 10^{-31}$ kg
\mathbf{m}	magnetic moment
μ_B	Bohr magneton $\mu_B = 9.274 \cdot 10^{-24}$ J/T
μ_0	vacuum permeability $\mu_0 = 4\pi \cdot 10^{-7} \frac{\text{Vs}}{\text{Am}}$
μ_w	domain wall mobility
N	number (e.g. of experiments, clock cycles)
\mathbf{n}	surface normal
$n_{RCP,LCP}$	complex refractive index
∇	Nabla operator: $\nabla f = \text{grad } f$, $\nabla \cdot \mathbf{V} = \text{div } \mathbf{V}$ and $\nabla \times \mathbf{V} = \text{rot } \mathbf{V}$,
ω	angular frequency
P_{nuc}	nucleation probability
Φ	polarization angle
$\phi_{i,j}$	angle between two spins \mathbf{S}_i and \mathbf{S}_j
φ	phase
$\varphi_{RCP,LCP}$	reflection phase shift
R	rate, e.g. of the ramp of a magnetic field
\mathbf{r}	position
r	radius (distance)
r	switching rate
$r_{RCP,LCP}$	reflection coefficient
$\hat{r}_{RCP,LCP}$	amplitude reflection coefficient
\mathbf{S}	electron spin $\mathbf{S} = S \cdot \mathbf{e}_s$
S	spin amplitude
σ_{nuc}	standard deviation of the nucleation field H_{nuc}
σ_w	domain wall energy density
T	temperature
t	time
t_{clock}	clocking field pulse time

t_{crit}	critical layer thickness
t_{depin}	depinning time
t_{eff}	effective (pulse) time
t_{layer}	layer thickness
t_{mag}	thickness of the magnetic material
t_{nuc}	nucleation time
t_{prop}	propagation time
t_{pulse}	pulse time
$\tau(H)$	switching time constant
τ_0	inverse of the attempt frequency f_0
θ	angle, e.g. between magnetization vector and easy axis
θ_k	Kerr angle
V	volume
V_a	activation volume
v_0	numerical prefactor [m/s]
v_{DW}	domain wall velocity
w_x	weight of the element x, e.g. of an input

Publications of the Author

- [SB11a] S. Breitzkreutz, J. Kiermaier, X. Ju, G. Csaba, D. Schmitt-Landsiedel, and M. Becherer, “Nanomagnetic Logic: Demonstration of Directed Signal Flow for Field-coupled Computing Devices,” in *Proceedings of the 41st European Solid-State Device Research Conference (ESSDERC)*, 2011, pp. 323–326.
- [SB11b] S. Breitzkreutz, J. Kiermaier, B. Neumeier, M. Becherer, and D. Schmitt-Landsiedel, “A combined Laser-scanning / Wide-field Kerr Microscope to Investigate the Switching Behavior of Nanomagnetic Logic Devices,” in *Verhandl. DPG (VI) 46,1*, 2011.
- [SB11c] S. Breitzkreutz, J. Kiermaier, C. Yilmaz, X. Ju, G. Csaba, D. Schmitt-Landsiedel, and M. Becherer, “Nanomagnetic Logic: Investigations on Field-coupled Computing Devices by Experiment-based Compact Modeling,” in *Proceedings of the 11th IEEE Conference on Nanotechnology (IEEE-NANO)*, 2011, pp. 1248–1251.
- [SB11d] S. Breitzkreutz, J. Kiermaier, C. Yilmaz, X. Ju, G. Csaba, D. Schmitt-Landsiedel, and M. Becherer, “Nanomagnetic logic: compact modeling of field-coupled computing devices for system investigations,” *Journal of Computational Electronics*, vol. 10, no. 4, pp. 352–359, 2011.
- [SB12a] S. Breitzkreutz, J. Kiermaier, I. Eichwald, X. Ju, G. Csaba, D. Schmitt-Landsiedel, and M. Becherer, “Majority Gate for Nanomagnetic Logic with Perpendicular Magnetic Anisotropy,” *IEEE Transactions on Magnetics*, vol. 48, no. 11, pp. 4336–4339, 2012.
- [SB12b] S. Breitzkreutz, J. Kiermaier, S. Vijay Karthik, G. Csaba, D. Schmitt-Landsiedel, and M. Becherer, “Controlled reversal of Co/Pt Dots for nanomagnetic logic applications,” *Journal of Applied Physics*, vol. 111, no. 7, p. 07A715, 2012.
- [SB13a] S. Breitzkreutz, I. Eichwald, D. Schmitt-Landsiedel, and M. Becherer, “Perpendicular Nanomagnetic Logic: Nonvolatile Computing with Field-coupled Magnets,” in *8th Workshop on Frontier Electronic (WOFE)*, 2013.

- [SB13b] S. Breitkreutz, J. Kiermaier, I. Eichwald, C. Hildbrand, G. Csaba, D. Schmitt-Landsiedel, and M. Becherer, “Experimental Demonstration of a 1-Bit Full Adder in Perpendicular Nanomagnetic Logic,” *IEEE Transactions on Magnetics*, vol. 49, no. 7, pp. 4464–4467, 2013.
- [SB13c] S. Breitkreutz, G. Ziemys, I. Eichwald, J. Kiermaier, G. Csaba, W. Porod, D. Schmitt-Landsiedel, and M. Becherer, “Domain Wall Gate for Magnetic Logic and Memory Applications with Perpendicular Anisotropy,” in *IEEE International Electron Devices Meeting (IEDM)*, Dec 2013, pp. 22.4.1–22.4.4.
- [SB13d] S. Breitkreutz, J. Kiermaier, I. Eichwald, X. Ju, G. Csaba, D. Schmitt-Landsiedel, and M. Becherer, “Investigations on Nanomagnetic Logic by Experiment-Based Compact Modeling,” in *Nanoelectronic Device Applications Handbook*, ser. Devices, Circuits, and Systems. CRC Press, Jun. 2013, ch. 62, pp. 779–790.
- [SB14a] S. Breitkreutz, I. Eichwald, J. Kiermaier, A. Papp, G. Csaba, M. Niemier, W. Porod, D. Schmitt-Landsiedel, and M. Becherer, “1-Bit Full Adder in Perpendicular Nanomagnetic Logic using a Novel 5-Input Majority Gate,” *EPJ Web of Conferences*, vol. 75, p. 05001, 2014.
- [SB14b] S. Breitkreutz, I. Eichwald, J. Kiermaier, G. Csaba, D. Schmitt-Landsiedel, and M. Becherer, “Compact modeling of perpendicular nanomagnetic logic based on threshold gates,” *Journal of Applied Physics*, vol. 115, no. 17, p. 17D104, 2014.
- [SB14c] S. Breitkreutz, I. Eichwald, J. Kiermaier, G. Hiblot, G. Csaba, W. Porod, D. Schmitt-Landsiedel, and M. Becherer, “Controlled domain wall pinning in nanowires with perpendicular magnetic anisotropy by localized fringing fields,” *Journal of Applied Physics*, vol. 115, no. 17, p. 17D506, 2014.
- [SB14d] S. Breitkreutz, I. Eichwald, G. Ziemys, D. Schmitt-Landsiedel, and M. Becherer, “Influence of the Domain Wall Nucleation Time on the Reliability of Perpendicular Nanomagnetic Logic,” in *Proceedings of the 14th IEEE International Conference on Nanotechnology (IEEE-NANO)*, 2014, pp. 104–107.
- [SB14e] S. Breitkreutz, R. L. Stamps, J. Akerman, A. V. Chumak, Y. Otani, G. E. W. Bauer, J.-U. Thiele, M. Bowen, S. A. Majetich, M. Kläui, I. L. Prejbeanu, B. Dieny, N. M. Dempsey, and B. Hillebrands, “The 2014 Magnetism Roadmap, section Nanomagnetic logic,” *Journal of Physics D: Applied Physics*, vol. 47, no. 33, p. 333001, 2014.

- [SB15a] S. Breitzkreutz, I. Eichwald, Z. Grazvydas, G. Hiblot, G. Csaba, D. Schmitt-Landsiedel, and M. Becherer, “Towards nonvolatile magnetic crossbar arrays: a 3D-integrated field-coupled domain wall gate with perpendicular anisotropy,” *Journal of Applied Physics*, vol. 17, p. 17D507, 2015.
- [SB15b] S. Breitzkreutz, A. Fischer, K. Silmi, S. Weigl, I. Eichwald, Z. Grazvydas, D. Schmitt-Landsiedel, and M. Becherer, “Time-dependent domain wall nucleation probability in field-coupled nanomagnets with perpendicular anisotropy,” *Journal of Applied Physics*, vol. 117, p. 17B503, 2015.

Contributions of the Author

- [BBE⁺15] M. Becherer, S. Breitzkreutz, I. Eichwald, G. Ziemys, J. Kiermaier, G. Csaba, and D. Schmitt-Landsiedel, “Low-power 3D integrated ferromagnetic computing,” in *Joint International EUROSIOI Workshop and International Conference on Ultimate Integration on Silicon (EUROSIOI-ULIS)*, Jan 2015, pp. 121–124.
- [BKB⁺10] M. Becherer, J. Kiermaier, S. Breitzkreutz, G. Csaba, X. Ju, J. Rezgani, T. Kiessling, C. Yilmaz, P. Osswald, P. Lugli, and D. Schmitt-Landsiedel, “On-chip Extraordinary Hall-effect sensors for characterization of nanomagnetic logic devices,” *Solid-State Electronics*, vol. 54, no. 9, pp. 1027–1032, 2010.
- [BKB⁺11] M. Becherer, J. Kiermaier, S. Breitzkreutz, G. Csaba, C. Werner, and D. Schmitt-Landsiedel, “Schaltungstechnik und Systemaspekte für Nanomagnetische Logik,” in *Kleinheubacher Tagung, Miltenberg*, 2011.
- [BKB⁺12] M. Becherer, J. Kiermaier, S. Breitzkreutz, I. Eichwald, G. Csaba, and D. Schmitt-Landsiedel, “A non-volatile low-power zero-leakage nanomagnetic computing system,” in *Frontiers in Electronic Materials: Correlation Effects, Spintronics, and Memristive Phenomena - Fundamentals and Applications*, J. Heber, D. Schlom, Y. Tokura, R. Waser, and M. Wuttig, Eds. Wiley-VCH, 2012, pp. 194–195.
- [BKB⁺13] M. Becherer, J. Kiermaier, S. Breitzkreutz, I. Eichwald, G. Csaba, and D. Schmitt-Landsiedel, “Nanomagnetic Logic Clocked in the MHz Regime,” in *IEEE Proceedings of the 43rd European Solid-State Device Research Conference (ESSDERC)*, 2013, pp. 276–279.
- [BKB⁺14] M. Becherer, J. Kiermaier, S. Breitzkreutz, I. Eichwald, G. Ziemys, G. Csaba, and D. Schmitt-Landsiedel, “Towards on-chip clocking of perpendicular Nanomagnetic Logic,” *Solid-State Electronics*, vol. 102, pp. 46–51, 2014.
- [CKB⁺12] G. Csaba, J. Kiermaier, M. Becherer, S. Breitzkreutz, X. Ju, P. Lugli, D. Schmitt-Landsiedel, and W. Porod, “Clocking magnetic field-

- coupled devices by domain walls,” *Journal of Applied Physics*, vol. 111, no. 7, p. 07E337, 2012.
- [EBK⁺12] I. Eichwald, A. Bartel, J. Kiermaier, S. Breitkreutz, G. Csaba, D. Schmitt-Landsiedel, and M. Becherer, “Nanomagnetic Logic: Error-Free, Directed Signal Transmission by an Inverter Chain,” *IEEE Transactions on Magnetics*, vol. 48, no. 11, pp. 4332–4335, Nov 2012.
- [EBK⁺14] I. Eichwald, S. Breitkreutz, J. Kiermaier, G. Csaba, D. Schmitt-Landsiedel, and M. Becherer, “Signal crossing in perpendicular nanomagnetic logic,” *Journal of Applied Physics*, vol. 115, no. 17, p. 17E510, 2014.
- [EBZ⁺14] I. Eichwald, S. Breitkreutz, G. Ziemys, G. Csaba, W. Porod, and M. Becherer, “Majority logic gate for 3D magnetic computing,” *Nanotechnology*, vol. 25, no. 33, p. 335202, 2014.
- [EKB⁺13] I. Eichwald, J. Kiermaier, S. Breitkreutz, J. Wu, G. Csaba, D. Schmitt-Landsiedel, and M. Becherer, “Towards a Signal Crossing in Double-Layer Nanomagnetic Logic,” *IEEE Transactions on Magnetics*, vol. 49, no. 7, pp. 4468–4471, July 2013.
- [JBK⁺11] X. Ju, M. Becherer, J. Kiermaier, S. Breitkreutz, P. Lugli, and G. Csaba, “Error Analysis of Co/Pt multilayer based Nanomagnetic Logic,” in *Proceedings of the 11th IEEE Conference on Nanotechnology (IEEE-NANO)*, Aug 2011, pp. 1034–1037.
- [JKS⁺12] X. Ju, J. Kiermaier, A. Savo, M. Becherer, S. Breitkreutz, I. Eichwald, D. Schmitt-Landsiedel, W. Porod, P. Lugli, and G. Csaba, “Modeling interaction between Co/Pt nanomagnets and Permalloy domain wall for Nanomagnet Logic,” in *Proceedings of the 12th IEEE Conference on Nanotechnology (IEEE-NANO)*, Aug 2012, pp. 1–5.
- [JSL⁺12] X. Ju, A. Savo, P. Lugli, J. Kiermaier, M. Becherer, S. Breitkreutz, D. Schmitt-Landsiedel, W. Porod, and G. Csaba, “Computational Study of Domain-Wall-Induced Switching of Co/Pt Multilayer,” in *15th International Workshop on Computational Electronics (IWCE)*, May 2012, pp. 1–3.
- [JWL⁺10] X. Ju, S. Wartenburg, P. Lugli, M. Becherer, J. Kiermaier, S. Breitkreutz, D. Schmitt-Landsiedel, and G. Csaba, “Computational Model of Partially Irradiated Nanodots for Field-coupled Computing Devices,” in *14th International Workshop on Computational Electronics (IWCE)*, Oct 2010, pp. 1–4.

- [JWR⁺12] X. Ju, S. Wartenburg, J. Rezgani, M. Becherer, J. Kiermaier, S. Breitkreutz, D. Schmitt-Landsiedel, W. Porod, P. Lugli, and G. Csaba, “Nanomagnet Logic from Partially Irradiated Co/Pt Nanomagnets,” *IEEE Transactions on Nanotechnology*, vol. 11, no. 1, pp. 97–104, Jan 2012.
- [KBC⁺12] J. Kiermaier, S. Breitkreutz, G. Csaba, D. Schmitt-Landsiedel, and M. Becherer, “Electrical input structures for nanomagnetic logic devices,” *Journal of Applied Physics*, vol. 111, no. 7, p. 07E341, 2012.
- [KBE⁺13a] J. Kiermaier, S. Breitkreutz, I. Eichwald, M. Engelstädter, X. Ju, G. Csaba, D. Schmitt-Landsiedel, and M. Becherer, “Information transport in field-coupled nanomagnetic logic devices,” *Journal of Applied Physics*, vol. 113, no. 17, p. 17B902, 2013.
- [KBE⁺13b] J. Kiermaier, S. Breitkreutz, I. Eichwald, X. Ju, G. Csaba, D. Schmitt-Landsiedel, and M. Becherer, “Programmable Input for Nanomagnetic Logic Devices,” *EPJ Web of Conferences*, vol. 40, p. 16007, 2013.
- [KBJ⁺10] J. Kiermaier, S. Breitkreutz, X. Ju, G. Csaba, D. Schmitt-Landsiedel, and M. Becherer, “Ultra-low volume ferromagnetic nanodots for field-coupled computing devices,” in *IEEE Proceedings of the 40th European Solid-State Device Research Conference (ESSDERC)*, Sept 2010, pp. 214–217.
- [KBJ⁺11] J. Kiermaier, S. Breitkreutz, X. Ju, G. Csaba, D. Schmitt-Landsiedel, and M. Becherer, “Field-coupled computing: Investigating the properties of ferromagnetic nanodots,” *Solid-State Electronics*, vol. 65-66, pp. 240–245, 2011.
- [KNB⁺11] J. Kiermaier, B. Neumeier, S. Breitkreutz, D. Schmitt-Landsiedel, and M. Becherer, “Variable and fast response 3D magnetic field module for magnetic force microscopy,” in *International Scanning Probe Microscopy Conference (ISPM)*, Garching, Munich, June 2011.
- [PNC⁺14] A. Papp, M. Niemier, A. Csurgay, M. Becherer, S. Breitkreutz, J. Kiermaier, I. Eichwald, X. Hu, X. Ju, W. Porod, and G. Csaba, “Threshold Gate-Based Circuits From Nanomagnetic Logic,” *IEEE Transactions on Nanotechnology*, vol. 13, no. 5, pp. 990–996, Sept 2014.

References

- [1] Engineering - Wikipedia, the free encyclopedia, Nov. 2014. [Online]. Available: <http://en.wikipedia.org/wiki/Engineering>
- [2] The International Technology Roadmap for Semiconductors (ITRS): Emerging Research Devices (ERD), 2013. [Online]. Available: <http://www.itrs.net/Links/2013ITRS/2013Chapters/2013ERD.pdf>
- [3] G. Moore, "Cramming More Components Onto Integrated Circuits," *Proceedings of the IEEE*, vol. 86, no. 1, pp. 82–85, Jan 1998, reprinted from *Electronics*, vol. 38, no. 8, pp. 114–117, April 1965.
- [4] C. Mack, "Fifty Years of Moore's Law," *IEEE Transactions on Semiconductor Manufacturing*, vol. 24, no. 2, pp. 202–207, May 2011.
- [5] R. Dennard, F. Gaensslen, H.-N. Yu, V. Rideout, E. Bassous, and A. R. Leblanc, "Design Of Ion-implanted MOSFET's with Very Small Physical Dimensions," *Proceedings of the IEEE*, vol. 87, no. 4, pp. 668–678, April 1999.
- [6] G. Shahidi, "Evolution of CMOS Technology at 32 nm and Beyond," in *IEEE Custom Integrated Circuits Conference (CICC)*, Sept 2007, pp. 413–416.
- [7] The International Technology Roadmap for Semiconductors (ITRS): Process Integration, Devices, and Structures(PIDS), 2013. [Online]. Available: <http://www.itrs.net/Links/2013ITRS/2013Chapters/2013PIDS.pdf>
- [8] The International Technology Roadmap for Semiconductors (ITRS). [Online]. Available: <http://www.itrs.net/Links/2013ITRS/Home2013.htm>
- [9] S. E. Thompson and S. Parthasarathy, "Moore's law: the future of Si micro-electronics," *Materials Today*, vol. 9, no. 6, pp. 20–25, 2006.
- [10] A. Thean, "Challenges of 10nm and 7nm CMOS Technologies," in *IEEE International Electron Devices Meeting (IEDM)*, 2013.
- [11] R. Isaac, "The future of CMOS technology," *IBM Journal of Research and Development*, vol. 44, no. 3, pp. 369–378, May 2000.

- [12] K. Rupp and S. Selberherr, “The Economic Limit to Moore’s Law,” *IEEE Transactions on Semiconductor Manufacturing*, vol. 24, no. 1, pp. 1–4, Feb 2011.
- [13] H. Iwai, “Future of nano CMOS technology,” in *Symposium on Microelectronics Technology and Devices (SBMicro)*, Sept 2013, pp. 1–10.
- [14] M. Bohr and K. Mistry. (2011) Intel’s Revolutionary 22 nm Transistor Technology. Intel. [Online]. Available: http://download.intel.com/newsroom/kits/22nm/pdfs/22nm-Details_Presentation.pdf
- [15] K. Kuhn, “CMOS scaling beyond 32nm: Challenges and opportunities,” in *46th ACM/IEEE Design Automation Conference (DAC)*, July 2009, pp. 310–313.
- [16] M. Frank, “High-k / metal gate innovations enabling continued CMOS scaling,” in *Proceedings of the 41st European Solid-State Device Research Conference (ESSDERC)*, Sept 2011, pp. 25–33.
- [17] K. Kuhn, “Considerations for Ultimate CMOS Scaling,” *IEEE Transactions on Electron Devices*, vol. 59, no. 7, pp. 1813–1828, July 2012.
- [18] K. Bernstein, R. Cavin, W. Porod, A. Seabaugh, and J. Welser, “Device and Architecture Outlook for Beyond CMOS Switches,” *Proceedings of the IEEE*, vol. 98, no. 12, pp. 2169–2184, Dec 2010.
- [19] D. Nikonov and I. Young, “Uniform methodology for benchmarking beyond-CMOS logic devices,” in *IEEE International Electron Devices Meeting (IEDM)*, Dec 2012, pp. 25.4.1–25.4.4.
- [20] R. Waser, Ed., *Nanoelectronics and Information Technology*, 3rd ed. Wiley-VCH, 2012.
- [21] D. Nikonov and I. Young, “Overview of Beyond-CMOS Devices and a Uniform Methodology for Their Benchmarking,” *Proceedings of the IEEE*, vol. 101, no. 12, pp. 2498–2533, Dec 2013.
- [22] J. Hutchby, G. Bourianoff, V. Zhirnov, and J. Brewer, “Extending the road beyond CMOS,” *IEEE Circuits and Devices Magazine*, vol. 18, no. 2, pp. 28–41, Mar 2002.
- [23] S. A. Wolf, J. Lu, M. Stan, E. Chen, and D. Treger, “The Promise of Nanomagnetism and Spintronics for Future Logic and Universal Memory,” *Proceedings of the IEEE*, vol. 98, no. 12, pp. 2155–2168, Dec 2010.

-
- [24] J. W. Lau and J. M. Shaw, “Magnetic nanostructures for advanced technologies: fabrication, metrology and challenges,” *Journal of Physics D: Applied Physics*, vol. 44, no. 30, p. 303001, 2011.
- [25] A. Hirohata and K. Takanashi, “Future perspectives for spintronic devices,” *Journal of Physics D: Applied Physics*, vol. 47, no. 19, p. 193001, 2014.
- [26] M. Becherer, *Nanomagnetic Logic in Focused Ion Beam Engineered Co/Pt Multilayer Films*, ser. Selected Topics of Electronics and Micromechatronics, G. Wachutka and D. Schmitt-Landsiedel, Eds. Shaker Verlag, 2011, vol. 38.
- [27] D. Hampel and R. O. Winder, “Threshold logic,” *IEEE Spectrum*, vol. 8, no. 5, pp. 32–39, May 1971.
- [28] J. Kiermaier, *Integrated Nanomagnetic Logic System in Perpendicular Magnetic Media*, ser. Selected Topics of Electronics and Micromechatronics, G. Wachutka and D. Schmitt-Landsiedel, Eds. Shaker Verlag, 2014, vol. 45.
- [29] R. C. Minnick, “Magnetic Switching Circuits,” *Journal of Applied Physics*, vol. 25, no. 4, pp. 479–485, 1954.
- [30] S. Guterman, R. Kodis, and S. Ruhman, “Logical and Control Functions Performed with Magnetic Cores,” *Proceedings of the IRE*, vol. 43, no. 3, pp. 291–298, March 1955.
- [31] D. Engelbart, “A new all-magnetic logic system using simple cores,” in *IEEE International Solid-State Circuits Conference (ISSCC), Digest of Technical Papers*, vol. II, Feb 1959, pp. 66–67.
- [32] U. F. Gianola, “Possibilities of All-Magnetic Logic,” *Journal of Applied Physics*, vol. 32, no. 3, pp. S27–S34, 1961.
- [33] D. R. Bennion, H. D. Crane, and D. Nitzan, *Digital magnetic logic*. McGraw-Hill, 1969.
- [34] R. J. Spain, “Controlled Domain Tip Propagation. Part I,” *Journal of Applied Physics*, vol. 37, no. 7, pp. 2572–2583, 1966.
- [35] R. J. Spain and H. I. Jauvtis, “Controlled Domain Tip Propagation. Part II,” *Journal of Applied Physics*, vol. 37, no. 7, pp. 2584–2593, 1966.
- [36] R. Spain and M. Marino, “Magnetic film domain-wall motion devices,” *IEEE Transactions on Magnetics*, vol. 6, no. 3, pp. 451–463, Sep 1970.
- [37] R. Sandfort and E. R. Burke, “Logic functions for magnetic bubble devices,” *IEEE Transactions on Magnetics*, vol. 7, no. 3, pp. 358–360, Sep 1971.

- [38] A. H. Bobeck, "Magnetic Bubble Devices," *Journal of Vacuum Science & Technology*, vol. 9, no. 4, pp. 1145–1150, 1972.
- [39] S. Lee and H. Chang, "Magnetic bubble logic," *IEEE Transactions on Magnetics*, vol. 10, no. 4, pp. 1059–1066, Dec 1974.
- [40] K. Kinoshita, T. Sasao, and J. Matsuda, "On Magnetic Bubble Logic Circuits," *IEEE Transactions on Computers*, vol. C-25, no. 3, pp. 247–253, March 1976.
- [41] J. A. Rajchman, "A Survey of Magnetic and Other Solid-State Devices for the Manipulation of Information," *IRE Transactions on Circuit Theory*, vol. 4, no. 3, pp. 210–225, Sep 1957.
- [42] E. Clark, "A survey of solid-state logic circuitry," in *IEEE International Solid-State Circuits Conference (ISSCC), Digest of Technical Papers*, vol. I, Feb 1958, pp. 49–49.
- [43] J. Wood and R. Ball, "Metal oxide semiconductor transistors in digital logic and storage," *Radio and Electronic Engineer*, vol. 32, no. 1, pp. 33–45, July 1966.
- [44] L. Terman, "MOSFET memory circuits," *Proceedings of the IEEE*, vol. 59, no. 7, pp. 1044–1058, July 1971.
- [45] S. Rege, "Cost, Performance, and Size Tradeoffs for Different Levels in a Memory Hierarchy," *Computer*, vol. 9, no. 4, pp. 43–51, April 1976.
- [46] C. Lent, P. Tougaw, W. Porod, and G. Bernstein, "Quantum cellular automata," *Nanotechnology*, vol. 4, no. 1, pp. 49–57, 1993.
- [47] G. L. Snider *et al.*, "Quantum-Dot Cellular Automata: Line and Majority Logic Gate," *Japanese Journal of Applied Physics*, vol. 38, no. Part 1, No. 12B, pp. 7227–7229, 1999.
- [48] G. Snider *et al.*, "Electronic quantum-dot cellular automata," in *9th International Conference on Solid-State and Integrated-Circuit Technology (IC-SICT)*, Oct 2008, pp. 549–552.
- [49] R. P. Cowburn and M. E. Welland, "Room Temperature Magnetic Quantum Cellular Automata," *Science*, vol. 287, no. 5457, pp. 1466–1468, 2000.
- [50] G. Csaba, A. Imre, G. Bernstein, W. Porod, and V. Metlushko, "Nanocomputing by field-coupled nanomagnets," *IEEE Transactions on Nanotechnology*, vol. 1, no. 4, pp. 209–213, Dec 2002.

-
- [51] G. Bernstein, “Quantum-dot cellular automata by electric and magnetic field coupling,” in *Proceedings of the IEEE Custom Integrated Circuits Conference*, Sept 2003, pp. 223–229.
 - [52] M. C. B. Parish and M. Forshaw, “Physical constraints on magnetic quantum cellular automata,” *Applied Physics Letters*, vol. 83, no. 10, pp. 2046–2048, 2003.
 - [53] A. Imre, G. Csaba, G. H. Bernstein, W. Porod, and V. Metlushko, “Investigation of shape-dependent switching of coupled nanomagnets,” *Superlattices and Microstructures*, vol. 34, pp. 513 – 518, 2003.
 - [54] G. Bernstein *et al.*, “Magnetic QCA systems,” *Microelectronics Journal*, vol. 36, no. 7, pp. 619 – 624, 2005.
 - [55] G. Csaba, P. Lugli, A. Csurgay, and W. Porod, “Simulation of Power Gain and Dissipation in Field-Coupled Nanomagnets,” *Journal of Computational Electronics*, vol. 4, no. 1-2, pp. 105–110, 2005.
 - [56] A. Imre, G. Csaba, L. Ji, A. Orlov, G. H. Bernstein, and W. Porod, “Majority Logic Gate for Magnetic Quantum-Dot Cellular Automata,” *Science*, vol. 311, no. 5758, pp. 205–208, 2006.
 - [57] D. A. Allwood *et al.*, “Submicrometer Ferromagnetic NOT Gate and Shift Register,” *Science*, vol. 296, no. 5575, pp. 2003–2006, 2002.
 - [58] D. A. Allwood, G. Xiong, C. C. Faulkner, D. Atkinson, D. Petit, and R. P. Cowburn, “Magnetic Domain-Wall Logic,” *Science*, vol. 309, no. 5741, pp. 1688–1692, 2005.
 - [59] S. S. P. Parkin, “Direction of motion and high speed of domain walls in nanowires with perpendicular anisotropy,” in *12th Joint MMM-INTERMAG Conference*, vol. CA-05, Chicago, 2013.
 - [60] M. Becherer *et al.*, “Focused ion beam structured Co/Pt multilayers for field-coupled magnetic computing,” *MRS Proceedings*, vol. 998, p. J06, 1 2007.
 - [61] M. Becherer, G. Csaba, W. Porod, R. Emling, P. Lugli, and D. Schmitt-Landsiedel, “Magnetic Ordering of Focused-Ion-Beam Structured Cobalt-Platinum Dots for Field-Coupled Computing,” *IEEE Transactions on Nanotechnology*, vol. 7, no. 3, pp. 316–320, May 2008.
 - [62] G. Csaba, P. Lugli, M. Becherer, D. Schmitt-Landsiedel, and W. Porod, “Field-coupled computing in magnetic multilayers,” *Journal of Computational Electronics*, vol. 7, no. 3, pp. 454–457, 2008.

- [63] M. Becherer, G. Csaba, R. Emling, W. Porod, P. Lugli, and D. Schmitt-Landsiedel, “Field-coupled nanomagnets for interconnect-free nonvolatile computing,” in *IEEE International Solid-State Circuits Conference (ISSCC), Digest of Technical Papers*, Feb 2009, pp. 474–475.
- [64] R. L. Stamps *et al.*, “The 2014 Magnetism Roadmap,” *Journal of Physics D: Applied Physics*, vol. 47, no. 33, p. 333001, 2014.
- [65] M. Niemier *et al.*, “Systolic architectures and applications for nanomagnet logic,” in *IEEE Silicon Nanoelectronics Workshop (SNW)*, June 2012, pp. 1–2.
- [66] M. Niemier *et al.*, “Boolean and non-boolean nearest neighbor architectures for out-of-plane nanomagnet logic,” in *13th International Workshop on Cellular Nanoscale Networks and Their Applications (CNNA)*, Aug 2012, pp. 1–6.
- [67] D. Ralph and M. Stiles, “Spin transfer torques,” *Journal of Magnetism and Magnetic Materials*, vol. 320, no. 7, pp. 1190–1216, 2008.
- [68] J. Katine and E. E. Fullerton, “Device implications of spin-transfer torques,” *Journal of Magnetism and Magnetic Materials*, vol. 320, no. 7, pp. 1217–1226, 2008.
- [69] S. Mangin, D. Ravelosona, J. A. Katine, M. J. Carey, B. D. Terris, and E. E. Fullerton, “Current-induced magnetization reversal in nanopillars with perpendicular anisotropy,” *Nature Materials*, vol. 5, pp. 210–215, 2006.
- [70] A. Fert, P. Grünberg, A. Barthélémy, F. Petroff, and W. Zinn, “Layered magnetic structures: interlayer exchange coupling and giant magnetoresistance,” *Journal of Magnetism and Magnetic Materials*, vol. 140-144, Part 1, pp. 1–8, 1995.
- [71] P. Grünberg, “Exchange anisotropy, interlayer exchange coupling and {GMR} in research and application,” *Sensors and Actuators A: Physical*, vol. 91, pp. 153–160, 2001.
- [72] S. S. P. Parkin *et al.*, “Giant tunnelling magnetoresistance at room temperature with MgO (100) tunnel barriers,” *Nature Materials*, vol. 3, pp. 862–867, 2004.
- [73] Z. R. Tadisina *et al.*, “Perpendicular magnetic tunnel junctions using Co-based multilayers,” *Journal of Applied Physics*, vol. 107, no. 9, p. 09C703, 2010.

-
- [74] M. Gajek *et al.*, “Spin torque switching of 20nm magnetic tunnel junctions with perpendicular anisotropy,” *Applied Physics Letters*, vol. 100, no. 13, p. 132408, 2012.
- [75] S. Liu, X. Hu, J. Nahas, M. Niemier, W. Porod, and G. Bernstein, “Magnetic-Electrical Interface for Nanomagnet Logic,” *IEEE Transactions on Nanotechnology*, vol. 10, no. 4, pp. 757–763, July 2011.
- [76] S. Liu *et al.*, “Exploring the Design of the Magnetic-Electrical Interface for Nanomagnet Logic,” *IEEE Transactions on Nanotechnology*, vol. 12, no. 2, pp. 203–214, March 2013.
- [77] A. Lyle, A. Klemm, J. Harms, Y. Zhang, H. Zhao, and J.-P. Wang, “Probing dipole coupled nanomagnets using magnetoresistance read,” *Applied Physics Letters*, vol. 98, no. 9, p. 092502, 2011.
- [78] A. Lyle *et al.*, “Spin transfer torque programming dipole coupled nanomagnet arrays,” *Applied Physics Letters*, vol. 100, no. 1, p. 012402, 2012.
- [79] D. Bhowmik, L. You, and S. Salahuddin, “Spin Hall effect clocking of nanomagnetic logic without a magnetic field,” *Nature Nanotechnology*, vol. 9, pp. 59–63, 2014.
- [80] M. Niemier, “Magnetic devices: Clocking with no field,” *Nature Nanotechnology*, vol. 9, pp. 14–15, 2014.
- [81] A. Hubert and R. Schäfer, *Magnetic Domains: The Analysis of Magnetic Microstructures*. Springer Verlag, 1998.
- [82] H. Kronmüller and S. Parkin, Eds., *Handbook of Magnetism and Advanced Magnetic Materials*, 1st ed. Wiley, 2007.
- [83] J. M. D. Coey, *Magnetism and Magnetic Materials*. Cambridge University Press, 2010.
- [84] L. Landau and E. Lifshits, “On the theory of the dispersion of magnetic permeability in ferromagnetic bodies,” *Physikalische Zeitschrift der Sowjetunion*, vol. 8, pp. 153–169, 1935.
- [85] L. Néel, “Anisotropie magnétique superficielle et surstructures d’orientation,” *Le Journal de Physique et le Radium*, vol. 15, no. 4, pp. 225–239, 1954.
- [86] W. F. Brown, “Theory of the Approach to Magnetic Saturation,” *Physical Review Letters*, vol. 58, pp. 736–743, Oct 1940.

- [87] F. Bloch, “Zur Theorie des Austauschproblems und der Remanenzerscheinung der Ferromagnetika,” *Zeitschrift für Physik*, vol. 74, pp. 295–335, 1932.
- [88] T. L. Gilbert and J. M. Kelly, “Anomalous rotational damping in ferromagnetic sheets,” in *Conference on Magnetism and Magnetic Materials*, Pittsburgh, June 1955, pp. 253–263.
- [89] T. Gilbert, “A phenomenological theory of damping in ferromagnetic materials,” *IEEE Transactions on Magnetics*, vol. 40, no. 6, pp. 3443–3449, Nov 2004.
- [90] G. Csaba and W. Porod, “Behavior of Nanomagnet Logic in the presence of thermal noise,” in *14th International Workshop on Computational Electronics (IWCE)*, Oct 2010, pp. 1–4.
- [91] The Object Oriented MicroMagnetic Framework (OOMMF) project. National Institute of Standards and Technology (NIST). [Online]. Available: <http://math.nist.gov/oommf/>
- [92] M. T. Johnson, P. J. H. Bloemen, F. J. A. den Broeder, and J. J. de Vries, “Magnetic anisotropy in metallic multilayers,” *Reports on Progress in Physics*, vol. 59, no. 11, pp. 1409–1458, 1996.
- [93] O. Hellwig, A. Berger, J. B. Kortright, and E. E. Fullerton, “Domain structure and magnetization reversal of antiferromagnetically coupled perpendicular anisotropy films,” *Journal of Magnetism and Magnetic Materials*, vol. 319, pp. 13–55, 2007.
- [94] A. P. Guimaraes, *Principles of Nanomagnetism*, ser. NanoScience and Technology. Springer Verlag, 2009.
- [95] P. Grünberg, “Layered magnetic structures: history, facts and figures,” *Journal of Magnetism and Magnetic Materials*, vol. 226-230, pp. 1688–1693, 2001, proceedings of the International Conference on Magnetism (ICM 2000).
- [96] P. F. Carcia, “Perpendicular magnetic anisotropy in Pd/Co and Pt/Co thin-film layered structures,” *Journal of Applied Physics*, vol. 63, no. 10, pp. 5066–5073, 1988.
- [97] Z. Zhang, P. E. Wigen, and S. S. P. Parkin, “Pt layer thickness dependence of magnetic properties in Co/Pt multilayers,” *Journal of Applied Physics*, vol. 69, no. 8, pp. 5649–5651, 1991.
- [98] M. Johnson, R. Jungblut, P. Kelly, and F. den Broeder, “Perpendicular magnetic anisotropy of multilayers: recent insights,” *Journal of Magnetism and Magnetic Materials*, vol. 148, pp. 118–124, 1995.

-
- [99] P. Carcia and W. B. Zeper, "Sputtered Pt/Co multilayers for magneto-optical recording," *IEEE Transactions on Magnetics*, vol. 26, no. 5, pp. 1703–1705, Sep 1990.
- [100] Y. Kawada, Y. Ueno, and K. Shibata, "Co-Pt multilayers perpendicular magnetic recording media with thin Pt layer and high perpendicular anisotropy," *IEEE Transactions on Magnetics*, vol. 38, no. 5, pp. 2045–2047, Sep 2002.
- [101] W. B. Zeper, H. W. van Kesteren, B. A. J. Jacobs, J. H. M. Spruit, and P. F. Carcia, "Hysteresis, microstructure, and magneto-optical recording in Co/Pt and Co/Pd multilayers," *Journal of Applied Physics*, vol. 70, no. 4, pp. 2264–2271, 1991.
- [102] S. Honda, H. Tanimoto, and T. Kusuda, "Magnetization process and coercivity of sputtered Co/Pt multilayered films," *IEEE Transactions on Magnetics*, vol. 26, no. 5, pp. 2730–2732, Sep 1990.
- [103] J. X. Shen, R. D. Kirby, K. Wierman, Z. S. Shan, D. J. Sellmyer, and T. Suzuki, "Magnetization reversal and defects in Co/Pt multilayers," *Journal of Applied Physics*, vol. 73, no. 10, pp. 6418–6420, 1993.
- [104] Y.-C. Cho, S.-B. Choe, and S.-C. Shin, "Magnetic field dependence of magnetization reversal behavior in Co/Pt multilayers," *Journal of Applied Physics*, vol. 90, no. 3, pp. 1419–1421, 2001.
- [105] S. Okamoto, T. Kato, N. Kikuchi, O. Kitakami, N. Tezuka, and S. Sugimoto, "Energy barrier and reversal mechanism in CoPt multilayer nanodot," *Journal of Applied Physics*, vol. 103, no. 7, p. 07C501, 2008.
- [106] M. Belmeguenai, T. Devolder, and C. Chappert, "Experimental analysis of the fast magnetization dynamics in high perpendicular anisotropy Co/Pt nanostructures," *Journal of Magnetism and Magnetic Materials*, vol. 307, no. 2, pp. 325–329, 2006.
- [107] A. Barman, S. Wang, O. Hellwig, A. Berger, E. E. Fullerton, and H. Schmidt, "Ultrafast magnetization dynamics in high perpendicular anisotropy [CoPt]_n multilayers," *Journal of Applied Physics*, vol. 101, no. 9, p. 09D102, 2007.
- [108] A. Ito, N. Kikuchi, S. Okamoto, and O. Kitakami, "Magnetization Switching Experiments on Sub-Micron Co/Pt Multilayer Dot Using a Pulse Field Generator With Nanoseconds Duration," *IEEE Transactions on Magnetics*, vol. 44, no. 11, pp. 3446–3449, Nov 2008.

- [109] M. Becherer *et al.*, “Characterizing magnetic field-coupled computing devices by the Extraordinary Hall-effect,” in *Proceedings of the European Solid State Device Research Conference (ESSDERC)*, Sept 2009, pp. 105–108.
- [110] P. Carcia, D. Coulman, R. McLean, and M. Reilly, “Magnetic and structural properties of nanophase Pt/Co multilayers,” *Journal of Magnetism and Magnetic Materials*, vol. 164, no. 3, pp. 411–419, 1996.
- [111] Y.-C. Cho, S.-B. Choe, and S.-C. Shin, “Dependences of the activation volumes on Ar sputtering pressure in Co/Pt multilayers prepared by dc magnetron sputtering,” *Applied Physics Letters*, vol. 80, no. 3, pp. 452–454, 2002.
- [112] W. B. Zeper, F. J. A. M. Greidanus, P. F. Carcia, and C. R. Fincher, “Perpendicular magnetic anisotropy and magneto-optical Kerr effect of vapor-deposited Co/Pt-layered structures,” *Journal of Applied Physics*, vol. 65, no. 12, pp. 4971–4975, 1989.
- [113] C. Vieu *et al.*, “Modifications of magnetic properties of Pt/Co/Pt thin layers by focused gallium ion beam irradiation,” *Journal of Applied Physics*, vol. 91, no. 5, pp. 3103–3110, 2002.
- [114] J. Fassbender and J. McCord, “Magnetic patterning by means of ion irradiation and implantation,” *Journal of Magnetism and Magnetic Materials*, vol. 320, pp. 579–596, 2008.
- [115] S. Hashimoto, Y. Ochiai, and K. Aso, “Perpendicular magnetic anisotropy and magnetostriction of sputtered Co/Pd and Co/Pt multilayered films,” *Journal of Applied Physics*, vol. 66, no. 10, pp. 4909–4916, 1989.
- [116] P. He, W. A. McGahan, J. A. Woollam, F. Sequeda, T. McDaniel, and H. Do, “Magneto-optical Kerr effect and perpendicular magnetic anisotropy of evaporated and sputtered Co/Pt multilayer structures,” *Journal of Applied Physics*, vol. 69, no. 7, pp. 4021–4028, 1991.
- [117] S. Hashimoto, Y. Ochiai, and K. Aso, “Film thickness dependence of magneto-optical and magnetic properties in Co/Pt and Co/Pd multilayers,” *Journal of Applied Physics*, vol. 67, no. 9, pp. 4429–4431, 1990.
- [118] A. Vernes, L. Szunyogh, and P. Weinberger, “Magneto-optical properties of Co|Pt multilayer systems,” *Journal of Applied Physics*, vol. 91, no. 10, pp. 7291–7292, 2002.
- [119] C. Chappert *et al.*, “Planar Patterned Magnetic Media Obtained by Ion Irradiation,” *Science*, vol. 280, no. 5371, pp. 1919–1922, 1998.

-
- [120] J. Fassbender, D. Ravelosona, and Y. Samson, "Tailoring magnetism by light-ion irradiation," *Journal of Physics D: Applied Physics*, vol. 37, no. 16, p. R179, 2004.
- [121] T. Devolder, "Light ion irradiation of Co/Pt systems: Structural origin of the decrease in magnetic anisotropy," *Physical Review B*, vol. 62, pp. 5794–5802, Sep 2000.
- [122] R. Hyndman *et al.*, "Modification of Co/Pt multilayers by gallium irradiation-Part 1: The effect on structural and magnetic properties," *Journal of Applied Physics*, vol. 90, no. 8, pp. 3843–3849, 2001.
- [123] P. Warin *et al.*, "Modification of Co/Pt multilayers by gallium irradiation-Part 2: The effect of patterning using a highly focused ion beam," *Journal of Applied Physics*, vol. 90, no. 8, pp. 3850–3855, 2001.
- [124] K.-J. Kim *et al.*, "Depinning Field at Notches of Ferromagnetic Nanowires With Perpendicular Magnetic Anisotropy," *IEEE Transactions on Magnetics*, vol. 45, no. 10, pp. 4056–4058, Oct 2009.
- [125] J. Pommier, P. Meyer, G. Pénissard, J. Ferré, P. Bruno, and D. Renard, "Magnetization reversal in ultrathin ferromagnetic films with perpendicular anisotropy: Domain observations," *Physical Review Letters*, vol. 65, pp. 2054–2057, Oct 1990.
- [126] A. Kirilyuk, J. Ferré, V. Grolier, J. Jamet, and D. Renard, "Magnetization reversal in ultrathin ferromagnetic films with perpendicular anisotropy," *Journal of Magnetism and Magnetic Materials*, vol. 171, pp. 45–63, 1997.
- [127] G. Hu, T. Thomson, C. Rettner, and B. Terris, "Rotation and wall propagation in multidomain Co/Pd islands," *IEEE Transactions on Magnetics*, vol. 41, no. 10, pp. 3589–3591, Oct 2005.
- [128] J. H. Franken, M. Hoeijmakers, R. Lavrijsen, and H. J. M. Swagten, "Domain-wall pinning by local control of anisotropy in Pt/Co/Pt strips," *Journal of Physics: Condensed Matter*, vol. 24, no. 2, p. 024216, 2012.
- [129] E. C. Stoner and E. P. Wohlfarth, "A Mechanism of Magnetic Hysteresis in Heterogeneous Alloys," *Philosophical Transactions of the Royal Society of London. Series A, Mathematical and Physical Sciences*, vol. 240, no. 826, pp. 599–642, 1948.
- [130] T. Thomson, G. Hu, and B. D. Terris, "Intrinsic Distribution of Magnetic Anisotropy in Thin Films Probed by Patterned Nanostructures," *Physical Review Letters*, vol. 96, p. 257204, Jun 2006.

- [131] J. W. Lau, R. D. McMichael, S. H. Chung, J. O. Rantschler, V. Parekh, and D. Litvinov, “Microstructural origin of switching field distribution in patterned Co/Pd multilayer nanodots,” *Applied Physics Letters*, vol. 92, no. 1, p. 012506, 2008.
- [132] L. San Emeterio Alvarez, G. Burnell, C. H. Marrows, K.-Y. Wang, A. M. Blackburn, and D. A. Williams, “Nucleation and propagation of domains walls in a Co/Pt multilayer wire,” *Journal of Applied Physics*, vol. 101, no. 9, p. 09F508, 2007.
- [133] R. Lavrijsen, J. H. Franken, J. T. Kohlhepp, H. J. M. Swagten, and B. Koopmans, “Controlled domain-wall injection in perpendicularly magnetized strips,” *Applied Physics Letters*, vol. 96, no. 22, p. 222502, 2010.
- [134] G. S. D. Beach, C. Nistor, C. Knutson, M. Tsoi, and J. L. Erskine, “Dynamics of field-driven domain-wall propagation in ferromagnetic nanowires,” *Nature Materials*, vol. 4, no. 10, pp. 741–744, 2005.
- [135] N. L. Schryer and L. R. Walker, “The motion of 180° domain walls in uniform dc magnetic fields,” *Journal of Applied Physics*, vol. 45, no. 12, pp. 5406–5421, 1974.
- [136] A. Mougin, M. Cormier, J. P. Adam, P. J. Metaxas, and J. Ferré, “Domain wall mobility, stability and Walker breakdown in magnetic nanowires,” *Europhysics Letters (EPL)*, vol. 78, no. 5, p. 57007, 2007.
- [137] P. Chauve, T. Giamarchi, and P. Le Doussal, “Creep and depinning in disordered media,” *Physical Review B*, vol. 62, pp. 6241–6267, Sep 2000.
- [138] V. Zablotskii, J. Ferré, and A. Maziewski, “Model for domain wall pinning by randomly distributed nanosized defects in ultrathin magnetic films,” *Journal of Physics D: Applied Physics*, vol. 42, no. 12, p. 125001, 2009.
- [139] P. J. Metaxas *et al.*, “Creep and Flow Regimes of Magnetic Domain-Wall Motion in Ultrathin Pt/Co/Pt Films with Perpendicular Anisotropy,” *Physical Review Letters*, vol. 99, p. 217208, Nov 2007.
- [140] S. Emori and G. S. D. Beach, “Roles of the magnetic field and electric current in thermally activated domain wall motion in a submicrometer magnetic strip with perpendicular magnetic anisotropy,” *Journal of Physics: Condensed Matter*, vol. 24, no. 2, p. 024214, 2012.
- [141] E. Martinez, “The stochastic nature of the domain wall motion along high perpendicular anisotropy strips with surface roughness,” *Journal of Physics: Condensed Matter*, vol. 24, no. 2, p. 024206, 2012.

-
- [142] S. Emori, D. C. Bono, and G. S. D. Beach, “Time-resolved measurements of field-driven domain wall motion in a submicron strip with perpendicular magnetic anisotropy,” *Journal of Applied Physics*, vol. 111, no. 7, p. 07D304, 2012.
- [143] M. Albert, M. Franchin, T. Fischbacher, G. Meier, and H. Fangohr, “Domain wall motion in perpendicular anisotropy nanowires with edge roughness,” *Journal of Physics: Condensed Matter*, vol. 24, no. 2, p. 024219, 2012.
- [144] K.-J. Kim and S.-B. Choe, “Analytic theory of wall configuration and depinning mechanism in magnetic nanostructure with perpendicular magnetic anisotropy,” *Journal of Magnetism and Magnetic Materials*, vol. 321, no. 14, pp. 2197–2199, 2009, current Perspectives: Modern Microwave Materials.
- [145] A. Himeno, S. Kasai, and T. Ono, “Depinning fields of a magnetic domain wall from asymmetric notches,” *Journal of Applied Physics*, vol. 99, no. 8, p. 08G304, 2006.
- [146] S. J. Noh, Y. Miyamoto, M. Okuda, N. Hayashi, and Y. Keun Kim, “Effects of notch shape on the magnetic domain wall motion in nanowires with in-plane or perpendicular magnetic anisotropy,” *Journal of Applied Physics*, vol. 111, no. 7, p. 07D123, 2012.
- [147] T. Gerhardt, A. Drews, and G. Meier, “Controlled pinning and depinning of domain walls in nanowires with perpendicular magnetic anisotropy,” *Journal of Physics: Condensed Matter*, vol. 24, no. 2, p. 024208, 2012.
- [148] J. H. Franken, H. J. M. Swagten, and B. Koopmans, “Shift registers based on magnetic domain wall ratchets with perpendicular anisotropy,” *Nature Nanotechnology*, vol. 7, no. 8, pp. 499–503, 2012.
- [149] J. E. Davies, O. Hellwig, E. E. Fullerton, G. Denbeaux, J. B. Kortright, and K. Liu, “Magnetization reversal of Co/Pt multilayers: Microscopic origin of high-field magnetic irreversibility,” *Physical Review B*, vol. 70, p. 224434, Dec 2004.
- [150] L. Néel, “Théorie du traînage magnétique des substances massives dans le domaine de rayleigh,” *Le Journal de Physique et le Radium*, vol. 11, no. 2, pp. 49–61, 1950.
- [151] W. F. Brown, “Thermal Fluctuations of a Single-Domain Particle,” *Physical Review*, vol. 130, pp. 1677–1686, Jun 1963.
- [152] M. P. Sharrock, “Time dependence of switching fields in magnetic recording media (invited),” *Journal of Applied Physics*, vol. 76, no. 10, pp. 6413–6418, 1994.

- [153] W. Wernsdorfer *et al.*, “Experimental Evidence of the Néel-Brown Model of Magnetization Reversal,” *Physical Review Letters*, vol. 78, pp. 1791–1794, Mar 1997.
- [154] M. Sharrock and J. McKinney, “Kinetic effects in coercivity measurements,” *IEEE Transactions on Magnetics*, vol. 17, no. 6, pp. 3020–3022, Nov 1981.
- [155] D. Weller and A. Moser, “Thermal effect limits in ultrahigh-density magnetic recording,” *IEEE Transactions on Magnetics*, vol. 35, no. 6, pp. 4423–4439, Nov 1999.
- [156] J. B. C. Engelen *et al.*, “Thermally induced switching field distribution of a single CoPt dot in a large array,” *Nanotechnology*, vol. 21, no. 3, p. 035703, 2010.
- [157] P. Gaunt, “The frequency constant for thermal activation of a ferromagnetic domain wall,” *Journal of Applied Physics*, vol. 48, no. 8, pp. 3470–3474, 1977.
- [158] P. Gaunt, “Magnetic viscosity and thermal activation energy,” *Journal of Applied Physics*, vol. 59, no. 12, pp. 4129–4132, 1986.
- [159] U. Hartmann, “The point dipole approximation in magnetic force microscopy,” *Physics Letters A*, vol. 137, no. 9, pp. 475–478, 1989.
- [160] J. Kerr, “On rotation of the plane of polarization by reflection from the pole of a magnet,” *Philosophical Magazine Series 5*, vol. 3, no. 19, pp. 321–343, 1877.
- [161] M. Faraday, “Experimental Researches in Electricity. Nineteenth Series,” *Philosophical Transactions of the Royal Society of London*, vol. 136, pp. 1–20, 1846.
- [162] M. Mansuripur, *The Physical Principles of Magneto-optical Recording*. Cambridge University Press, 1995.
- [163] E. Hecht, *Optics*. Addison-Wesley Publishing Company, 1987.
- [164] v. Višňovský, *Optics in Magnetic Multilayers and Nanostructures*, B. J. Thompson, Ed. CRC Press, Taylor & Francis Group, 2006.
- [165] W. Clegg, N. Heyes, E. Hill, and C. Wright, “Development of a scanning laser microscope for magneto-optic studies of thin magnetic films,” *Journal of Magnetism and Magnetic Materials*, vol. 95, no. 1, pp. 49 – 57, 1991.

-
- [166] N. A. E. Heyes, C. D. Wright, and W. W. Clegg, "Observations of magneto-optic phase contrast using a scanning laser microscope," *Journal of Applied Physics*, vol. 69, no. 8, pp. 5322–5324, 1991.
- [167] T. J. Silva and A. B. Kos, "Nonreciprocal differential detection method for scanning Kerr-effect microscopy," *Journal of Applied Physics*, vol. 81, no. 8, pp. 5015–5017, 1997.
- [168] U. Hartmann, "Magnetic Force Microscopy," *Annual Review of Materials Science*, vol. 29, no. 1, pp. 53–87, 1999.
- [169] D. Rugar *et al.*, "Magnetic force microscopy: General principles and application to longitudinal recording media," *Journal of Applied Physics*, vol. 68, no. 3, pp. 1169–1183, 1990.
- [170] J. J. Sáenz *et al.*, "Observation of magnetic forces by the atomic force microscope," *Journal of Applied Physics*, vol. 62, no. 10, pp. 4293–4295, 1987.
- [171] Y. Martin and H. K. Wickramasinghe, "Magnetic imaging by "force microscopy" with 1000 Å resolution," *Applied Physics Letters*, vol. 50, no. 20, pp. 1455–1457, 1987.
- [172] S. Foner, "Versatile and Sensitive Vibrating-Sample Magnetometer," *Review of Scientific Instruments*, vol. 30, no. 7, pp. 548–557, 1959.
- [173] D. O. Smith, "Development of a Vibrating-Coil Magnetometer," *Review of Scientific Instruments*, vol. 27, no. 5, pp. 261–268, 1956.
- [174] A. Gerber *et al.*, "Extraordinary Hall effect in magnetic films," *Journal of Magnetism and Magnetic Materials*, vol. 242–245, pp. 90 – 97, 2002, proceedings of the Joint European Magnetic Symposia (JEMS'01).
- [175] J. Moritz, B. Rodmacq, S. Auffret, and B. Dieny, "Extraordinary Hall effect in thin magnetic films and its potential for sensors, memories and magnetic logic applications," *Journal of Physics D: Applied Physics*, vol. 41, no. 13, p. 135001, 2008.
- [176] W. Kern, "The Evolution of Silicon Wafer Cleaning Technology," *Journal of The Electrochemical Society*, vol. 137, no. 6, pp. 1887–1892, 1990.
- [177] J. Jaworowicz *et al.*, "Magnetic logic using nanowires with perpendicular anisotropy," *Nanotechnology*, vol. 20, no. 21, p. 215401, 2009.
- [178] P. D. Tougaw and C. S. Lent, "Logical devices implemented using quantum cellular automata," *Journal of Applied Physics*, vol. 75, no. 3, pp. 1818–1825, 1994.

- [179] E. Varga *et al.*, “Experimental demonstration of fanout for Nanomagnet Logic,” in *Device Research Conference (DRC)*, June 2010, pp. 95–96.
- [180] W. Wang, K. Walus, and G. Jullien, “Quantum-Dot Cellular Automata Adders,” in *3rd IEEE Conference on Nanotechnology (IEEE-NANO)*, vol. 1, Aug 2003, pp. 461–464.
- [181] N. Weste and K. Eshraghian, *Principles of VLSI CMOS Design: A Systems Perspective*, ser. VLSI system series. Pearson Education, 2002.
- [182] E. Varga, G. Csaba, G. Bernstein, and W. Porod, “Implementation of a Nanomagnetic Full Adder Circuit,” in *11th IEEE Conference on Nanotechnology (IEEE-NANO)*, Aug 2011, pp. 1244–1247.
- [183] R. Perricone, X. Hu, J. Nahas, and M. Niemier, “Design of 3D nanomagnetic logic circuits: A full-adder case study,” in *Design, Automation and Test in Europe Conference and Exhibition (DATE)*, March 2014, pp. 1–6.
- [184] X. Ju, M. Niemier, M. Becherer, W. Porod, P. Lugli, and G. Csaba, “Systolic Pattern Matching Hardware With Out-of-Plane Nanomagnet Logic Devices,” *IEEE Transactions on Nanotechnology*, vol. 12, no. 3, pp. 399–407, May 2013.
- [185] S. Hu, *Threshold Logic*. University of California Press, Berkeley, 1965.
- [186] R. O. Winder, *Applied Automata Theory*. Academic Press, New York, 1968, ch. Fundamentals of threshold logic, pp. 235–318.
- [187] M. T. Niemier *et al.*, “Nanomagnet logic: progress toward system-level integration,” *Journal of Physics: Condensed Matter*, vol. 23, no. 49, p. 493202, 2011.
- [188] H. Kung, “Why Systolic Architectures?” *Computer*, vol. 15, no. 1, pp. 37–46, Jan 1982.
- [189] M. Crocker, X. Hu, and M. Niemier, “Design and comparison of NML systolic architectures,” in *IEEE/ACM International Symposium on Nanoscale Architectures (NANOARCH)*, June 2010, pp. 29–34.
- [190] X. S. Hu, M. Crocker, M. Niemier, M. Yan, and G. Bernstein, “PLAs in quantum-dot cellular automata,” in *IEEE Computer Society Annual Symposium on Emerging VLSI Technologies and Architectures*, March 2006, pp. 1–6.
- [191] M. Crocker, M. Niemier, and X. S. Hu, “A Reconfigurable PLA Architecture for Nanomagnet Logic,” *Journal on Emerging Technologies in Computing Systems*, vol. 8, no. 1, pp. 1:1–1:25, 2012.

-
- [192] H. Cho and E. Swartzlander, “Adder Designs and Analyses for Quantum-Dot Cellular Automata,” *IEEE Transactions on Nanotechnology*, vol. 6, no. 3, pp. 374–383, May 2007.
- [193] K. Narayanapillai and H. Yang, “Control of domain wall motion at vertically etched nanotrench in ferromagnetic nanowires,” *Applied Physics Letters*, vol. 103, no. 25, p. 252401, 2013.
- [194] U. Bauer, S. Emori, and G. S. D. Beach, “Voltage-controlled domain wall traps in ferromagnetic nanowires,” *Nature Nanotechnology*, vol. 8, no. 6, pp. 411–416, 2013.
- [195] T. J. Hayward and D. A. Allwood, “Magnetic domain walls: Traps with potential,” *Nature Nanotechnology*, vol. 8, no. 6, pp. 391–392, 2013.
- [196] L. Ji, A. Orlov, G. Bernstein, W. Porod, and G. Csaba, “Domain-wall trapping and control on submicron magnetic wire by localized field,” in *9th IEEE Conference on Nanotechnology (IEEE-NANO)*, July 2009, pp. 758–762.
- [197] D. Petit *et al.*, “High efficiency domain wall gate in ferromagnetic nanowires,” *Applied Physics Letters*, vol. 93, no. 16, p. 163108, 2008.
- [198] S.-M. Ahn, K.-W. Moon, C.-G. Cho, and S.-B. Choe, “Control of domain wall pinning in ferromagnetic nanowires by magnetic stray fields,” *Nanotechnology*, vol. 22, no. 8, p. 085201, 2011.
- [199] M. Alam, M. Siddiq, G. Bernstein, M. Niemier, W. Porod, and X. Hu, “On-Chip Clocking for Nanomagnet Logic Devices,” *IEEE Transactions on Nanotechnology*, vol. 9, no. 3, pp. 348–351, May 2010.
- [200] M. Siddiq *et al.*, “Integration of Nanomagnetic Logic Gate with On-Chip Clock and Multiple-Programmable-Electrical Inputs,” in *IEEE International Magnetism Conference*, 2014, pp. EC–1.
- [201] I. M. Miron *et al.*, “Perpendicular switching of a single ferromagnetic layer induced by in-plane current injection,” *Nature*, vol. 476, no. 7359, pp. 189–193, 2011.
- [202] P. P. J. Haazen, E. Mure, J. H. Franken, R. Lavrijsen, H. J. M. Swagten, and B. Koopmans, “Domain wall depinning governed by the spin Hall effect,” *Nature Materials*, vol. 12, no. 4, pp. 299–303, 2013.
- [203] J. H. Franken *et al.*, “Precise control of domain wall injection and pinning using helium and gallium focused ion beams,” *Journal of Applied Physics*, vol. 109, no. 7, p. 07D504, 2011.

- [204] R. Mansell, A. Beguivin, A. Fernandez-Pacheco, D. Petit, J. H. Lee, and R. Cowburn, “Data injection and propagation in NOT gate chains with perpendicularly magnetized dipole coupled nanomagnetic elements,” in *Digest Book of the 2014 IEEE International Magnetism Conference (INTERMAG)*, vol. EC-10, Dresden, 2014.

Related Theses

- [Bre09] Stephan Breitzkreutz. Aufbau eines magneto-optischen Messplatzes zur Charakterisierung von Co/Pt Mehrlagenschichten. Master's thesis, Technische Universität München, 2009.
- [Che10] Dong Chen. Optimization and characterization of the switching field from a Co/Pt multilayer film. Master's thesis, Technische Universität München, 2010.
- [Clo09] Laurent Cloquette. Optimization of a magneto-optical measurement setup in order to characterize ion beam patterned field-coupled nanomagnets. Master's thesis, Technische Universität München, 2009.
- [Erh10] Simon Erhard. Einfluss der Geometrie und Ionenbestrahlung auf feldgekoppelte Nanomagnete. Master's thesis, Technische Universität München, 2010.
- [Fer10] Holger Fernengel. Charakterisierung des Koppelfeldes von feldgekoppelten Nanomagneten. Master's thesis, Technische Universität München, 2010.
- [Fla11] Fabian Flach. Nanomagnetic Logic: controlled switching of field-coupled devices by ion beam irradiation. Master's thesis, Technische Universität München, 2011.
- [Hib12] Gaspard Hiblot. Field-coupled domain wall logic. Master's thesis, Technische Universität München, 2012.
- [Hil12] Christian Hildbrand. Nanomagnetische Logik: Herstellung und Charakterisierung eines 1-bit Volladdierers. Master's thesis, Technische Universität München, 2012.
- [Hue11] Sebastian Huebner. Impact of heavy ion beam irradiation on the switching behavior of multilayered Co/Pt nanomagnets. Master's thesis, Technische Universität München, 2011.
- [Lun11] Benedikt Lünz. Kontrollierte Ausbreitung von Domänenwänden in Co/Pt Nanostrukturen für Anwendungen in Nanomagnetischer Logik. Master's thesis, Technische Universität München, 2011.

- [Mit12] Iris Mittelbach. Bestimmung von Domänenwandgeschwindigkeiten in Co/Pt-Nanostrukturen. Master's thesis, Technische Universität München, 2012.
- [Neu09] Benedikt Neumeier. Konstruktion und Aufbau eines X-Y-Rastertisches zur Charakterisierung magnetischer Schichten an einem optischen Messplatz. Master's thesis, Technische Universität München, 2009.
- [Sch10] Michael Scholz. Feldgekoppelte Nanomagnete: Charakterisierung des Schaltverhaltens von Einzeldots. Master's thesis, Technische Universität München, 2010.
- [Sch12] Daniel Schiessl. Analyse und Optimierung von Bestrahlungsparametern zur Schaltfeldminimierung partiell bestrahlter Co/Pt-Nanomagnete. Master's thesis, Technische Universität München, 2012.
- [Sta11] Michael Stacheter. Charakterisierung von feldgekoppelten Nanomagneten hinsichtlich Kopplung und Schaltfeldvariationen. Master's thesis, Technische Universität München, 2011.
- [Yil10] Cenk Yilmaz. Simulation von Bauelementen und Systemen aus feldgekoppelten Nanomagneten. Master's thesis, Technische Universität München, 2010.
- [Zie13] Grazvydas Ziemys. Influence of sub-100ns current pulses on the domain wall motion in magnetic nanowires. Master's thesis, Technische Universität München, 2013.

Danksagung

Mein erster Dank geht an meine Doktormutter Prof. Doris Schmitt-Landsiedel, die mir diese Arbeit am Lehrstuhl für Technische Elektronik ermöglicht hat. Besonders bedanken möchte ich mich für das Vertrauen in meine Arbeit und für die Möglichkeit, viele führende internationale Konferenzen zu besuchen um unsere mittlerweile sehr anerkannte Forschungsarbeit zu präsentieren.

Ein besonderer Dank geht an Dr. Markus Becherer, der während meiner Diplomarbeit mein Interesse für die Magnete geweckt und anschließend in größtem Maße zu den wissenschaftlichen Erfolgen dieser Arbeit beigetragen hat. Mit seiner un-nachahmlichen Leidenschaft für Forschung und Lehre und seiner andauernden freundlichen, hilfsbereiten und wertschätzenden Art war und ist er für mich eine große Unterstützung in all den Jahren. Unvergessen bleiben die zahlreichen Kaffeerunden, denen (gerade Freitag nachmittags) immer wieder faszinierende und erfolgreiche Ideen für unsere wissenschaftliche Arbeit entsprungen sind.

Ein herzlicher Dank geht an alle weiteren Mitarbeiter der Magnetik-Gruppe am LTE. Danke an Josef Kiermaier, der mir bei technologischen und messtechnischen Herausforderungen jederzeit uneingeschränkt mit Rat und Tat zur Seite stand und auch vor so mancher ungeplanten Spätschicht nicht zurückgeschreckt ist. Danke an Irina Eichwald, die uns neue und faszinierende wissenschaftliche Ansätze gegeben und uns in so mancher, zweifelnder Phase mit ihrer guten Laune wieder aufgerichtet hat. In guter Erinnerung habe ich auch die gemeinsamen Unternehmungen mit den beiden bei diversen Exkursionen und Konferenzen. Danke auch an Grazvydas Ziemys, der viel Energie in die Magnete steckt und für mich mit seiner stets engagierten Art ein neuer Ansporn in den entscheidenden Momenten war und ist.

Danke an Prof. György Csaba für seine ungebrochene Faszination für die Magnetik am LTE und die gemeinsamen Konferenzen mit anregenden und unterhaltsamen Postersessions und eindrucksvollen Wandertouren (Garibaldi Lake!). Danke auch an Prof. Wolfgang Porod für seinen Einsatz und seine unnachlässige Förderung der Magnetik an der TUM.

Ein großer Dank geht an alle weiteren Mitarbeiter am LTE, als da wären Silke Boche (Danke für die stetige Unterstützung im Reinraum), Rainer Emling (Danke für den unnachlässigen Maschinensupport - "Ich schau gleich mal nach..." - und die sofortige Bewältigung von IT-Problemen), das Sekretariat (Bettina Cutrupia, Lydia Thalau und Marta Giunta, Danke für die stete Hilfsbereitschaft bei Organisation und Abrechnungen), die Werkstatt (Danke für die schnellen und passgenauen Bauteile, gerade für die magneto-optischen Messgeräte, und für die Organisation diverser Feiern), Stefan Drapatz (Danke für die gemeinsamen Kaffeerunden, Radel- und Langlauftouren, Skitage und McDonalds-Besuche, sowohl einzeln als auch in Kombination), Dr. Uwe Penning (Danke für die jederzeit verfügbare Problemlösung - "kein Problem, das kriegen wir hin" - und den ein oder anderen Kaffee vor TE). Danke auch an Martin Wirnshofer (für Radeltouren und diverse Pausen), Werner Kraus (für IT- und Reinraum-Support), Cenk Yilmaz (für die unterhaltsame Atmosphäre bei unzähligen TE- und EBE-Korrekturen), Leonhard Heiß (für TE und alles weitere drumherum), und viele weitere...

Ein sehr großer Dank geht an meine Familie für die fortwährende Unterstützung vor und während dieser Arbeit, dass sie mir im Laufe der Jahre stets den Rücken gestärkt und mir alle Freiheiten gegeben hat.

Mein größter Dank aber geht an meine Frau Cornelia von Gamm, die mich in meinem Weg stets bestärkt und mich durch die vielen Tiefen einer Promotion begleitet und aus diesen wieder herausgeholt hat. Danke, dass Du immer für mich da bist!